SCUOLA DI DOTTORATO
UNIVERSITÀ DEGLI STUDI DI MILANO-BICOCCA

Department of Earth and Environmental Sciences

PhD program in: Chemical, Geological and Environmental Sciences Cycle 35°

Curriculum in: Earth Sciences

THE POST-VARISCAN EVOLUTION OF THE CENTRAL SOUTHERN ALPS: INSIGHTS FROM SYNCHRONOUS FAULT ACTIVITY, HYDROTHERMALISM AND MAGMATISM IN THE OROBIC AND COLLIO BASINS

LOCCHI SOFIA
Registration number: 854357

Tutor: Prof. Stefano Zanchetta

Co-Tutor: Prof. Andrea Zanchi

Coordinator: Prof. Marco Giovanni Malusà

ACADEMIC YEAR 2021/2022

TABLE OF CONTENTS

ABSTRACT

During the Early Permian, the post-Variscan evolution of the present-day Alpine region was characterized by crustal extension combined with strong magmatic activity at different crustal levels, which finally led to the development of intracontinental extensional basins filled with volcanoclastic sediments (e. g. the Orobic Basin, N Italy). In the central Southern Alps (cSA), the opening of these basins was controlled by complex fault system that were active at the same time of plutons intrusion and volcanic activity at the surface. Relationships among magmatism, tectonics and hydrothermal activity related to the formation of ore deposits in the Early Permian so far have been only briefly addressed.

This Ph.D. research project focuses on the investigations of the above described features, trying to consider the geological processes active in the Early Permian in an integrated scenario. Several Early Permian faults of the Orobic Basin have been investigated with special emphasis on the recognition of their original features, as they have exceptionally escaped most of the Alpine deformation. In the past, the architecture of Permian basins was described as horst-and-graben structures, formed in response of wrench tectonics developed during the activity of a megashear zone that led to the Pangea B to Pangea A transformation after the collapse of the Variscan orogen. However, thanks to the most recent studies, a different fault architecture has been suggested to had controlled the opening of the Permian basins: a combination of Low-Angle Normal faults (LANFs) and High-Angle Normal Faults (HANFs).

The identified LANFs of the Orobic Basin represent the best site to study the interplay among tectonics and magmatism, as they are characterized by cataclastic bands sealed with cm to dm thick layers of dark, aphanitic tourmalinites. These latter are proof of fluids circulation channelled along higher permeability fault zones related to opening of the Orobic Basin. Such tourmaline breccias also crop out in the Trompia Valley (BS) and are interpreted as having formed by magmatic-hydrothermal fluids that produced metasomatic tourmalines with different compositions at different distances from their source. Several authors suggested that tourmalinites from Orobic Alps, tourmalinites from Trompia Valley together with uranium mineralization of Novazza - Vedello Valley are genetically linked. They are seen as products of a large-scale high-temperature hydrothermal system coeval with the Early Permian plutonic-volcanic activity and tectonism, which was also responsible for the emplacement of various types of magmatic-hydrothermal ore deposits in the Southern Alps (Sn-W, U-Mo-Zn, Fe carbonates, sulphides, quartz). However, their genesis has never been fully characterized and the connection between tourmalinites and U ore bodies has also not been deeply investigated so far.

The tourmalinized faults were first noted in various sites of the cSA during the 1990's, when the tectonic importance of LANFs was not yet recognized. In this thesis, the occurrences of tourmalinites are further characterized, looking for the cause of the regional hydrothermalism in the context of intracontinental extension during the Early Permian. Furthermore, due to the likely connection with U ore deposits, the borosilicate study is proposed as tool for better understanding the genesis of the mineralizations. New field based structural analysis are combined with mineral and whole-rock geochemistry, geochronology, microstructural studies and boron- isotopic analysis of tourmalinites from different sectors of the study area, in order to evaluate the origin of these fluids. Results coming out from this study demonstrate, together with B isotope ratios, a temporal and genetical relationship between tourmalinites and Early Permian magmatism in the cSA. Furthermore, the geochemical data on trace elements provide more clues on a direct connection between tourmalinites and the U-mineralization. All these results are finally discussed in the frame of the interplay between tectonic, magmatic and ore generation processes that interested the present day cSA area in the Early Permian.

RIASSUNTO

Durante il Permiano Inferiore, l'evoluzione post-Varisica dell'attuale regione Alpina è stata caratterizzata da una importante estensione crostale, combinata con intensa attività magmatica a diverse profondità, che infine ha favorito lo sviluppo di bacini estensionali intra-continentali con deposizione di sedimenti vulcanoclastici (e.g. Bacino Orobico, N Italia). Nel settore centrale delle Alpi Meridionali, l'apertura di questi bacini era controllata da complessi sistemi di faglia, attivi contemporaneamente con l'intrusione di plutoni e l'attività vulcanica in superficie. Ad oggi, i rapporti tra magmatismo, tettonica e attività idrotermale correlata alla formazione di giacimenti durante il Permiano Inferiore sono stati brevemente affrontati.

Il seguente progetto di dottorato si focalizza sullo studio delle caratteristiche sopra descritte, con l'intento di approfondire i processi geologici attivi durante il Permiano Inferiore. Diverse faglie di età permiana sono state indagate nel Bacino Orobico, con particolare enfasi sul riconoscimento dei loro tratti originali, poiché esse sono eccezionalmente sfuggite in maggior parte alla deformazione Alpina. Nel passato, l'architettura dei bacini Permiani era stata descritta con strutture a horst-graben, formatesi in risposta ad una tettonica transtensiva, sviluppatasi durante l'attività di una vasta zona di taglio che ha portato alla trasformazione da Pangea B a Pangea A in seguito al collasso dell'orogene Varisico. Tuttavia, grazie a studi più recenti, è stato indicato un diverso setting di faglie che hanno controllato l'apertura dei bacini Permiani: si tratta infatti di una combinazione di faglie normali a basso e alto angolo.

Le faglie normali a basso angolo identificate lungo il Bacino Orobico rappresentano il miglior luogo in cui osservare l'interazione tra attività tettonica e magmatismo, dal momento che i loro nuclei di faglia sono caratterizzati da bande cataclastiche, successivamente sigillate da scuri livelli di tormaliniti spessi da alcuni cm a dm. Queste ultime testimoniano la circolazione di fluidi arricchiti in boro e incanalati lungo importanti zone di faglia a maggior permeabilità, che sono correlate all'apertura del Bacino Orobico. Simili brecce a tormalina affiorano anche in Val Trompia (BS) e sono interpretate come il risultato di fluidi magmatico-idrotermali che hanno prodotto tormaline con diverse composizioni a diverse distanze dalla loro sorgente. Molti autori hanno suggerito che le tormaliniti delle Alpi Orobie, quelle della Val Trompia unitamente alla mineralizzazione di uranio del distretto di Novazza-Val Vedello potrebbero essere genericamente correlate. Esse sono state interpretate come prodotti di un sistema idrotermale di alta temperatura su ampia scala, coevo con l'attività tettono-magmatica del Permiano Inferiore che è responsabile anche della messa in posto di svariati depositi di minerali metalliferi nelle Alpi Meridionali (Sn-W, U-Mo-Zn, carbonati di Fe,

solfuri, quarzo). Tuttavia, la genesi delle tormaliniti non è mai stata dettagliatamente caratterizzata e la loro connessione con i giacimenti di uranio finora non è mai stata investigata.

Le faglie tormalinizzate sono state riconosciute in molte località del settore centrale delle Alpi Meridionali durante gli anni ’90, quando ancora non era nota l’importanza tettonica delle faglie normali a basso angolo di età Permiana. In questa tesi di dottorato, vengono ulteriormente caratterizzate le aree con i primi ritrovamenti e anche quelle in cui sono state riconosciute nuove tormaliniti, ricercando la causa dell’idrotermalismo regionale nel contesto di estensione intra-continentale durante il Permiano Inferiore. Inoltre, per via del possibile link genetico con i giacimenti di uranio, lo studio dei borosilicati viene proposto come strumento per meglio caratterizzare la genesi delle mineralizzazioni. Nuove osservazioni di terreno su tormaliniti provenienti da diversi settori dell’area di studio, sono combinate con lo studio della geochimica dei minerali e della roccia totale, insieme alla geocronologia, a studi microstrutturali e analisi isotopiche del boro, con lo scopo finale di definire l’origine di questi fluidi arricchiti in boro. I risultati ottenuti da questa ricerca, inclusi i rapporti isotopici del B, dimostrano che le tormaliniti e il magmatismo Permiano delle Alpi Meridionali sono in stretta correlazione temporale e genetica. Inoltre, i dati geochimici sugli elementi in tracce forniscono maggiori indizi su una diretta connessione tra tormaliniti e la mineralizzazione a uranio dell’area di Novazza-Val Vedello. Tutti questi dati, per concludere, sono discussi nel contesto di interazione di processi tettonici, magmatici e di formazione di giacimenti che hanno interessato l’attuale settore centrale delle Alpi Meridionali durante il Permiano Inferiore.

1. INTRODUCTION

The post-orogenic evolution of the Central Variscan belt was characterized by intensive crustal extension active between the Late Carboniferous and the Early Permian, just after the collapse of the orogen (McCann et al. 2006, Stampfli and Kozur 2006; Ziegler et al. 2006). The entire area was interested by the development of several intracontinental fault-controlled basins filled with volcano-sedimentary successions, as a consequence of the strong crustal extension combined with intense magmatic activity developed at different crustal levels (Schaltegger and Brack 2007; Schuster and Stüwe 2008).

In the central Southern Alps (cSA), new structural evidence of Early Permian crustal extension after the collapse of the Variscan orogen have been recognized. The understanding of the role played by extensional faults during the passage from the Variscan orogeny to the Permian extension is of extreme importance to interpret the geodynamic events that affected Southern Europe after the Variscan orogenesis, which is still a under debate. In the whole Southern Alps area, other Permian evidence is represented by the coeval magmatism, which is diffused from the Ivrea-Verbano zone to the west, to the eastern Southern Alps in the east. In the cSA, the sector comprised between Lake Como and the Giudicarie belt, the Early Permian magmatic products occur both as intrusive bodies and volcanic-volcaniclastic products (e.g. Schaltegger and Brack 2007; Berra et al. 2016). The volcanic-volcaniclastic products are interlayered in the sedimentary successions that filled the intra-continental basins (Cadel et al. 1996; Cassinis et al. 2012). The opening of these basins was controlled by fault systems that developed in response of the extensional regime, active on the whole Variscan belt.

Several segments of the Permian fault systems are still observable in the Orobic Basin area, as they exceptionally escaped the Alpine deformation (Froitzheim et al. 2008; Pohl et al. 2018; Zanchi et al. 2019; Locchi et al. 2022; Zanchetta et el. 2022) and thus allow the reconstruction of the basin's faults architecture. The most important structures are recently recognized (Zanchi et al., 2019; Locchi et al., 2022) low-angle normal faults (LANFs), which mainly developed at the contact between the Lower Permian sedimentary cover in the hangingwall and the Variscan basement in the footwall. Until now, two major well-preserved Permian LANFs are documented at the head of the Brembana Valley (Bergamo, N Italy). In the past, the architecture of Permian basins was described by a combination of horsts and grabens controlled by high angle normal faults and wrench tectonics (Cassinis et al. 2008), in response to the progressive evolution of a transform margin interesting part of the European area. However, thanks to the most recent studies, the occurrence of LANFs combined with High-Angle Normal Faults (HANFs) point to different geometries. Furthermore, in the proximity of these systems soft-sediment deformation structures occur, testifying to the simultaneity of deposition of the sedimentary sequence and of the faults activity. For these reasons, further investigations on the tectonic mechanism of basin' opening and on other eventual LANF-HANF systems in the Orobic Basin are necessary.

The relationship between Early Permian tectonics and magmatism has never been deeply investigated, except for the temporal overlapping of volcanism and opening of the intracontinental fault-controlled basins. The recognition of well-preserved LANFs fault core offers new insights on the interplay between magmatism and tectonics, since they are characterized by peculiar rocks that could be indication for hydrothermal fluids rising from depth. For this reason, the present Ph.D. thesis focuses on the analysis of fault rocks.

In particular, cataclastic bands characterize the LANFs fault core, which are always sealed by centimetric layers of dark aphanitic tourmalinites (Zanchi et al., 2019; Zanchetta et al. 2022). Tourmalinites are uncommon rocks containing ≥ 20 vol.% tourmaline (Slack 1982; Bates and Jackson, 1987) and are evidence of intense metasomatic effects by boron-rich fluids along the Permian fault cores (Zhang et al. 1994; Slack et al. 1996; De Capitani et al. 1999; Zanchetta et al. 2022). The occurrence of tourmalinites has been also documented as veins with a brecciated texture, intruding the Variscan basement in the eastern cSA, within the thermal aureole of magmatic intrusive bodies, emplaced in the Early Permian.

Tourmaline is a common accessory phase that can be found in several types of rocks in a wide range of pressure-temperature conditions (Krosse 1995; Ota et al. 2008) and in a wide range of geological settings like metamorphic, magmatic, and hydrothermal contexts (Henry and Dutrow 1996; Van Hinsberg et al. 2011). It also occurs associated to a variety of hydrothermal ore deposits, including porphyry-type Cu–Mo and Au deposits (e.g. Slack 1996; Lynch and Ortega 1997; Yavuz et al. 1999a), granite-related Sn-W deposits (e.g. Taylor 1979; Pollard et al. 1987; Jiang et al. 2004; Mlynarczyk and Williams-Jones 2006) and U deposits (e.g. Rich 1976; Yavuz et al. 2008). Tourmaline can be used as proxy for better understanding the origin of many ore deposits (Fuchs and Maury 1995) and it can be considered also for the cSA area, as several hydrothermal manifestations and ore deposits occur close to the tourmalinites. The most important is the U-rich mineralizations of the Novazza-Vedello Valley district, occurring within the volcanics of the Early Permian basins or along branches of LANFs that controlled the opening of the same basins (Cassinis et al.1986; Philippe et al. 1987; Zhang et al. 1994; Cadel et al. 1996; Slack et al. 1996; De Capitani et al. 1999). Together with the uranium ore deposits, other significant coeval mineralizations occur in the proximity of the magmatic aureole of the Permian intrusives from Trompia Valley area, such as swarms of siderite- sulphide-quartz veins associated with Sn-W greisens. the Torgola fluorite vein system and the large Maniva Pass-Val di Vaia quartz vein system (Moroni 1994; Frizzo 1995;

Cassinis et al. 1995; De Capitani et al. 1999; Martin et al. 2017) being the major ore manifestations. All these evidence point to a strong and complex magmatic-hydrothermal activity involving the entire area of the Orobic and Collio Basins.

The strict relationships between tourmalinites and the structures that controlled the opening of the Orobic Basin, suggest a direct correlation among them. The hydrothermal event producing tourmalinites along LANFs fault core and tourmalinitic breccias in Trompia Valley was supposed to be the same, and genetically linked to the Permian magmatism (Cadel et al. 1996; De Capitani et al. 1999). In addition, due to the link between tourmalines and ore deposits in other geological contexts, the study of borosilicates and determinations of their physic-chemical stability can be important tools for better understanding the ore deposits origin and use tourmaline and tourmalinites as proxies (Fuchs and Maury 1995). A direct correlation between Early Permian tectonics and magmatism, B-metasomatism along LANFs and the formation of uranium ore deposits has been only suggested in the past and briefly addressed by recent works (e. g. Cadel et al. 1986; Zanchetta et al. 2022). However, the genesis of tourmalinites and the origin of boron-rich fluids has never been fully explained, as well as the connection with the uranium deposits of the Novazza-Vedello Valley district. The complexity of the Permian context and the unsolved questions are the spotlight of the present research project, which attempts to define the Early Permian evolution in the cSA through new insights on the tectonic, magmatic and hydrothermal activity.

To demonstrate the interplay among tectonics, magmatism and B-rich hydrothermalism with possible genetic link to U-mineralizations, it was necessary defining first of all the tectonic setting of the Orobic Basin. This Ph.D. thesis endeavours to provide a better characterization of the genetic mechanism of Low-Angle Normal Faults (LANF) or extensional detachments, which have been extensively described in current areas of continental extension. Due to the complexity of this case study, the project will take account the already available data, and apply a multimethodological approach on new findings, in order both to exalt the originality of the work done in the past and to provide innovative points of view. The main planned methodologies include geological-structural mapping, mesoscopic and microstructural analysis, reconstruction of fault systems architecture in order to display the geometry of low angle and associated high angle normal faults.

Areas of the cSA with structural and geological setting similar to the already documented LANFs have been investigated. A previously unknown Permian fault system related to the opening of the Orobic basin is identified: combination of low- and high-angle normal faults characterizes the structure of the western termination of the Orobic Basin in the upper Gerola Valley, within the northern portion of the cSA. These newly described normal faults, together with LANFs recognized in other locations of the cSA (Zanchi et al. 2019 and references therein), and the Grassi Detachment in Valsassina (Froitzheim et al. 2008; Pohl et al. 2018) provide a significant contribution for the reconstruction of the Early Permian Orobic Basin architecture and indirectly testify also to the ongoing magmatic activity. Furthermore, the Early Permian basins of the cSA are here compared to modern orogenic collapse structures: the Orobic Basin can be considered as a fossil equivalent of recent tectonically-controlled extensional basins. For this reason, the analysis of the Permian tectonic structures in the cSA, preserved as unique relicts of an ancient tectonic history, can also provide important insights on active tectonic extensional contexts. Then, the tectonic evolution of the Orobic Basin is discussed in the frame of the large-scale geodynamic scenario active during the Permian, and these investigations help also to better understand the following tectonic control exerted by the inherited LANFs during the Alpine shortening.

In parallel to the definition of the tectonic background, the research was focused on the characterization of the boron-rich hydrothermalism associated to the Early Permian magmatism. Indeed, the first hypothesis is that these fluids in the Trompia Valley are products of the magmatic activity, for this reason the already available data on Permian intrusives are considered to define a thorough dataset. The information gaps were solved with the production of new data, such as updated whole rock analysis and U-Pb dating on zircons of the Trompia Valley intrusives. Then, the already available material of tourmalinites was combined with the recent identification of these rocks in the cSA. A brief definition of a sample of uranium mineralization, provided by a geologist who worked in the exploring tunnels of the Vedello Valley mine, concludes the description of the analysed material. This sample is used to determine the age with chemical dating on uraninite.

The selected locations with tourmalinites are four, and are distributed all along the Orobic and Collio Basins (Fig. 2.4). Tourmalinites from these locations (green and blue stars of Fig. 4.1) were compared, providing new field observations and new petrographic analysis for many samples listed in Appendix 1, together with whole rock and minerochemical analysis. For selected thin sections, representative for each locality, advanced analyses were performed to quantify the trace element contents in single crystals of tourmaline with LA-ICPMS, and also the boron isotope composition with SIMS. Furthermore, U-Pb dating was applied for the first time on rutiles of tourmalinites from the Trompia Valley area and provide a very important time constrain. All the outcoming results have been considered in order to address the source of this regional boron-rich hydrothermalism in the context of the Early Permian intracontinental extension and magmatism. Geochronological results are then compared with the analysed intrusives and uranium mineralization, and are discussed in the frame of the interplay between tectonic, magmatic and ore generation processes that interested the present day cSA area in the Early Permian.

The present Ph.D. thesis concludes with a reconstruction of the geological scenario of the cSA in the Early Permian times, where all the new structural, geochemical and geochronological insights are evaluated to propose also a reasonable genetic model for the uranium mineralization of the Novazza-Vedello district.

Some results of my Ph.D. work have been published in International Journal of Earth Sciences ("Evidence of Early Permian extension during the post-Variscan evolution of the central Southern Alps (N Italy)" 111, 1717–1738 (2022)) and some chapters are extracted from Minerals ("Metasomatism by Boron-Rich Fluids along Permian Low-Angle Normal Faults (Central Southern Alps, N Italy)" 2022, 12, 404).

2. GEOLOGICAL SETTING

2.1 Transition from the Variscan Orogenesis to the Early Permian extension

The post-Variscan evolution in Europe was characterized by a large crustal reorganization from Late Carboniferous to Early Permian (McCann et al. 2006, Stampfli and Kozur 2006; Ziegler et al. 2006) generally related to a transtensional regime active during or just after the orogenic collapse of the Variscan belt (e.g. Wickham and Oxllurgh, 1987; Dewey, 1988; Mènard and Molnar, 1988; Krohe and Eisbacher, 1988). The former Variscan hinterland appears to have been strongly controlled by the collapse of the mountain belt followed (or partially coeval)by an extensional regime starting in the Early Permian, and resulting in the lithospheric thinning of the Variscan overthickened crust (Brunet and Le Pichon 1982; Brodie and Rutter 1987; Brodie et al. 1989; Prijac et al. 2000; Marotta et al. 2009) from Northern to Southern Europe and in the northernmost portion of the Gondwana plate, including the Adria spur (Van Wees et al. 2000; McCann et al. 2006; Timmerman et al. 2009, Zech et al. 2010). Conversely, the former foreland was mostly dominated by late Variscan wrench tectonics in the Stephanian-Autunian times (Van Wees et al. 2000), especially along the boundary between the Precambrian and the Phanerozoic Europe (Dadlez et al. 1995). This transtensional regime is often interpreted to be related to the transition from the Early Permian Pangea B configuration, with Gondwana further to the East (Irving 1977; Muttoni et al. 2013), to the Late Permian Pangea A setting, following a counter-clockwise rotation of Gondwana with respect to Laurasia, as suggested by palaeomagnetic data (Muttoni et al. 1996, Muttoni et al. 2001, Muttoni et al. 2003, Muttoni et al. 2009; Bachtadse et al. 2018; Muttoni and Kent 2019a, 2019b; Kent and Muttoni 2020).

According to this hypothesis, ~3,500-km of dextral horizontal displacement took place along a WSW-ENE-trending mega shear zone between Pangea’s northern part (Laurasia) and its southern part (Gondwana) (Arthaud and Matte 1977; Ziegler 1986, 1988), transforming the Late Palaeozoic Pangea B situation into the Mesozoic Pangea A situation (Fig. 2.1; Irving, 1977). However, this geodynamic interpretation is currently under debate, and the Permian Basins in the Southern Alps in Italy have played a prominent role in the Pangea A versus B controversy (Pohl et al. 2018). Despite some authors define them as pull-apart basins (Cassinis and Perotti 1994; Cadel et al. 1996; Cassinis et al. 1997; Cassinis et al. 2008; Cassinis et al. 2012), according to recent findings of faults related to pure extension (e.g. Froitzheim et al. 2008; Pohl et al. 2018; Zanchi et al. 2019; Zanchetta et al. 2022; Locchi et al. 2022), these basins are evidence of a different tectonic scenario, at least in the present-day Southern Alps area.

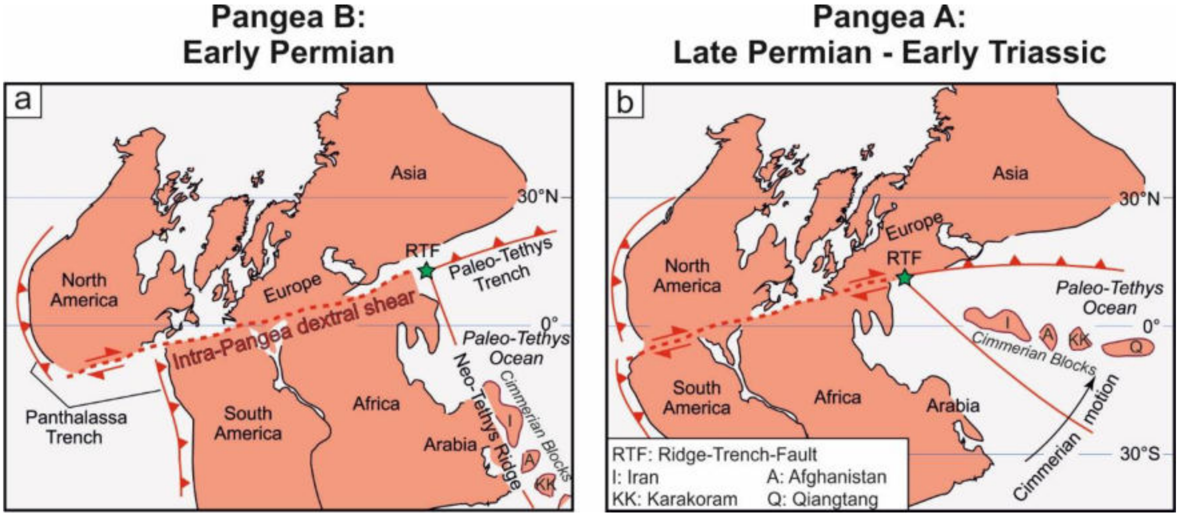

Figure 2.1 - The transformation of Early Permian configuration Pangea B to Late Permian-Early Triassic Pangea A, by displacement along a dextral megashear (modified after Muttoni et al. 2009).

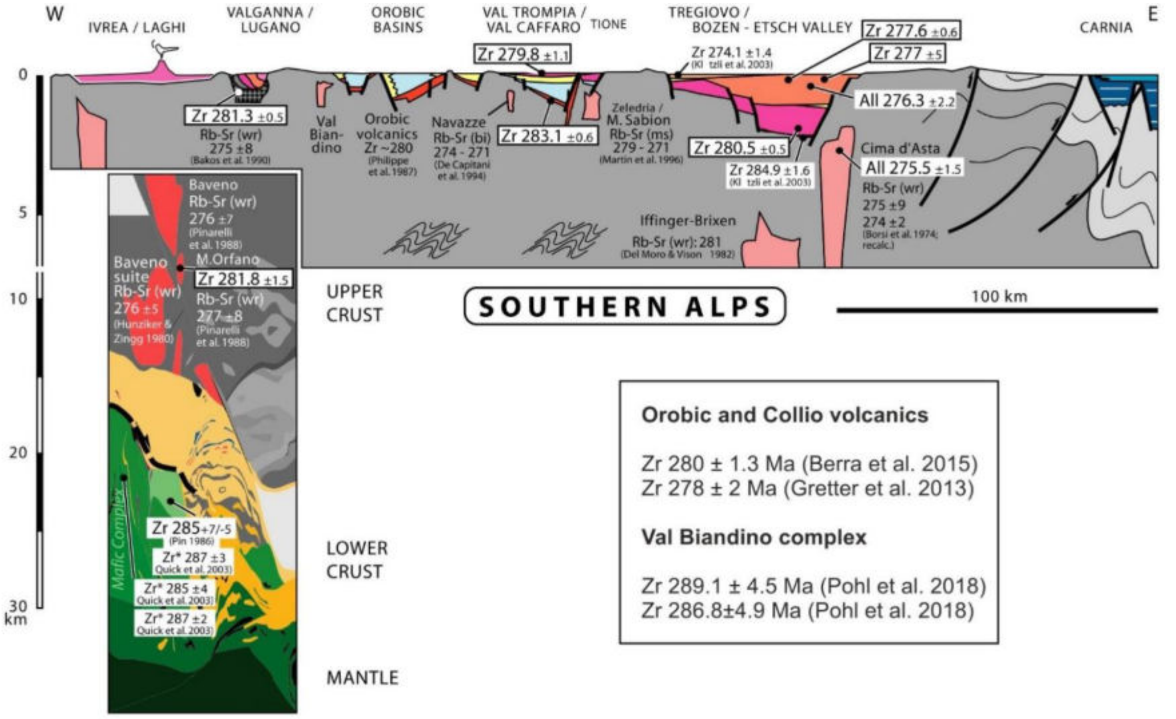

Figure 2.2 - Schematic E–W cross section of the Early Permian of the Southern Alps with geochronological constrains, modified from Schaltegger and Brack (2007). In this sketch the it is noteworthy the widespread distribution of intrusives and volcanic rocks, which are represented in red colours.

Combined to crustal extension, HT metamorphism at middle to lower crustal depths and intense magmatic activity developed in southern Europe at different crustal levels, with emplacement of mafic to intermediate magmatic bodies in the lower crust, intermediate to acid bodies at shallower levels and diffuse volcanic activity at the surface (Fig. 2.2; Marotta and Spalla, 2007; Schaltegger and Brack 2007; Schuster and Stüwe 2008; Spalla et al., 2014). These processes resulted from active rifting, triggered by a progressive lithospheric thinning and asthenospheric upwelling (Diella et al.

1992; Bertotti et al. 1993; Schuster et al. 2001; Stähle et al. 2001; Schuster and Stüwe, 2008; Marotta et al. 2009; Spalla et al. 2014).

The post-orogenic magmatism occurred in several pulses of short duration along the entire central Variscan belt (Schaltegger 1997). In the Alps, traces of Permian intrusions are chiefly preserved in the Pennidic, Austroalpine and South-alpine domains and are widespread from Ivrea-Verbano zone to eastern Southern Alps as shown in Fig. 2.3. In the central Southern Alps (cSA) occur the Trompia Valley (De Capitani et al. 1994) and Valsassina intrusives (Pohl et al. 2018), which will be further considered in the next chapters. At the same time of the Permian magmatism, intracontinental fault-controlled basins evolved in the upper crust in response to the extensional regime (Diella et al. 1992; Bertotti et al. 1993; Schuster et al. 2001; Stähle et al. 2001; Schuster and Stüwe, 2008; Marotta et al. 2009; Spalla et al. 2014).

In the cSA, they were filled by volcanics, volcaniclastic and terrigenous deposits (e.g. Cassinis et al. 2008; Berra et al. 2016; Zanchi et al. 2019; Locchi et al. 2022; Zanchetta et al. 2022). As suggested by the age of volcanism and magmatism, ranging from ca. 290 to 270 Ma (e.g. Schaltegger and Brack 2007; Gretter et al. 2013; Berra et al. 2015), and by the stratigraphic record (Berra and Carminati 2010; Berra et al. 2015, 2016), the Early Permian subsidence and magmatic activity lasted for about four decades of Ma, representing an episodic event. The Lower Permian units were unconformably sealed by the Upper Permian successions after a sedimentary gap during most of the Middle Permian (Cassinis et al. 2012).

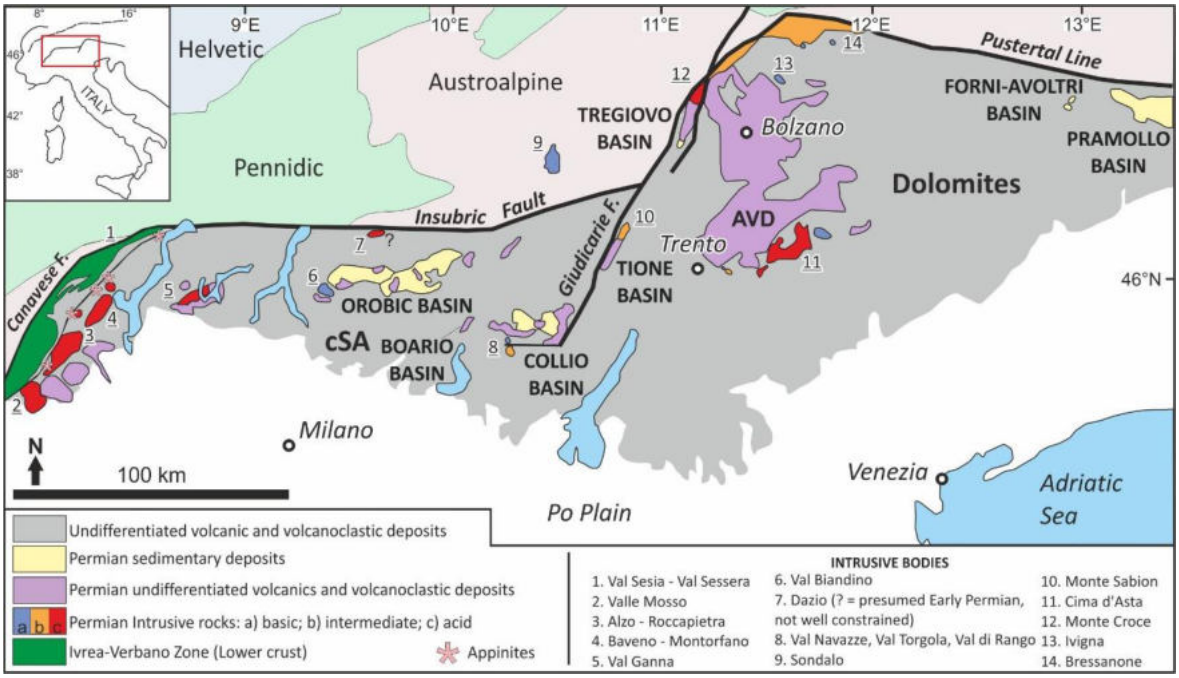

Figure 2.3 - Map representing the Permian magmatism and intra-continental basins lower crust, intrusive bodies, volcanics, and sedimentary cover identified in the Southern Alps (N Italy). The names of the intracontinental fault-controlled basins formed during the Early Permian extensional phases are, from W to E, Orobic, Boario, Collio, Tione, Tregiovo, Forni-Avoltri and Pramollo Basins. The Orobic Basin, our study area, is in the central Southern Alps (cSA). AVD = Athesian Volcanic District.

2.2 The central Southern Alps

The central Southern Alps (cSA, Fig. 2.4) are a thick-skinned fold-and-thrust belt grown since the early stages of the Alpine orogeny (Schönborn 1992; Carminati et al. 1997; Zanchetta et al. 2012, 2015). The northern border is the Insubric Fault (Fig. 2.3 and 2.4) whereas the cSA extends to the south beneath the Quaternary infill of the Po plain, forming the so-called “Milano belt” (Fantoni et al. 2004). They are characterized by S-vergent structures that, in the northern sector of the belt, nucleated before the onset of the continental collision, between the Late Cretaceous and the Eocene, as suggested by pseudotachylyte ^{49}Ar/^{39}Ar ages obtained along major thrust zones (Zanchetta et al. 2011). The main structures inherited from the Permian and Triassic rifting phases were inverted as reverse faults and facilitated the development of this fault system (Castellarin et al. 2006), and they deeply involved the pre-Alpine basement, which is now widely exposed in the northern sector as shown in figure 2.4 (Laubscher 1985; Blom and Passchier 1997; Schönborn 1992; Carminati et al. 1997). The Variscan crystalline basement chiefly consists of two mica-paragneisses and mica-schists (“Morbegno Gneiss” and “Edolo Schists” Auct., respectively, Boriani et al. 2012) with minor lenses of leucocratic orthogneiss (“Gneiss Chiari del Corno Stella” Auct., referred as Gneiss Chiari through the text and in the figures). The Variscan basement was thrusted to the south on the Permian–Mesozoic sedimentary cover along the Orobic-Porcile-Gallinera thrust (OPGT) system, which extends E-W for more than 80 km (Zanchetta et al. 2015). Immediately south of the OPTG, an array of three basement-cored WSW-ENE–trending anticlines, the “Orobic Anticlines” (Orobic, Trabuchello-Cabianca and Cedegolo Anticlines, Fig. 2.5) of De Sitter and De Sitter-Koomans (1949), includes the Lower Permian volcanic, volcaniclastic, and siliciclastic sequence, unconformably covered by the Upper Permian to Lower Triassic units (Forcella and Jadoul 2000; Berra and Siletto 2006). A fourth anticline, the “Camuna Anticline”, occurs to the SE of the other ones, displaying similar features (Forcella and Jadoul, 1990; Schönborn, 1992).

Alpine deformations were preceded by the D_1 and D_2 syn-metamorphic events, which are only recorded in the Variscan basement (Milano et al. 1988; Filippi et al. 2021). Alpine metamorphism affected the structures inherited from the Permian-Jurassic evolution of the area, reaching lower greenschist-facies conditions north of the Orobic–Porcile–Gallinera thrust system and south of the Periadriatic fault system (Crespi 1981; Spalla et al. 1999; Spalla and Gosso 1999; Carminati and Siletto 2005; Filippi et al., 2022). During the Alpine orogenic event, crustal shortening was accommodated by S-SE-verging thrusting and folding in two distinct stages, D_3 and D_4, respectively predating and postdating the 42 to 29 Ma intrusion of the Adamello Batholith (Brack 1981; Schönborn 1992; Carminati et al. 1997; Fantoni et al. 2004; D’Adda et al. 2011; Zanchetta et al. 2011, 2015; D’Adda and Zanchetta 2015; Mittempergher et al. 2021, 2022).

In the northern area of the belt, the basement and the Permian to Lower Triassic successions crop out between the Orobic-Porcile-Gallinera thrust to the north and the Valtorta-Valcanale Fault to the south (Fig. 2.4), which is along the forelimb of the Orobic Anticlines and has been interpreted as back-thrust (Zanchetta et al. 2015 with references). Moving further to the south, tectonostratigraphic units made of Middle Triassic carbonates dominate the area (Fig. 2.4 and 2.5).

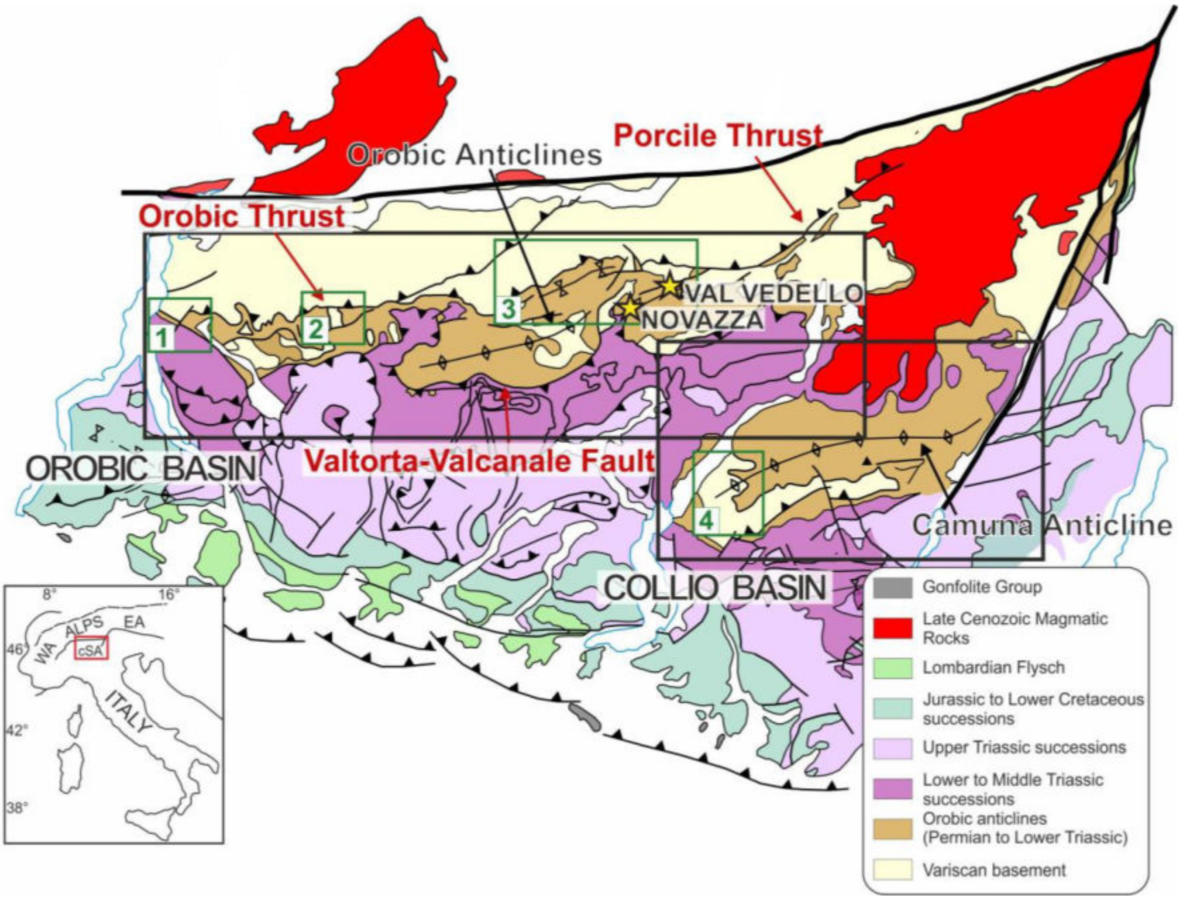

Figure 2.4 - Geological setting of the central southern Alps, modified after Zanchetta et al. 2015. In this tectonic map are shown the main tectono-stratigraphic units that characterize the Orobic and Collio Basins. Here are represented also the most important folds and thrusts characterizing the cSA belt. The yellow stars indicate the occurrences of uranium mineralizations of Novazza and Vedello Valley. The most important areas for the present study are: 1 = Valsassina; 2 = Gerola Valley area; 3 = Forcellino-Vedello Valley and Lake Aviasco area; 4 = Trompia Valley area.

2.3 The Early Permian magmatic and hydrothermal activity in the central Southern Alps

The Early Permian rifting phase was accompanied by HT metamorphism, intense magmatic activity developed at different crustal levels and with heterogeneous geochemistry, and widespread volcanic activity (Fig. 2.2; Schaltegger and Brack 2007; Schuster and Stüwe 2008). The Permian magmatism in the Southern Alps displays a calc-alkaline affinity, resulting from extensive contamination of basaltic magmas, likely derived from enriched lithospheric mantle sources, with felsic crustal melts (e.g. Voshage et al. 1990; Rottura et al. 1998; Marotta and Spalla 2007; Spalla et al. 2014). In the central Southern Alps (cSA), a few intrusive bodies occur within the basement, whereas the effusive products of the magmatic activity are now exposed within the partially deformed Permian basins, like the Orobic and Collio basins.

In the Orobic Basin, most of the volcanic products are represented by the Cabianca Volcanite, belonging to the Laghi Gemelli Group (e.g. Berra and Felletti, 2016). It consists of smaller volumes of andesitic magma associated with several large rhyolitic ash-flow sheets that form ignimbrites (Cadel et al. 1996; Cassinis et al. 2012; Berra and Felletti 2016), with an estimated age of 280 ± 2.5 Ma based on U-Pb zircon geochronology (Philippe et al. 1987; Berra et al. 2015). In the Collio basin, the volcanic member is represented by the Lower Quartziferous Porphyry with an age of 278 ± 2 Ma (Brack and Schaltegger 1999; Gretter et al. 2013). In the study area, the only intrusive bodies broadly coeval with the volcanic units are, to the E the Trompia Valley intrusives (De Capitani et al. 1994) close to the Collio Basin, and to the W the Val Biandino Complex (Pasquarè 1967; De Capitani et al., 1988; Thöni et al. 1992; Sciunnach 2001b; Pohl et al. 2018) at the western end of the Orobic Basin (Fig. 2.3).

In the Trompia Valley area, granitic to granodioritic bodies crop out along the Navazze, Torgola and Rango valleys (Giuseppetti 1959; Martina 1966; De Capitani et al. 1994) (see Fig. 4.17 in chapter 4.1 for localization), whereas a small body of gabbric composition was recognized in the Cavallina valley close to Pezzazze (De Capitani et al. 1992). De Capitani et al. (1994) emphasized a marked variability in the geochemistry of the Trompia Valley magmatic rocks, possibly related to a single compositionally heterogeneous plutonic mass. According to the major elements, they have a subalkaline to shoshonitic composition, with a VAG (Volcanic Arc Granite) affinity. Rb-Sr geochronological data on biotites indicate a cooling age of 274-271 Ma (De Capitani et al. 1994).

In Valsassina, two distinct intrusive bodies form the Val Biandino Complex: the “Val Biandino Quartz-diorite” (Pasquarè, 1967; De Capitani et al., 1988) and the “Valle di San Biagio Granite” (Sciunnach, 2001; Pohl et al., 2018). They crop out in the footwall of the Grassi Detachment, a low-angle normal fault separating the Permian sedimentary succession from the underlying Variscan basement (Froitzheim et al., 2008; Pohl et al. 2018). The occurrence of minor bodies of gabbroic composition have also been reported (Pasquarè, 1967). According to the geochemical data (De Capitani and Liborio 1988; De Capitani et al. 1988) the Val Biandino intrusive Complex displays typical high-K calc-alkaline affinity. The intrusion age has been constrained by U-Pb zircon ages at 289.1 ± 4.5 Ma for the Val Biandino Quartz Diorite and 286.8 ± 4.9 Ma for the Valle San Biagio Granite (Pohl et al., 2018).

The Early Permian magmatism that affected central and southern Europe was likely related to several hydrothermal manifestations and ore genesis (e.g. Dill 1993, Moroni 1994). In the cSA area, evidence of hydrothermal activity and mineralizations related to the Late Carboniferous - Early Permian waning stages of the Variscan orogeny and the onset of a rifting stage are widespread. In the Trompia Valley area, were Permian intrusives crop out to surface and produce a magmatic aureole, swarms of siderite sulphide-quartz veins associated with Sn-W greisens can be found together with the Torgola fluorite vein system and the large Maniva Pass-Val di Vaia quartz vein system (Moroni, 1994; Frizzo 1995; Cassinis et al. 1997; De Capitani et al. 1999; Martin et al. 2017). Tourmaline-quartz breccia bodies (tourmalinites) represent an additional product of hydrothermal activity in the area.

A detailed study of siderite occurrences was reported by Martin et al. (2017) who estimated the temperatures of fluids producing the ores in different localities along the cSA. In their study, one of the most relevant and largest deposit of uranium in Italy, within the Novazza-Vedello Valley district, was considered too (Fig. 2.4).

The U-mineralization is distributed in two different settings: at Novazza, the ore body is hosted in fractures in the volcanic rocks of the Cabianca Volcanite (D. Ravagnani, personal communication), whereas in Vedello Valley it is constrained along the basement-cover contact (Cadel, 1986; Cadel et al. 1987; Fuchs and Maury 1995). The U-Pb chemical dating applied on uraninite from Novazza uranium deposits, which is in textural equilibrium with siderite and Fe-rich dolomite (Martin et al. 2017), provided 275 ± 13 Ma. In addition to these hydrothermal evidence, Cadel (1986) mentioned that pyritization, Na-depletion, silicification and boron metasomatism, possibly related to the earliest stages of hydrothermal activity, were superimposed on the host rocks of the Novazza-Vedello district.

The boron-bearing rocks, namely tourmalinites, were noticed in different sectors of the cSA (Zhang et al. 1994; Slack et al. 1996; De Capitani et al. 1999, Pohl et al. 2018; Zanchi et al. 2019; Zanchetta et al. 2022; Locchi et al. 2022) and several authors related them to the genesis of the uranium mineralization (Cadel et al. 1996; Slack et al. 1996; De Capitani et al. 1999).

2.4 The Early Permian Orobic and Collio Basins

Despite the Alpine event, the Lower Permian stratigraphic successions are still well preserved in the central Southern Alps (cSA) (Zanchetta et al. 2015; Berra et al. 2016). This succession was deposited in fault-controlled intracontinental extensional basins, from west to east, the Orobic, Boario, and Collio basins (Fig. 2.3). The Orobic and Collio basins, the study areas of this work, have been already largely described from the stratigraphic point of view and are filled by the Upper Carboniferous-Permian successions, characterized by two major sedimentary systems.

In this study we mainly define Permian faults of the Orobic Basin because they crop out (Fig. 2.5), and in this case the Lower Permian terrigenous and volcanic units are gathered in the Laghi Gemelli Group (Cassinis et al. 1986; Cadel et al. 1996; Boriani et al. 2012; Cassinis et al. 2012; Berra et al. 2016), unconformably covered by a younger succession, consisting of the Upper Permian continental red beds of the Verrucano Lombardo (Casati and Gnaccolini 1967).
The Lower Permian units of the Orobic Basin are, from the bottom, the up to 100 m thick Basal Conglomerate, covered by the up to 800 m thick Cabianca Volcanite, including large ignimbrite sheets (290 to 270 Ma; Berra et al. 2015). The ignimbrites are conformably covered by the Pizzo del Diavolo Formation, which consists of sandstones, siltstones, slates and, along the external portions of the basin, of coarse-grained proximal conglomerates (Mt. Aga Conglomerate to the north, Ponteranica Conglomerate to the west, and Val Sanguigno Conglomerate to the south). These conglomerates interfinger with fine-grained deposits (volcaniclastic sandstone and dark slates) in the depocentral area of the basin. Mixed continental carbonate terrigenous facies occur in the upper part of the Pizzo del Diavolo Fm. (Berra et al. 2016; Berra et al. 2019). On the base of stratigraphic and tectonic evidence, Berra et al. (2016) suggest that the succession of the Laghi Gemelli Group was deposited in an intracontinental fault-controlled basin developed in semi-arid conditions, strongly recalling the present-day Basin and Range Province (Eaton 1982; Lister and Davis 1989; Berra et al. 2016). A rich ichnofossil association preserved in the uppermost arenitic-pelitic lithofacies of the Pizzo del Diavolo Fm., interfingering with coarse-grained conglomerates of the same unit ("Conglomerato del Ponteranica" of Casati and Gnaccolini, 1967) in the Gerola Valley (see Fig. 2.4 for the position), suggests a latest Kungurian age (Petti et al. 2014; Marchetti et al. 2015, Marchetti 2016). Red sandstones and conglomerates of the Verrucano Lombardo (Lopingian?) were deposited above an angular unconformity, testifying to tectonic activity often accompanied by a deep erosion of the Laghi Gemelli Group during the Middle Permian (Casati and Gnaccolini 1967; Berra et al. 2016).

The stratigraphy and architecture of the Orobic Basin reflect the Permian syn-depositional tectonic activity, associated to the development of E-W striking faults and related facies belts (Casati and Gnaccolini 1967; Cadel et al. 1996). The northern boundary of the basin is defined by the Mt. Aga Conglomerate overlying the Variscan basement along the exceptionally well-preserved Aga-Vedello Low-Angle Normal Fault (LANF), separating the Variscan basement in the footwall from the Early Permian sedimentary sequence in the hangingwall. This fault, together with the Masoni LANF, documents the Early Permian extension (Zanchi et al. 2019; Zanchetta et al. 2022), generating asymmetric half-grabens that deep toward the basins depocenters.

This LANF system interacted with high-angle normal faults active in the hanging wall during the deposition of the lowermost Pizzo del Diavolo Fm., where co-seismic soft-sediment deformation structures are abundant (Berra and Felletti 2011; Zanchi et al. 2019, 2021; Zanchetta et al. 2022). Evidence of synsedimentary tectonics during the Early Permian in the cSA are recorded in the volcanic and terrigenous successions of the Laghi Gemelli Group, which are characterized by the occurrence of abrupt facies variations often associated with coarse-grained deposits.

These features are generally attributed to syn-sedimentary tectonic activity demonstrated by the local occurrence of sediments deformation (Berra et al., 2011) such as liquefaction or slumping due to seismic shaking. These structures are mainly concentrated in the fine-grained sediments of the Pizzo del Diavolo Fm., which were deposited on top of the volcaniclastic succession of the Cabianca Volcanite and crossed by synsedimentary faults (e.g. Aga Growth Fault, Zanchi et al. 2019).

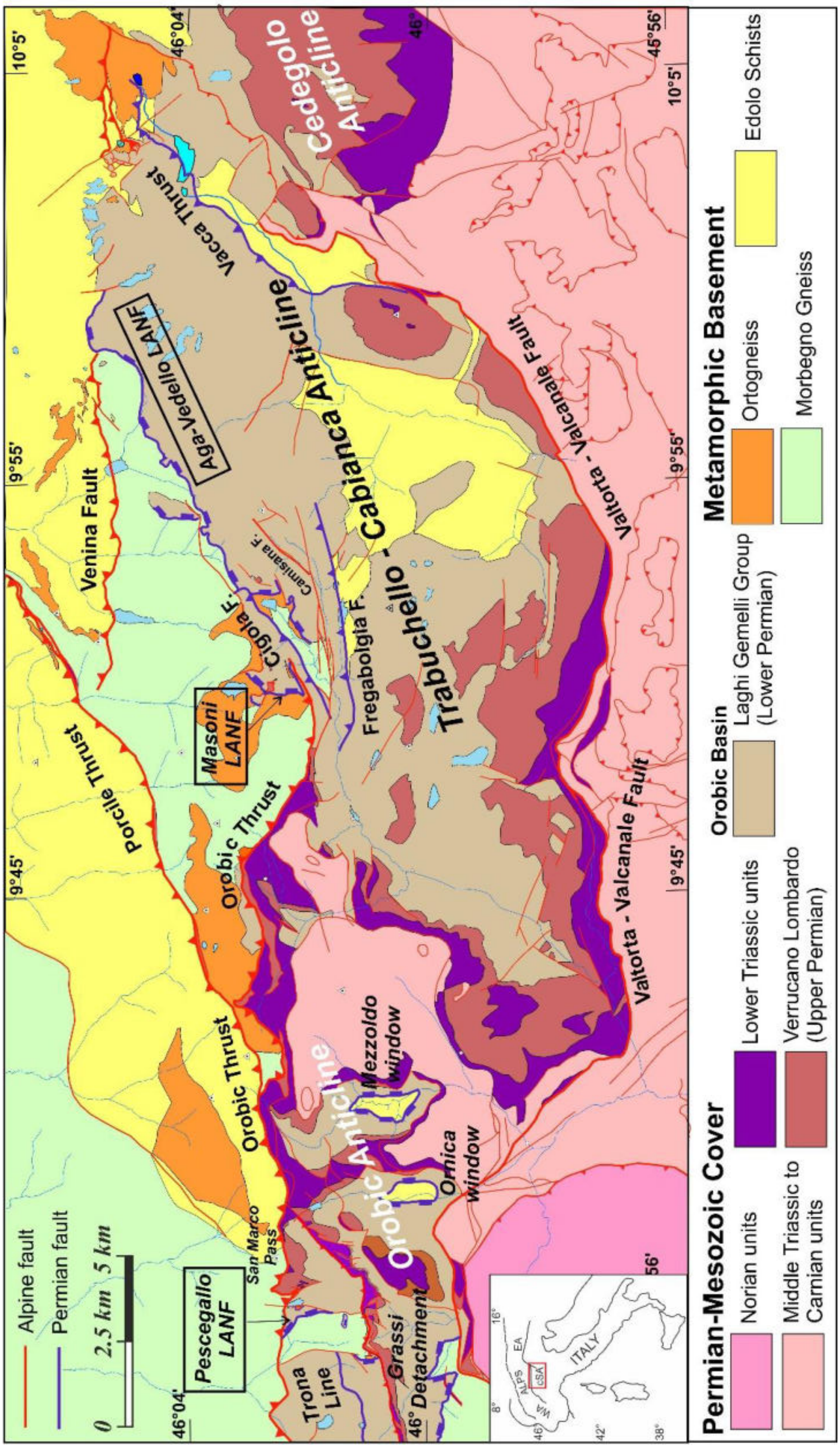

Figure 2.5 - Structural setting of the northern portion of the cSA, focused on the Orobic Basin, modified after Zanchi et al., 2019. Blue faults are related to the Permian evolution of the basin (LANF, Low-Angle Normal Fault and Grassi Detachment of Froithzheim et al. 2008) and the red ones to the Alpine event.

2.5 Permian fault systems and tourmalinites occurrences

As above mentioned, despite the pervasive Alpine overprint, several portions of the Permian fault system determining the architecture of the basins are still well preserved, showing their original structural features. Among these, Low-Angle Normal Faults (LANFs; Zanchi et al. 2019; Locchi et al. 2022; Zanchetta et al. 2022;) and detachment systems (e.g. Grassi detachment, Fig. 2.5; Froitzheim et al. 2008; Pohl et al. 2018) combined with high-angle normal faults (Sciunnach 2001; Zanchi et al., 2019; Locchi et al. 2022) seem to have played a major role in accommodating the Early Permian crustal extension in in the upper crust of the cSA area.

LANFs are found in several parts of this sector of the Alps (Fig. 2.5, Zanchi et al. 2019; Zanchetta et al. 2022; Locchi et al. 2022) namely at the boundaries of the Orobic basin. They generally strike ENE-WSW and they presently dip to south (Zanchi et al. 2019; Zanchetta et al. 2022), except for the recently studied Pescegallo LANF (Fig. 2.5; Locchi et al. 2022) that dips to the northern sectors (see more details in chapter 4.1). The fault planes related to the Permian extensional system are often decorated with cryptocrystalline to aphanitic tourmalinites, impregnating cataclasites formed along the basement-cover fault contacts (Zhang et al. 1994; De Capitani et al. 1999; Zanchi et al. 2019; Locchi et al. 2022; Zanchetta et al. 2022). As it will be further described in chapter 4.3, they occur at the Forcellino Pass, the Mt. Aga and the Mt. Masoni area (see Fig. 2.4 for the position of localities; Zhang et al. 1994; Zanchi et al. 2019; Zanchetta et al. 2022), the Lake Aviasco where uranium showings occur (Fig. 2.4; Cadel 1986), the Gerola Valley (Locchi et al. 2022) and the Valsassina along Sassi Rossi Fault (Fig. 2.4; Schiunnach 2011b; Pohl et al. 2018).

Tourmalinites were likely formed after circulation of boron-rich hydrothermal fluids released by the emplacement of granitic and granodioritic bodies in the upper crust (De Capitani et al. 1999) in the 290 – 275 Ma time interval (Pohl et al. 2018) but they have never been defined in details. Tourmalinites are only poorly deformed, with the exception of local folding and cleavage due to deformation of Alpine age (Zanchi et al., 2019; Locchi et al., 2022). This constrains the metasomatic event at the end or just before the cessation of tectonic activity along the Early Permian fault systems. These rocks are made of 50-70 % in volume of an aphanitic matrix consisting of extremely fine-grained (< 0.02 μm) tourmaline crystals (Zhang et al. 1994). As suggested by former geochemical analyses (Slack et al. 1996; Zanchi et al. 2019), they formed from B- and Al-rich fluids that migrated along cataclastic fault zones, and are characterized by an increase in Al, Fe, Mg and Na with respect to cataclasites, coupled with a significant decrease of Si (Zanchi et al. 2019). Furthermore, according to results on whole rock analysis acquired by X-ray fluorescence, Slack et al. (1996) stressed higher concentration of Be, Y, As and U in the tourmalinites.

3. METHODS

3.1 Fieldwork – Permian structures and tourmalinites sampling

The areas of interest for this research project are from west to east the Valsassina, the Gerola Valley, the Forcellino-Vedello Valley-Lake Aviasco area and the Trompia Valley (Fig. 2.4). For Gerola Valley was performed a detailed geological mapping carried out at a 1:5,000 scale, integrated with mesoscopic structural analyses of faults and shear zones here exposed (see chapter 4.1). The focus on this area is motivated because a new segment of low-angle normal fault partially escaped to the Alpine deformation was recognized (Locchi et al. 2022). The results of our fieldwork are synthetized in a geological-structural map (Fig. 4.3), where Alpine and Permian structures have been distinguished according to our structural interpretation. Mesoscopic faults and foliations were measured in several sites (Fig. 4.4a) to reconstruct the relative chronology among different deformational events, as well as fault kinematics. We used kinematic indicators to establish the sense of motion along faults as suggested in Petit et al. (1983), using growth fibres and Riedel secondary fractures when displaced markers were not available. Tension gashes were interpreted according to Hancock (1985). S-C fabrics, foliations and folds were also analysed, and the collected data are shown as stereographic projections (Fig. 4.4).

The other sectors of interest for the present study were already documented from the structural point of view (i.e. Sassi Rossi Fault according to Sciunnach 2001 and Pohl et al. 2018; Aga-Vedello LANF, Masoni LANF, according to Zanchi et al. 2019 and Zanchetta et al. 2022; Val Trompia Lineament according to De Capitani et al. 1999 and references therein) so our field work on those locality was mainly aimed to better characterize tourmalinites occurrences (see Fig. 4.1 for samples position) and their relationships with intrusive bodies and tectonic elements inherited from the Permian extensional phase. The collected samples of tourmalinites are necessary to investigate on the origin of Boron-rich fluids, so in chapter 4.3 they will be characterized from the microscopic, geochemical, isotopic and geochronologic point of view. We provide microscopic analyses of the fault rocks sampled along the main tectonic structures to complete the fieldwork, with the aim of characterizing the different fabrics developed at the microscale. At Gerola Valley in particular, we devoted particular care to the description and distinction of the possible original fabrics formed during the Permian extension and the ones related to the effects of Alpine deformation, often resulting in a reactivation of older tectonic structures.

3.2 Whole rock analyses

47 rock samples (overview in Appendix 1), representative of tourmalinites from different localities of the central Southern Alps and Permian intrusives from Valsassina and Trompia valley areas were analysed for major, minor and selected trace elements at the ACME Analytical Laboratories Ltd. in Krakow (Poland). Total abundances of the major oxides were obtained by ICP-ES (Inductively Coupled Plasma Emission Spectroscopy), whereas REE (Rare Earth Element), refractory elements and precious and base metals by ICP-MS (Mass Spectroscopy). Sample preparations follow a $LiBO_2$ fusion and dilute nitric digestion for major oxides, REE and refractory elements, whereas precious and base metals were digested in aqua regia. Analytical errors are within 2% for major elements and in the 5% - 10% range for trace elements. We provided about 20 g of material grinded with Agate grinder, from which only 2 mg were analysed, and the results are summarized in tables of Appendix 2.

3.3 Electron Microprobe analyses –mineral chemistry and geochemical dating

77 thin sections of rocks of the analysed samples were polished and, for a first description, they were observed at the optical microscope (overview in Appendix 1). The most representative thin sections were carbon-coated and their textural and mineralogical features were inspected using back-scattered electron (BSE) and secondary electron maps.

Major element compositions of tourmaline, tourmalinites matrix and other silicates were determined on the selected carbon-coated thin sections (Appendix 3) at the Electron Microprobe Lab of the Earth Sciences Department of the University of Milan, Italy. The JEOL 8200 Superprobe, equipped with five WDS (Wavelength Dispersive Spectrometers), was used with an accelerating voltage of 15 kV, a beam current of 5 nA and a spot size of c.a. 3 µm. Natural oxide and silicates have been used as reference materials. Tourmaline structural formulae were calculated following Selway and Xiong (2002), with B_2O_3, H_2O and Li_2O calculated by stoichiometry; B is 3 apfu, OH+F is 4 apfu and Li is equal to 15-total (T+Z+Y).

To obtain preliminary information on the geothermometry of fluids precipitating tourmalinites the quantitative microchemical composition of the arsenopyrite crystals (Appendix 6) was determined on a polished and carbon-coated thin section from Lake Aviasco (see Fig. 4.1 for location and Fig. 4.33a for detail) with the JEOL JXA-8900R EPMA instrument, using wavelenght-dispersive X-ray spectroscopy (WDS). The acceleration voltage was set to 25 kV, the beam current to 27 nA and the beam diameter to 1–2 µm. A natural arsenopyrite (Asp 123, Univ. Toronto Canada) was used as calibration standard to quantify As, Fe, S contents. Measurement counting times were set to 10 sec for element peaks and to 5 sec. for the background.

The U-Pb content of uraninite was determined on polished and carbon-coated chips of uranium mineralization at the Electron Microprobe Lab of the Earth Sciences Department of the University of Milan. Uraninite composition was measured with the JEOL 8200 Superprobe, with an accelerating voltage of 15 kV, a beam current of 20 nA, and a counting time of 60 s for the peak and 30 s for the backgrounds. The standards were synthetic UO2, ThO2 and PbO. Detection limits were 290 ppm for U and 170 ppm for Th and Pb. U, Th and Pb concentrations were calculated (Appendix 8) on the basis of the average of 5 repetitions of the same measurement, however as suggested by Cocherie and Albarède (2001), we considered 2% as more realistic minimum relative error for U, Th and Pb concentrations N7500 ppm. Chemical maps were preliminarily acquired on the mineralization to pinpoint the area with higher concentration of U and Pb. Prior to calculating ages, we excluded the analyses that showed obvious contaminations, low totals or anomalously high Pb contents relative to adjacent points as suggested by Toffolo et al. (2017).

3.4 LA-ICP-MS - trace elements and U-Pb dating

In-situ trace element analyses of tourmaline were obtained on polished thin sections using a Teledyne Cetac Technologies Analyte Excite 193 nm Laser Ablation System inductively coupled to a Thermo Scientific ICP-MS iCAP RQ single quadrupole (LA-ICP-MS) at the LASA laboratories ("Laboratori Acceleratori e Superconduttività Applicata") of the INFN institute ("Istituto Nazionale di Fisica Nucleare", MI - Italy). The standard material and the samples were ablated using a 20 μm spot size, 10 Hz repetition rate, and corresponding energy density of ~2.5 J/cm2 with a flux of He gas carrier of 0.75 L/min. The standard glass NIST 612 (produced by the National Institute of Standards and Technology) and the reference material BCR2G (a fused glass of the Columbia River Basalt) were repeatedly analysed after 18 spot analysis each time (Appendix 4). Raw data revision, calculation and elaboration were performed using Glitter software.

Zircon grains were extracted from three samples of the Val Navazze – Val di Rango intrusive bodies (MVN3, VNE3 VNE4, see Fig. 4.17 for location) to collect the isotopic ratio of ^{207}Pb/^{206}Pb, ^{206}Pb/^{238}U and ^{207}Pb/^{235}U with LA-ICP-MS (Appendix 7.1). Standard heavy liquid and magnetic separation techniques were used after crushing and sieving. No preferential selection of zircon was made during the handpicking process based on size, colour, shape, roundness, and metamictization. The remaining zircon grains were mounted in epoxy 2" mount and polished to reveal half-sections. Zircon internal structures were analysed and interpreted from cathodoluminescence images, taken at the Electron Microprobe Lab of the Earth Sciences Department of the University of Milan, Italy. The analysis with LA-ICP-MS U-Pb zircon dating were carried with 25 um spotsize, 5 Hz repetition rate, a fluence of 2.5 J/cm2 and a flux of He gas carrier of 0.7 L/min. The standards used as reference materials are the natural zircons 91500 and as quality control the Plesovice, another natural zircon. Raw data revision, calculation and elaboration of the isotopic ratios were performed using Glitter and Isoplot software (Ludwig, 2003).

With the same technique, in sample VM8 (see Fig. 4.1 for location) rutile grains were selected for U-Pb dating. A thin section of about 50 µm thickness was polished and analysed to collect with a spotsize of 30 µm the isotopic ratio of $^{207}Pb/^{206}Pb$, $^{206}Pb/^{238}U$ and $^{207}Pb/^{235}U$ (Appendix 7.2). The repetition rate was of 10 Hz with a fluence of 3 J/cm2 and a flux of He gas carrier of 0.7 L/min. Two rutile samples from granulite facies metasedimentary rocks, Sugluk-4 (Sugluk-4-87 of Parrish, 1989) and PCA-S207 (PCA-S207-90-A), were used as reference materials and were repeatedly analysed after 10 rutiles each time. U–Pb isotopic ratios and their uncertainties are calculated using the software Glitter, the Concordia plots are constructed and age uncertainties are calculated using Isoplot (Ludwig, 2003).

3.5 SIMS Boron isotopes composition

The Boron isotope composition of tourmalines was determined by secondary ion mass spectrometry (SIMS; Appendix 5) with the CAMECA ims 1280-HR instrument at the GFZ (German Research Center for Geosciences) in Potsdam. We prepared 2.5 cm round thin sections from the same samples analysed at the electron microprobe, we polished them and coated with a ~35 nm thick high purity gold coat. For the Boron isotopic analyses, the 1280-HR employed a nominally 13 kV $^{16}O^{-}$ primary beam, which was focused to about 10 µm diameter on the sample surface, and a beam current set at 8 nA or 4 nA. The mass spectrometer was operated at mass resolving power $M/\Delta M \approx 1200$, sufficient to separate the isobaric interference of $^{10}B^{1}H$ on the ^{11}B mass station and the $^{9}Be^{1}H$ peak on ^{10}B. Instrumental mass fractionation (IMF=0,977) and analytical quality were assessed by replicate analyses of tourmaline reference materials dravite (HS #108796) and schorl (HS #112566) from the Harvard Mineralogical Museum (Dyar et al., 2001). During the analytical session the 1 SD individual uncertainties were typically below ± 0.7‰ and the repeatability on reference samples was around 0.82‰ (1 SD).

4. RESULTS

This chapter is organized in two different parts, discussing the main topics of the present research project. In the first part, the studied areas are defined from the structural point of view, with a focus on the Permian tectonics and the occurrences of tourmalinites along Early Permian structures. The second part is preceded by a brief description of the Permian intrusives of Trompia Valley area, followed by the characterization of tourmalinites of the central Southern Alps (cSA) from the microscopic, geochemical, isotopic and geochronologic points of view.

4.1 Structural analysis

The structural analysis on Permian structures is here introduced for each sector of the cSA, with special emphasis on the relationships with boron-rich hydrothermalism.

From west to east, the areas of interest are respectively the Valsassina, the Gerola Valley, the Forcellino-Vedello Valley-Lake Aviasco area and finally the Trompia Valley (Fig. 2.4). We describe the structural setting in Gerola Valley based on the new field observations (Locchi et al. 2022), whereas the other sites are mainly defined according to information available from former literature. A description of the outcrops with tourmalinites is also provided, because we collected samples from each site in order to define the hydrothermalism widespread in the entire sector of Southern Alps (Fig. 4.1).

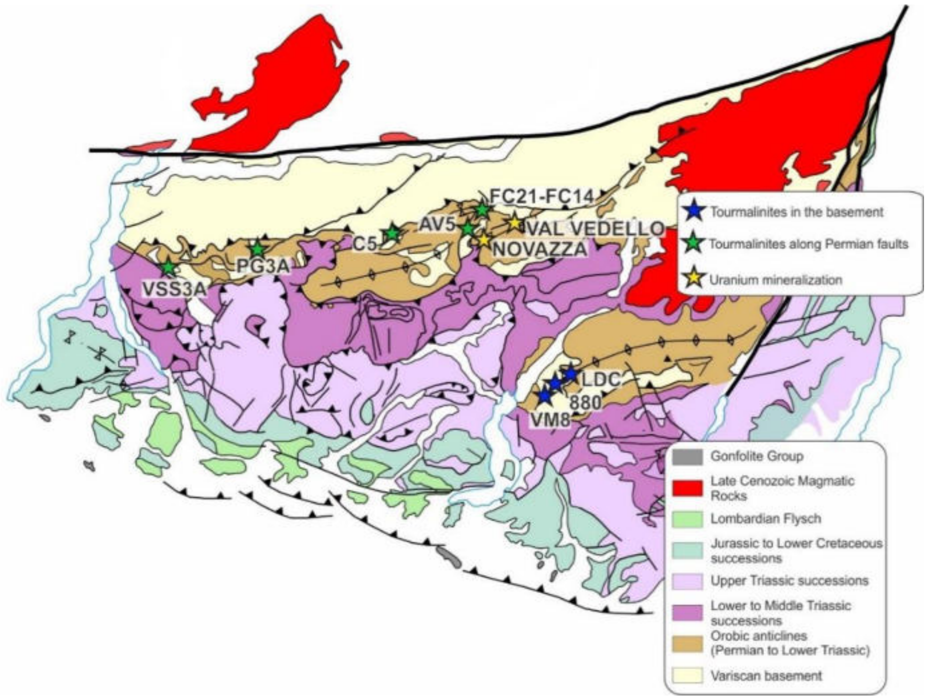

Figure 4.1 - Simplified tectonic scheme of the cSA, showing the occurrences of tourmalinites along the Orobic and Collio Basins (modified after Zanchetta et al. 2015).

1) VALSASSINA

In Valsassina (Fig. 2.4), two distinct intrusive bodies form the Val Biandino Complex: the “Val Biandino Quartz-diorite” (Pasquarè, 1967; De Capitani et al. 1988) and the “Valle di San Biagio Granite” (Sciunnach 2001; Phol et al. 2018) occur. They crop out in the footwall of the Grassi Detachment, a low-angle normal fault separating the Permian sedimentary succession from the underlying Variscan basement (Froitzheim et al., 2008). The occurrence of minor bodies of gabbroic composition have also been reported (Pasquarè, 1967). According to the geochemical data (De Capitani, 1982; De Capitani and Liborio, 1988; De Capitani et al., 1988) the Val Biandino intrusive Complex displays typical high-K calc-alkaline affinity. The intrusion age has been constrained by U-Pb zircon dating at 289.1 ± 4.5 Ma for the Val Biandino Quartz Diorite and 286.8 ± 4.9 Ma for the Valle San Biagio Granite (Pohl et al., 2018).

Combined to the low angle normal fault, a E-W trending high angle normal palaeofault occurs and couples the San Biagio granite in the hanging wall and the Val Biandino quartz diorite in the footwall (Fig. 4.2a, Sciunnach 2001b, Pohl et al. 2018). The pre-Upper Permian age of the fault is indirectly suggested by the Verrucano Lombardo that unconformably covered it. The thick forest cover and the poor outcrops conditions severely hampered a detailed field structural analysis of tourmalinite-bearing faults. Tourmalinized cataclasites occur as spot outcrops chiefly along the Sassi Rossi fault (Fig. 4.2a), a NS striking and westward dipping normal fault (Sciunnach, 2001) that brought in contact the granophyres of the Valle di San Biagio Granite, with the Variscan basement intruded by the Biandino Quartzdiorite (Fig. 4.2a).

Tourmalinites occur as discontinuous subvertical veins within the Sassi Rossi fault zone (Fig. 4.2b), partially substituting the pre-existing catclasites. Tourmalinite matrix is composed of fine-grained tourmaline, where small clasts of quartz and granitoids of former cataclasites derived by the fault activity are sparsely distributed (Fig. 4.2c). Associated to the tourmalinites, thinner quartz-veins occur.

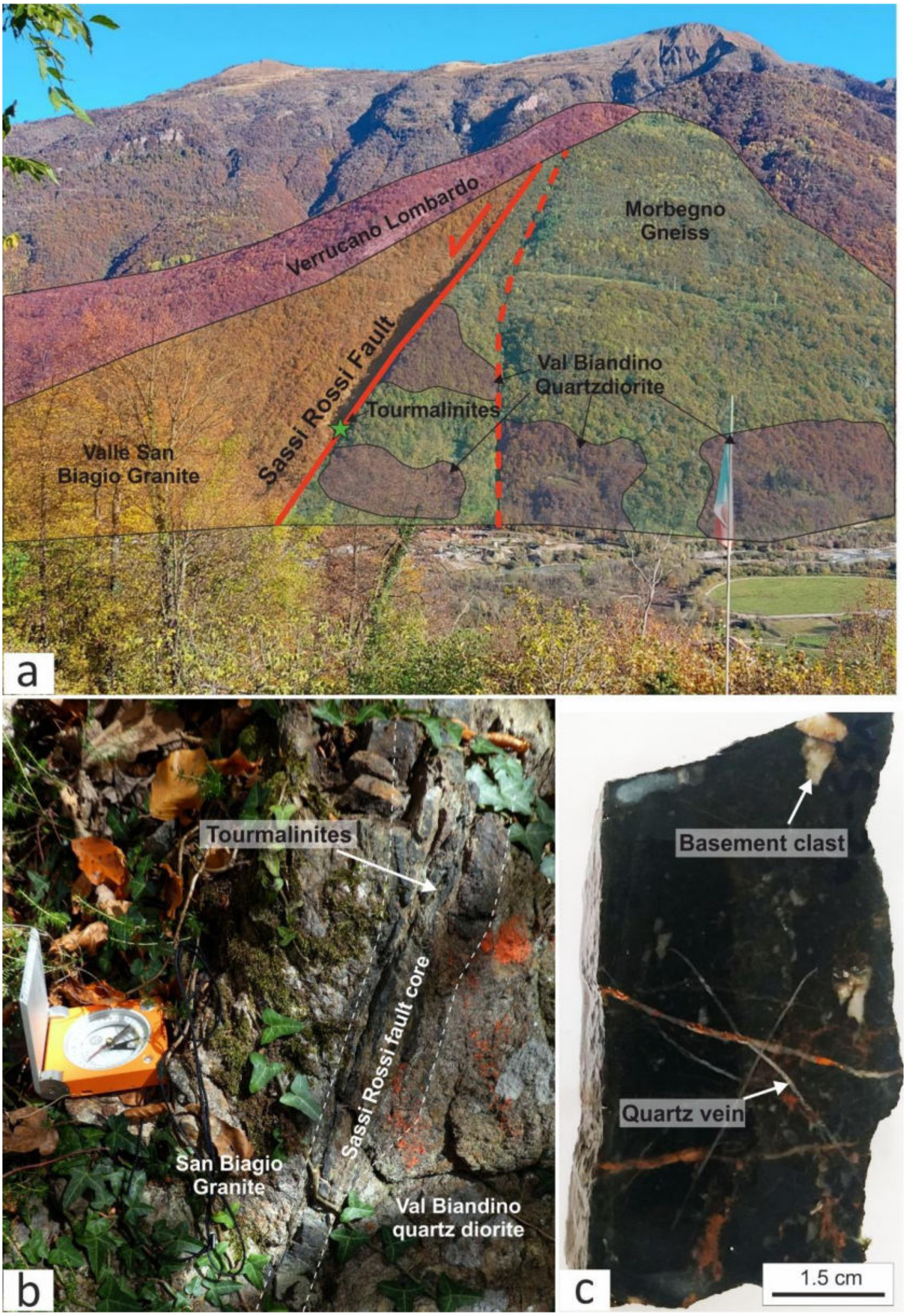

Figure 4.2 - Representative pictures of tourmalinites from Valsassina. a) panoramic view of Sassi Rossi fault with position of collected tourmalinites; b) outcrop of Sassi Rossi fault in Valsassina, with the core sealed by fluids precipitating tourmaline; d) hand-specimen with clasts of the host rocks cemented by dark matrix of tourmaline, cut by quartzous and oxide veins.

2) THE GEROLA VALLEY AREA

For the Gerola Valley are we provide a thorough analysis of the Permian and Alpine structures (from Locchi et al. 2022), in order to define the tectonic evolution of the area (see chapter 2.2, Fig. 2.4), and all the geological and structural information are represented in figures 4.3 and 4.4.

Alpine deformation

Starting with the description of the more recent deformation, the most important Alpine structure of this area is the E-W trending Orobic Thrust (sites 1 and 2 of Fig. 4.4a), along which the Variscan polymetamorphic basement overthrusts the Lower Permian to lowermost Triassic successions (Carminati and Siletto 2005; Zanchetta et al. 2011, 2015). As above mentioned, this thrust is one of the most relevant tectonic structures of the central Southern Alps (cSA) and it can be clearly recognized eastward, beyond the Forcellino Pass (NE corner of Figs. 4.3 and 4.4). Indeed, the thrust clearly crops out along the trail leading to the pass, forming a duplex between the Variscan Morbegno Gneiss in the hanging wall and the Verrucano Lombardo in the footwall. Two small horses including a thin tectonic slice of Gneiss Chiari and conglomerates of the Pizzo del Diavolo Fm. (Fig. 4.5) are juxtaposed between the roof and the floor thrust. Moving from the bottom to the overlying duplex structure, the fault damage zone is progressively characterized by S-C structures indicating a top-to-SE sense of movement along the floor thrust, with foliated cataclasites at the fault core involving both the Gneiss Chiari and the Pizzo del Diavolo Fm. conglomerates.

Pseudotachylytes develop especially along the roof thrust within the Morbegno Gneiss (see plots of site 1 and 2, Fig. 4.4a). Their occurrence was already documented a few kilometres to the east, in the San Marco Pass area, within the damage zone of the Orobic Thrust (Fig. 2.5, Zanchetta et al. 2011). Mesoscopic structures such as S-C shear bands, cataclastic foliations, striated faults and pseudotachylytes show a mean attitude consistent with the thrust orientation, striking ENE-WSW with a NNW dip direction (Fig. 4.5). Mesoscopic faults mainly show dip-slip movements, indicated by kinematic indicators as striations and quartz growth fibres. Alpine deformation in the sedimentary cover is recorded in the Lower Triassic Servino, where the development of close E-W trending disharmonic folds is evident at Pizzo della Nebbia (PA_3 and A_3 in plot of Fig. 4.4b).

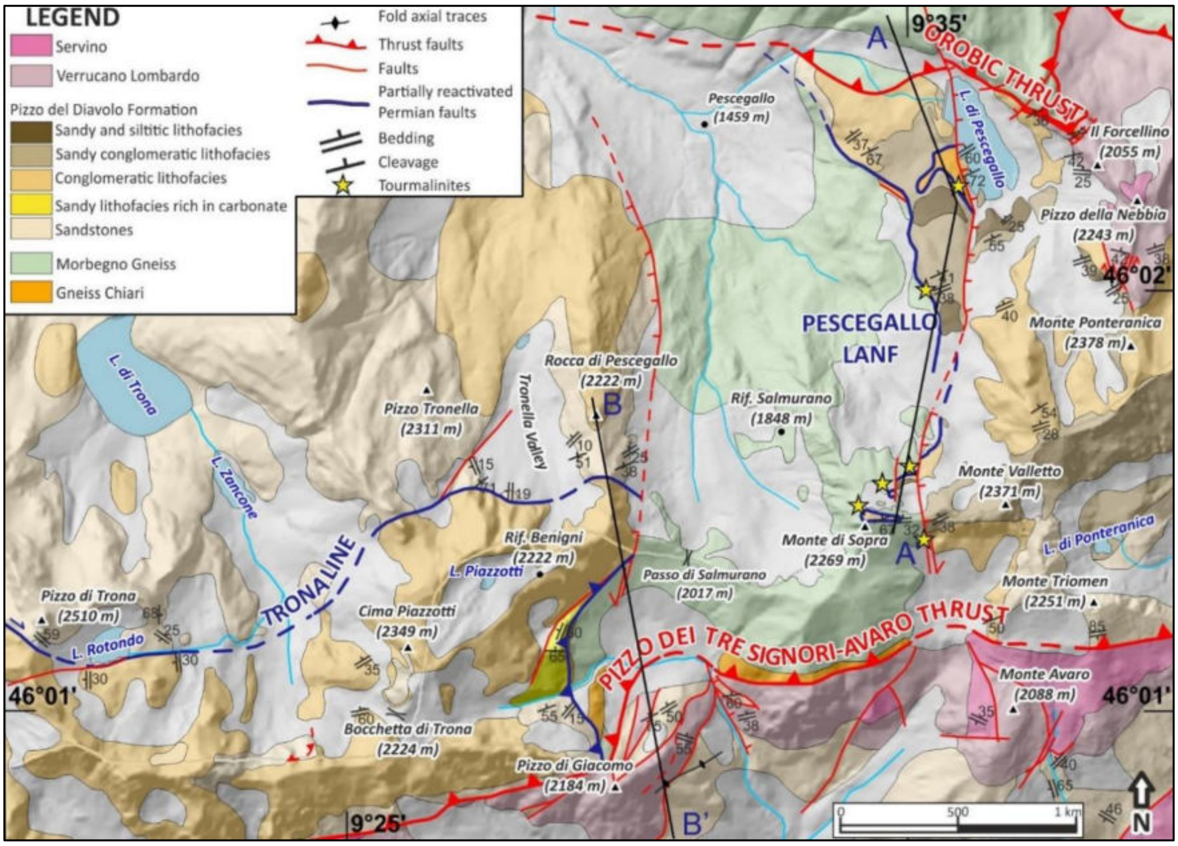

Figure 4.3 - Geological map of the Gerola Valley from Casati and Gnaccolini (1967) and from our own data surveyed at a 1:5,000 scale. Cross sections AA' and BB', shown in Fig. 4.6 and 4.9, were selected to illustrate the architecture of the Permian faults. Yellow stars indicate the position of studied samples with tourmalinites in the area.

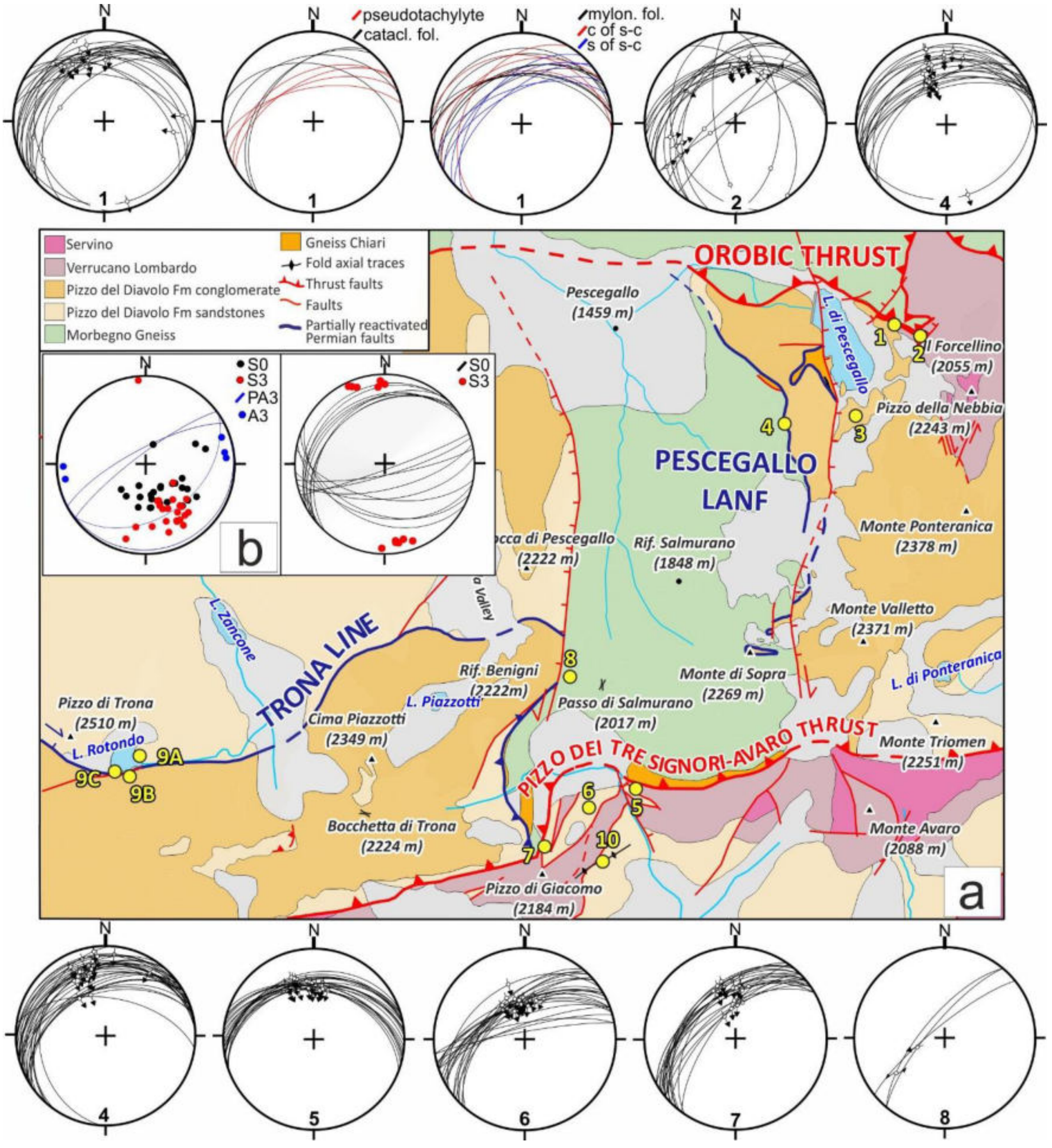

Figure 4.4 - a) Geological and structural map with the structural data related to key sites. Sites 1 and 2 are along the Orobic Thrust; at site 4 the reactivation of the Pescegallo LANF can be observed; sites 5, 6 and 7 are close to the Pizzo dei Tre Signori-Avaro Thrust; in site 8, two N-S trending oblique normal faults respectively with a left-lateral and a dextral oblique component of motion are responsible for the horst of the Morbegno Gneiss between the Salmurano Pass and the Lake Pescegallo; in site 10 open folds with ENE-WSW axial planes and hinges develop in the Pizzo del Diavolo Fm. b) plot with bedding attitude S_0 and Alpine disjunctive cleavage S_3, developed in the Permian-Triassic sedimentary cover, together with close disharmonic E-W trending folds at Pizzo della Nebbia. Sites 3 and 9 are reported in Fig. 4.11. Fault planes are given projected as cyclographics with fault striations and sense of motion; coloured points are poles to foliations; see legend for additional details. Discussion of the data is in the text.

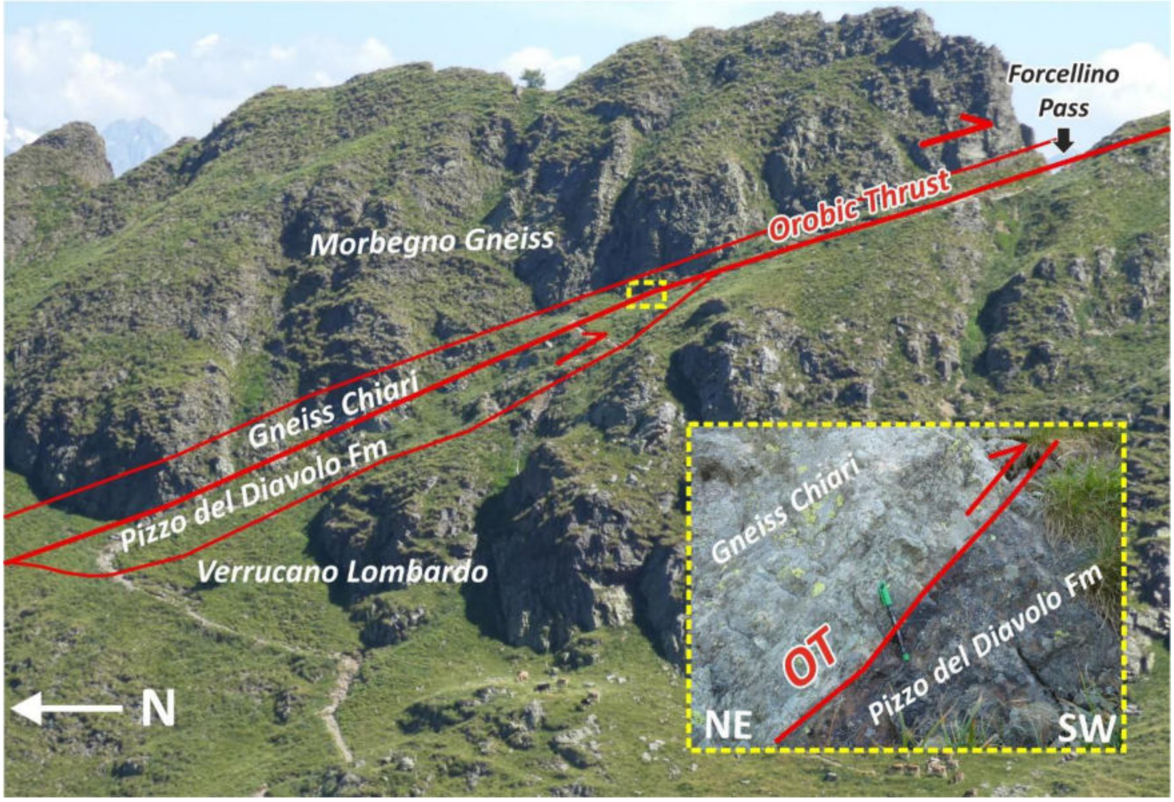

Figure 4.5 - Panoramic view of the Forcellino Pass, with the Orobic Thrust (OT) trace and duplex structures developed along the main fault plane. The yellow inset shows a detail of the OT fault core cropping out along the trail: it is mainly composed of foliated cataclasites with pseudotachylytes at the contact between Gneiss Chiari and Pizzo del Diavolo Fm.

In the southern part of the study area (Fig. 4.3), another ENE-WSW striking and N-NW dipping thrust, the Pizzo dei Tre Signori - Avaro Thrust (SAT, named “San Giacomo thrust” in Casati and Gnaccolini, 1967), develops along the northern limb of the Orobic Anticline with a slightly oblique strike compared to the Orobic Thrust (Fig. 4.3). It extends for more than 20 kilometres from the Biandino Valley (see Fig. 2.4 for location) to the San Marco Pass (Fig. 2.5), where it joins the Orobic Thrust interacting with a system of NNE-SSW trending left-lateral transtensional faults, at the centre of figures 4.3 and 4.4. The Pizzo dei Tre Signori - Avaro Thrust is another important thrust fault, along which the Variscan basement and the Lower-Permian sedimentary cover overthrust the Verrucano Lombardo and Servino formations in the footwall. Mesoscopic faults occur along this contact at sites 5, 6, and 7 (Fig. 4.4a), where dip-slip NW-dipping reverse fault surfaces occur both in the hanging wall and in the footwall, and are oriented similarly to the Orobic Thrust. The Pizzo del Diavolo Fm. is interested by open folds with ENE-WSW trending hinge, their attitude is consistent with the main structures of the cSA fold-and-thrust belt (plot of site 10 Fig. 4.4a).

Data on bedding attitude (S_0) and Alpine disjunctive cleavage (S_3) were collected, and it is noticeable that S_3 is developed especially in the most fine-grained portions of the Permian-Triassic sedimentary cover. S_3 surfaces along the whole study area strike ENE-WSW and dip to N-NW as S_0, but with steeper dip angles (S_0 and S_3 plotted in figure 4.4b). During the Alpine shortening, the Permian normal faults were partially inverted; leading to peculiar structural features that will be discussed in the next paragraphs. Subsequent strike-slip, oblique and normal faults crosscut all the previous structures. Two N-S trending oblique normal faults with a left-lateral and a dextral oblique component of motion (plot of site 8, Fig. 4.4a) are responsible for the additional uplift of the Morbegno Gneiss between the Salmurano Pass and the Lake Pescegallo, forming a horst within the central portion of the study area (Fig. 4.3 and 4.4).

The Pescegallo Low-Angle Normal Fault

The Variscan basement cropping out between the Orobic-Porcile-Gallinera Thrust and the Pizzo dei Tre Signori - Avaro Thrust in the upper part of the Gerola Valley (Fig. 4.4a) tectonically underlies the Pizzo del Diavolo Fm., forming a tectonic window with young-on-old relationships, typically characterizing normal faults. The western boundary of the window is discontinuously exposed from the summit of Monte di Sopra down to the Lake Pescegallo and to the Pescegallo village, where it is crosscut by the Orobic-Porcile-Gallinera thrust system (Fig. 4.3 and Fig. 4.6).

Nice exposures of the fault plane occur close to the southern shore of the Lake Pescegallo, where the Gneiss Chiari and the Pizzo del Diavolo Fm., which respectively represent the lower and upper blocks of the extensional system, are in contact along a W-dipping low-angle normal fault (LANF), forming a small isolated tectonic window. Fault rocks mainly consist of cataclasites reaching a thickness of a few decimetres, which strictly follow the fault plane (Fig. 4.6 and 4.7). Cataclasites display different degrees of tourmalinization, resulting from metasomatic effect.

The occurrence of tourmalinites along Early Permian faults zones represents a common feature already described for other fault systems of the same age in the Aga-Vedello area (Zanchi et al., 2019; Zanchetta et al., 2022). Preserved sectors of the fault plane can be followed hundred meters south of the Lake Pescegallo (site 4 in figure 4.4a) towards the northern slopes of Monte di Sopra and around its top (Fig. 4.3 and 4.4). Here a thick layer of tourmalinite (Fig. 4.7c) with a brecciated texture seals the fault surface. Angular clasts (up to few cm large) of the underlying basement chiefly made of polycrystalline quartz and fragments of volcanic rocks, derived from the Lower Permian Cabianca Volcanite, are well recognizable in the outcrop. In this sector, the LANF cuts horizontally the summit of Mt. di Sopra (Fig. 4.3 and 4.4) isolating a “klippe” forming a sort of “extensional allochthon”.

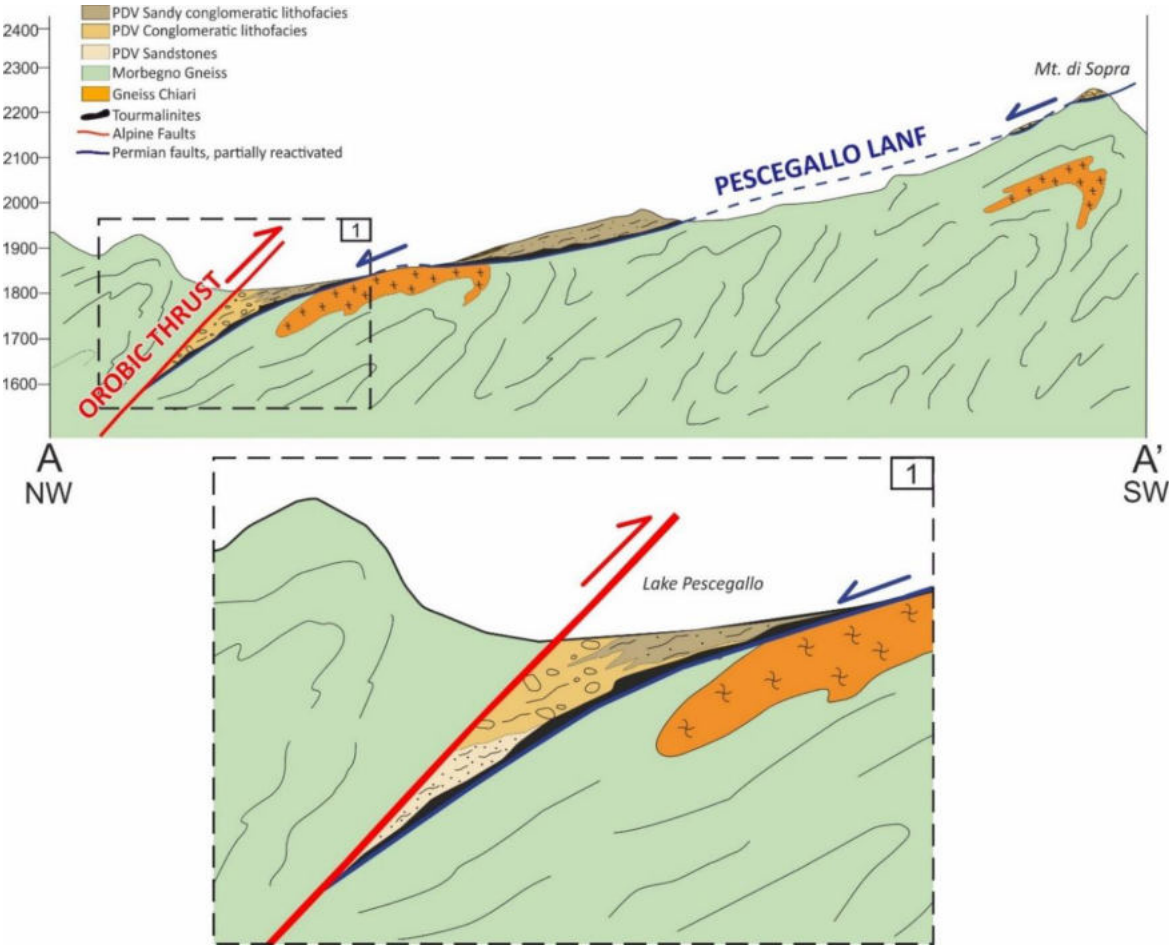

Figure 4.6 - Cross-section AA' going from the Lake Pescegallo to the summit of Mt. di Sopra. The low-angle normal fault surface is progressively reactivated getting closer to the Alpine Orobic Thrust, where cataclastic foliation and S-C fabric overprints Permian structures (see Fig. 4.8), but still preserving the young-on-old relationships. However, the reactivation is not so pervasive, the lithofacies variation of Pizzo del Diavolo Fm. (PDV) can be appreciated and, according to the stratigraphic relationships, it suggests that the deepening of the basin controlled by the activity of the low-angle normal fault is to the north.

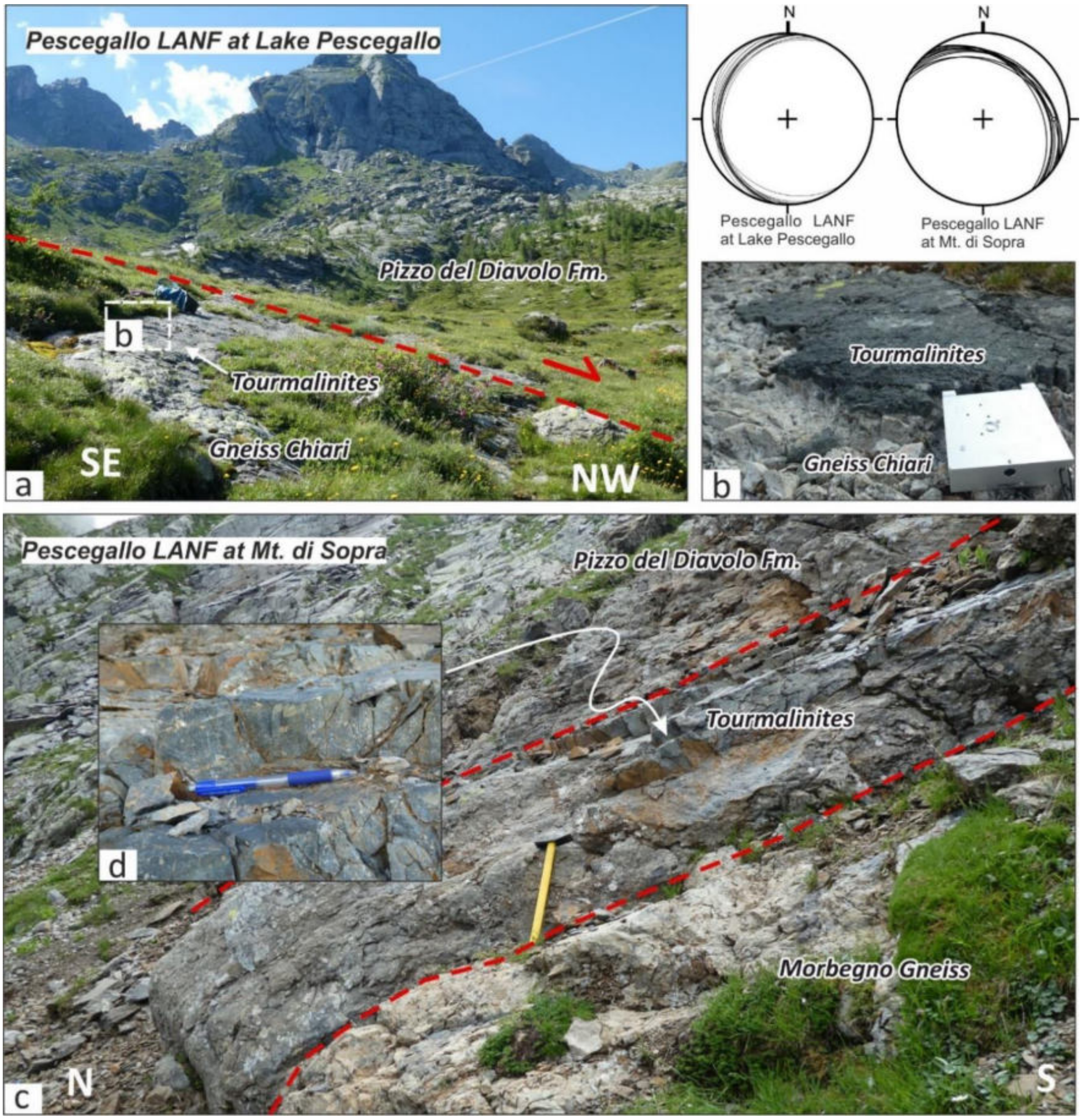

Figure 4.7 - Tourmalinites exposed in the Gerola Valley, along the low-angle normal fault core. The plots represent the attitude of the Pescegallo LANF at Lake Pescegallo and at Mt. di Sopra. Their different attitudes suggest a deformation of the original plane. a) At the Lake Pescegallo, the tectonic window represented in cross section AA' (Fig. 4.6) provides the exposure of the low-angle normal fault core, with cataclasites permeated by tourmalinites, which are shown in detail in b). c) Below Mt. di Sopra, a metre thick layer of tourmalinite separates the Variscan basement from the Lower Permian sedimentary cover and it is composed of several generations of tourmalinite veins, suggesting a multiphase fluids circulation. d) Fault core detail, characterized by cataclased basement and sedimentary cover. Clasts are cut by different generation of boron-rich fluids precipitating tourmalinites.

Although some parts of the original LANF show a partial inversion due to the Alpine reactivation as reverse faults (Fig. 4.8), most segments of the exposed fault surface still preserve their original Permian fabrics, characterized by breccias formed at shallow crustal levels, which were later impregnated by boron-rich fluids.

The tourmalinization and the subsequent Alpine deformation deeply transformed the texture of the original fault rocks, taking to their present-day cohesive fabrics. Relicts of former coarse-grained breccia textures together with the record of synsedimentary tectonic activity in the hanging wall, suggest that the Pescegallo LANF developed at very shallow depths, likely at 1-1.5 kilometres, which is the maximum thickness of the Permian succession deposited on top of the fault. The shallow depth of the Pescegallo LANF fits with the general tectonic context, in which the Variscan basement was already exposed at the beginning of the Early Permian, as testified by the composition of the Basal Conglomerate at the base of the succession (Zanoni and Spalla, 2018).

Evidence of the subsequent Alpine shortening is given by the development of S-C fabric indicating a reverse dip-slip top-to-SE sense of shear, both in the hanging wall and in the footwall of the Pescegallo LANF (Fig. 4.8a), developed in semi-brittle to brittle conditions. Detailed observations at the outcrop scale (plots of site 4 of Fig. 4.4a) suggest that the identified structures are consistent with the general trend of Alpine ones in this sector of the Southern Alps, which is characterized by S-verging thrusting, as shown by the kinematics of the Orobic-Porcile-Gallinera Thrust (Zanchetta et al. 2011, 2015). However, the LANF reactivation was not strong enough to erase the Permian fabrics, as can be observed in Fig. 4.8b where tourmalinites are still recognizable and can be continuously followed along the fault plane.

Similar features occur along the northernmost exposure of the fault planes just above the Pescegallo village, where the LANF plane is folded in an open asymmetric antiform in response to the Alpine shortening along the Orobic-Porcile-Gallinera Thrust (Fig. 4.6). In the hanging wall of this segment of the LANF, sandstones of the Pizzo del Diavolo Fm. lay below the Pizzo del Diavolo Fm. conglomeratic lithofacies (Fig. 4.6). Despite the likely Alpine reactivation of the fault, young-on-old relationships are still preserved, and the fault planes clearly deepens to the north (Fig. 4.6).

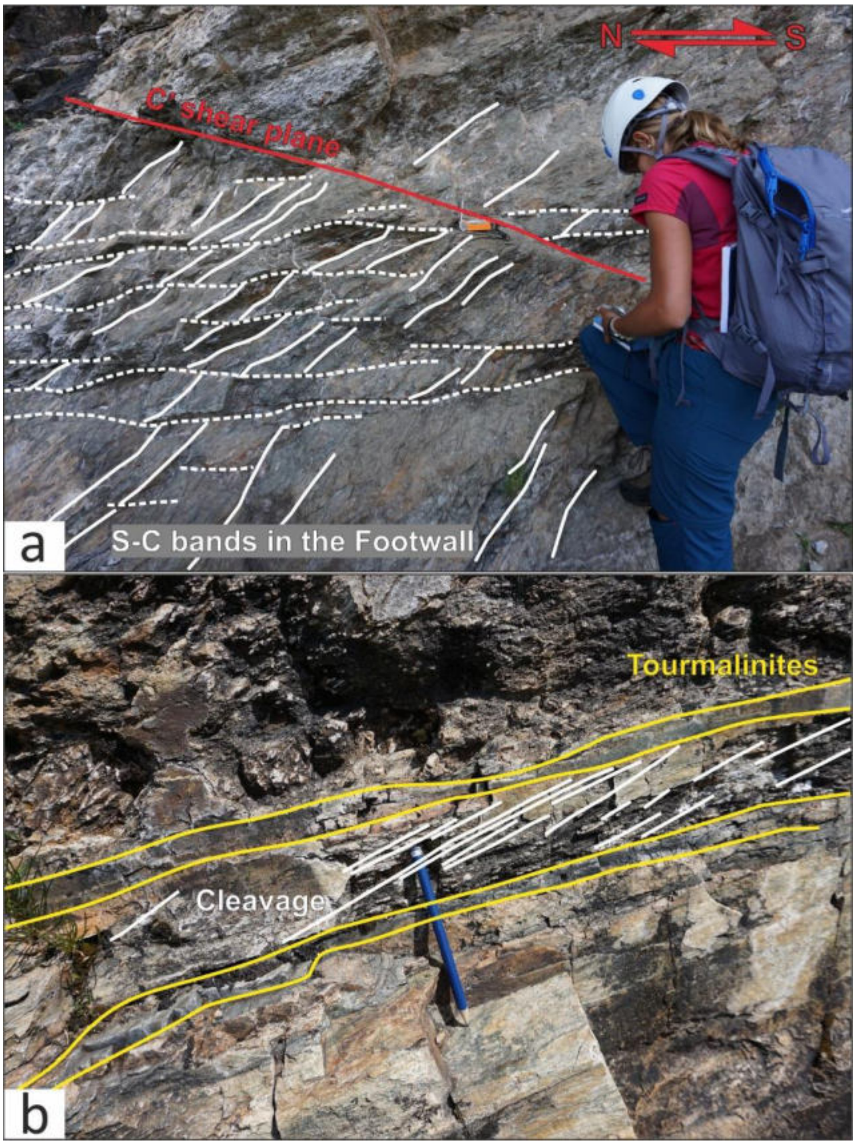

Figure 4.8 - a) At site 4 the reactivation of the Pescegallo LANF generates an S-C fabric, both in the hangingwall and the footwall, and different C' shear planes. They show a displacement with top-to-the-south and are consistent with the kinematics of the Orobic Thrust (see plots of sites 1 and 4 of Fig. 4.4). b) Close to site 4, a cleavage occurs and develops especially in the fine-grained cataclasites and in the finest portions of the Pizzo del Diavolo Fm The tourmalinite bands are poorly deformed.

The Pescegallo LANF is displaced by a N-S trending dip-slip normal fault extending from Monte di Sopra to the Lake Pescegallo to the east and by another N-S trending left-lateral normal fault bounding the Salmurano Pass and the Rocca di Pescegallo (e. g. plot of site 8 of Fig. 4.4) to the west. Here the contact is exposed to the south of the watershed below the high cliff of Cima Piazzotti, where the LANF, still showing preserved younger-on-older relationships (Fig. 4.9), has been strongly reactivated by the Alpine tectonics and interacts with the Pizzo dei Tre Signori - Avaro Thrust.

The Trona High-Angle Normal Fault (Trona Line)

In the study area the recognized LANFs are tectonically combined with High-Angle Normal Faults (HANFs), as already observed in adjacent areas (Zanchi et al. 2019), forming a complex syn-depositional faults system that controlled the opening of the Orobic Basin.

The most relevant high-angle normal fault is the Trona Line, originally identified in Casati and Gnaccolini (1967) and in Marchetti et al. (2015). The fault develops with an E-W trend within the Pizzo del Diavolo Fm. from the Rocca di Pescegallo up to the Pizzo di Trona (Figs. 4.3 and 4.4), running through the Tronella Valley and Lake Rotondo, steeply dipping to the N. The fault marks the boundary between different lithofacies of the Pizzo del Diavolo Fm.: well-bedded fine-grained volcanoclastic sandstones to the north and coarse-grained conglomerates (Ponteranica Conglomerate Auct.) to the south.

Along the fault trace, as will be explained in detail in the next paragraphs, we analysed several mesoscopic small-scale synsedimentary normal faults, suggesting that the Trona Line was active during sedimentation, possibly accompanying the extension along the Pescegallo LANF. A similar low- and high-angle normal fault interaction in the cSA is reported at Mt. Aga in the nearby upper Brembana Valley, where the development of the Aga Growth Fault (Zanchi et al. 2019) was accompanied by the formation of several mesoscopic soft-sediment deformation structures formed in hydroplastic conditions within the fine-grained lithofacies of the Pizzo del Diavolo Fm.

The present-day Trona Line corresponds to a subvertical fault plane resulting from an Alpine reactivation (Fig. 4.9) and inversion as a high-angle reverse fault in the Tronella Valley (Fig. 4.4a). Conversely, around Lake Rotondo, the Trona Line shows a southward dipping with normal dip-slip motion (Fig. 11b, plot site 9b).

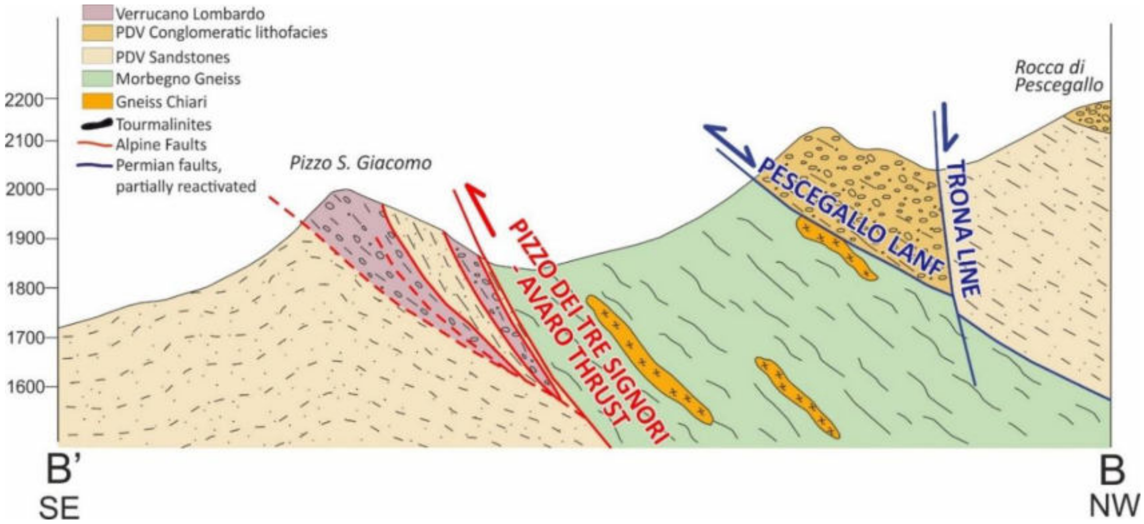

Figure 4.9 - Cross section BB'; the trace is shown in Fig. 4.3. The trace crosses the Pescegallo LANF and the Trona Line, here showing a strong reactivation with a partial inversion. The Pescegallo LANF maintains the young-on-old relationship and the Trona Line abruptly separates different lithofacies of the Pizzo del Diavolo Fm. (PDV). The Pizzo dei Tre Signori-Avaro Thrust (SAT) juxtaposes the Variscan basement onto the Permian cover, involving some tectonic slices of Verrucano Lombardo.

Boron metasomatism along the Pescegallo LANF

In the study area, as in other parts of this sector of the Alps that will be described successively (Zhang et al. 1994, Slack et al. 1996; De Capitani et al. 1999; Zanchi et al. 2019; Zanchetta et al. 2022), the low-angle normal fault (LANF) planes are invariably decorated with cataclasites frequently transformed into tourmalinites, precipitated from boron-rich fluids circulating during or shortly after fault activity. These metasomatic rocks at Gerola Valley are well exposed especially around Lake Pescegallo and in the Monte di Sopra area, invariably marking the main LANF plane. Nice outcrops occur just below the summit of Monte di Sopra, where cataclasite and related tourmalinites are up to 40 cm thick (Fig. 4.7c).

Samples coming both from preserved and from reactivated LANF' segments have been studied to provide a full characterization of their microstructure and mineralogical composition (see chapter 4.3).

Synsedimentary deformation

Evidence of synsedimentary tectonics, recorded by soft-sediment deformation and small-scale normal faults accompanied by liquefaction structures, has been recognized in the hanging wall of the Pescegallo extensional system. These features occur in several sectors of the study area and are very similar to the synsedimentary structures documented in other parts of the Orobic Basin (Berra and Felletti, 2011; Zanchi et al. 2019; Zanchetta et al. 2022).

Examples of small-scale synsedimentary faults occur in the Pescegallo area within the fine-grained sandy to silty lithofacies of the Pizzo del Diavolo Fm. We analysed decimetric normal faults with a displacement of few centimetres especially close to the Trona Line, where they are concentrated along the shore of Lake Rotondo (site 9 of map in Fig. 4.4). Similar examples of small-scale conjugate normal fault in association with tension gashes also occur close to Lake Pescegallo (site 3, Fig. 4.4). Normal faults show different styles and associations, varying from domino-type systems (e.g. Fig. 4.10a) to Andersonian conjugate systems accompanied by the development of small horst and grabens at a centimetric scale.

All the measured faults show evidence of synsedimentary deformation in hydroplastic conditions testified by dewatering structures at different scales. Plastic folding of laminated layers, flames and small neptunian dikes can be observed in association with these structures. Small faults often crosscut sandy layers, dying out in the fine-grained layers of the unit. At Lake Rotondo (Zanchi et al., 2021), we also observed a small mud volcano with a diapiric structure with a diameter of about 20 centimetres, folding and disrupting the upper sandy beds (e.g. Fig. 4.10h). Ball-and-pillows, small slumps and disrupted bedding (e.g.: Fig. 4.10e, f and g) are mostly distributed along the contacts between arenaceous and silty layers.

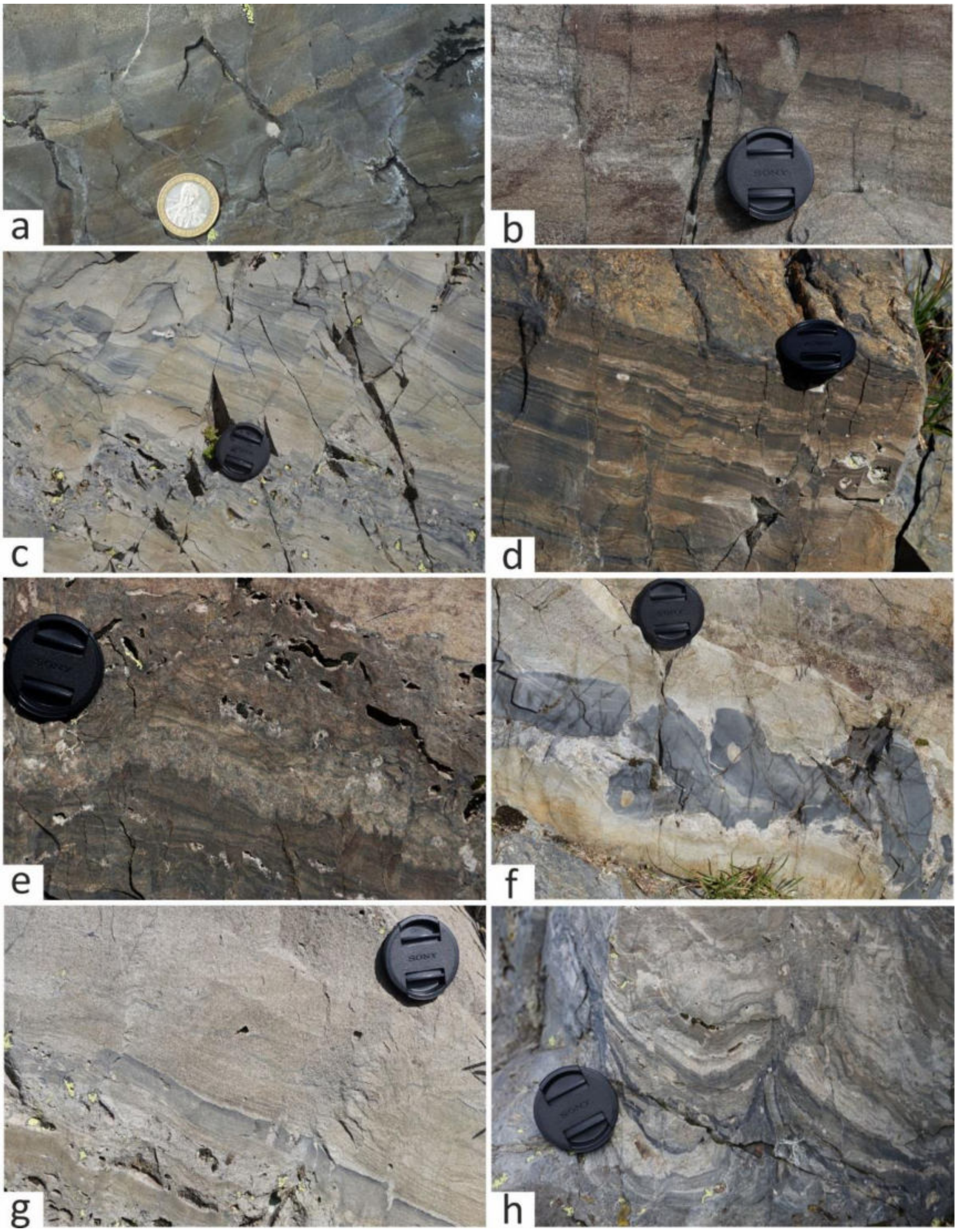

Figure 4.10 – Examples of synsedimentary structures close to Lake Rotondo (site 3 of Fig. 4.4a). a), b), c), d) Synsedimentary mesoscopic normal faults organized in domino systems; e), f), g) disrupted strata; h) extrusive structure along a small mud volcano.

Rose diagrams including more than 80 fault planes show a dominant ENE-WSW strike with NNW (N330) dip direction and a dip angle ranging mainly from 35° to 75° (Fig. 4.11a), consistently with the orientation of the Trona Line (see plot site 9). Stress directions suggested by Andersonian conjugate systems and tension gashes are clear evidence of a vertical σ1 and a horizontal WNW-ESE trending σ 3 in present day coordinates.

The occurrence of such structures in the hanging wall of Permian LANFs is consistent with observations carried out in other areas of the northern portion of the cSA on small-scale synsedimentary faults (Berra et al. 2011; Zanchi et al. 2019; Locchi et al. 2021; Zanchi et al. 2021), which show similar strikes and features including about 500 measured faults.

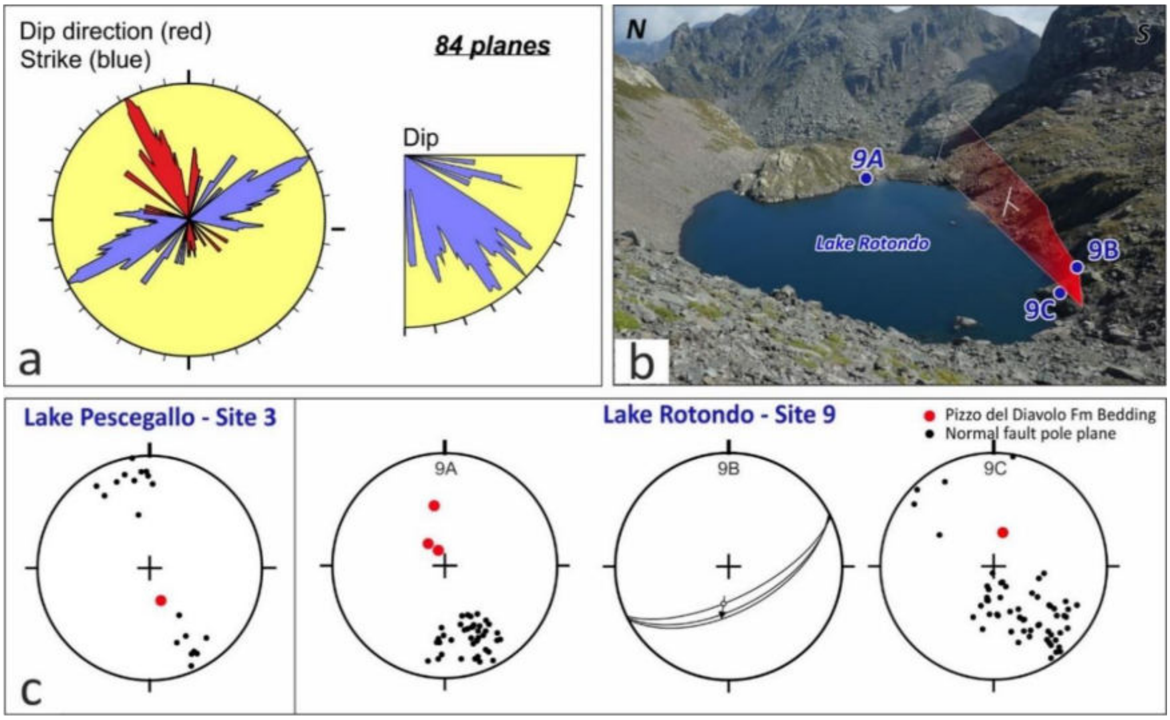

Figure 4.11 - a) Rose diagram related to the synsedimentary mesoscopic normal faults measured at sites 3 and 9 around Lake Rotondo. b) Overview of site 9, with the trace of the normal fault (site 9b) nucleated close to the Trona Line and the position of the measured synsedimentary faults (site 9a and 9c); c) Plots of the data related to mesoscopic synsedimentary normal faults, collected at sites 3 and 9.

3) THE FORCELLINO-VEDELLO VALLEY AND LAKE AVIASCO AREA

In this area (Fig. 2.4), two major low-angle normal faults (LANFs) occur (Aga-Vedello and Masoni LANFs, AVF and MF in Fig. 4.12, Blom and Passchier 1997, Zanchi et al. 2019, Zanchetta et al. 2022) and document the early Permian extension. They are ENE-WSW trending SSE-dipping and define the northern border of the Orobic Basin, interacting with synthetic high angle normal faults (Aga Growth Fault AGF, Fig. 4.12) active in a syn-sedimentary context during the deposition of the base of the Pizzo del Diavolo Fm. similarly to the Gerola Valley (Locchi et al. 2022), where soft-sediment deformations at very shallow levels produced mesoscopic structures possibly related to seismic shaking (Berra et al. 2011, Zanchi et al. 2019). Other types of Permian high-angle normal faults are ENE-WSW-trending and NNW-dipping (e.g. Cigola-Longo and Fregabolgia faults, FF in

Fig. 4.12). They have been partially inverted as reverse faults during the Alpine deformation but still preserve young-on-old relationships (Zanchi et al. 2019). However, the Alpine event deformed both the Masoni and the Aga-Vedello LANFs, which are overthrust by Alpine thrust sheets stacking the Variscan basement southward (Fig. 4.12).

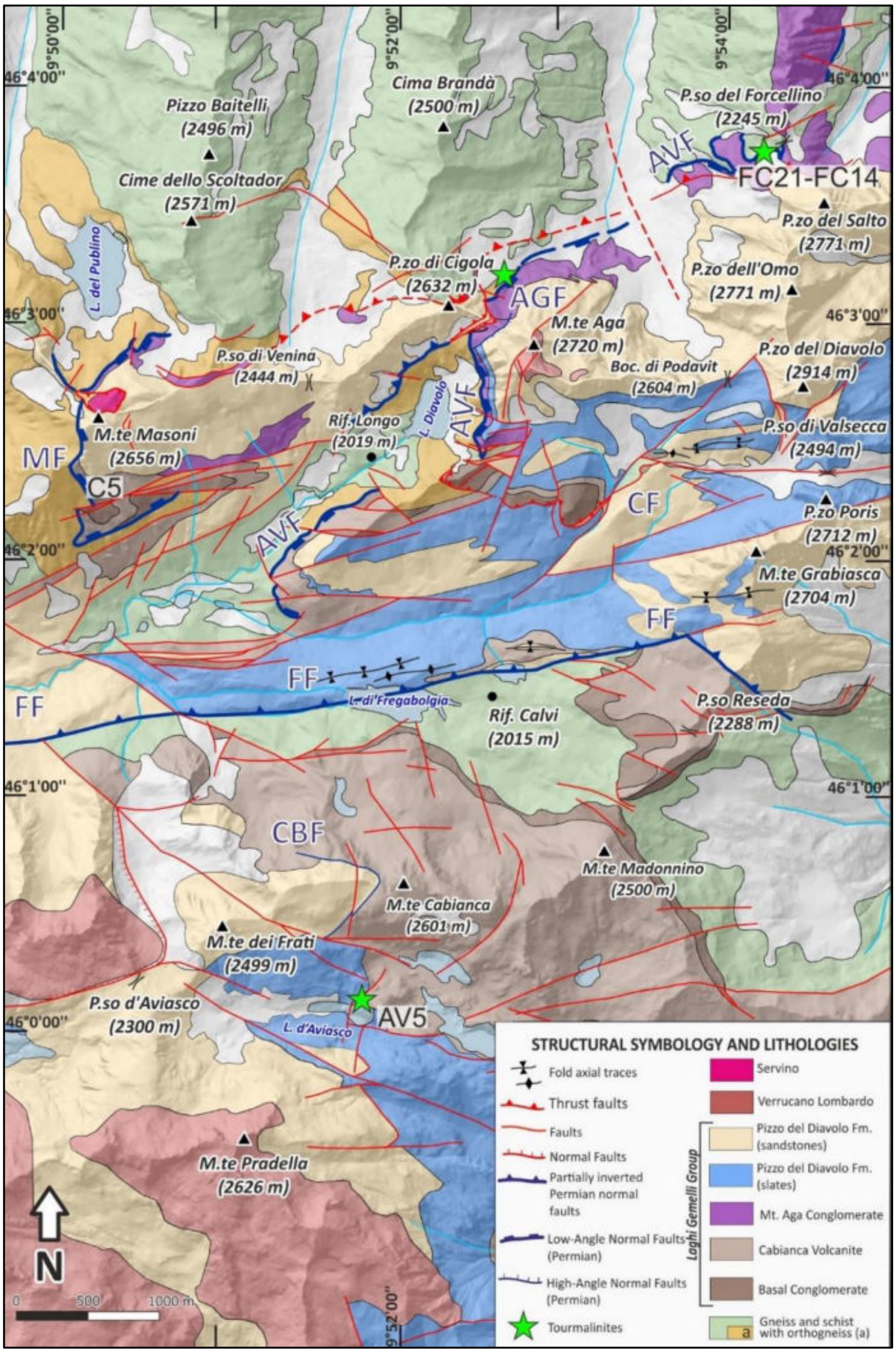

Figure 4.12 - Simplified geological maps of the upper Brembana, Vedello and Valgoglio valleys displaying the traces of the Aga-Vedello (AVF) and Masoni (MF) LANFs. AGF Aga Growth Fault; CF Camisana Fault; FF Fregabolgia Fault. The Forcellino Pass is in the NE corner of the map. Modified from Zanchi et al. 2019. The green stars represent the position of sampled tourmalinites.

The Aga-Vedello LANF represents the most important structure of the area, it continues eastward across the Vedello Valley (Fig. 4.12) and it is constantly exposed for kilometres around the western slopes of Mt. Aga above the Lago del Diavolo. Its importance is also exalted by the occurrence of U mineralization along its fault core at Vedello Valley mine, as testified by Geol. Pessina.

At the Forcellino Pass area (green star in Fig. 4.12 and detail of the geologic map in Fig. 4.13) a several meters-wide outcrop of the fault zone is nicely preserved and well exposed with a smoothed surface (Zanchetta et al. 2022), thanks to the glacier erosion. The outcrop is about 10 x 7 m, the main plane attitude of the LANF surface in this area (Fig. 4.14a) dips to SSE, with a dip angle of 5–10 (see cyclographics with fault plane in Fig 4.15). The hanging wall is made of coarse-grained proximal conglomerates (Mt. Aga and Vedello conglomerate) with boulders of basement-derived gneisses and mica schists, whereas the footwall consists of two mica gneisses with diffuse albite peciloblasts ("Morbegno Gneiss" Auct.). The fault zone is characterized by 40–50 cm thick reddish cataclasites derived by the conglomerates in the hanging wall and less supply from the footwall basement paragneisses (Fig. 4.14b).

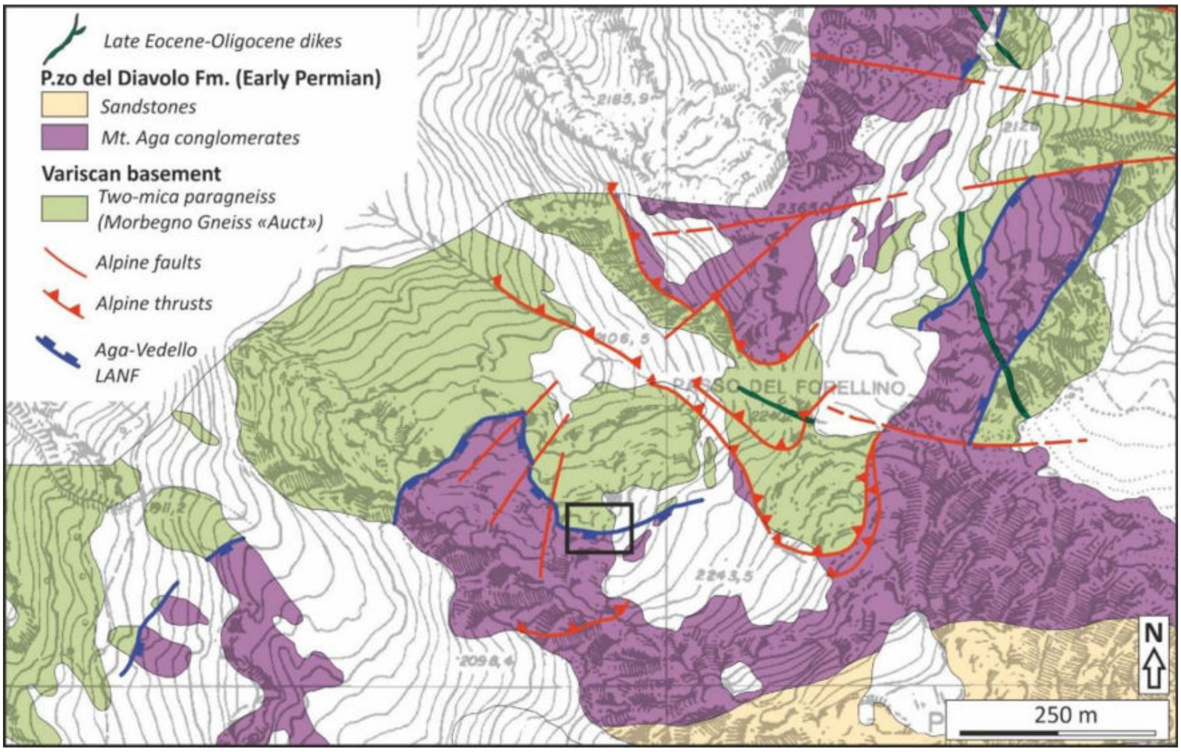

Figure 4.13 - Geological map of the Forcellino Pass area, see position in Fig. 4.12. Parts of the Permian LANF are preserved both in the hanging wall and footwall of the Alpine thrusts. The best outcrops where the LANF structure is observable are in the footwall, at the centre of the map (black box). See Fig. 4.14 for details.

Similarly to the Pescegallo LANF at Gerola Valley, the cataclasites are partially to completely substituted by tourmalinites (Fig. 4.14c and 4.15b) that maintain the same attitude of the LANF plane (Fig. 4.15), with only minor intrusion in the footwall as injected veins (Fig. 4.15c). The contact between tourmalinites and host rocks is generally sharp and straight.

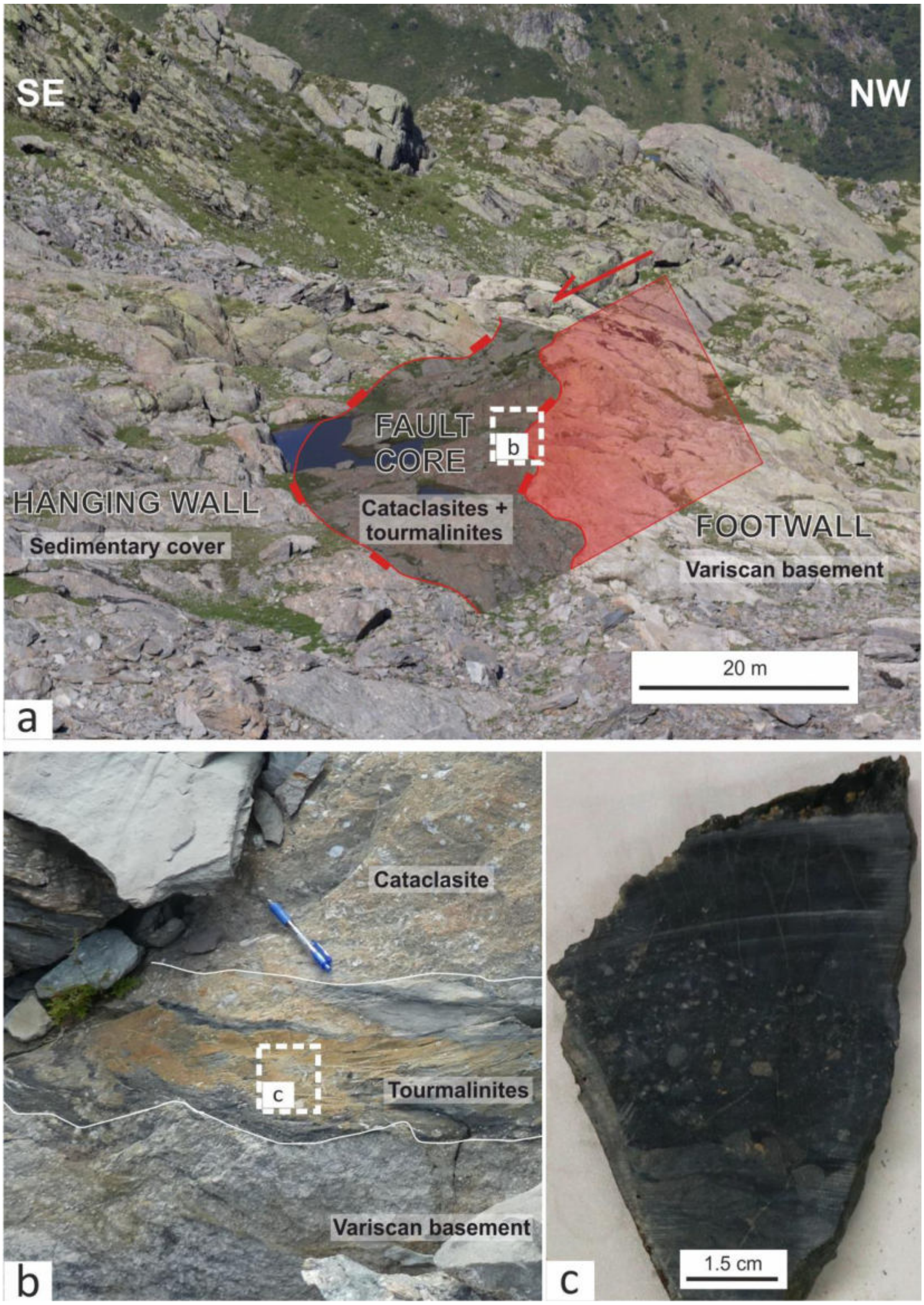

Figure 4.14 - Representative pictures of Aga-Vedello LANF and tourmalinites. a) The main outcrop viewed from the Forcellino Pass (see Figure 4.13 for location), where the fault core is well exposed thanks to the glacial erosive action; b) cataclasite sealed by tourmalinites; c) hand-specimen of layered tourmalinites.

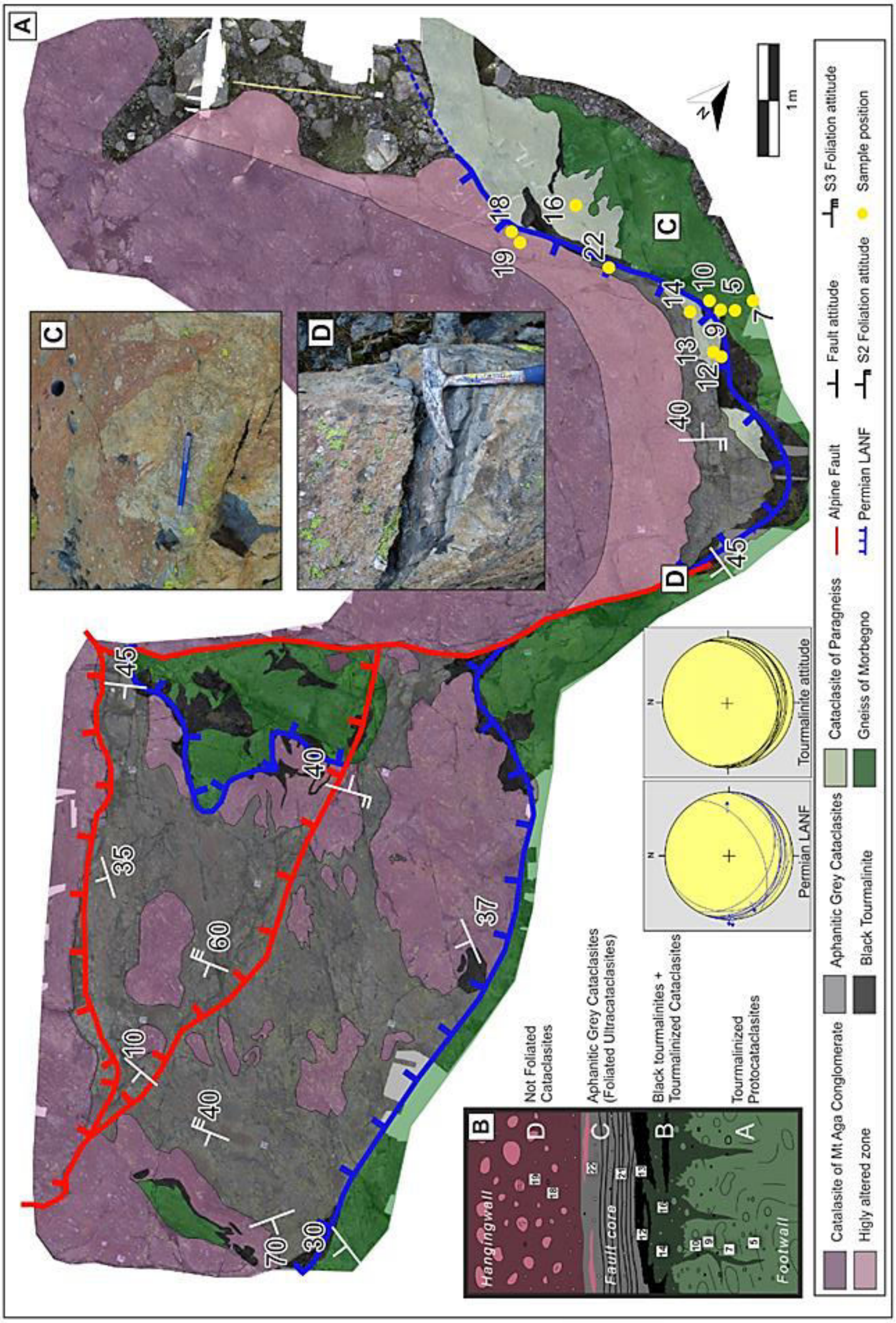

Figure 4.15 - a) Detailed map of the outcrop exposing the preserved Permian fault structure modified after Zanchetta et al. 2022. The map has been obtained from manual photogrammetric reconstruction of the outcrop. Here is shown the sketch of the LANF structure with sampling locations and the attitude of tourmalinites layers and LANF slip planes. b) Reconstruction of the fault structure with sampling locations. c) contact between crystalline basement and reddish cataclasites derived from the Mt. Aga conglomerates. d) typical banded texture of the fault core characterized by alternating black tourmalinites and gray cataclasites levels.

Similar faults of Early Permian age that were influenced by metasomatism were also found at the Lake Aviasco (e.g. AV5 of Fig. 4.1 and position indicated with a green star in Fig. 4.12), which is located to the south of Fregabolgia fault. In this area the Cabianca Volcanite reaches its maximum thickness, resting below the Pizzo del Diavolo Fm. The Cabianca Volcanite is the host rock of the Novazza mineralization, in which the U-bearing minerals are distributed along the volcaniclastic strata and fractures (personal communication of D. Ravagnani). These rocks crop out also close to the Lake Aviasco (Fig. 4.16) and are cut by Permian faults which were interested by boron-rich fluids circulation. Here, the fault cores are characterized by fine-grained dark tourmalinites replacing cataclasites mainly composed of clasts derived from the volcaniclastic portions of the Cabianca Volcanite. Minor U-mineralizations were reported in this locality by Cadel et al. (1986) and Ravagnani (1974), exactly located along tourmalinized faults.

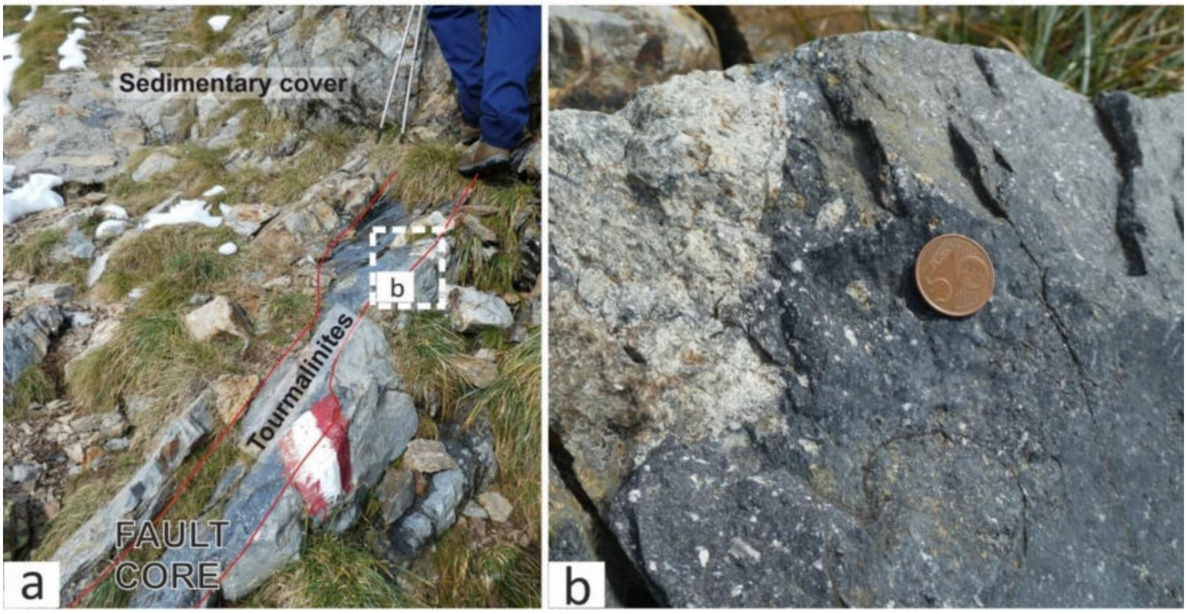

Figure 4.16 - Lake Aviasco site, see position in Fig. 4.12. a) outcrop of the fault cutting the sedimentary cover enriched in volcanoclastic products of the Cabianca Volcanite; b) detail of the tourmalinite sealing the fault core with volcanic clasts.

4) THE TROMPIA VALLEY AREA

The Trompia Valley is geologically located within the Collio Basin (Fig. 2.4), another Early Permian basin just to the east of the Orobic one. Here, tourmalinites of supposed hydrothermal origin occur within the magmatic aureole of Permian intrusions (De Capitani et al. 1999).

This area represents the southernmost exposure of the Variscan basement consisting of phyllite, paragneiss and orthogneiss (Giobbi Origoni and Gregnanin, 1983; Diella e t al., 1992; Cadel et al., 1996; Gosso et al., 1997), which crops out for about 15 km in an ENE-WSW direction to the north of the Val Trompia Lineament (Fig. 4.17). This important tectonic lineament active during Permian time (Cassinis and Perotti, 1993) and separates the Variscan basement from the Permian sedimentary cover, like the low-angle normal faults recognized in the Orobic basin. It underwent limited Alpine reactivation as south-verging thrust fault, with deformation intensity that was not enough to completely obliterate Permian structures and fabrics.

This area of the cSA is characterized by the occurrence of pre-Alpine magmatic rocks, now exposed at shallow crustal levels, that are roughly aligned to the Val Trompia Lineament (De Capitani et al. 1994). They are sparsely exposed along the central and western sector of the Val Trompia Lineament and are respectively the Val Torgola-Val Navazze calc-alkaline granite complex and the Val Cavallina mildly alkaline gabbro stock (De Capitani and Moroni, 1992). Other intrusives, the Val di Rango quartz-diorite and the Maniva Pass Al-rich granodiorite (Mora, 1992), occur to the north of the Val Trompia Lineament. According to stratigraphic evidence and geochronological data, this intrusive complex appears to be broadly coeval with the Collio volcanics and may represent a portion of the magmatic chamber that fed volcanism in the Collio basin (De Capitani et al. 1994).

Directly associated to the magmatic aureole of the described intrusions (Fig. 4.17), there is abundant evidence of hydrothermal activity within the schists and the upper Palaeozoic cover units near the Val Trompia Lineament. The distribution of some of the main deposits, generally is accompanied by the presence of tourmalinites (De Capitani et al. 1999). In this area, the tourmalinites close to the magmatic bodies, are often associated to quartz veins and they crosscut the basement made of chlorite-muscovite phyllites (Fig. 4.18a). They commonly form dm- to m-thick, pseudo-concordant to discordant pods and dark veins with respect to the main foliation. The texture is typically the hydraulic breccia-type with whitish, angular, quartz clasts and metamorphic fragments cemented by a black microcrystalline matrix of tourmaline (Fig. 4.18b). In some cases, the tourmalinization is intense and has produced a black, massive, very hard rock made of more than 80% in volume of very fine-grained tourmaline (Fig. 4.18c). The replacement by tourmaline commonly follows discontinuities such as foliation planes, mylonitic bands in strained quartzite levels and discordant fractures (De Capitani et al. 1999). Tourmalinites contain also small clasts of fine-grained leucogranite (Fig. 4.18d).

Samples of tourmalinites from Trompia Valley are distinguished from the other tourmalinites of the Orobic basin, which are respectively named Type 1 and Type 2 tourmalinites. In chapter 4.3, they are compared from the microscopic, geochemical, isotopic and geochronologic point of view (see Appendix 1 for the analytical overview).

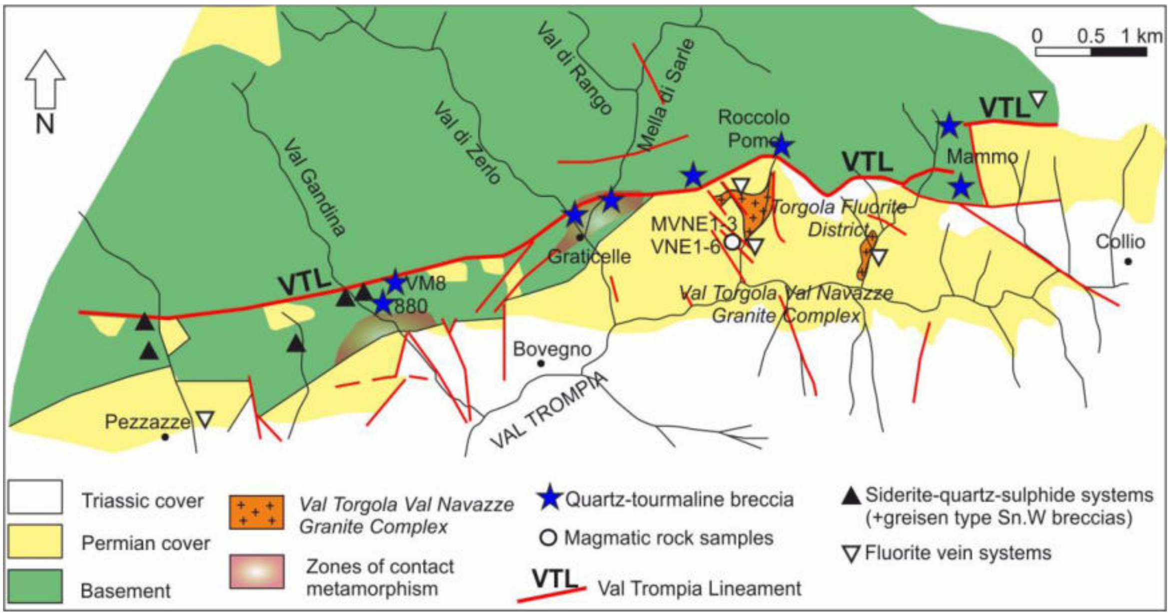

Figure 4.17 - schematic geological map of the Trompia Valley area modfied after De Capitani et al. 1999. Here are shown the positions of tourmaline-breccia bodies, mineralized vein systems, granitic rocks of the Val Torgola-Val Navazze granitoid complex, zones of thermal metamorphism (magmatic aureole) in the basement and the “Val Trompia Lineament”.

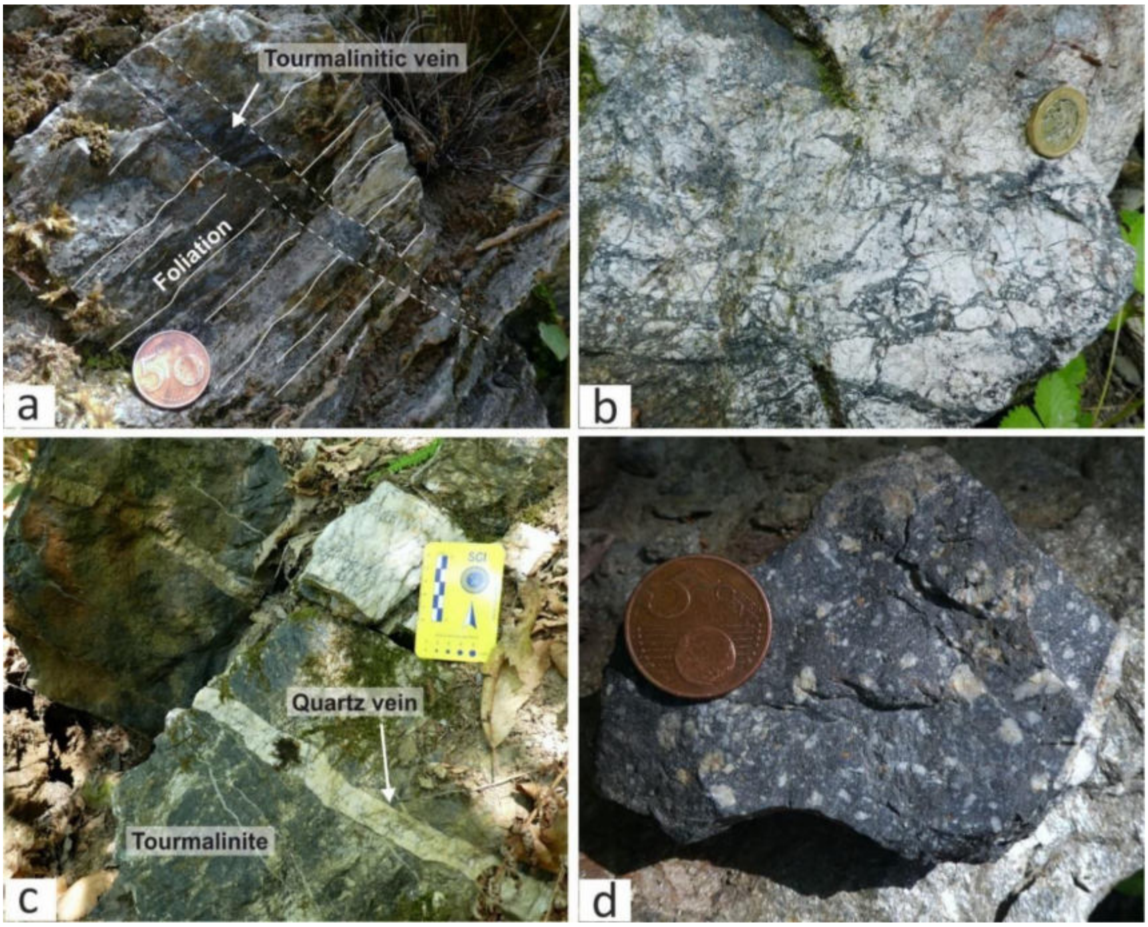

Figure 4.18 - Representative pictures of tourmalinites from Trompia Valley. a) Tourmalinitc vein crosscutting the Variscan basement foliation; b) hydraulic breccia of tourmalinite in the basement, producing a stockwork of veins cementing the clasts; c) example of pod of dark fine grained tourmalinites including clasts of basement and cut by quartzous veins; d) hand-specimen with clasts of basement well-recognizable in the dark matrix of tourmaline.

4.2 Petrography and geochemistry of the Trompia Valley intrusives

To verify the possible genetic link of boron-rich fluids with magmatism, the Permian intrusives and volcanic rocks of the central Southern Alps (cSA) are considered. Recent studies provide the geochronological constrain based on U-Pb zircon dating for the volcanites of this sector of the Alps (Gretter et al. 2013; Berra et al. 2015). The Valsassina intrusives have been lastly analysed both from geochemical (Crippa 2017) and geochronological point of view (Pohl et al. 2018); the Trompia Valley intrusives characterization instead, is based on old-fashioned analytical techniques (De Capitani et al. 1994). For this reason, to complete and update the dataset on the magmatism of the study area, we analysed with modern techniques the intrusives of Trompia Valley area from the geochemical and geochronological (see chapter 4.3.7) point of view.

To provide a complete characterization of the possible source of boron-rich fluids we analysed 9 samples (Fig. 4.17; VNE-1, VNE-2, VNE-3, VNE-4, VNE-5, VNE-6, MVN-1, MVN-2, MVN-3) collected in Val Navazze, a secondary valley of the Trompia Valley to the east of Bovegno and in particular they come from the tunnels of the Torgola Fluorite mine (Fig. 4.17, De Capitani et al. 1994).

These outcrops of igneous rocks are located at the bottom of the valley from elevation 750 m to 1000 m, in direct contact with the Permian sedimentary cover, or they intrude the South-Alpine metamorphic basement (De Capitani et al. 1994). The analysed rocks can be classified as granites and granodiorites, with the major mineral represented by quartz, K-feldspar, plagioclase, biotite and, locally, amphibole and this description matches with the former provided by De Capitani et al. (1994). Plagioclase and K-feldspar are deeply weathered to secondary phyllosilicates (clay minerals and sericite) and biotite partially to completely substituted by chlorite and epidote, as an effect of the greisen alteration accompanying the Sn-W mineralization (Moroni, 1994). Apatite, allanite, opaque minerals and zircon are accessory phases.

De Capitani et al. (1994) emphasized that the relatively wide geochemical variability of the intrusive bodies from Trompia Valley is variable and classified as calc-alkaline to shoshonitic. The bulk chemistry of these samples was quantified on whole rock with more accurate methods with respect to the ones applied in the study of De Capitani et al. (1994). The results are listed in Appendix 2, and on the overall, they show that the intrusives are characterized by about 68 wt% of SiO_2, 16 wt% of Al_2O_3, 8 wt% of alkali, 4 wt% of Fe_2O_3 and 1.3 wt% of MgO.

The trace elements are plotted and normalized to chondrite in Fig. 4.19 and 4.20. The REEs diagram shows L-REE>H-REE with an Eu negative anomaly, and are 100 times higher than chondrite values. The incompatible elements are characterized by positive anomaly of Ba, Th, U, and negative anomalies of Pb and Ti. Noteworthy is the value of U, that is on the average of 3.17 ppm, higher than the U content of the Upper Continental Crust (U-UCC=2.7 ppm, Rudnick and Gao 2003).

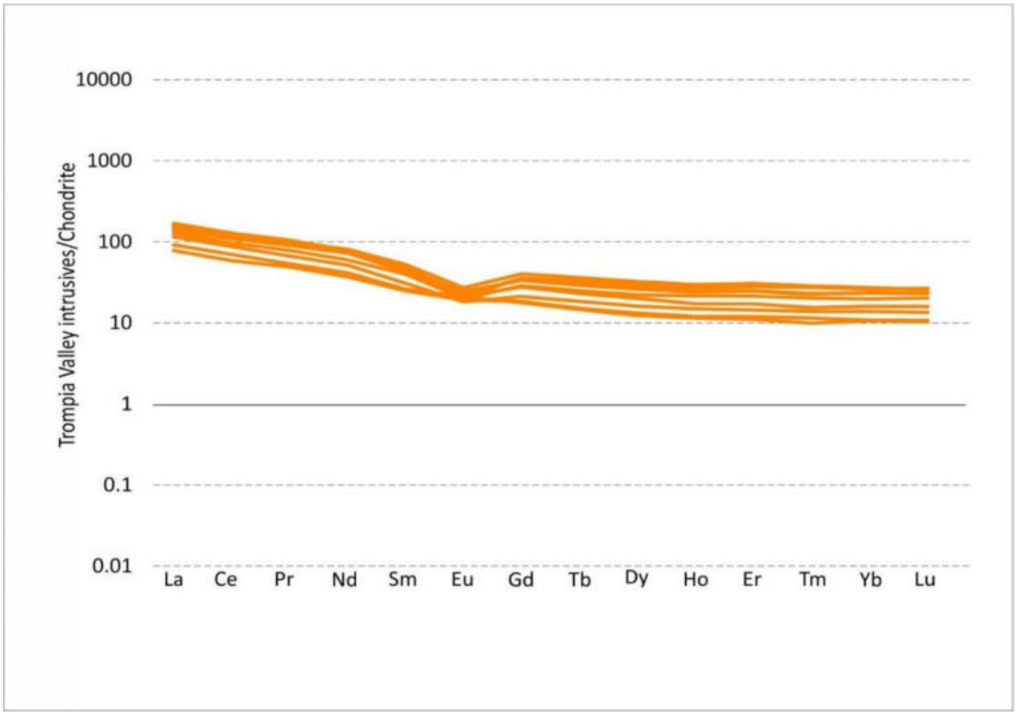

Figure 4.19 - REEs pattern of Trompia Valley granites normalized to chondrite (McDonough and Sun 1995).

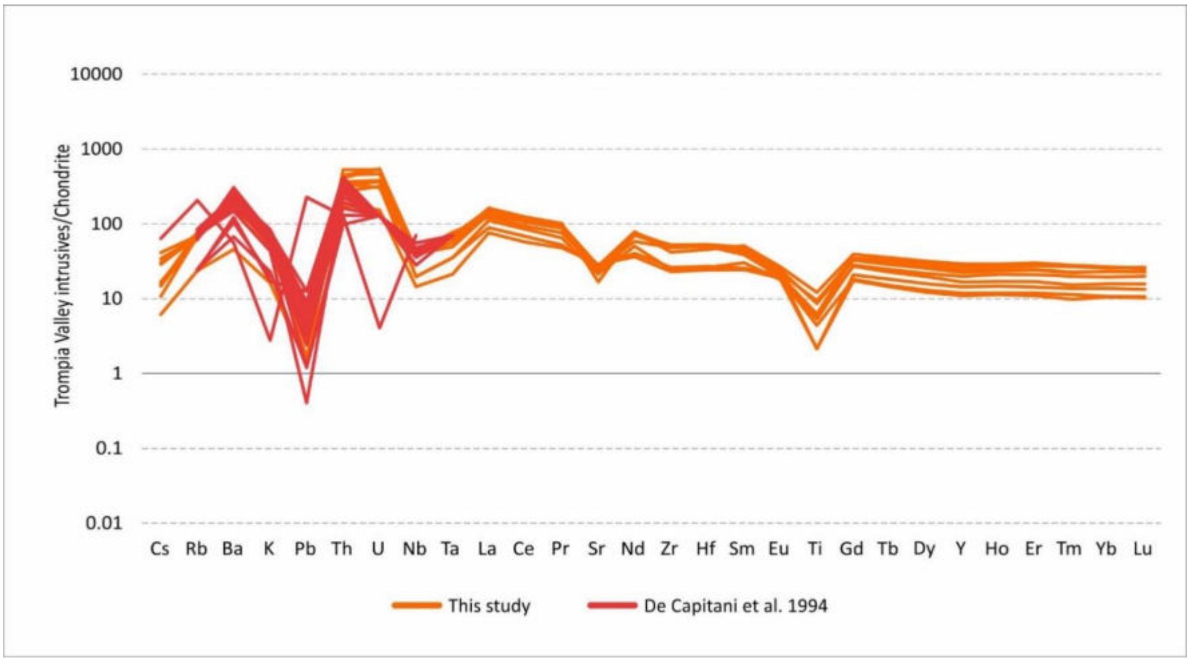

Figure 4.20 - Incompatible elements distribution of Trompia Valley granites analysed in the present study and compared with data of De Capitani et al. (1994), where REEs contents are lacking. Data are normalized to chondrite (McDonough and Sun 1995).

4.3 Tourmalinites

From the new field analyses described in the previous chapter, the tourmalinites of the central Southern Alps (cSA) can be distinguished in two types: “Type 1” are the supposed hydrothermal tourmalinites from Trompia Valley and “Type 2” are the metasomatic tourmalinites along Permian fault cores of Valsassina, Gerola Valley, Forcellino-VedelloValley, and Lake Aviasco area (Fig. 2.4 and Fig. 4.1). In particular, in the sectors where tourmalinites seal the fault core of the Early Permian LANFs (Aga-Vedello LANF (Fig. 4.14), Mt Masoni LANF, Pescegallo LANF (Fig. 4.7)), the metasomatic rocks show almost the same textural features (Zhang et al. 1994; Slack et al.1996; De Capitani et al. 1999; Zanchi et al. 2019; Locchi et al. 2022; Zanchetta et al. 2022) so the microscopic description that we provide is shared.

To evaluate the source of the boron-rich fluids responsible for the formation of tourmalinites, we performed new microscope observations for several thin sections, and we selected the most representative samples for each locality (Fig. 4.1). Their names are respectively from W to E the VSS3A (Valsassina) PG3A (Lake Pescegallo), FC21 and FC14 (Forcellino Pass), C5 (Mt. Masoni Aga), AV5 (Lake Aviasco), and 880, LDC and VM8 (Trompia Valley). We provide new petrographic, geochemical, and geochronological analyses on the Trompia Valley quartz-tourmaline veins after the study of De Capitani et al. (1999). Tourmalinites from this area (Type 1) and other locations (Type 2, see green and blue stars of Fig. 4.1) were investigated and compared to address the source of this regional boron-rich hydrothermalism in the context of the Early Permian intracontinental extension and magmatism. In the present chapter, the obtained results are shown.

4.3.1 Tourmalinites petrography and micro-fabric

Despite the similar dark aspect of all tourmalinites at the mesoscopic scale, from the microscopic point of view the two types of tourmalinites are well distinguishable on the base of petrographic and microstructural features.

Type 1 tourmalinites

On the overall, at the optical microscope the tourmalinites occur as veins mainly composed of prismatic pleochroic crystals up to 100 μm long (Fig. 4.21a-4.23a), with a marked optical zoning, bluish and green to brown. Tourmaline crystals are combined and crosscut by dense felt-like aggregates of microcrystalline, pale green, acicular tourmaline crystals with average size of about 10 μm (Fig. 4.21a-b, 4.23b), pervasively replacing the brecciated basement. Furthermore, comb-textured quartz veins, polycrystalline quartz fragments of metamorphic origin and clasts of leucogranite can be recognized and sometimes are partly overgrown by the microcrystalline aggregates of tourmaline. A detailed microscopic description of tourmalinites from Trompia Valley is provided by De Capitani et al. (1999), who distinguished 4 generations of tourmalines according to their textures. The SEM images exalt the core-rim zoning, suggesting a different composition (Fig. 4.23a-b).

Other common mineral phases are sericite, chlorite and abundant rutile crystallized together with quartz and tourmaline (Fig. 4.21c), especially in sample VM8, that we considered for the U-Pb geochronology (see more detail in chapter 4.3.7). Furthermore, as accessory mineral there is oxidized pyrite and small secondary veins of tourmaline and quartz occur (Fig. 4.21b), generally rimmed by radiating aggregates of acicular green tourmaline, cutting the breccia matrix.

Type 2 tourmalinites

The tourmalinized cataclasites along the Sassi Rossi fault core in the Valsassina area (Fig. 4.2) share some of the features of Type 1 tourmalinites, however they are different from the textural point of view, because here the boron-rich fluids interacted with the pre-existing fault rocks. Tourmalinites are composed by fine-grained matrix made of deep green coloured tourmaline with high-interference colours at crossed polarized light (Fig. 4.21d-f). Quartz and sericite are very widespread in the matrix. Abundant basement-derived clasts as quartz, plagioclase and granitoids (Fig. 4.21e-f) occur. Relicts of tourmalinites of first generations are also recognized as rounded aggregates composed of felt-like aggregates of about 30 μm prismatic (Fig. 4.21e-f) and zoned bluish-green to brown tourmalines. This testifies for a polyphase fluid circulation. Veins of quartz and oxides are frequent.

The tourmalinites at the basement-sedimentary cover contact along the low-angle normal faults (LANFs; Zhang et al. 1994; Slack et al. 1996; Zanchi et al. 2019; Locchi et al. 2022; Zanchetta et al. 2022) were firstly described by Zhang et al. (1994). They differ from the Valsassina tourmalinites for the grain size, indeed they have an aphanitic or cryptocrystalline texture, resulting from the replacement of cataclasites clasts by ca. 70% in volume of very fine-grained crystals of tourmaline composing the matrix (Fig. 4.22a-b-d, Zhang et al. 1994), as verified with EDS analyses. Minor sheet silicates (e.g. sericite) are included, together with quartz, altered plagioclase, and rare pyrite, rutile and titanite. Only few and small examples of sparse subhedral tourmaline crystals occur, whose identification has been qualitatively checked by EDS-SEM analyses (Fig. 4.22b-4.23d). They have brown-to green pleochroism, high interference colours and no core-rim zoning (e.g. sample FC14), with exception for the tourmaline along the foliation or fractures in the basement, in which there are zoned aggregates (e.g. FC21, Fig. 4.22c-4.23e).

The pre-existing clasts of the tourmaline-impregnated cataclasite occupy 30% of the volume and their dimension ranges from 10 μm to 3 mm, with a mean size of 0.2 mm (Fig. 4.22a). They are sub-angular to round-shaped, especially in the portions of cataclasites that were most metasomatized.

This feature suggests that dissolution by fluids circulation was effective (Locchi et al. 2022), causing mass transfer, which is a typical trait of metasomatism. Tourmalinites include fragments derived from the Variscan basement and the sedimentary cover, together with few rounded relicts of former tourmalinites (Fig. 4.22d), probably developed during the earlier stages of a long-living circulation of boron-rich fluids along fault planes.

As already noticed by Zhang et al. (1994), when the Alpine deformation affects the tourmalinites, clasts and tourmaline crystals rims are locally recrystallized with the development of phyllosilicate-bearing strain shadows associated with strain caps enriched in opaque minerals, consistent with the Alpine cleavage. These microstructural features indicate that a pressure solution mechanism was effective, attesting to dissolution and partial tourmalinites' re-mobilization during the Alpine shortening (Philippe et al. 1987; Zanchetta et al. 2022, Locchi et al. 2022). As above mentioned, a deformation of the tourmalinite is visible at the microscopic scale but it is not strong enough to obliterate the original features of the LANF core, which can be still recognized.

The relative chronology among cataclasites and tourmalinization emerges from the microstructural features, being the cataclasites replaced by tourmalinites. Indeed, the obliteration of cataclastic fabrics and the lack of deformation, except for the occurrence of an Alpine reactivation, suggests that tourmalinite formation postdates the main activity of the normal fault, as assumed for the Masoni and the Aga Vedello LANFs (Zhang et al. 1994; Zanchetta et al. 2022) in the Mt. Masoni and Mt. Aga area (Fig. 4.12).

The tourmalinites crystallized in the fault cutting the Cabianca Volcanite at Lake Aviasco (AV5 in Fig. 4.1 and 4.16) are microscopically different from the others along low- and high-angle normal faults: the matrix is not as dark as the former examples, it is composed of fine-grained tourmaline, quartz, muscovite, oxides and abundant sericite (Fig. 4.22e-4.23f). In this matrix are sparse some euhedral zoned green-bluish and pleochroic crystals of tourmaline (Fig. 4.23f), which sometimes show jaggy edges because they are partially substituted by sericite. Nevertheless, the tourmalines are in equilibrium with aggregates of arsenopyrite (Fig. 4.22f), which is a mineral phase included in the paragenesis of the uranium mineralization (Cadel 1986), and that we use (see chapter 4.3.5 and 4.3.6) to estimate the equilibrium temperature of the boron-rich fluids (see chapter 4.3.6).

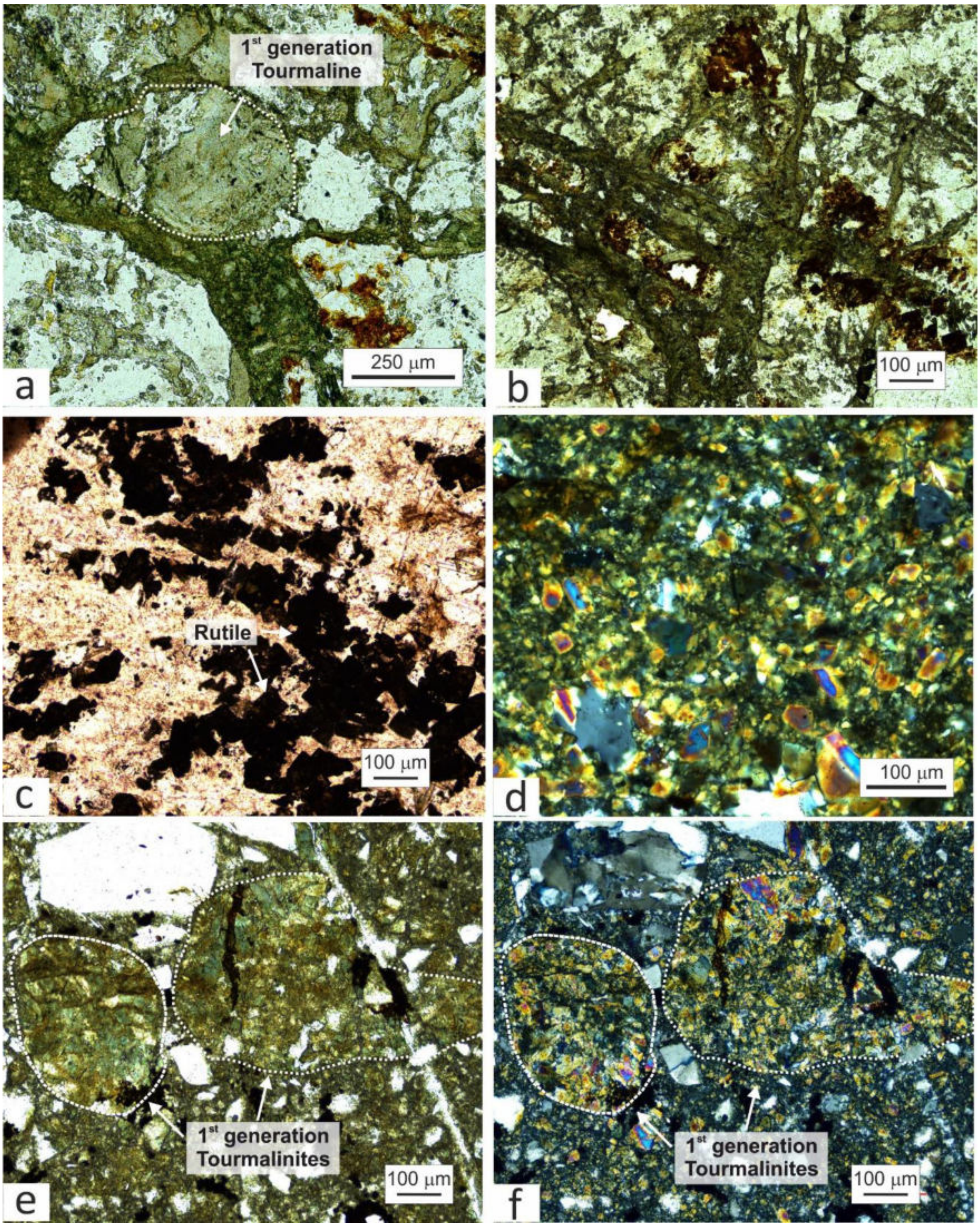

Figure 4.21 - Representative pictures of microscopic features for Type 1 tourmalinites in the basement of Trompia Valley (a-b) and for Type 2 from Valsassina (d-e-f). a) different generation of tourmalines are recognized at plane polarized light, with larger bluish-green tourmalines cut by felt-like dark green dense aggregate of finer crystals; b) stockwork of tourmaline veins at plane polarized light; c) rutile in equilibrium with tourmaline at plane polarized light; d) detail of tourmalinites groundmass in Valsassina; e-f) relicts of first generation tourmalinites with clasts of basement and quartz cemented in the tourmalinitc matrix at plane and crossed polarized light, cut by quartz vein.

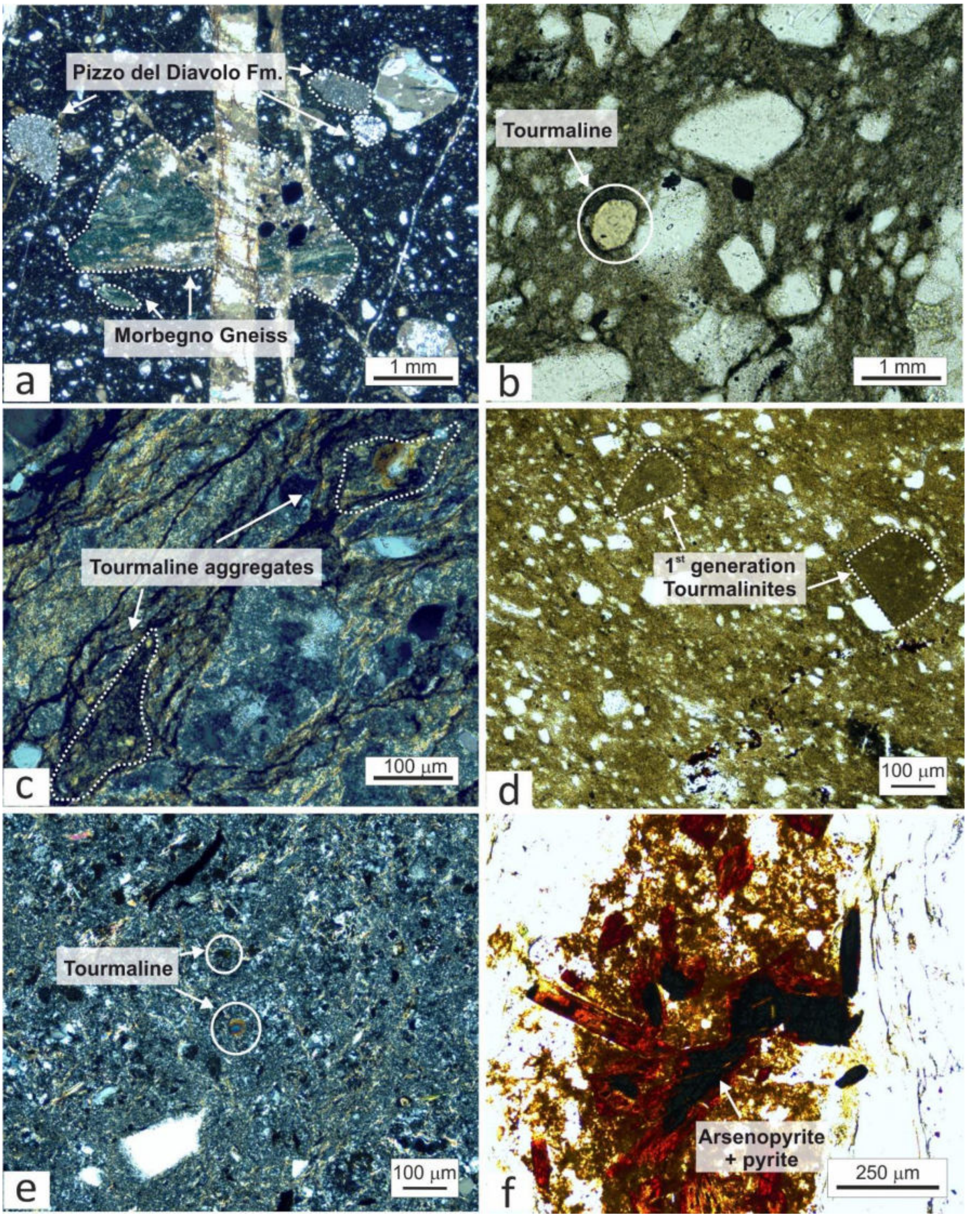

Figure 4.22 - Images of representative textures of Type 2 tourmalinites at the basement-sedimentary cover contact and in the sedimentary cover. a) clasts of former cataclasites derived from the Variscan basement (Morbegno gneiss) and sedimentary cover (Pizzo del Diavolo Fm.), cut by carbonates veins, at crossed polarized light; b) example of subhedral crystal of tourmaline merged in the dark fine grained matrix at plane polarized light; c) tourmaline aggregates along discontinuities the LANF fault core at crossed polarized light; d) relicts of former generations of tourmalinite at plane polarized light; e) tourmalinites in the sedimentary cover of Lake Aviasco at crossed polarized light, showing higher percentage of quartz and phyllosilicate, with two examples of high interference coloured crystals of tourmaline; f) arsenopyrite partially replaced to pyrite in Lake Aviasco tourmalinites, at plane polarized light.

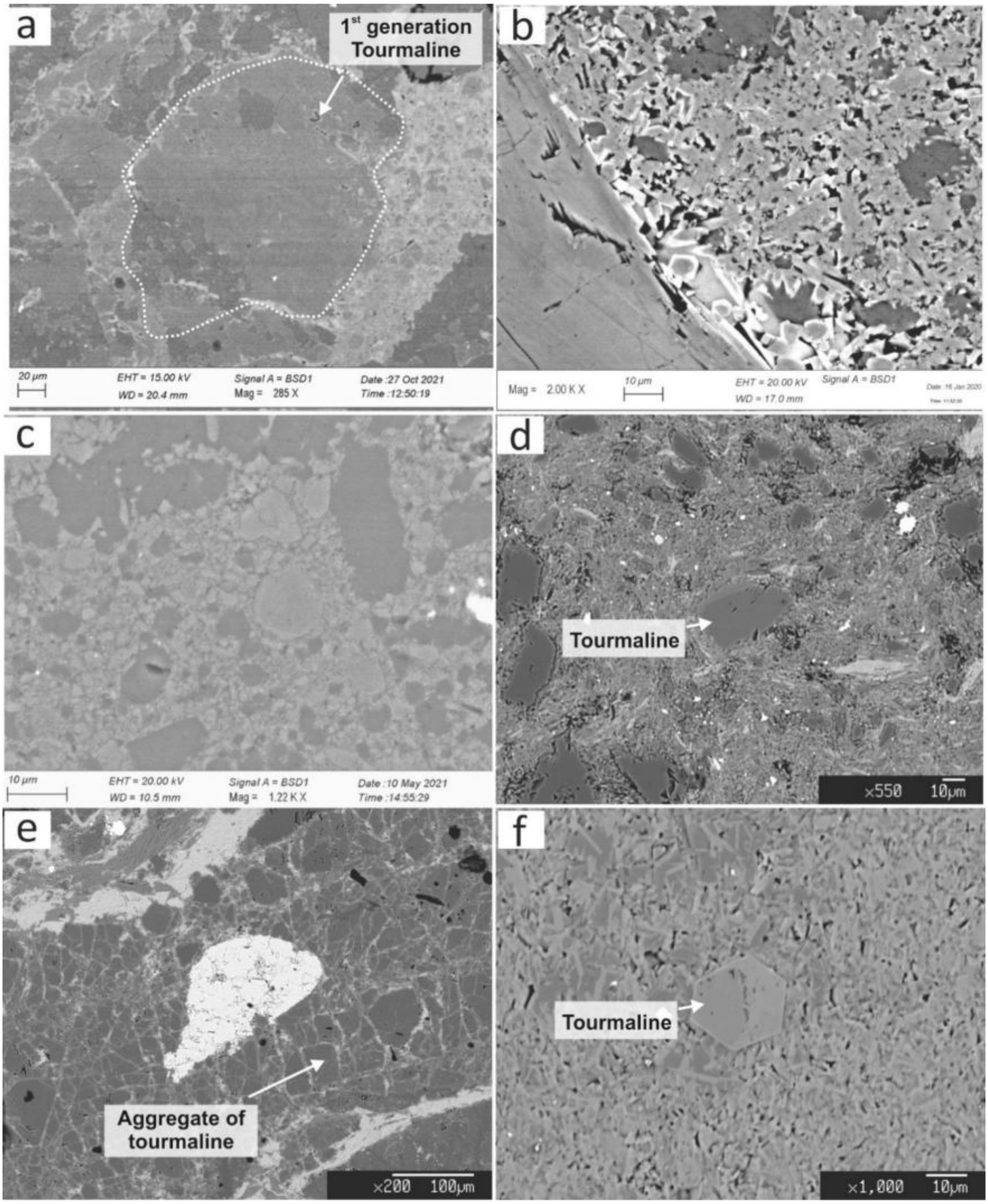

Figure 4.23 - Tourmalinites from the cSA at the electron microscope. A) type 1 tourmalinites from Trompia Valley, with two generations of tourmalines, where the larger crystals are generally cut by fine-grained aggregates; b) detail on the aggregates with clear core-rim zoning; c) type 2 tourmaline from Valsassina with a matrix of tourmaline including bigger crystals and clasts from former cataclasite and relicts of tourmalinites; d) subhedral tourmaline crystal of type 2; e) type 2 tourmaline aggregate along discontinuity, which show rims of different tourmaline composition sealing the fractured tourmalines; f) type 2 tourmaline from Lake Aviasco (AV5 position in Fig. 4.1), merged in a matrix composed of fine grained tourmaline phyllosilicate and quartz.

4.3.2 Tourmalinites mineral chemistry

Representative analyses of the cSA tourmalines composing the Type 1 and Type 2 tourmalinites are given in Appendix 3. The microprobe analysis here shown are mainly related to single crystals of tourmaline, but we also analysed the matrix. However, the analysis of these latter is rather a mixed bulk analysis, and were only used for comparison with crystal analyses and to indicate the "tourmalinization" degree of the rocks.

Compositions of most of the analysed points may be generally ascribed to the schorl-dravite solid solution series all over the study area, as shown in classification diagrams based on the principal constituent at the X-site (Hawthorne and Henry 1999) and on the Al–Fe–Mg ternary diagram from Henry and Guidotti (1985) in Fig. 4.24-4.25, both for microanalysis on crystals and matrix composition.

In diagram 4.24a, there is a positive correlation between Fe/Fe+Mg content and the X vacancy while in diagrams 4.24a-b-c the data are organized in clusters. The tourmalines belong to the Schorl-Dravite series, mainly differing in terms of Fe and Mg content.

Diagrams 4.25a-b-c are related to matrix spot analysis with Al_2O_3 and SiO_2 reasonably referable to tourmaline composition. The matrix geochemistry can represent bulk analysis of the very fine-grained mineral phases and we discarded the data with composition too different by tourmaline. It is noticeable that the data are scattered and enriched in Al and X-vacancy.

The optical zoning in the tourmaline crystals observed at the microscope, is related to compositional zoning (see Fig. 4.23). Using the microprobe we quantified the chemical variation, as easily discernible in Fig. 4.26-4.27 which represent X-ray element maps of single crystals of tourmaline from samples AV6 of Lake Aviasco and 880 of Trompia Valley. In the X-ray elements map distributions, principal variations of core-rim zoning mainly involve Fe, Mg and Al contents. The rims are generally enriched in Fe and depleted in Mg (sample 880 small crystal, FC21, AV5, Fig. 4.28); combined to the Fe enrichment there is also a higher content in Al, except for sample 880 that is depleted also in Al. In the larger crystals the trend is opposite (Fig. 4.28). In sample VSS3A the optical zoning is not marked from the chemical point of view, so it is not reported. The Fe/Mg ratio varies from 0.7 in sample C5 to 3.49 a.p.f.u. in sample 880 showing generally a negative correlation; Na content is about 0.7 a.p.f.u. for all samples; X-site vacancy varies from 0.16 a.p.f.u. in sample 880 to 0.25 a.p.f.u. in sample VSS3A and in every sample there is a positive correlation between Ti and Ca.

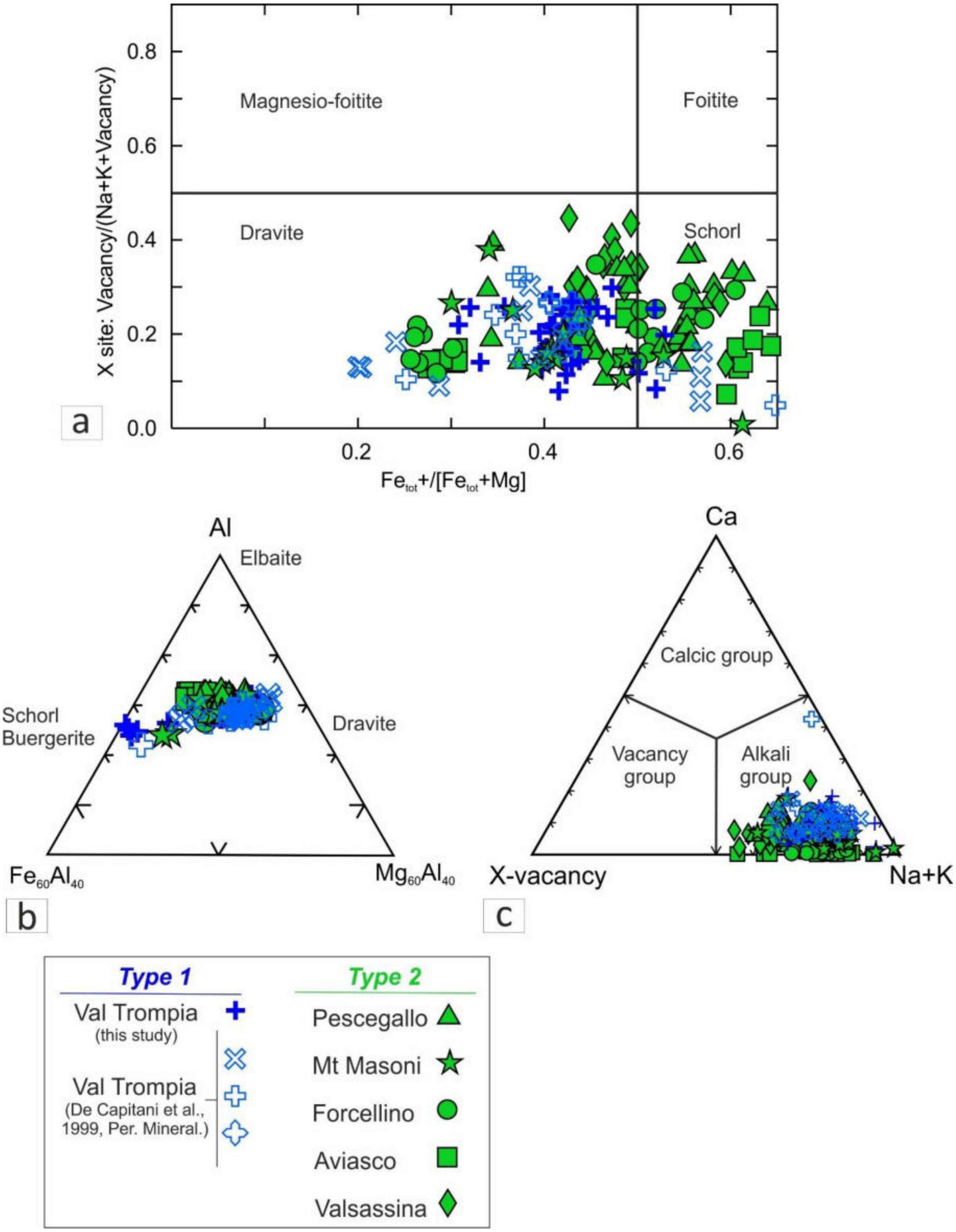

Figure 4.24 - Classification diagrams (Hawthorne and Harry, 1999) of analysed tourmaline crystals. The 3 types of tourmalines from the study of De Capitani et al. (1999) are referred to 3 different generation of tourmalines.

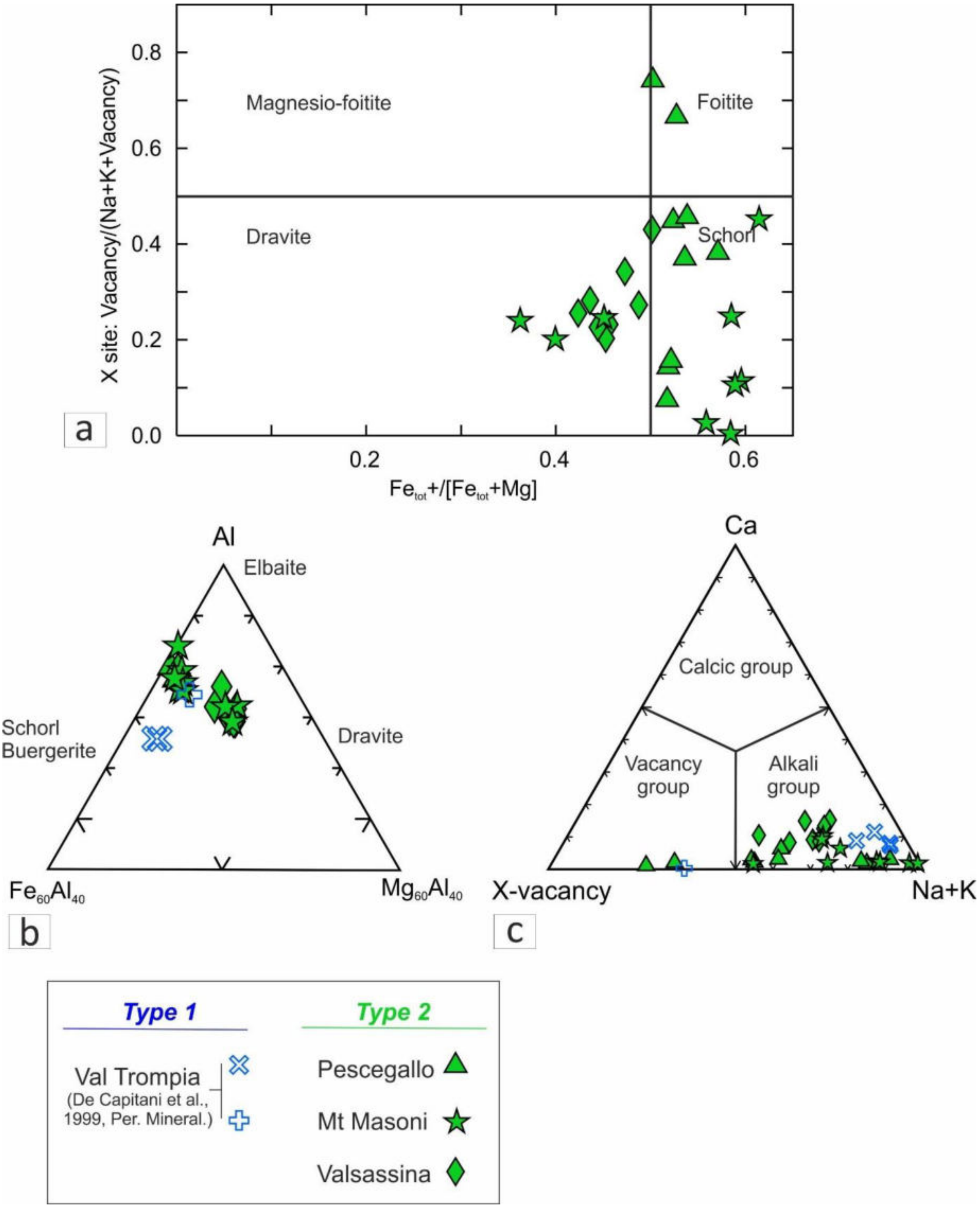

Figure 4.25 - Classification diagrams of the matrix based on major elements for tourmalinitic matrix. The 2 types of tourmalines from the study of De Capitani et al. (1999) are referred to 2 different generations of tourmalines.

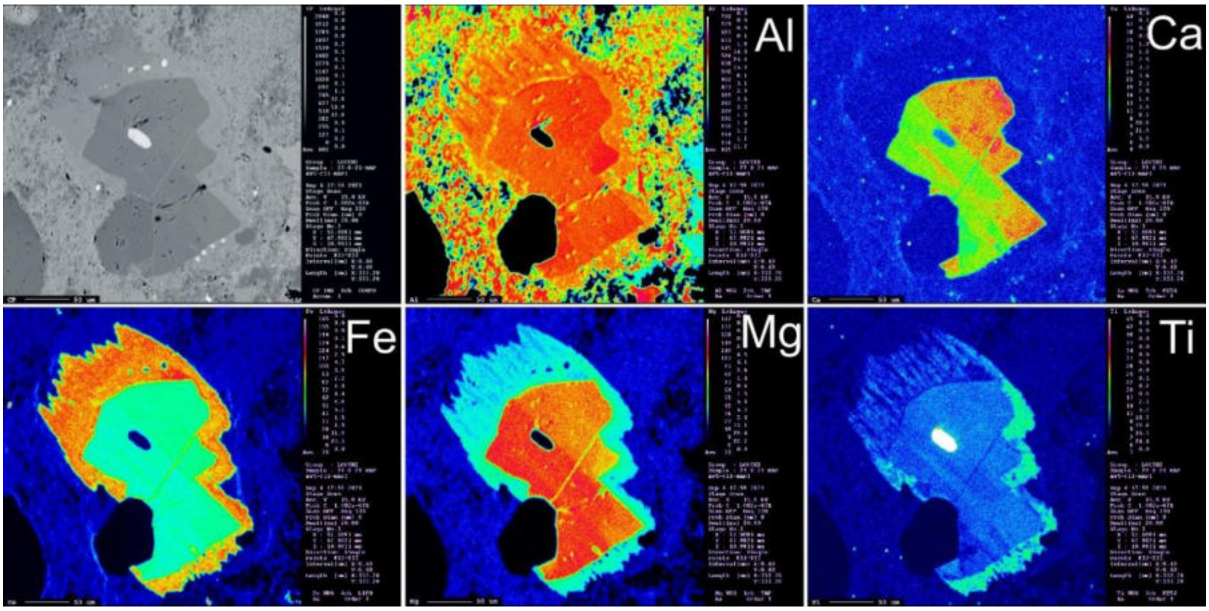

Figure 4.26 - X-ray element distribution in tourmaline crystal from Lake Aviasco, see position of sample AV5 in map of Fig. 4.1.

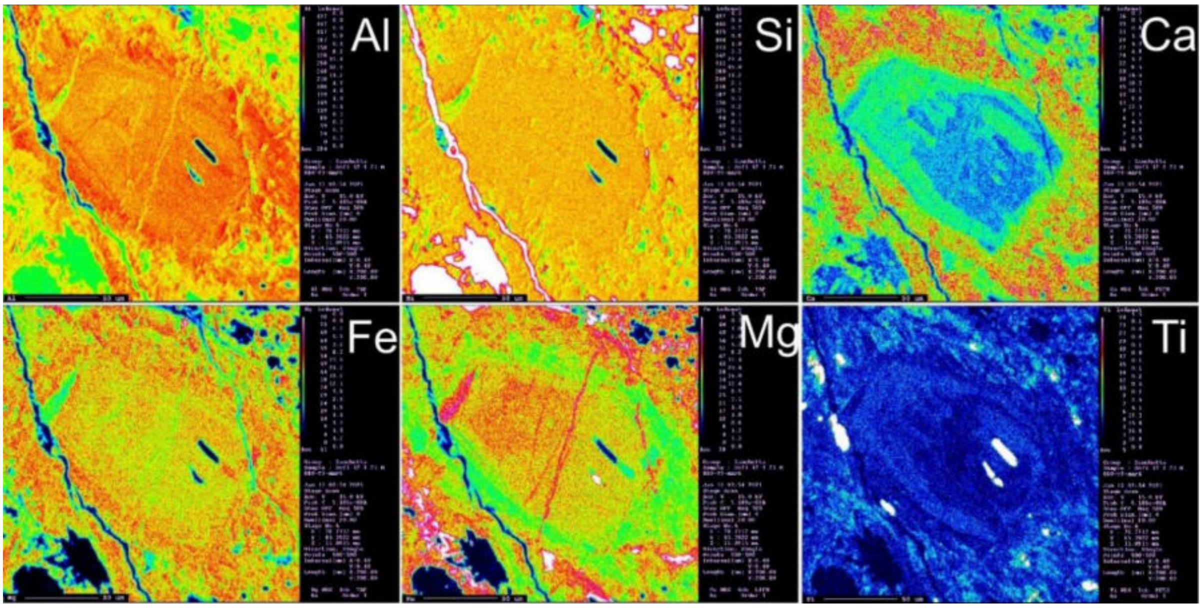

Figure 4.27 -X-ray element distribution in tourmaline crystal from Trompia Valley, see position of sample 880 in map of Fig. 4.1.

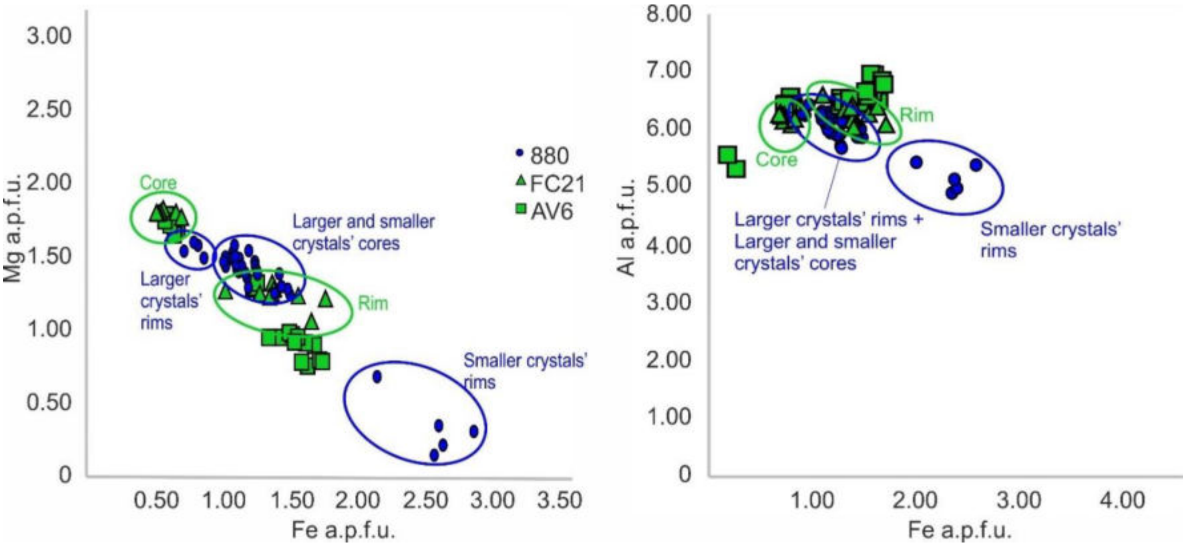

Figure 4.28 - Major elements differences in some samples characterized by optical and chemical core-rim zoning. The blue data are related to type 1 tourmalines and the green ones are about type 2.

4.3.3 Trace elements of tourmalines

In-situ LA-ICP-MS analyses were performed for the determination of trace element contents in tourmaline crystals and tourmalinite matrix. A total of 70 analytical spots of 7 samples is listed in Appendix 4. Matrix analyses are difficult to be interpreted, as they mainly represent a mixing from newly formed tourmaline and pre-existing rock-mass. Tourmaline analyses have been obtained from samples 880, LDC, VSS3A, FC21, and AV5 (Fig. 4.1).

On the average, tourmaline crystals of all samples show high concentrations of V, Ni, Zn, Ga and Sr (several tens to hundreds of ppm) but contain lower concentration of total REEs (5.05 to 13.2 ppm), except for sample AV5 which has 42.2 ppm ΣREEs, that stands out also for the up to 10 ppm U concentration.

In chondrite-normalized REE patterns, two main different patterns can be distinguished (Fig. 4.29). The Type 1 tourmalines of Trompia Valley, plotted in light to dark blue in Fig. 4.29, show depleted L-REE contents with respect to the H-REE, with the only exception of sample 880 (dark blue line in Fig. 4.29). All analysed samples display a positive Eu anomaly, with again the only exception of tourmalines from sample 880 that show no Eu anomaly.

Type 2 tourmalines from the Valsassina area show a similar REE pattern to Type 1 tourmalines, characterized by positive Eu anomalies.

Type 2 tourmalines of Lake Aviasco (AV5 in Fig. 4.1) that occur along a fault zone crosscutting the sedimentary cover and close to U mineralization, have strongly marked negative slope with L-REEs higher than H-REEs. On the other hand, the other Type 2 tourmalines along LANFs, show patterns inverting the slope in correspondence of Sm or Eu, M-REEs, and have positively sloped H-REEs.

Comparing all the tourmalines, we can notice that they differ also in the incompatible elements distribution patterns (Fig. 4.30). The positive Ba, U, Th, Ta, Sr, Ti anomalies are a common trait for all samples, as well as for the negative Rb, K, Zr anomalies, with respect to chondritic vakues. The Type 2 tourmalines of Lake Aviasco differ from the others especially in terms of Ba, K, Th, U, Zr and Hf contents, which are about 2 to 3 orders of magnitude higher.

Trace elements based on whole rock analysis for Trompia Valley (our study) and Biandino Valley Permian intrusives (Crippa 2017) are plotted in orange in Fig. 4.29-4.30 as reference, together with the Variscan basement shown in black (Bergomi 2004). We can notice that the Type 2 Valsassina tourmalines have opposite Eu anomalies in REEs diagram with respect to the Permian intrusives, whereas the Lake Aviasco tourmalines (AV5 in Fig. 4.1) share similar REEs and incompatible elements trends (Fig. 4.29-4.30) with the Permian intrusives.

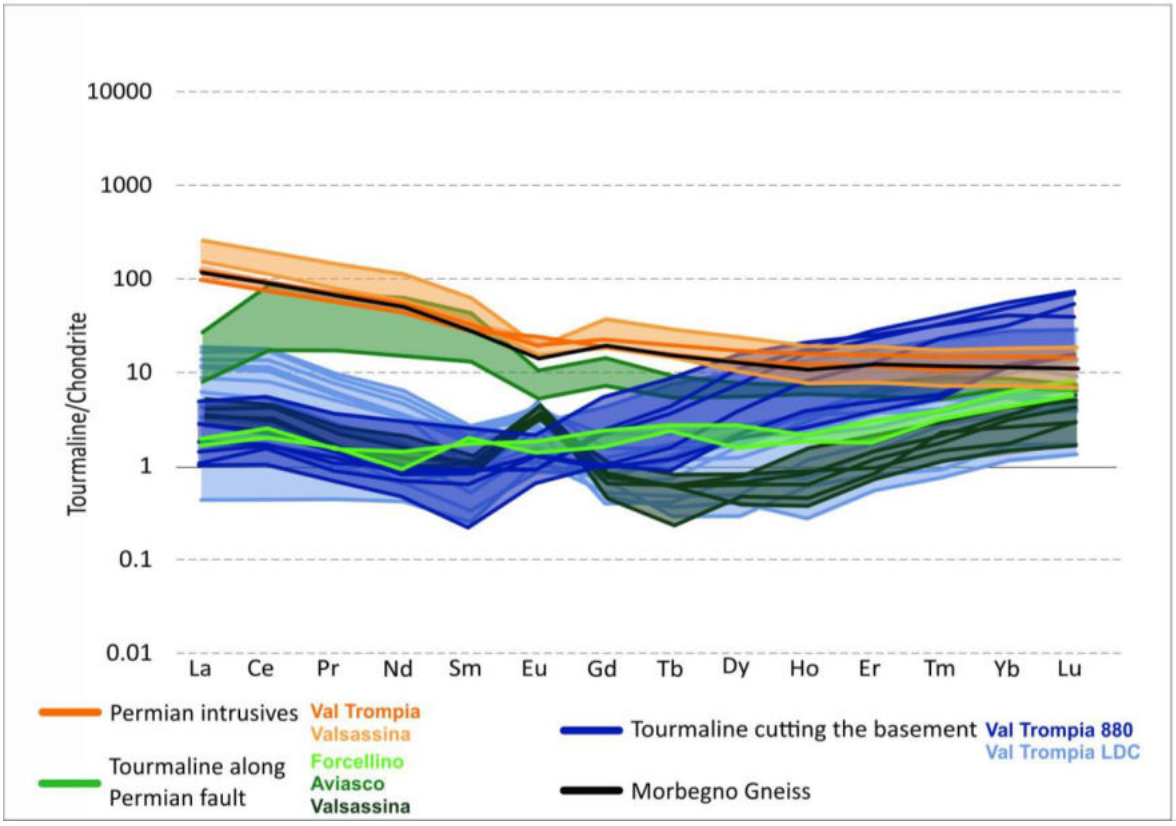

Figure 4.29 -REEs distribution of type 1 (in blue) and type 2 (in green) tourmalines, compared to Permian intrusives and the typical Variscan basement (Morbegno Gneiss Auct.). Data are normalized to chondrite (McDonough and Sun 1995).

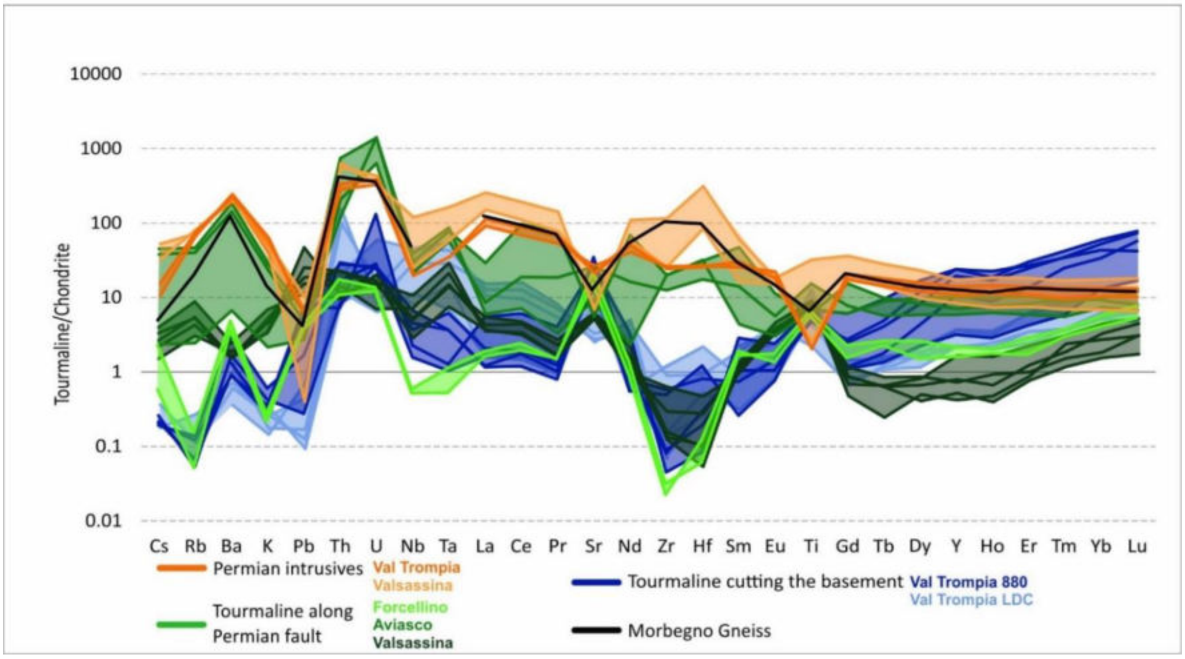

Figure 4.30 -Incompatible elements distribution of type 1 (in blue) and type 2 (in green) tourmalines, compared to Permian intrusives and Variscan basement. Data are normalized to chondrite (McDonough and Sun 1995).

4.3.4 Boron isotopic compositions of tourmalines

The isotopic composition of boron contained in tourmalines has been analysed by SIMS (Fig. 4.31). Analyses were performed on samples (about 15 analytical spots for each) with crystals large enough for the SIMS beam (about 10 microns) to avoid mixed analysis. Internal tourmaline zoning was not resolvable as growth rims was below the beam resolution. On the other hand, for the samples with smaller crystals (e.g. FC14, Fig. 4.31c-d), for several analytical spots the beam went over the grain boundary, providing a mixed boron isotopic composition. The total range in boron isotope compositions determined in our sample suite, expressed as $\delta^{11}B$ values, for tourmalines close to the intrusive bodies is on the average from –10.5 to –5.1‰, for tourmalines along low-angle normal faults (LANFs) is from –7.0 to –3.6‰ and -10.7‰ for the ones closest to the U-mineralization, i.e. the Lake Aviasco tourmalinites (Table 4.1 and Appendix 5).

The compositional zoning based on major elements is not identified in the boron isotopic composition, and this suggests that the source of the fluids must have been the same, without external isotopic contribution during the interaction with host rocks. Nearly all samples analysed are isotopically homogeneous within the uncertainty of 1.6‰ (1 SD) except for FC14 and C5 that are the samples with spots analysis at the grain boundary of crystals and partially measuring the matrix. An overview of the results is shown as a histogram in Fig. 4.32, and in detail, the statistical summary of the B-isotope results for the seven samples is as follows:

LOCALITY	SAMPLE	δ^{11}B (average)	N
Trompia Valley	880	-5.1±1.6‰	15
Valsassina	VSS3A	-10.5±1.2‰	13
Forcellino Pass	FC21	-5.7±1.0‰	7
Forcellino Pass	FC14	-8.2±2.7‰	15
Pescegallo-Gerola Valley	PG3A	-3.6±1.5‰	10
Mt Aga	C5	-6.97±2.5‰	9
Lake Aviasco	AV5	-10.7±1.5‰	10

Table 4.1 - Tourmalines samples analysed with SIMS – here are shown the values of boron isotope composition, obtained for different spot analyses ("N" column).

From the isotopic point of view, we can split the values of δ^{11}B in two main group: about -10.5‰ is the value of VSS3A and AV5 (Fig. 4.32c and 4.32e), and around -5‰ is the value for 880 (Fig. 4.32a), FC21 and PG3A (Fig. 4.32b and 4.32g) whereas FC14 and C5 are not strongly reliable because of the SIMS spots out of the target (Fig. 4.32d and 4.32f). The tourmalines close to the two different intrusive bodies, 880 and VSS3A, are different also from the isotopic point of view, as already noticed with the REEs distribution.

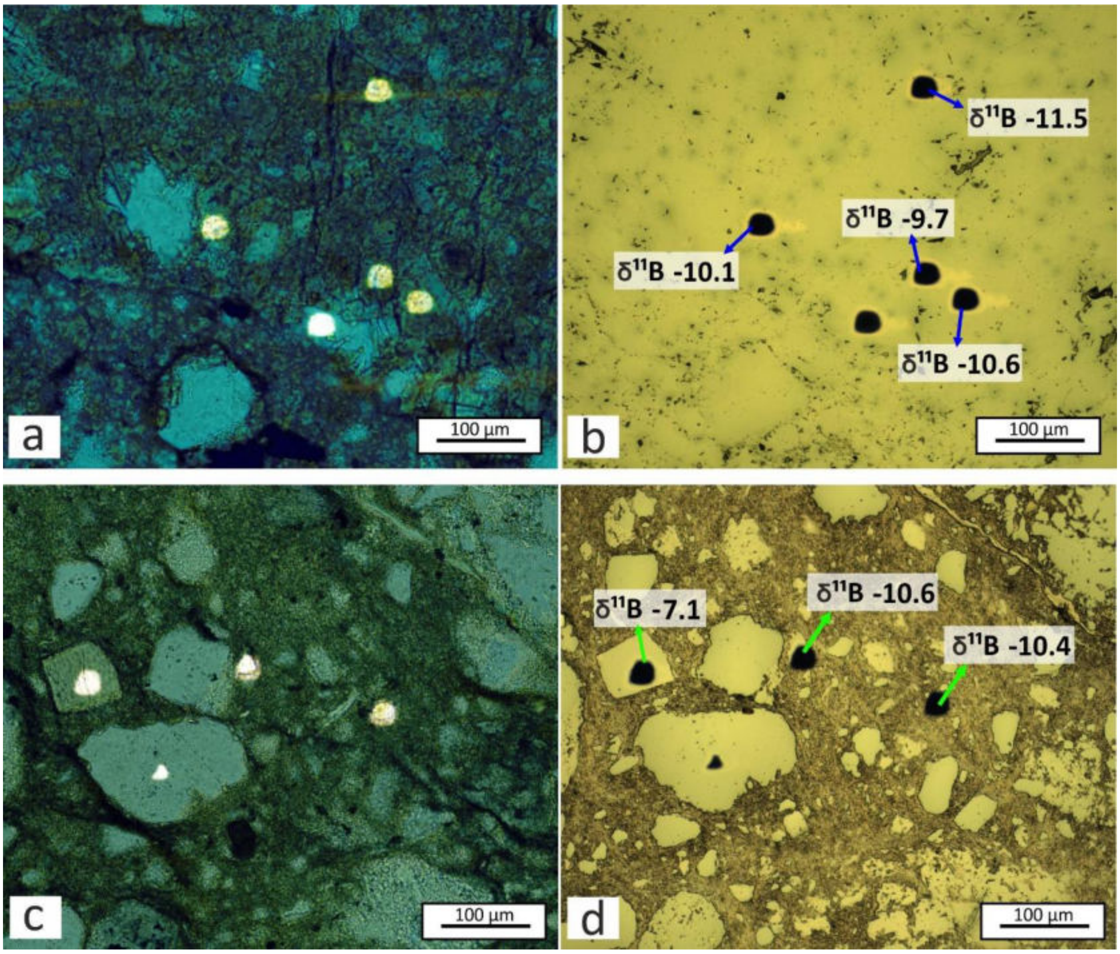

Figure 4.31 –thin section of sample VSS3A and FC14 at the microscope, with transmitted and reflected light. a) shows the craters produced in tourmalines of VSS3A by the SIMS analysis, which does not completely destroy the single crystals; b) δ^{11}B values for each crater; c) craters in tourmalines of FC14, with some analytical spots over the grain boundary; d) δ^{11}B values for each crater.

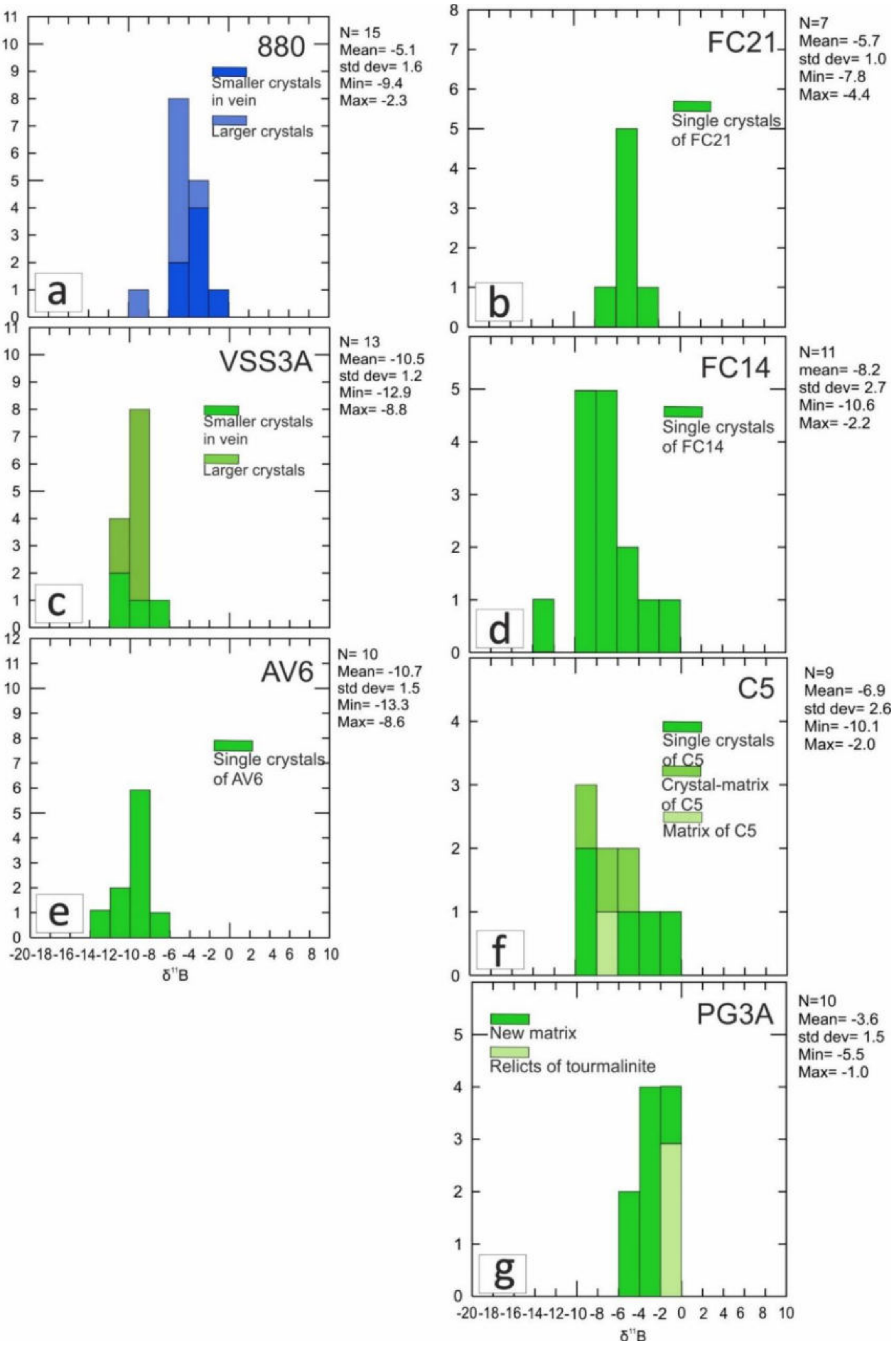

Figure 4.32 - Histograms representing the boron isotopic ratios of type 1 (in blue) and type 2 (in green) tourmalines from cSA.

4.3.5 Temperature estimates of tourmalinites formation

The SIMS analysis provides the boron isotope composition of tourmaline crystals, but not of the fluids precipitating tourmalines, from which is possible to reconstruct the source of boron (Trumbull et al. 2008). It is possible to obtain information on the fluids, considering the boron fractionation factor $\Delta^{11}B_{\text{(tour–fluid)}}$ which can be calculated with different formulas (e.g. Palmer et al. 1992, Meyer et al. 2008) that consider the fluid temperature.

The fluids temperatures for most of the localities in the cSA are indirectly estimated by a study on siderite ore-deposit in this sector of the Alps by Martin et al. (2017). These temperatures can be assigned also for the tourmalinitization because the siderites define a similar scenario to the one described so far by us. Indeed, they are widespread in the same areas, they are constrained to Permian and are in direct relationship with the uranium mineralization of Novazza-Vedello Valley district (Martin et al. 2017).

However, for the locality of Lake Aviasco (see position in Fig. 4.1), close to the uranium mineralization of Novazza, we could provide further information on estimated temperature of boron-rich fluids, because crystals of arsenopyrite occur in equilibrium with tourmalines and can be used as geothermometer. The arsenopyrite is used as geothermometer since the ‘70s, when Kretschmar and Scott (1976) proposed a phase diagram to reconstruct the temperature by means of the atomic % of As. This phase diagram nowadays is still used and is useful to quickly provide preliminary temperature (Nayak et al. 2021).

In Fig. 4.33a the still preserved crystals of arsenopyrite can be well-distinguished, which sometimes are replaced by pyrite, starting from their rims. 44 crystals of arsenopyrite were analysed at the microprobe to quantify the As content (Appendix 6). According to the phase diagram, for fluids precipitating arsenopyrites and tourmalines in Lake Aviasco area we obtained a preliminary temperature of about 380°C as shown with the pink dashed line in Fig. 4.33b.

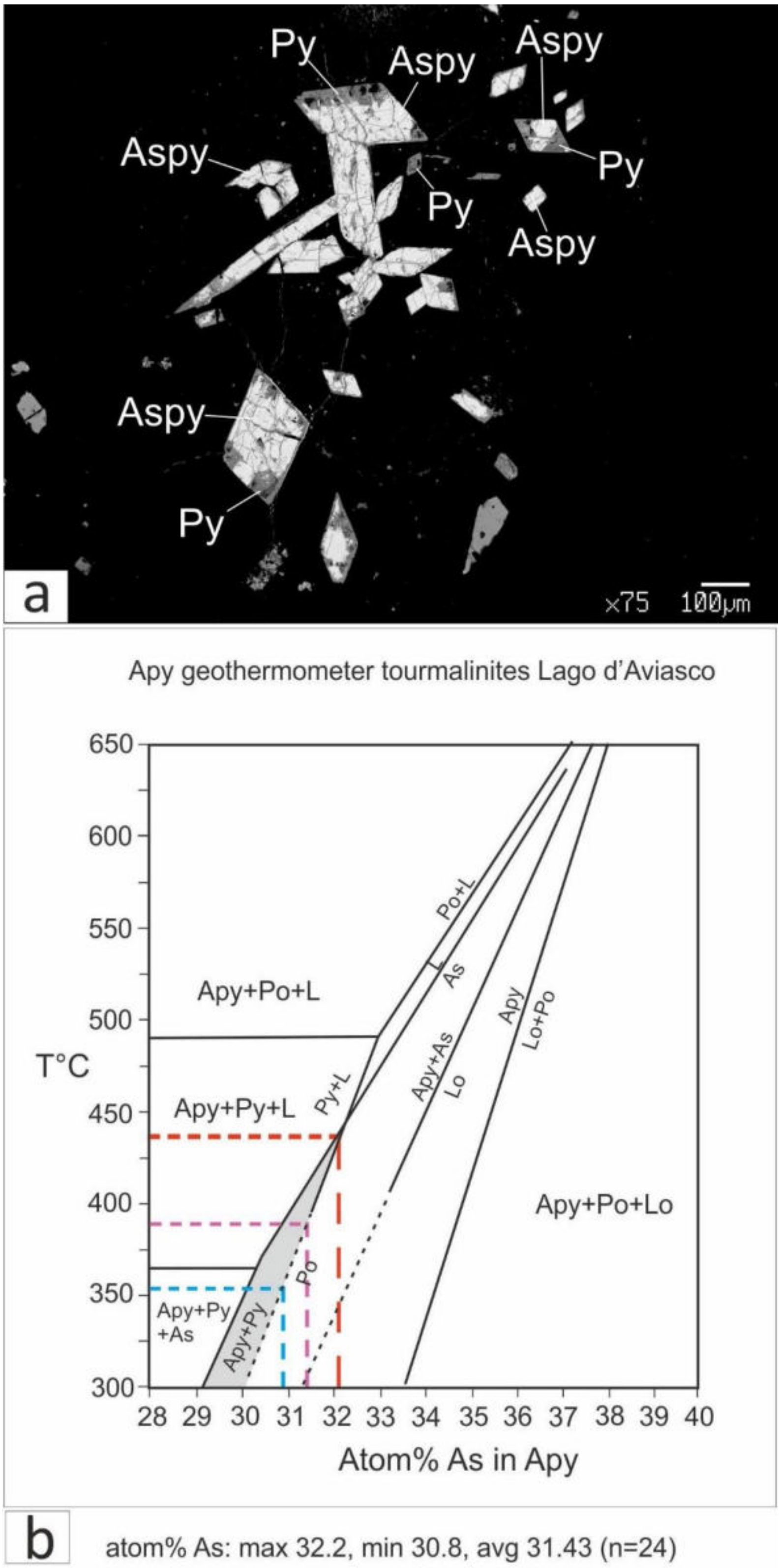

atom% As: max 32.2, min 30.8, avg 31.43 (n=24)

Figure 4.33 - a) SEM image of arsenopyrite (Aspy), analysed at the microprobe: sometimes the crystals rims are replaced by pyrite (Py); b) Atomic % of As in arsenopyrite is plotted in the phase diagram of Kretschmar and Scott (1976) depicts the temperature regime of arsenopyrite crystallization between 335 and 425 ◦C.

4.3.6 Modelling the source of boron-rich fluids

To assess the hypothesis of a magmatic source for these boron-rich fluids, first it was necessary to estimate the boron isotopic composition of single crystals (Fig. 4.31-4.32), to finally obtain the boron isotopic composition of the fluids responsible for their precipitation. The fluid precipitating tourmaline has a different boron isotopic composition because of the boron fractionation occurring at the state change. This difference is described with the boron fractionation factor $\Delta^{11}B_{(tour-fluid)}$, that can be calculated having temperature estimates (e.g. Palmer et al. 1992; Meyer et al. 2008).

In this study, the formula proposed by Meyer et al. 2008 is applied considering the estimated temperatures (Fig. 4.33 and Martin et al. 2017) of the Permian hydrothermal event characterized by siderite vein swarms in the studied localities with tourmalinites and the temperature estimated with the Arsenopyrite geothermometer (Fig. 4.33). We considered temperature variations, for this reason we obtained two different values of boron fractionation factor, as shown in Tab. 4.2. According to the T values and the fractionation factors, for each locality we obtained two boxplots (Fig. 4.34) which are slightly different and the calculated isotopic compositions $\delta^{11}B$ for fluids are from a minimum of -12‰ to maximum 5‰.

These results will be discussed in chapter 5.5 and compared with other possible boron sources (Fig. 5.6), in order to reconstruct the origin of the boron-rich fluids interesting the cSA.

Locality	**Sample**	**T in K**	$\mathbf{\Delta^{11}B_{(tour-fluid)}}$ **=** **4.2*(1000/T)-3.52** (Meyer et al. 2008)
Trompia Valley	880	673-823	2.7-1.6
Valsassina	VSS3A	623-773	3.2-1.9
Forcellino Pass	FC21	473-573	5.4-3.8
Forcellino Pass	FC14	473-573	5.4-3.8
Monte Aga	C5	473-573	5.4-3.8
Lake Pescegallo	PG3A	473-573	5.4-3.8
Lake Aviasco	AV6	573-673	3.8-2.7

Table 4.2 - Samples of tourmalines from different localities, analysed with the SIMS. Here is shown the range of temperature expressed in Kelvin, which is used to obtain different values of $\Delta^{11}B_{(tour-fluid)}$.

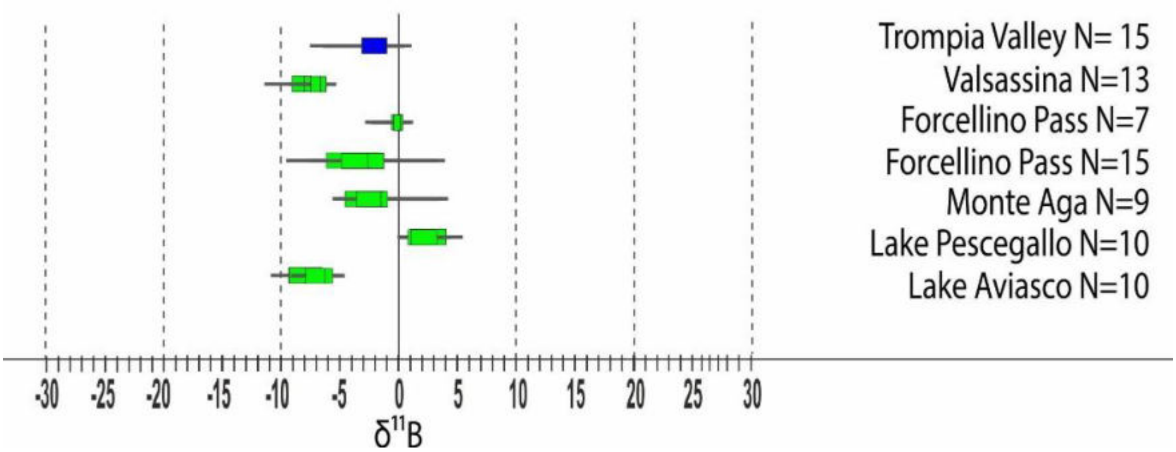

Figure 4.34 - The Δ ^{11}B (tour–fluid) is used to obtain the boron isotope composition of fluid precipitating tourmalines of cSA, which are here plotted as boxplots. This graphic representation is useful for further discussions that will be commented in chapter 5.5.

4.3.7 Geochronology

In order to constrain the timing of magmatism, hydrothermalism, boron metasomatism and the formation of uranium ores, geochronological data on the different geological manifestations of the above phenomena are crucial and described in the next paragraphs. In particular, due to the field-relationship between intrusive bodies and boron-rich hydrothermalism in Trompia Valley area, a genetical link can be assumed and it is confirmed also by the isotope compositions. Thus the geochronology of intrusive bodies and tourmalinites from Trompia Valley is here provided.

Age of Magmatism in Trompia Valley area

As described in chapter 4.2, zircons are accessory phases of Trompia Valley intrusives and were used to determine the age of the intrusive rocks with U-Pb geochronology of e samples coming from the personal collection of De Capitani. In the past, the age of these rocks was already constrained with Rb-Sr dating on biotites (De Capitani et al. 1994) and the obtained cooling time interval is about of 274-271 Ma. However, the Rb-Sr provides a wide range of variation, so a more accurate dating was necessary and for this reason on zircons is a more accurate method because we applied U-Pb dating on zircons of samples MVN3, VNE3 and VNE4 using the LA-ICPMS which results are summarized in Appendix 7.1.

The samples are respectively a granite (MVN3) and two granodiorites with different grain size (VNE3 and VNE4) sampled at locality Ester, close to Collio in Trompia Valley, where the Torgola Fluorite Mine occurs (Fig. 4.17).

For sample MVN3 we analysed 18 zircons with 44 spot analyses; for sample VNE3, 11 spots analyses were applied to 4 zircons better preserved with respect to the others badly fractured; in sample VNE4, 33 spot analyses were performed on 23 zircons.

Zircons from sample MVN3 are prismatic, colourless to pale pink or brown, and transparent with fluid and mineral inclusions. They are 40–150 μm long, with an aspect ratio of 1:2 or 1:1. In cathodoluminescence images, they appear dark with faint and thin oscillatory zoning and sometimes inherited irregular cores with magmatic overgrowths occur (Fig. 4.35a). U and Pb isotopic composition determined on single zircons with LA-ICPMS provides 287.7±0.83 Ma (MSWD=2.1) for sample MVN3.

In sample VNE3 the zircons are highly fractured and/or metamictic and they provide 286.2±2.1 Ma (MSWD=0.20).

Sample VNE4 shows similar features to sample MVN3 and the respective Concordia gives 284.9±1.2 Ma (MSWD=0.061).

In all samples, some cores of zircons were dated as more ancient than 450 Ma as shown in Fig. 4.35b, 4.36b and 4.37b. These data were discarded because they are representative for inherited relicts of Ordovician zircons. However, on the average, the age for all samples is c.a. 286 Ma (Early Permian), thus the U-Pb dating constrains the magmatism of Trompia Valley to about 10 Ma years before the 274-271 Ma obtained with the Rb-Sr isotopic system of biotites (De Capitani et al. 1994).

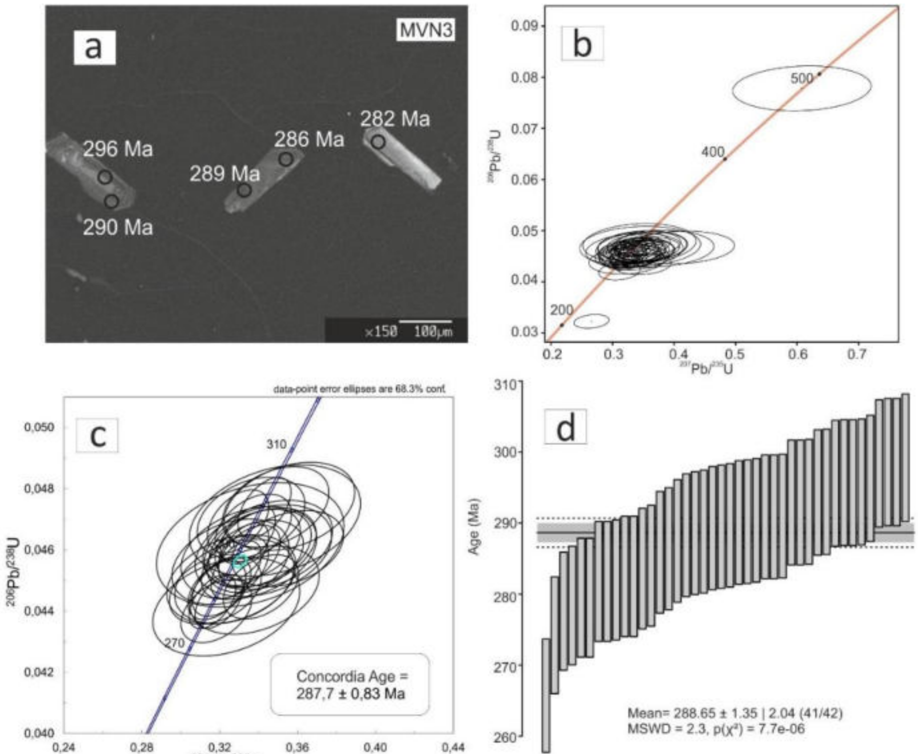

Figure 4.35 - a) Cathodoluminescence image of zircons separated from sample MVN3; b) Concordia diagram obtained for all spot analyses, representative also for cores of inherited Ordovician zircons; c) Concordia diagram of selected data, representative for spot analysis on Permian zircons; d) histogram representing the selected results.

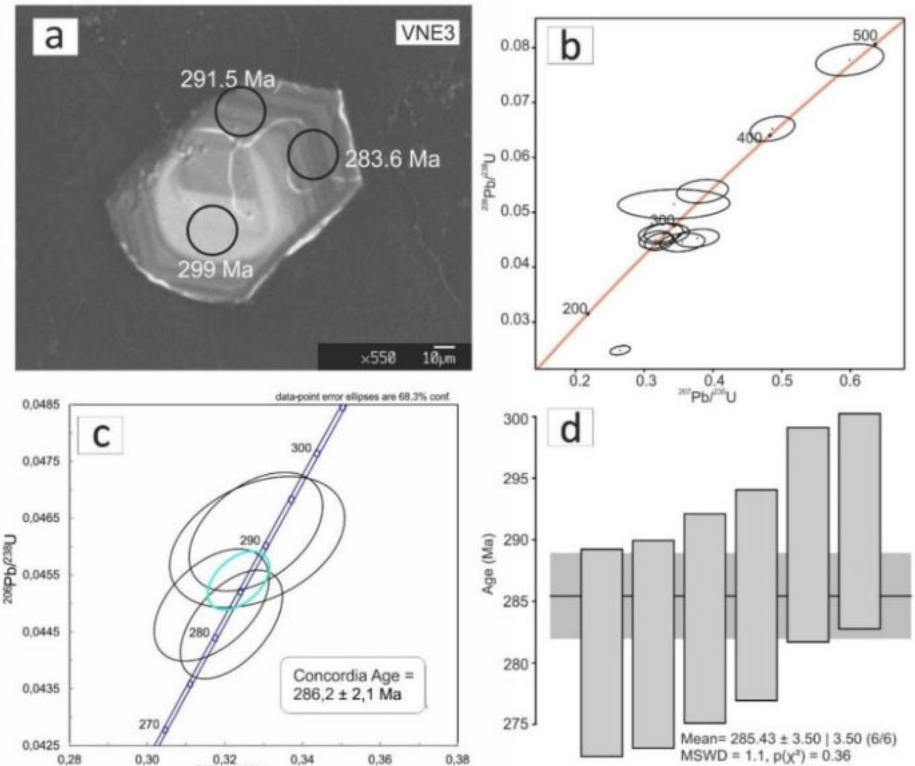

Figure 4.36 - a) Cathodoluminescence image of zircons separated from sample VNE3; b) Concordia diagram obtained for all spot analyses, representative also for cores of inherited Late-Palaeozoic zircons; c) Concordia diagram of selected data, representative for spot analysis on Permian zircons; d) histogram representing the selected results.

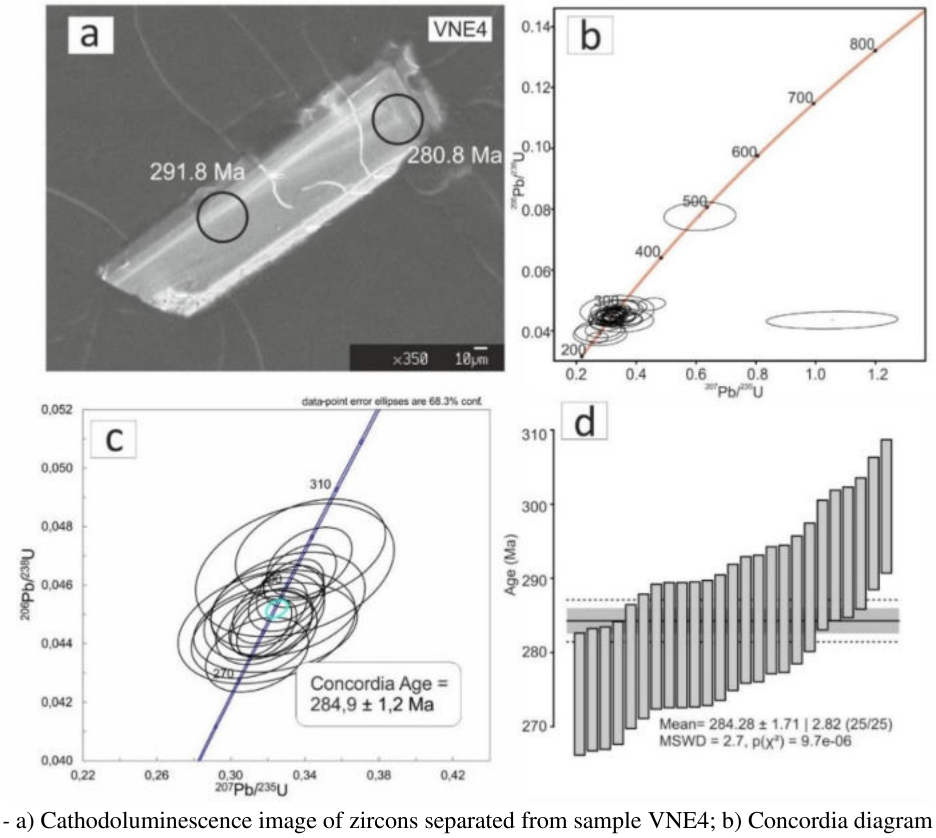

Figure 4.37 - a) Cathodoluminescence image of zircons separated from sample VNE4; b) Concordia diagram obtained for all spot analyses, representative also for cores of inherited Ordovician zircons; c) Concordia diagram of selected data representative for spot analysis on Permian zircons; d) histogram representing the selected results.

Age of Tourmalinites in Trompia Valley area

For tourmalinites' geochronology, a total of 36 measurements on single rutile crystals were performed on sample VM8 from the TrompiaValley area. The sample for geochronological analyses has been selected as it was the only one containing crystals large enough for the laser ablation spotsize. As observed at the SEM, rutile crystals in VM8 are euhedral with a prismatic habit, displaying no internal zoning. They reach about 40 µm in length, and occur as polycrystal aggregates in equilibrium with quartz and tourmaline.

Results for rutile U–Pb analyses are listed in Appendix 7.2 and shown in Fig. 4.38. The obtained mean $^{206}Pb/^{238}U$ age is 280±38 Ma (MSWD = 13).

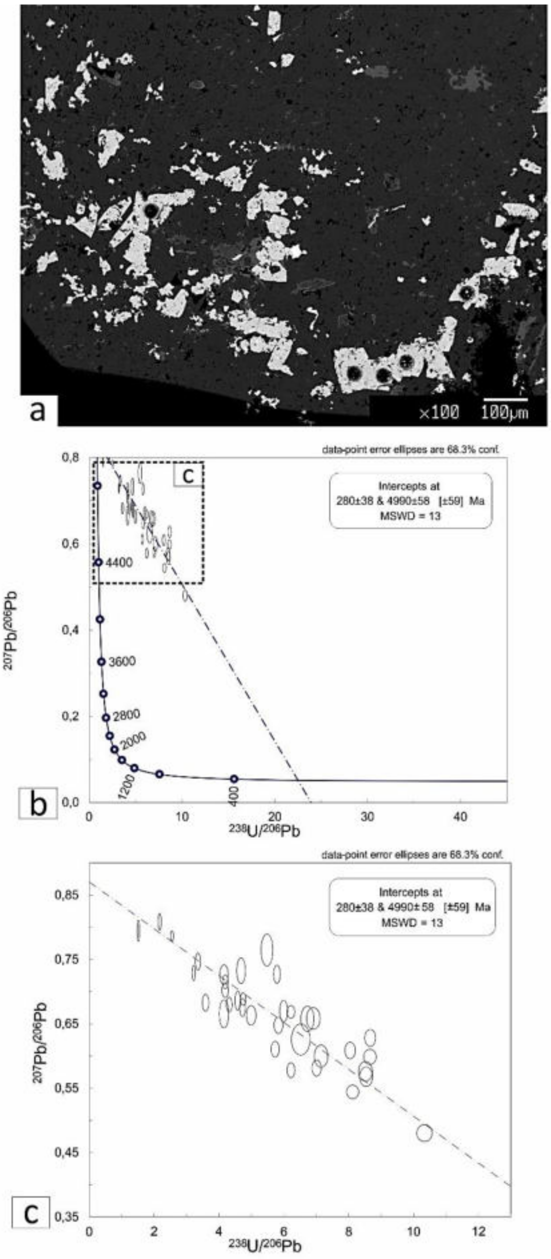

Figure 4.38 - a) Rutile grains in tourmalinites of Trompia Valley (position in Fig. 2.4) and b) plot of U-Pb data for Trompia Valley tourmalinites, with a close up of the results in c). Error ellipses are 2-sigma.

Age of Uraninite in Vedello Valley area

In addition to the intrusives and tourmalinites ages, new geochronological data are also provided for the uranium mineralization of Vedello Valley district, which is confined to the Aga-Vedello LANF (Zanchetta et al. 2022). The main ore deposit in this sector does not crop out to surface and the access of the exploring tunnels were completely closed. However, thanks to the provision of a geologist who worked in the exploring tunnels of Val Vedello mine, Geol. C. Pessina, we obtained a sample of the mineralization collected in the underground, named VV1.

Chemical dating of Uraninite contained in this sample has been used to constrain the age of the mineralization. These results are finally discussed in the frame of the interplay between tectonic, magmatic and ore generation processes that interested the present day cSA area in the Early Permian.

As documented in a personal communication of Geol. Pessina, the uranium mineralization of Vedello Valley is composed of disseminated submicron- to micron-sized crystals of rare uraninite (UO_2) and widespread polyphasic pitchblende (UO_2 in colloidal habit), which represents the most characteristic uranium ore mineral of Vedello Valley deposit (Fig. 4.39a). It is associated with brannerite (UTi_2O_6), blende, chalcopyrite, pyrite, arsenopyrite, tetrahedrite, and carbonates such as calcite, magnesite and siderite, and also rutile and haematite (Cadel 1986).

Chips VV1A and VV1B were cut from sample VV1 which come from the exploring tunnels, where former uraninite is often replaced by alteration products containing common lead. This makes difficult to date the sample by the U-Th-Pb microchemical method, which relies on the assumption that all the Pb measured in uraninite is radiogenic. However, we polished and carbon-coated the chips of the same sample VV1, in which we recognized at the microprobe few unaltered uraninite grains, typically a few microns in size, distributed in the groundmass together with 20 μm brannerite crystals (Fig. 4.39b).

Chemical ages for these grains are highly scattered and spread from ~190 Ma to about ~50 Ma (Fig. 4.39c, Appendix 8). The significances of these results are discussed in chapter 5.6.

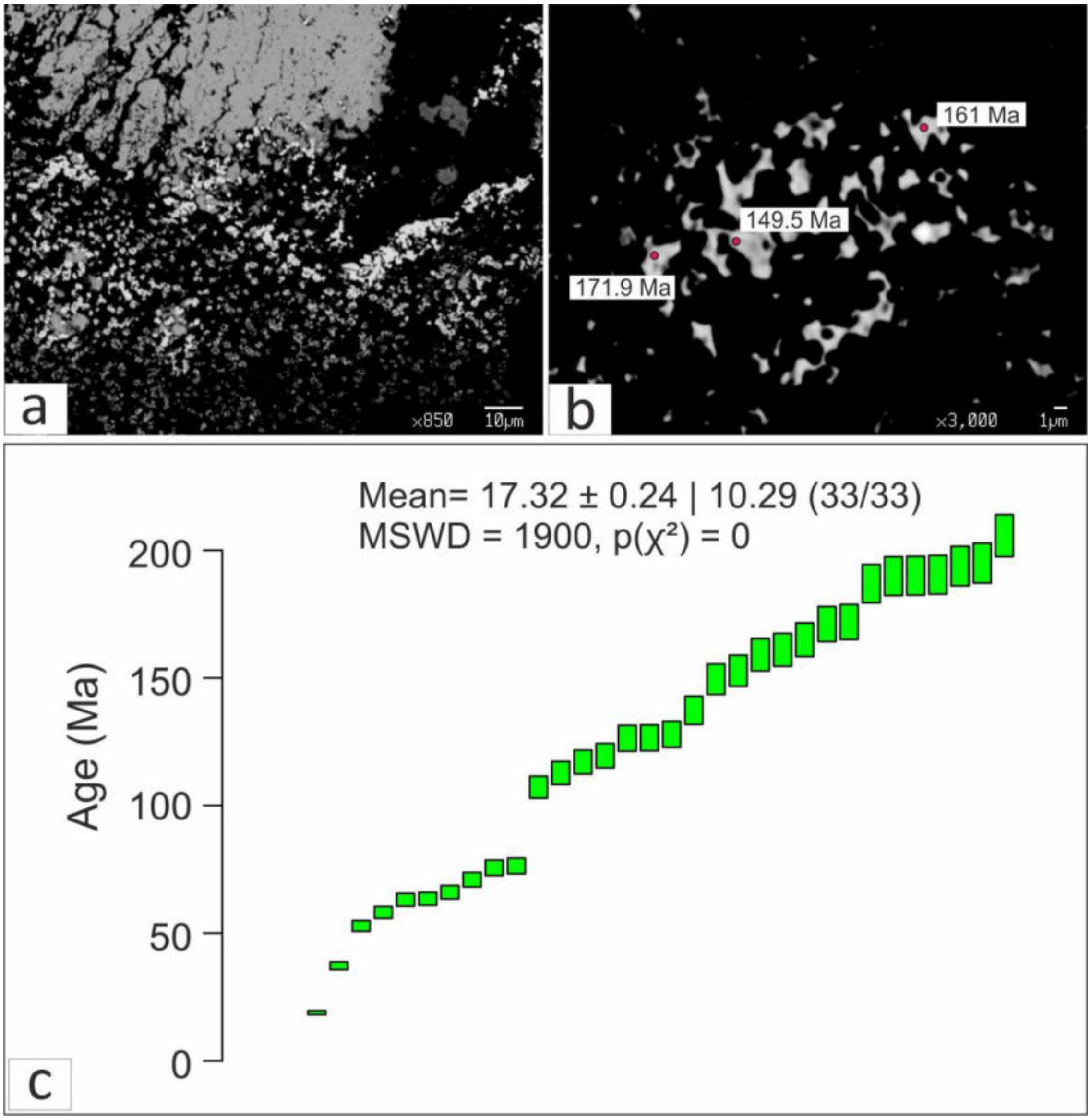

Figure 4.39 - a) disseminated submicron- to micron-sized crystals of pitchblende mineralization, sometimes silicitized; b) pitchblende grains preserved, used for chemical dating.

5. DISCUSSIONS

In this chapter are summarized and discussed the most relevant results obtained by the present Ph.D. project. The interest in this area of the Alps is led by the occurrence of preserved Permian Low-Angle Normal Faults (LANF), recently recognized (Zanchi et al. 2019; Zanchetta et al. 2022). To understand if this structural setting was representative for a single sector or of entire central Southern Alps (cSA), the research of other possible Permian LANF in areas with similar geological setting was performed. The best chance to find new evidence was represented by the Gerola Valley area, where large portions of Variscan basement crop out in contact with the Lower Permian sedimentary sequence.

In addition to the extensional tectonics, the other issue addressed was the relationships between the Permian magmatic activity and the widespread hydrothermal manifestations represented by tourmalinites sealing the Permian LANFs. The origin of the boron-rich fluids precipitating tourmaline has never been traced, so this is another one of the main goals to achieve.

The Permian scenario in this area is further complicated by the occurrence of uranium ore deposits in Novazza-Vedello Valley district, supposed to be related to Permian tectonics and boron-rich hydrothermalism. However, also in this case no direct evidence has never been provided so far. Thus, in the tourmalinites of the cSA a boron source is questioned and for any other clue indicative for the possible genetic link with the uranium mineralization.

In the following paragraphs, the fieldwork performed in the Gerola Valley area is discussed in comparison with other Permian evidence considered by previous studies in the cSA. Subsequently to the structural setting and its geodynamic consequences, the geochemical analysis of tourmalinites from different sectors is here interpreted with the aim of inserting the boron-rich hydrothermalism in the frame of the Early Permian geodynamic scenario. Finally, the insights obtained from the tourmalinites analysis are discussed together with their likely connections with the uranium ore deposit of Novazza-Vedello district, which are demonstrated for the first time to be genetically linked.

5.1 The Gerola Valley extensional system

Field analyses performed in the Gerola Valley area pointed out the occurrence of Early Permian extensional fault system characterized by a combination of low- and high-angle normal faults (Fig. 5.1). Several lines of evidence indicate their development. All along the Orobic Thrust, large exposures of the Variscan basement cropping out just below the thrust plane occur only in the Gerola

Valley and in the Valsassina area (Sciunnach 2001a; Froitzheim et al. 2008; Pohl et al. 2018). In both cases, the basement exposure is related to the occurrence of extensional fault systems likely representing the superficial expression of the Early Permian crustal thinning (Filippi at al. 2021 and references therein). This can be explained with the Permian extensional tectonics that brought the Variscan basement at shallower crustal levels, further uplifted by the Orobic Anticlines during the Alpine orogenesis.

In the Gerola Valley area, the tectonic contact between the underlying basement and the Permian sedimentary cover is interested by Alpine thrust structures, however it maintains young-on-old stratigraphic relationships, which are typical of normal faults. The Orobic Thrust is the most important Alpine structure of the area, however, moving southwards, the deformation accommodated along the thrust plane is minor. The Lower Permian succession was deposited forming a low angle with respect to the the Pescegallo fault, suggesting that this fault was propagating toward the present-day northern quadrants with a low dip angle (Fig. 4.6). According to the combined mesoscopic and microscopic analyses of the cataclasites developed within the Pescegallo fault core, some original parts of it are well preserved. The presence of remnants of non-foliated coarse-grained fault breccias with angular to rounded clasts together with the maximum thickness of the Permian succession (1000-1500 m) suggest a shallow structural environment, not exceeding a few kilometres of depth.

Close similarities with the Aga-Vedello LANF, which is also associated to a high-angle synsedimentary fault in its hanging wall (“Aga Growth Fault”, Zanchi et al. 2019), and abundant tourmalinites along the fault plane (Zhang et al. 1994; Cadel et al., 1996, Blom and Passchier 1997; Zanchi et al. 2019), indicate that the Pescegallo fault, as well, can be related to the Early Permian tectonics. In our interpretation, the Pescegallo LANF is a Permian low-angle normal fault that was only re-activated during the Alpine tectonics, preserving most of its original features (Fig. 5.1).

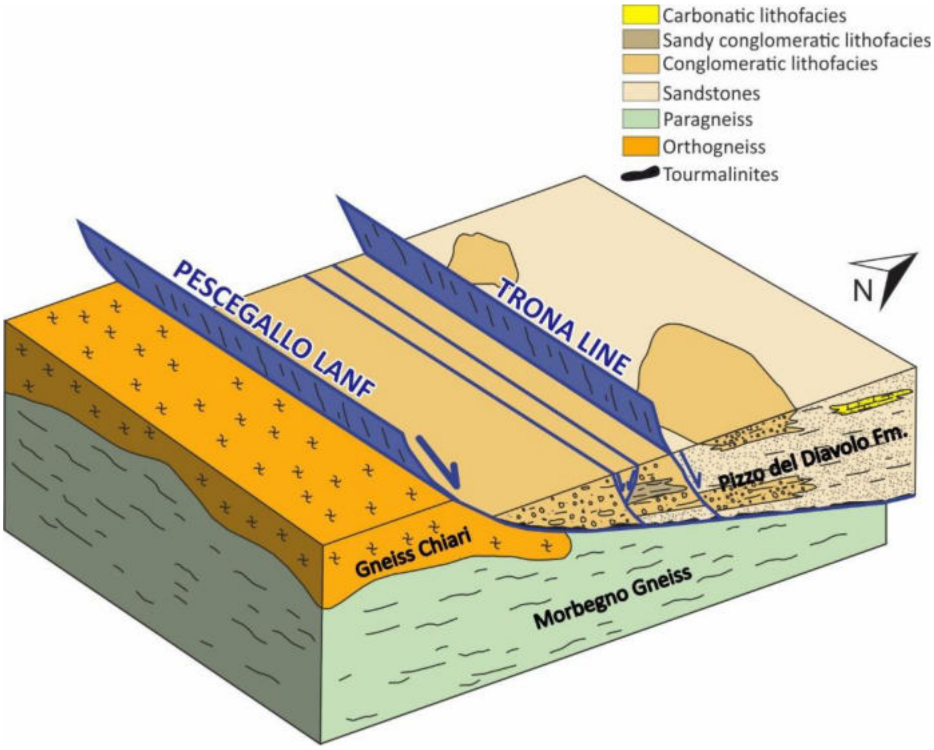

Figure 5.1 - 3D model representing the Early Permian evolution of the Gerola Valley area, during which the extensional regime led to the development of low- and high-angle normal fault system, responsible for the opening of the intracontinental Orobic Basin (after Locchi et al. 2022). The Pizzo del Diavolo Fm. deposited contemporary with the tectonic activity, producing some peculiar structures in the sandy portions indicative for soft-sediments deformation (i.e. Fig. 4.10).

In this framework, the Trona Line is also interpreted as an Early Permian high-angle normal fault (Fig. 5.1), active during the deposition of the Pizzo del Diavolo Fm., as suggested by abrupt contacts among different lithofacies and by kinematically coherent mesoscopic synsedimentary normal faults, occurring along the main fault trace. In addition, the tectonic boundary separating the metamorphic basement from the Lower Permian successions within the deepest portion of the Orobic Anticline (Fig. 2.5), already noticed by the Dutch geologists ("the Mezzoldo window" in De Sitter and De Sitter Koomans 1949), may represent the lateral equivalent of other components of important extensional systems, directly related to the opening of the Orobic Basin. The Grassi Detachment, identified in the Valsassina area to the W of Gerola Valley (Fig. 5.2), may represent the deeper expression of this extensional system (Froitzheim et al. 2008; Pohl et al. 2018).

The Pescegallo LANF, in this frame, could represent the upper crustal termination of the Grassi detachment, which is NNE dipping, it is extended for few km and its fault core consists of a cataclasite layer underlain by mylonites (Froitzheim et al. 2008; Pohl et al. 2018). However, a direct connection of the two fault systems is prevented by the occurrence of Alpine tectonic structures that displaced Early Permian structures and coupled tectonic units that were at different crustal levels during the opening of the Orobic Basin. Compared to the Grassi Detachment, the Gerola extensional system shows different features linked to a shallow crustal environment characterized by brittle deformations, similarly to the Aga-Vedello and Masoni LANFs (Zanchi et al., 2019), which are part of a complex association of low- and high-angle normal faults, active at superficial levels.

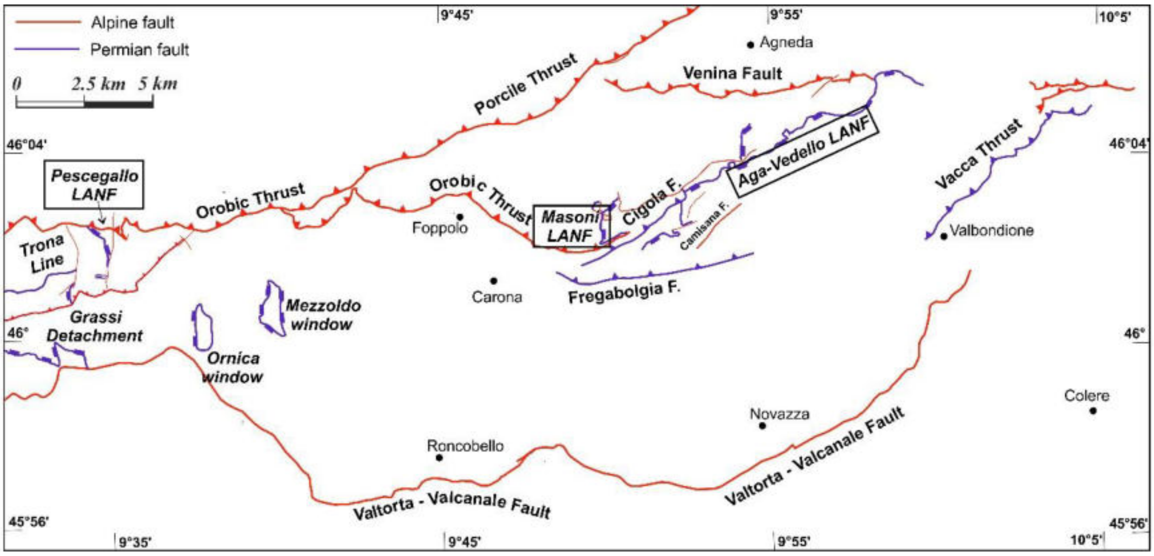

Figure 5.2 - Simplified structural sketch obtained from Fig. 2.5, in which are represented the Early Permian faults in relationship with the most relevant Alpine structures. For the present study, respectively from E to W, the Aga-Vedello, the Masoni and the Pescegallo LANFs together with the Grassi Detachment are the most relevant Permian faults. Detailed discussions are provided in the text.

The fault attitude, kinematics, fault rocks and the occurrence of tourmalinites suggest all together that the Low- and High-Angle Normal Fault (LANF-HANF) system of the Gerola Valley could be considered as part of the original architecture of the fault-controlled extensional Orobic Basin. The LANF-HANF structures, before now, were recognized only in restricted locality represented by the Masoni-Aga-Vedello area (Zanchi et al. 2019, Fig. 5.2). The occurrence of the Pescegallo LANF, which is further to the west (Fig. 5.2), suggests that these extensional structures represent a peculiar feature of the architecture of the entire Orobic Basin, the opening of which was dominated by low-angle master normal faults with high-angle normal fault nucleating in their hanging wall. In this tectonic frame, the mesoscopic synsedimentary faults affecting the loose water-saturated sandy layers of the Pizzo del Diavolo Fm. resulted from tectonic activity, acting in hydroplastic conditions at a maximum depth of few tens of meters from the surface (Obermeier 1996; Montenat et al. 2007) and preceding sediments consolidation and diagenesis along the paleo-Trona Line (Locchi et al. 2022).

A suitable parallelism of geological context could be done with the one of supradetachment basin systems, which are characterized by highly extended terrains formed in an overthickened crust with high heat from depth, that permits rapid extension and promotes low-angle faulting (Freidman and Burbank 1995). Indeed, these basins' history, as the Orobic Basin, may be relatively short lived (5-10 Myr) and developed within thickened crust influenced by volcanism in a back-arc setting, where the magmatism is typically calc-alkaline (Gans et al. 1989) and contains evidence of crustal contamination and magma mixing. The two-dimensional geometry of these basins is mostly controlled by a combination of fault geometry and footwall uplift, as suggested by the high contribution of this latter in the detritus. The geomorphological evolution of detachment footwalls is strongly controlled by shape of the detachment and characteristics of footwall lithology (Friedman and Burbank 1995). For all these common features, the geologic background described in the present study is very similar to a supradetachment basin. However, the Orobic Basin lacks of a real detachment, because the Grassi Detachment solely exposes upper crust (Pohl et al. 2008). The Dervio-Olgiasca area, further to the west of the Orobic Basin, is the only example of deeper crustal levels exposure to surface, in response to the Mesozoic rifting influencing the Southern Alps (Real et al. 2018). Furthermore, the opening of the Orobic Basin is controlled by low-angle normal faults developed at shallow depth, as assumed by the cataclastic textures of their fault core rocks, so it could not be defined as supradetachment basin.

Many examples of low-angle normal faults are documented in the upper crust, even in the necking domain of supradetachment basin, which is thinner compared with a crustal thickness of ca. 27 km in the proximal domain of these basins, as in the case of Norwegian rifted margin (Muñoz-Barrera et al. 2022). Also the Southern and Central Apennines in Italy are famous for evidence of extensional tectonics and the low-angle normal faults responsible for the opening of basins developed at shallow crustal levels, e.g. the Crati Graben Detachment Fault and the Altotiberina Fault respectively at 8.8 km and 4 to 16 km (Brozzetti et al. 2017; Valoroso et al. 2017). The low-angle normal faults represent a paradox in a brittle, elastic homogeneous crust, since Anderson-Byerlee frictional fault reactivation theory predicts no slip along normal faults dipping less than 30° in an extending crust characterized by a vertical σ^1 (Byerlee, 1978). However, fault core separating hangingwall and footwall blocks affected by brittle processes is not uncommon in low-angle normal faults (e.g. Chemehuevi-Sacramento, Zuccale, Err Nappe, Collettini 2011). Another clue attesting to the shallow environment for LANFs of the Orobic extensional system is the contemporaneity between low- and high-angle normal faults, as testified by the stratigraphic record and by the synsedimentary deformation related to high-angle growth faults influencing the Permian sedimentary cover. These faults accompanied the development of the Orobic Basin in the hangingwall, but also the footwall was crossed by high-angle normal faults, e.g. the Sassi Rossi fault, and they eased the ascent of boron-rich fluids as testified by the occurrence of tourmalinites along their fault core.

5.2 Early Permian pure extension versus transtension in the Southern Alps

The extensional regime in the Southern Alps, during the Early Permian, was defined based on metamorphic, igneous and structural data obtained from different crustal levels (Marotta et al. 2009; Roda et al. 2019 and references therein). The wide distribution of the Permian extensional systems all across southern Europe and northern Gondwana points to a large-scale extensional phase and related crustal thinning in the latest stage and after the Variscan orogeny (e.g. Rey et al. 1992; Pitra et al 1994; McCann et al. 2006; Roger et al. 2015). In this geodynamic context, the Early Permian basins are the shallow expression of the post-Variscan crustal extension. These basins have been generally interpreted to have formed in response to a dextral transtension, that affected the whole southern Europe margin and the northern portion of the Gondwanan terranes including Adria (e.g. Arthaud and Matte 1977; Stähle et al. 2001; Cassinis et al. 2008, 2012; Schaltegger and Brack 2007; Muttoni et al. 2009; Gretter et al. 2013). In particular, according to paleogeographic reconstructions (Muttoni et al. 2003, 2009; Meijers et al. 2010; Gallo et al. 2017; Muttoni and Kent 2019), the activity of the dextral mega-shear zone led to a Wegenerian Pangea A configuration from a first Pangea B configuration (Fig. 2.1), as originally proposed by Irving and Parry (1963) and Irving (1977). In their interpretation, the dextral mega-shear zone active during the Early Permian, was extending across the Southern Europe and the present-day Alpine region, and finally reaching the southern margin of the Palaeotethys to the east. However, this hypothesis is still strongly debated (Pohl et al. 2018; Muttoni and Kent 2019) as field structural evidence supporting the existence of a wrench-tectonics dominated regime related to the opening of the Early Permian basins in the Southern Alps is lacking (Pohl et al. 2018).

In the cSA, most of the authors interpret the Early Permian tectonic setting as the result of a dextral transtension giving origin to pull-apart basins (Cassinis et al. 2008). Nevertheless, no robust evidence of Permian strike-slip faults has been yet documented in the Southern Alps (e.g. Cadel et al. 1996; Schaltegger and Brack 2007 and ref. therein; Berra et al. 2016). Proposed models for the opening and evolution of the Early Permian basins of the Southern Alps are mainly based on the reconnaissance of shallow structures as high-angle conjugate normal faults sets developing horst and graben structures, with E-W faults subparallel to the supposed regional trend of the dextral mega-shear zone (Muttoni et al. 2009).

Field data recently collected in several sectors of the cSA revealed that the architecture of the Early Permian fault systems was instead characterized by LANFs, often associated with high-angle normal faults, possibly accompanied in the western areas by extensional structures developed at deeper crustal levels (Fig. 5.2, e.g. the Grassi Detachment, Froitzheim et al. 2008; Pohl et al. 2018; Zanchi et al. 2019). Both shallow and deep extensional structures along the entire cSA are consistent with a NW-SE direction of extension in present-day coordinates (Pohl et al. 2018; Zanchi et al. 2019, 2021).

As already observed by Pohl et al. (2018) the orientation of the dextral mega-shear zone displacing the northern margin of Gondwana should be roughly oriented E-W or ENE-WSW resulting at odds with the extensional fault systems identified in the cSA, which are more consistent with a left-lateral rather than with a right-lateral shear in their present-day orientation. No evidence of Middle to Late Permian left-lateral shearing have been up to now documented in the Alps and in the Central Europe. This points to a more complex geodynamic evolution, in which the dextral shearing was likely separated in time from the Early Permian extension. Nevertheless, the Middle Permian sedimentary gap (Jadoul and Gaetani and 1986; Cadel et al., 1996; Cassinis et al. 2012; Sciunnach, 2001) followed by the deposition of the Upper Permian Verrucano Lombardo upon the deeply eroded faulted and gently folded Lower Permian successions (Jadoul and Gaetani 1986; Berra and Felletti, 2011; Berra et al. 2016; Pohl et al. 2018), may be reconciled with the activity of a large-scale shear zone causing inversion of the Early Permian basins. An alternative scenario may involve a strong partitioning between extensional and strike-slip regimes in Southern Europe, producing extensional basins to the south, across the northern portion of Gondwana (e.g. the Orobic Basin in the cSA) and transtensional basins to the north in the present-day Central Europe area (Montaigne Noire, e.g. Echtler and Malaveille 1990). This scenario has already been proposed by McCann et al. (2006), suggesting a different post-orogenic evolution of the Variscan hinterland (the Alps area and the Southern Alps) and the foreland: a major component of pure extension developed in the hinterland and a wrench tectonics in the foreland, i.e. to the north of the present-day Alps area. Thus, the present study proposes that the Orobic LANF-HANF extensional systems represent a new definition for the structural architecture of the Permian basins in the entire Alpine region, which were previously interpreted as pull-apart basins controlled by major strike-slip and connected normal faults (Cassinis et al. 1997; Cassinis et al. 2008), in response to a mid-European dextral megashear zone (Fig. 2.1; e.g., Arthaud and Matte 1977; Ziegler 1986, 1988).

Strong partitioning of deformation in active crustal extensional setting is not uncommon. One of the most studied intracontinental areas undergoing crustal extension is the Basin and Range Province of western North America (e.g. Lister and Davis 1989). Here, the simultaneous activity of low-angle listric normal faults and parallel arrays of steep domino-faults in the hanging wall (Hayman et al. 2003) produces N-S trending grabens and half-grabens dominating the structural setting of the whole region. The tectonic framework of this area is interpreted to derive from a diffuse extensional collapse of the Cordilleran overthickened continental crust of the Western USA in the past 15 My. This scenario is related to the regional stress distribution and orientation induced by the growth of the NW-SE trending right lateral San Andreas Transform Fault (Wernicke et al. 1988; Lister and Davis 1989). The present-day landscape of the Basin and Range Province, with basins filled with Miocene sedimentary and volcanic strata deposited in arid environments (Eaton 1982; Lister and Davis 1989), is likely close to the aspect of the Early Permian intracontinental basins formed in Southern Europe and Northern Gondwana (Menard and Molnar 1988) and in particular within the cSA (Berra et al. 2016). The geometry and structural features of the fault-controlled basins in the Basins and Range Province testify to the occurrence of pure extensional half-graben basins in a more complex tectonic frame, with strike-slip dominated tectonics close to the San Andreas Fault (Wernicke et al. 1988, 1989).

The Orobic Basin could be interpreted as an ancient analogue of the modern Basin and Range Province, both from the stratigraphic and structural point of view (Berra et. al, 2016; Locchi et al. 2022). As abovementioned, in this scenario pure extensional basins developed in a semi-arid condition before the inception of the activity of the Pangea A to Pangea B dextral mega-shear zone (Fig. 2.1; Muttoni et al. 2009; Muttoni and Kent 2019), as a first post-orogenic response preannouncing the mega-plate reorganization taking to the Wegenerian Pangea A configuration. It is worth noting that the present-day location of the San Andreas Transform within the Gulf of California strictly follows for more than 1000 kilometres the western margin of the Basin and Range Province, which is represented by the NNW-SSE trending main Gulf escarpment. Dextral faults related to the transform reactivate Late Miocene pure normal faults with dextral motions since Pliocene following a jump of the transform from the continental borderland west of the Baja California Peninsula to the Gulf region (Angelier et al. 1981; Colletta and Angelier 1983; Zanchi 1994; Umhoefer et al. 2020). Following such a geodynamic scenario, a possible parallelism among the inferred Middle Permian dextral mega-shear and the Early Permian extensional structures might be related to their subsequent reactivation in a dextral wrench-dominated regime following previous zones of crustal weakness induced by a generalized extension (Locchi et al., 2022).

As mentioned before, another suitable parallelism of geodynamic context could be done with the one of supradetachment basin systems, which are characterized by highly extended terrains formed in an overthickened crust with high heat from depth (Freidman and Burbank 1995). These short lived basins developed within a thickened crust influenced by volcanism in a back-arc setting, where the magmatism is typically calc-alkaline and shows evidence of crustal contamination and magma mixing, as for the Permian magmatism (Schaltegger and Brack 2007, Spalla et al. 2014).

5.3 The effect of Alpine shortening on Permian structures and structural evolution

Due to the favourable attitude of most Permian LANFs, which were originally perpendicular to the Alpine direction of shortening, the Alpine deformation partially to completely inverted most of these structures, deleting their original features. However, anomalous stratigraphic relationships, i.e. young-on-old, recognized along some of the major thrust faults of the cSA, allowed to recognize them as old normal faults reactivated during the Alpine shortening (Blom and Passchier 1997; Zanchetta et al. 2015). The Pescegallo LANF is one of the few examples of preserved Permian normal faults strictly comparable to the Aga-Vedello and Masoni LANFs, which also preserve most of their original Permian features (Zanchi et al. 2019; Zanchetta et al. 2022).

In the studied area, the overprinting effects on the Permian structures by the Alpine tectonics are limited both to the outcrop and to the microscale. Even though the Pescegallo LANF has been folded by the Orobic Thrust in its northern portion (Fig. 4.6a), the reactivation of the fault is generally weak and original fabrics of fault rocks can be still recognized around the area of Lake Pescegallo (Fig. 4.7c). The effects of the Alpine deformation produced a limited partial inversion accompanied by the formation of S-C fabrics and reverse faults along the main contacts both in the hanging wall and in the footwall around the Lake Pescegallo and Monte di Sopra (site 4, Fig. 4.8a). Nevertheless, despite the occurrence of the Alpine overprint, tourmalinite layers can be followed all along the reactivated contacts, suggesting a limited amount of the Alpine finite strain, also at the microscopic scale. During the Alpine event, deformation and inversion were more intensive to the west of the Salmurano Pass and to the south of the watershed below the high cliff of Cima Piazzotti (Fig. 4.3). Here the former LANF only preserves younger-on-older relationships (Fig. 4.9), whereas the original fault rocks were completely reworked during the Alpine reactivation with the formation of pervasively foliated cataclasites. The high-angle normal fault, the Trona Line, of the Gerola Valley extensional system was involved as well in the Alpine shortening, but due to its unfavourable attitude it has been only weakly reactivated in terms of displacement, even if with complex motions (Fig. 4.9).

Based on our geological and structural analyses, a polyphase evolution of the area is suggested and characterized by a first extensional stage during the Early Permian, leading to the development of low- and high-angle normal faults and controlling the opening and development of the Orobic Basin (Fig. 5.1). These structures were responsible for the final stages of exhumation of the Variscan basement, which was already at shallow crustal level at that time (Filippi et al. 2021 and references therein) in response to the ongoing crustal thinning. Then they have been reactivated and partially inverted during the Alpine shortening (Fig. 5.4a), that triggered the Orobic Thrust development starting from the Late Cretaceous, at a crustal depth close to the brittle-ductile transition (Zanchetta et al. 2011, 2015). The Permian normal faults and Alpine thrusts are later crosscut by high-angle normal and strike-slip faults entirely developed in brittle conditions (Fig. 5.4b), resulting in the final uplift and large exposure of the Variscan basement across the Orobic watershed.

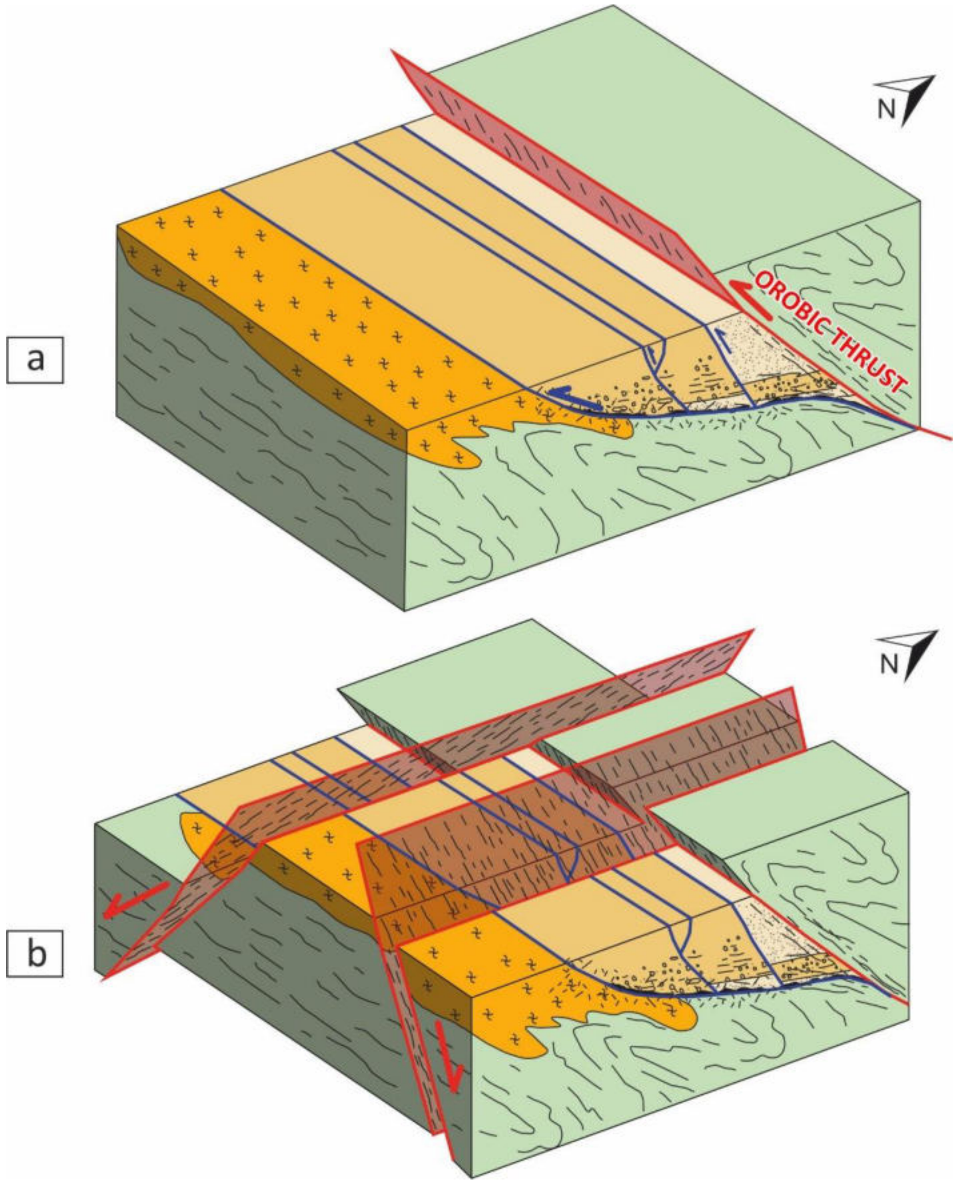

Figure 5.4 – 3D reconstruction evolution following Fig. 5.1 – a) Alpine stage D_3 with compressional regime that partially reactivated and inverted the Permian structures developing just a cataclastic foliation and S-C fabric. B) Late-Alpine stage, during which all the previous structures have been crosscut by N-S normal to oblique faults, resulting in an additional uplift of the Variscan basement forming a horst (Locchi et al. 2022).

5.4 The occurrence of tourmalinites and uranium mineralization along Permian faults

Metasomatic tourmalinite impregnating cataclasites along LANFs occurs in several sectors of the cSA (Zhang et al. 1994; Slack et al. 1996; Blom and Passchier 1997; Cadel et al. 1996; De Capitani et al. 1999; Zanchi et al. 2019, 2021; Zanchetta et al. 2022) like the Aga-Vedello and Masoni LANFs. The low-angle tectonic contact is defined almost everywhere by coarse-grained cataclasites impregnated with tourmalinites, which have been recognized in the Gerola Valley area for the first time, all along the fault surface of the newly identified Pescegallo LANF (Locchi et al. 2022). These faults acted as important preferential channels for the circulation of boron-rich fluids, supposed to be related to the Early Permian magmatism (Zhang et al. 1994; Slack et al. 1996, De Capitani et al. 1999).

One of these well-preserved Permian faults is the Aga-Vedello LANF, extending for at least 10 km across the Orobic Alps watershed (Fig. 2.5 and 4.12). The WSW-ENE trending Aga-Vedello LANF brings in contact the Variscan basement with the Lower Permian succession of the Pizzo del Diavolo Fm., including volcanic and volcanoclastic deposits (Berra et al. 2016) and the Forcellino Pass is the best location to see its fault core. It is sealed by tourmalinites too, and it is a very important spot because is the nearest LANF exposure to the Vedello Valley uranium ore deposits.

As reported by personal communication of Geol. C. Pessina, who worked in the exploring tunnel of the Vedello Valley mine, the uranium mineralization in this area is concentrated along the Variscan basement-Lower Permian deposits contact, i.e., along the NE extension of the Aga-Vedello LANF. The ore genesis of the Vedello uranium deposit has been considered of hydrothermal origin, with a primary mineralization contained within fractures or veins and along several layers of the Monte Cabianca ignimbrites in the Novazza ore deposit (D. Ravagnani, personal communication; Cadel 1986; Cadel et al. 1996). The occurrence of uranium-bearing ores in the Vedello Valley has been until now interpreted as a remobilization due to a Late Permian-Early Triassic geothermal event that leached uranium from the Lower Permian ignimbrites and transported it along existing faults with final concentration and deposition along the basement cover contact in the Vedello area (Dal Piaz et al. 1986; Philippe et al. 1987). The major evidence of fluids circulation along Permian faults in the study area are the tourmalinites, which have been already proposed to be correlated to the formation of the U Vedello ores (Slack et al. 1996) even if evidence of the genetical link have not been provided so far.

In the next paragraphs, after the definition of the boron source for fluids precipitating tourmalinites, new data obtained in the frame of this PhD project will be discussed.

5.5 The interplay among boron-hydrothermalism, magmatism and tectonic activity in the central Southern Alps

Boron-hydrothermalism have been documented also in relationship with the Permian U mineralization of the Novazza-Vedello district (Cadel 1986; Fuchs and Maury 1995), especially in relationship with the Cabianca Volcanite (D. Ravagnani, personal communication). Also in the Trompia Valley, tourmalinization occur in the magmatic aureole of Permian intrusives (De Capitani et al. 1999) and it is supposed to be one of the numerous hydrothermal products characterizing the area.

Despite the several information available on these boron-rich fluids that interest the cSA, a thorough study defining the boron-hydrothermalism has never been performed. Thanks also to the new structural evidence, that exalts the close connection between tourmalinites and Early Permian low-angle normal faults, a complete description and reconstruction is here proposed.

Field relationships of tourmalinites in Trompia Valley suggest that the boron-rich hydrothermalism is genetically linked to the Early Permian magmatism. This is firstly suggested by the occurrence in the area of Permian intrusive bodies producing a magmatic aureole, within and close to which a strong hydrothermal activity has been documented (De Capitani et al 1999). Hydrothermal products consist here of swarms of siderite and sulphide-quartz veins, known as the Torgola fluorite vein system, and associated Sn-W mineralizations (Moroni 1994). The hydraulic breccia textures of tourmalinites and the pods of quartz-tourmaline suggest that the tourmalinization represents an additional product of hydrothermal activity during the Early Permian (De Capitani et al. 1999). These features are only observed in this area of the cSA, and for this reason the Trompia Valley tourmalinites are distinguished from other occurrences of tourmalinites and have been classified in this work as “Type 1 tourmalinites”. At the same time of the intrusions in the Trompia Valley, low angle normal faults (LANF) were developing in response to the Early Permian extensional regime. The features of these faults were partially preserved by Alpine deformation and they share the passage of boron-rich fluids precipitating metasomatic tourmalinites along their fault cores, named by us “Type 2 tourmalinites” (see chapter 4.3).

Assuming the same boron-rich hydrothermalism precipitating tourmalinites in different localities of the cSA, then a magmatic source can be preliminarily suggested also for fluids precipitating metasomatic Type 2 tourmalinites in the LANFs of the Orobic Basin. However, contrary to Type 1, in the proximity of Type 2 tourmalinites there is no direct evidence of exposed Permian intrusives. The only exception is for the Valsassina Type 2 tourmalinites, which occur along the Permian Sassi Rossi fault (Fig. 4.2), directly in contact with the Val Biandino intrusive complex (Sciunnach 2001; Pohl et al. 2018). Despite the restricted distribution of Permian intrusives in this western sector, however, abundant volcanic products of Lower Permian age were deposited at the base of the sedimentary succession of the Orobic Basin, where also tourmalinites occur.

According to the proposed hypothesis, thus the boron-rich fluids produced by the Permian magmatic activity close to the Orobic Basin, in their ascent, encountered as first discontinuity the LANFs controlling the opening of the Permian basin. Thus, the regional distribution of tourmalinites was facilitated by the presence of these important pre-existing faults that preferentially channelled the boron-rich fluids for several kilometres.

The simplified model in Fig. 5.5 is useful to visualize how the Permian magmatic activity, hydrothermalism and extensional tectonics likely interacted. However, to assess this hypothesis all samples of tourmalinites are investigated in detail, and the applied methodologies to tourmaline crystals of Type 1 and Type 2 tourmalinites provide important information on the boron-rich hydrothermal event that interested this area.

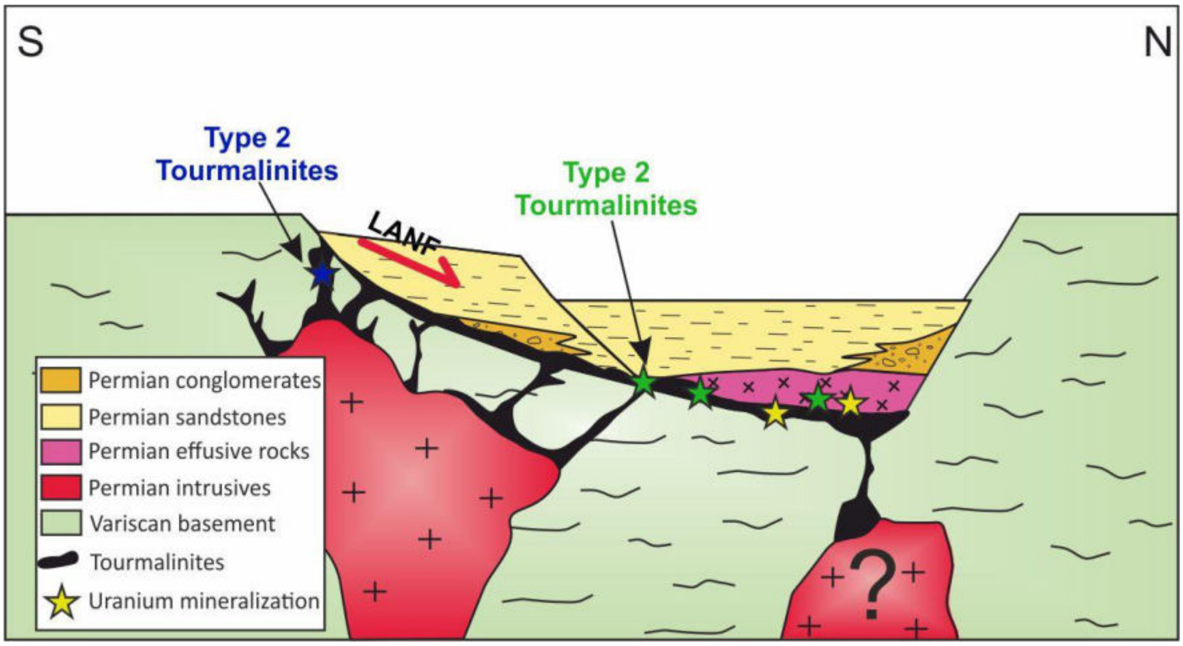

Figure 5.5 – Conceptual model, not to scale, of the Early Permian evolution, characterized by contemporaneous tectonics, magmatism, volcanism and boron-hydrothermalism. The crustal thinning is related to a combination of extensional tectonics, with development of Low-Angle Normal Fault (LANF), and magmatic activity at different crustal levels. The Permian inrtusives produced different expressions of hydrothermalism, one of which is characterized by boron-rich fluids precipitating tourmalinites. During their ascent, these fluids encountered as first discontinuity the LANFs fault core, which worked as preferential channel for fluids circulation for several kilometres. For these reasons, the LANF can be interpreted as the best site to see the interplay among tectonic, magmatic and hydrothermal activity during the Early Permian.

From the microstructural point of view, Type 1 and Type 2 tourmalinites of the cSA are similar, except for the dimensions of tourmaline crystals distributed in the matrix. In both cases, different generations of tourmaline veins and relicts of former tourmalinites are indicative for a polyphasic nature of the hydrothermal event. This is further supported by the optical zoning of some tourmaline crystals and by the layers of different intensity of tourmalinization in metasomatic tourmalinites (Type 2). The polyphasic nature of the hydrothermalism is indicated also from the compositional point of view, because the optical zoning is reflected also in a chemical zoning, as observable in the X-ray element maps (Fig. 4.26-4.27). However, according to the major elements measured in core and rim of single crystals, the tourmalines of the cSA are classified as Schorl-Dravite, displaying chiefly compositional variations in terms of Fe and Mg content. The chemical zoning could be likely related to changing of temperature, redox conditions and, possibly, also to changes in fluids composition during the metasomatic event.

To assess the hypothesis of a magmatic source for these boron-rich fluids, it was necessary to estimate the boron isotopic composition of single crystals, to obtain the boron isotopic composition of the fluids responsible for their precipitation. As commented in chapters 4.3.5-4.3.6, a fluid precipitating tourmaline has a different boron isotopic composition because of the boron fractionation occurring at the state change. The obtained calculated $\delta^{11}B$ values for fluids are from -12‰ to 5‰ (Fig. 4.34) and comparing them with other possible boron sources (Fig. 5.6) they match with different ones (Trumbull et al. 2020).

Seawater and meteoric water could be excluded as the $^{11}B/^{10}B$ ratios of modern seawater is about 40‰ and rains show a large range of variations, from −1.5 ± 0.4‰ to +26.0 ± 0.5‰ (Rose-Koga et al. 2006). On the base of the geological setting of the area, several options can be excluded. "Marine evaporites and carbonates" are heavier, over 10‰ so they are excluded in advance. "MORB" and "OIB" type basalts (or their corresponding metamorphic equivalent) do not occur in the cSA area, neither within the volcanic-sedimentary cover, neither in the Variscan basement. Some minor layers of carbonates-bearing sandstones occur close to the top of the Pizzo del Diavolo Fm. (Berra et al., 2016; Berra et al. 2019) together with "Non-marine evaporites". However there is no direct evidence of fault system involving these formations and reaching the depth of LANFs, estimated at about 2.5 km at the time of carbonates deposition (Zanchi et al. 2019; Locchi et al. 2022). A-type and S-type intrusives lack in the area, so they should be excluded. The $\delta^{11}B$ values displayed by the cSA tourmalites partially overlap typical values characterizing the clastic (meta)sediments, but are shifted to higher values. Consequently, the "Arc volcanic rock" and "I-type" intrusives" are the most suitable source for boron-rich fluids in the cSA.

Lower Permian intrusive and volcanic rocks of the cSA have a wide range in chemical composition, ranging from gabbros to granophyric granites for the intrusive terms, whereas the volcanic terms are mainly rhyolitic, even if some minor dacites and andesites also occur (Schaltegger and Brack, 2007). Despite these compositional variations, they all show a calc-alkaline affinity (De Capitani et al. 1994; Schaltegger and Brack, 2007). In addition, field observations in the Trompia Valley area clearly show that tourmaline-quartz veins are genetically related to intrusive bodies. This is another important evidence, together with geochronology and geochemistry, that points to the Early Permian magmatism as the source of boron-rich fluids and they all confirm that the proposed model in Fig. 5.5 could well explain the interplay that occurred in this area between tectonics, magmatism and boron metasomatism in the Early Permian.

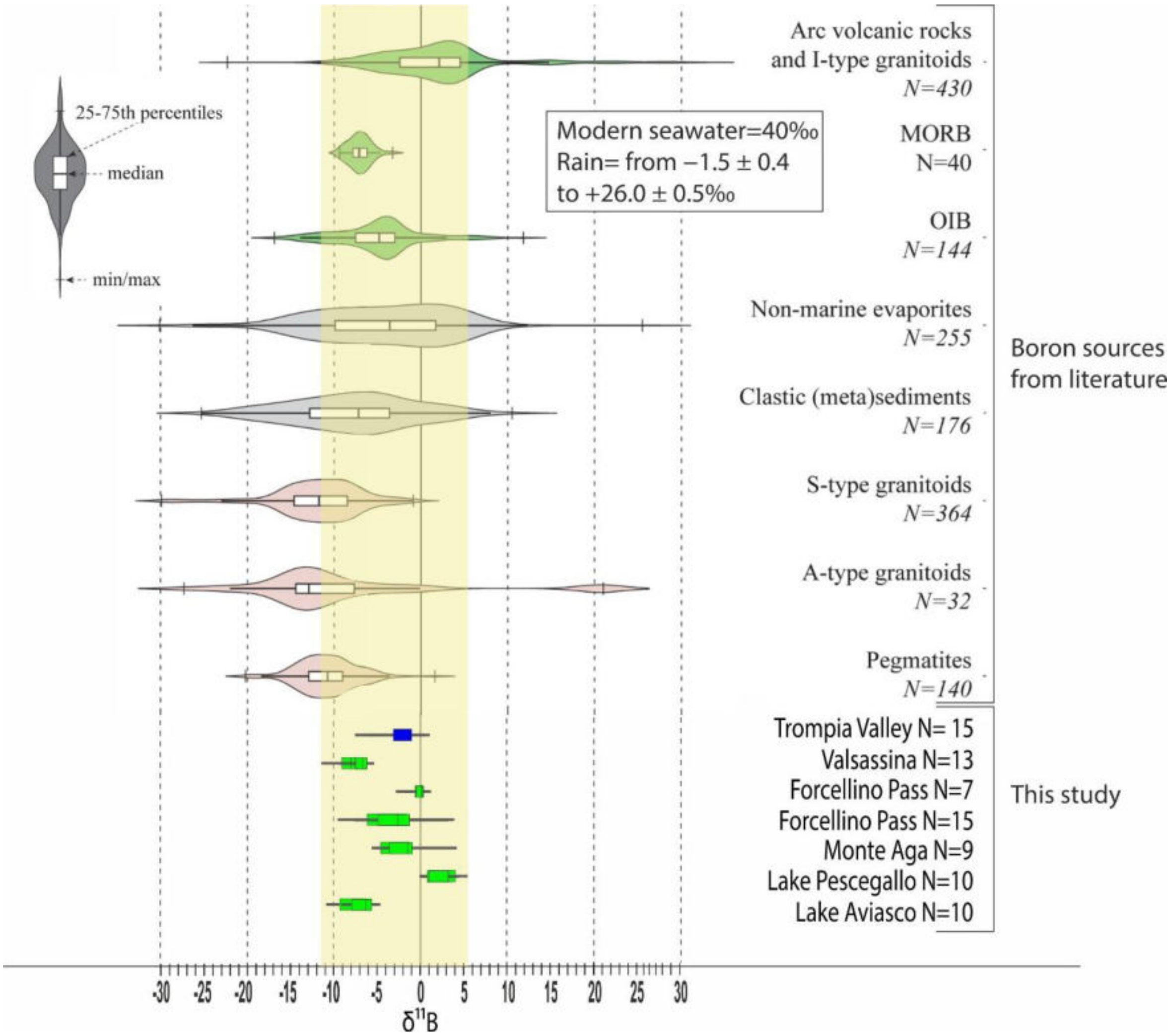

Figure 5.6 - the boron isotope composition of fluids precipitating tourmalines of the cSA (see chapter 4.3.6) are here compared with other potential sources of boron coming from literature (modified after Trumbull et al. 2020). The blue (Type 1 tourmalinites) and green (Type 2 tourmalinites) field represents the range of $\delta^{11}B$ values of tourmaline obtained in the present study.

Tourmalinites that metasomatized cataclasites along LANFs planes appear to be non-deformed, with the only exception where Alpine structures affected them, such as the Alpine cleavage in Gerola Valley (Fig. 4.8). For this reason, the maximum age for tourmalinization is the Early Permian, i.e. the age of fault activity related to the tectonic opening of the intracontinental basins. The minimum age is instead provided by the occurrence of tourmalinite's clasts within conglomerates of the Pizzo del Diavolo Fm. (Ponteranica Conglomerate Auct.) in the Valsassina area. Here, other age constraints are provided by the intrusion of the San Biagio Granite (286.8 ± 4.9; Pohl et al, 2018) and the deposition of the Upper Permian Verrucano Lombardo. Indeed, as shown in Fig. 4.2, the tourmalinite-bearing Sassi Rossi fault is younger than the granite and is sealed in non-conformity by the fluvial conglomerates of the Verrucano Lombardo. Thus, the boron-rich fluids circulated along the Sassi Rossi Fault after the emplacement of the Biandino and San Biagio intrusives but before the deposition of the Verrucano Lombardo.

This suggests that, as in the case of Type 1 tourmalinites, boron metasomatism occurred in the cSA area when the tectonic control on the deepening of the Orobic Basin was waning. This is supported first by the preservation of the original metasomatic texture of tourmalinites, which are never cataclasated, and is also suggested by the syn-sedimentary deformation only confined to the lower units of the Permian sedimentary cover.

In the case of Type 2 tourmalinites, the geochronological constrain is based on indirect observations coming from field-relationship and stratigraphic features. A direct age constrain instead is available for Type 1 tourmalinites, in which the U-Pb dating was applied on hydrothermal rutiles in equilibrium with tourmaline mineralization: because of the lower contents of U and Pb in this mineral, a wide range of ages was obtained, that however is included in the entire time interval of the Permian age, as shown in Fig. 5.7. These values are compatible with other Permian magmatic and hydrothermal evidence occurring in this sector of the Alps (Fig. 5.7). According to the isotope composition and geochronologic constrain, the interplay between magmatism, hydrothermalism and tectonics was very strong during the Early Permian in the cSA area.

No direct evidence for the depth of emplacement of the tourmalinites could be provided. However, according to the structural setting and the petrographic and geochronological data, indirect assumptions can be made. Based on the results of the present study and according to the genetic model proposed in Figure 5.5 the Trompia Valley tourmalinites together with those of Valsassina along the Sassi Rossi Permian fault (see locations in Fig. 4.1) represent a deep level of fluids circulation.

The first have hydraulic breccia texture crosscutting the basement, that indicates fluid overpressure conditions and favours hydro-fracturing and development of the various tourmaline vein sets (Dini et al. 2008). In Valsassina instead, the tourmalinites are along high-angle normal fault crosscutting the basement in the footwall, and are an important evidence of fluids circulating through deeper conduits, possibly interconnected with low-angle normal faults in the upper crust. Indeed, the capability of fluids to be channelled through rocks volumes is strictly related to the existence of interconnected discontinuities promoting a suitable network of communicating portions of rock with higher permeability (Caine et al. 1996; Rowland and Sibson 2004; Sibson 2000) and a suitable secondary permeability, that has been demonstrated to be essential for efficient geothermal fluid flow (Zucchi et al. 2022 and reference therein).

Despite fluids are not documented so far to circulate favourably along LANFs fault core (Brogi and Novellino 2015), in the cSA tourmalinites are found for several kilometres at the edges of the Orobic Basin, along cataclasites of low-angle normal faults. These fault rocks and the stratigraphic features of this basin suggest that the LANFs, responsible for its opening, formed at shallow crustal levels. It has been demonstrated that the permeability of a fault zone is anisotropic, and at its maximum if the fluid flow is parallel to the fault zone (Sibson 1996; Evans et al. 1997; Caine and Forster 1999; Jourde et al. 2002). The widespread occurrence of tourmalinites along LANFs suggests that boron-rich fluids circulated laterally thanks to the secondary permeability intrinsic of LANF cataclasites formed at upper crustal levels. Furthermore, tourmalinites are not brecciated, so the boron-rich fluids permeated during or immediately after the fault activity.

A similar case study is the Elba Island (Tuscany), where the Capoliveri–Porto Azzurro shear zone and the Zuccale normal fault interacted with boron-rich fluids precipitating tourmaline during their activity (e.g. Dini et al. 2008; Spiess et al. 2021). In this case, tourmaline is polyphasic and cataclastic and the boron-rich fluids possibly played a role in fault weakening and permeability enhancement during fault activity (Liotta et al. 2021).

Even if the mechanism of fluid circulation along LANF might have been different in the Elba Island and in the Orobic Basin context, there some similarities among these two geothermal systems. In the first case study, the spatial distribution of tourmaline veins indicates that fluids circulated close to their magmatic source (Dini et al. 2008), namely the Porto Azzurro pluton, belonging to the Tuscan Magmatic Province (Innocenti et al. 1992). This happens also for the Orobic tourmalinites: at the Aviasco Lake (see location at Fig. 4.12), volcaniclastic sediments and volcanic products of the Cabianca Volcanite, dominate the entire area and are interpreted as products of a collapsed volcanic chamber active during the Early Permian (Cadel 1986). Here the tourmalinites occur along Permian faults directly crosscutting the volcano-sedimentary rocks. The same also occur in the Novazza mine district (Cadel 1986; Ravagnani 1974), where the uranium mineralizations occur along veins and faults that crosscut a rhyolitic body in which also tourmalinite veins have been identified (personal communication of Ravagnani).

The short distance between the source and hydrothermal products occurs also in the Trompia Valley and Valsassina where the tourmalinites are in direct contact with Permian granitoid bodies. Those cases in which neither volcanic nor magmatic bodies crop out at surface, e.g. the Pescegallo tourmalinites (see location in Fig. 4.1), are interpreted to be fed by granitoids that intruded at shallow levels but are not exposed.

According to these observations, the magmatic bodies, sources of the boron-rich fluids, were emplaced not too far from the LANFs, which are sometimes crossed by high-angle normal faults in the footwall (e.g. Sassi Rossi Fault) that eased the circulation of fluids from deeper levels. An assumption of shallow depth for the magmatic bodies feeding the boron-hydrothermal system perfectly fits with the Permian magmatic occurrences at different crustal levels, which are documented all along the Southern Alps (Schaltegger and Brack 2007).

The structural, geochemical, isotopic and geochronological results, coming out from the present research, together with the geodynamic background of the study area during Permian, support the proposed model of Figure 5.5, describing the Orobic Basin as a complex geothermal and extensional system fed by a magmatic source at shallow levels, as now exposed in the Trompia Valley and Valsassina areas (see locations in Fig. 4.1).

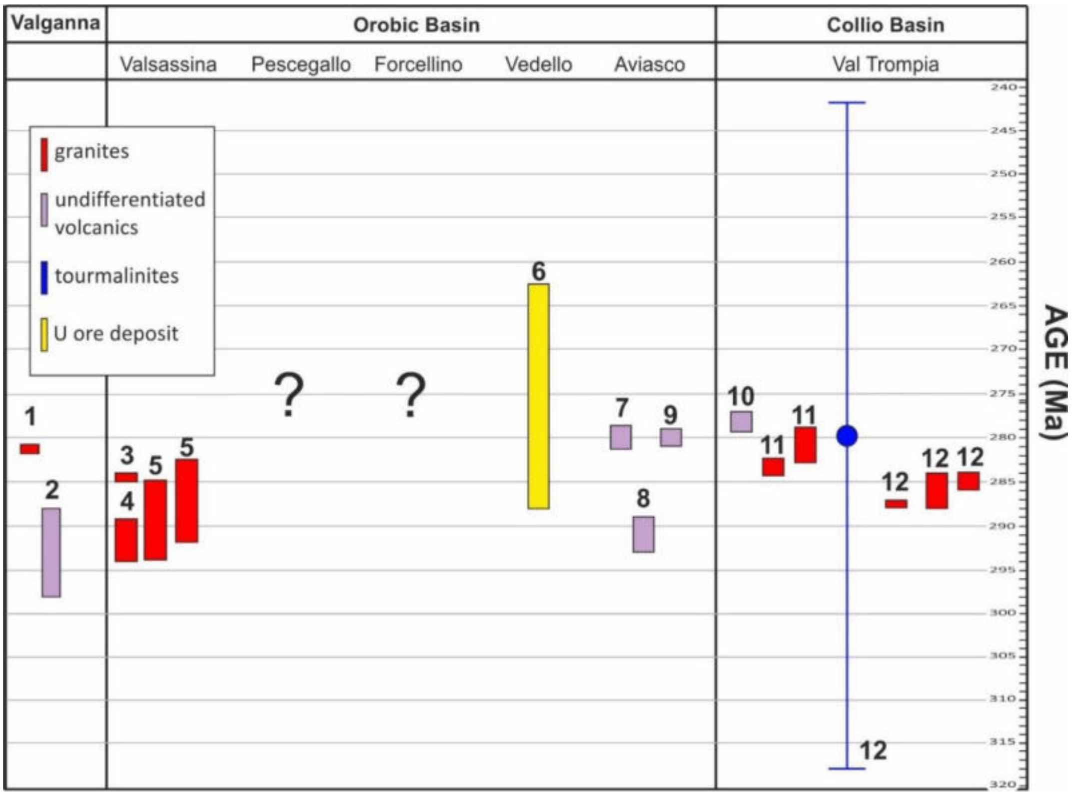

Figure 5.7 - Localities of the cSA and age data of Permian evidence recognized in the entire area, such as granitoids, volcanic rocks, tourmalinites and uranium mineralization of Novazza-Vedello district. The data references are respectively 1 = Bakos et al. 1990; 2 = Schaltegger and Brack 2007; 3 = Crippa, 2017; 4 = De Capitani et al 1988; 5 = Pohl et al. 2018; 6 = Martin et al. 2017; 7 = Philippe et al. 1987; 8 = Cadel et al. 1987; 9 = Berra et al. 2015; 10 = Gretter et al. 2013; 11 = De Capitani et al. 1994; 12 = this study.

5.6 New insights on the uranium ore deposits genesis of Novazza-Vedello Valley district

The detailed analysis performed *in-situ* on tourmaline crystals coming from each locality provided important information for our study, which aim is also defining a possible genetic link between tourmalinites and uranium mineralization of the Novazza-Vedello district, as supposed by several authors in the past (e.g. Cadel 1986; Fuchs and Maury 1995).

The first thing noticed on trace elements contents and patterns is that, contrary to the major elements and the boron isotopic compositions, there are differences among tourmalinites from different localities. The Type 1 tourmalines of the Trompia Valley and the Type 2 tourmalines of the Valsassina share the same REEs distribution, likely because they both occur close to the Permian intrusives. The REEs trend of the Permian intrusives is opposite to the one of these tourmalines.

Furthermore, it is noticeable that the Type 2 tourmalines from the Lake Aviasco (Fig. 4.29-4.30), the locality very close to the Novazza uranium mineralization, are characterized by trace element patterns similar to those of the Permian intrusive bodies, with higher L-REE relative to H-REE, and a slightly negative Eu anomalies. About the incompatible elements, some tourmalines of the cSA are strongly enriched in uranium, such as the Type 2 tourmalines from the Lake Aviasco that have contents up to 10 ppm. This is the first very important clue to investigate the relationships between boron-rich hydrothermalism and the uranium ore deposit of Novazza-Val Vedello district. For this reason, a more focalized analysis on this element was necessary.

The uranium content of whole rock analyses performed on tourmalinites and Permian intrusives (Appendix 2), respectively plotted in blue/green and orange in Fig. 5.8, was considered and normalized to the U content of the UCC (Upper Continental Crust, Fig. 5.8). The U-UCC is about 2.7 ppm (Rudnick and Gao 2003), close to the value of 2.61 ppm obtained for the typical Variscan basement of the cSA (Bergomi 2004), that represents the host rock for Type 1 tourmalinites and it is also the footwall of Early Permian faults, where Type 2 tourmalinites occur. The majority of plotted data in Fig. 5.8 are over the line 1, equal to the U-UCC, so it means that both tourmalinites and Permian intrusives are enriched in uranium with respect to the upper continental crust and the Variscan basement of the cSA (Fig. 5.8).

Then, the *in-situ* determined uranium contents (LA-ICP-MS data, Appendix 4) normalized to UCC is considered to further focus on tourmalinites (Fig. 5.9). Spot analyses were performed on larger crystals of Type 1 tourmalinites, in blue, and both on crystals and matrix of Type 2 tourmalinites in green. The data in Fig. 5.9 emphasize an enrichment of uranium for Type 2 tourmalinites, both crystals and matrix, attesting that the uranium was included in the lattice of tourmalines but also in other mineral phases sparse in the matrix, which are in equilibrium with the boron-rich fluids. However, because of the very fine-grained size of the matrix it is not possible to easily recognize the mineral assemblage.

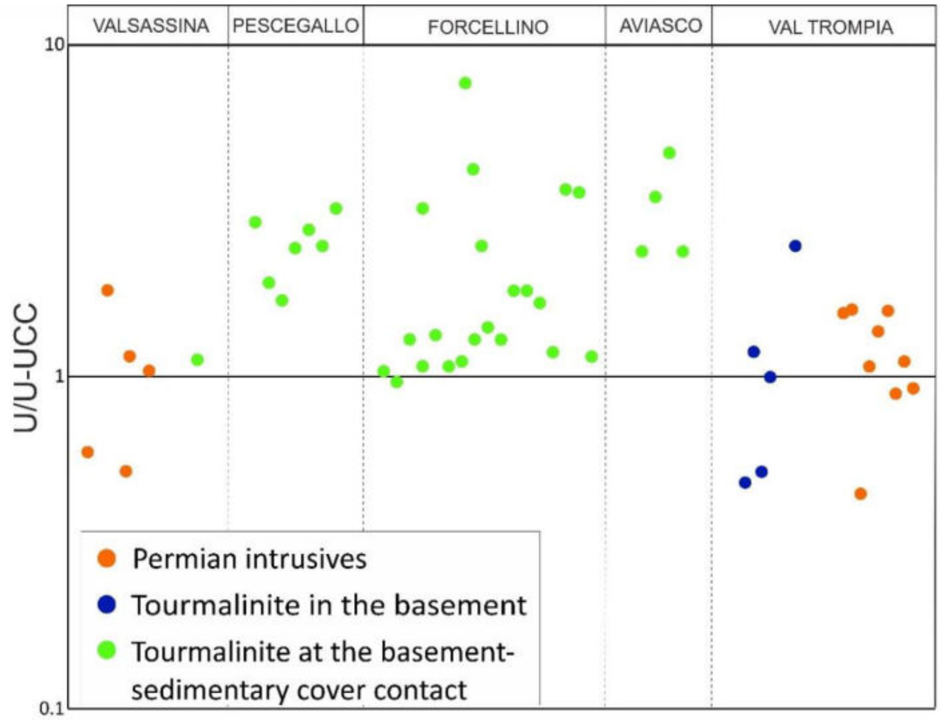

Figure 5.8 - Uranium content from whole rock analysis of Permian intrusives and tourmalinites of the cSA, normalized to uranium content of the Upper Continental Crust (UCC). The line 1 represents the 2.7 ppm of uranium in the UCC (Rudnick and Gao 2003). For the Permian intrusives of the Valsassina area are shown the data produced by Crippa,2017, whereas for the Trompia Valley intrusives and tourmalinites (type 1 in blue and type 2 in green) the data obtained from this study are plotted.

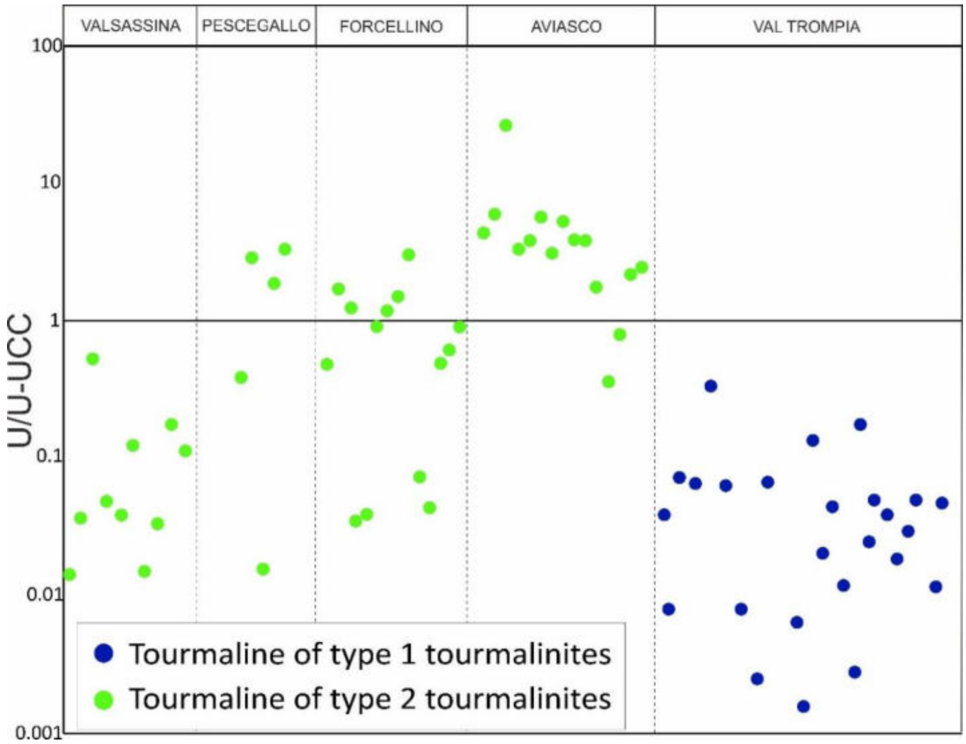

Figure 5.9 - Uranium content of tourmaline crystals obtained *in-situ* (LA-ICPMS) of type 1 and 2 tourmalinites, plotted respectively in blue and green, and normalized to uranium content of the Upper Continental Crust (UCC). The line 1 represents the 2.7 ppm of uranium in the UCC (Rudnick and Gao 2003). For type 1 are shown data of single tourmaline crystals; for type 2 are plotted data related both to single crystals and matrix of tourmalinites.

According to the results on the trace element contents coming from bulk and *in-situ* analyses, it is evident that boron-rich fluids coming from the Permian intrusives, were able to mobilize the uranium from a fertile source in the area and concentrated it along discontinuities with favourable conditions to precipitate uranium. Models for the formation of U ore deposits commonly involve mobilization and transport of oxidized U^{6+} in a fluid and deposition by reduction to U^{4+}, as U^{6+} minerals or by adsorption on mineral surfaces (Brennecka et al. 2010; 2011; Shiel et al. 2013; Chernyshev et al. 2014; Uvarova et al. 2014). It mainly precipitates in solid phase when the transporting fluids reach a reducing environment or favourable ambient conditions. However, the source and the conditions that allowed the high concentration of uranium in the Novazza-Vedello district are unknown. The limited information is consequence of the Italian State's decision to ban the nuclear activity in Italy during the '80s, so the access to the uranium mineralizations of both localities have been since then inaccessible and no materials (e.g. reports on mining activity, samples and so on) are available.

Despite the source of uranium is not well defined, a solid evidence is the genetic link between tourmalinites and magmatism, and because of the enrichment in uranium of the Permian intrusives, over 2.7 ppm, it is reasonable assuming that they could be the source. The Permian volcanic rocks of the Cabianca Volcanite as well could be considered as possible candidates, as they are product of an enriched magmatism and some portions of the volcanic sequence reach up to 7 ppm (Cadel 1986). Other uranium ore deposits, smaller than Novazza-Vedello Valley mineralization, occurring in the Central Alps and related to the Permian evolution, are always combined to tuffs and ignimbrites related to the Permian volcanism (Ravagnani, 1974). A similar background to the Orobic Basin is represented by the Permian volcanic rocks in Valganna (Varese area, N Italy) intruded by the subvolcanic, pink-coloured granophiric stock (''Ganna granite'', Schaltegger and Brack 2007), interpreted as the result of the foundering of a caldera (Bakos et al. 1990), and that are accompanied by uranium ore deposits (Ravagnani, 1974). In this case, the boron-rich fluids could have leached the outer portion of the intrusive bodies or the volcanic rocks and mobilized U with other incompatible elements that were transported along the high permeability channels offered by the Early Permian faults.

Some features that tourmalinites share with the uranium mineralization in the Vedello Valley (Geol. Pessina, personal communication) further support this hypothesis. As described in chapter 4.3.7, the U mineralization is mainly represented by pitchblende always related to the presence of sulphides such as pyrite, chalcopyrite, blende and arsenopyrite, which are widespread also apart from the U ore deposits. This is the case of tourmalinites of Lake Aviasco (location in Fig. 4.1 and details in Fig. 4.22f and 4.33a), that we studied to define the geothermometry of boron-rich fluids in the area (chapter 4.3.5) and they indicate a temperature of about 380°C (Fig. 4.33b). Another common point is represented by the geochronological constrain: the uraninite dated from the Vedello Valley provides a scattered and wide time range (50-190 Ma), indicating partial re-mobilization and re-precipitation during later tectonic events (Martin et al., 2017), as suggested also by the presence of Alpine structures recognized in the field. However, more accurate ages come from the Novazza area, which was not so much involved in the Alpine deformation as the Vedello area, with an age of the mineralization of 275 ± 13 Ma (Martin et al., 2017), namely contemporaneous to the magmatism, the boron-rich hydrothermalism and the volcanic-sedimentary cycle of the area. Thus, the link between U ore deposit genesis and magmatic-hydrothermal activity of Permian age seems to be reasonable.

As described in the present work, more than a clue suggests that tourmalinites and the uranium ore deposit of Novazza-Vedello district are genetically linked. The outcoming results outline a scenario where the Permian hydrothermalism is strictly related to a magmatism that produced intrusive and volcanic rocks enriched in uranium with respect to the UCC. In addition, the temperature suggested for the boron-rich fluids and the contemporaneous hyrothermalism widespread in the area (e.g. Permian siderite ore deposits, Martin et al. 2017), attributable to the Permian evolution, are important evidence that testify for the occurrence of a geothermal system sustained by the high geothermal gradients during the Early Permian crustal thinning.

The most common types of U ore-deposits nowadays are mainly classified with two genetic models, which are the U-unconformity type, and the IOCG deposit (Iron-Oxide-Copper-Gold). The most famous ore deposits classified within these two categories are respectively the Proterozoic Athabasca Basin U deposit, Canada (e.g. Hoeve and Sibbald 1978; Kyser and Cuney 2009; Potter et al. 2022) and the Olympic Dam Cu-Au-U-Ag deposit, South Australia (e.g. Roberts and Hudson 1983; Hitzman and Valenta, 2005; Ehrig et al., 2012). Because of the complexity of U-ore deposits, these genetic models are still under debate, and have been recently investigated with the analysis of tourmalines in relationship with the ore formation (e.g. Kelly et al. 2020; Potter et al. 2022).

In the first case, the mineralizations are structurally controlled and typically located at, or within a few hundred metres above or below a prominent regional non-conformity between the sedimentary units and underlying basement rocks (Kyser and Cuney 2009; Bruce et al. 2020). Tourmalines and uranium phases precipitate at low temperatures from NaCl- and $CaCl_2$-rich brines derived from an isotopically heavy boron source, up to 26‰ (e.g. evaporated seawater) and interacted with basement rocks (low $\delta^{11}B$ source) to precipitate tourmaline with intermediate $\delta^{11}B$ compositions (Potter et al. 2022).

The Iron Oxide Copper Gold (IOCG) deposits, instead, are considered to be metasomatic expressions of large crustal-scale alteration events driven by intrusive activity (Corriveau et al. 2016), which typically form within provinces where several deposits of similar age and genesis form within common geologic settings (Roberts and Hudson 1983). In this case, the tourmalines combined to U-mineralizations can precipitate from a boron- and metal-enriched magmatic-hydrothermal fluid (Ootes et al. 2010) characterized by a boron isotopic composition further lighter, up to -15‰, and by temperature of at least 400°C (Kelly et al. 2020).

The Novazza-Vedello district of the cSA develops in a complex hydrothermal context characterized by pervasive albitization-sericitization-pyritization, Na depletion, silicification, carbonatization, sulphide deposition and F mobilization (Cadel 1986), contemporaneously to a boron-hydrothermalism. This latter shows boron isotopic compositions consistent with a calc-alkaline magmatic source, typical for the Permian intrusives, and indicate a high temperature (c.a. 380°C, Fig. 4.33b). All these features, combined with the structural setting of the area and with the geochronological constrains of tourmalinites and uranium mineralization events, are more suitable with a IOCG genetic model, rather than an unconformity-type deposit derived by low-temperature basinal brines. The occurrence of uranium mineralization concentrated along the Early Permian Aga-Vedello LANF in the Vedello area can be considered a coincidence. Here the U ores occur at the basement-cover contact, like in the U-unconformity type deposits, but the contact is a tourmalinite-bearing LANF along which boron- and uranium-rich fluids coming from deeper crustal levels circulated.

In other sectors of Europe, the mobilization of U during the Permian crustal extension was documented (Ballouard et al. 2017) and attributed to hydrothermal fluids leaching metals such as U, Sn, and W starting from enriched magmatic sources of Variscan age (Cuney et al. 1990). These metals were following remobilized and possibly concentrated after the Permian reactivation of Late-Variscan shear zones in a brittle stage. According to this interpretation, the efficiency of metal remobilization was dependent on the available uranium-rich minerals and on a close spatial relationship between magmatic structures enriched in uranium and brittle structures channelling the hydrothermal fluids (Cuney et al. 1990; Cuney 2014).

In our case study, the potential source of uranium cannot be directly defined, because in the Novazza-Vedello district nor Variscan basement neither Permian intrusives crop out at the surface. However, despite no intrusive bodies occur in the area, the Variscan basement (2.6 ppm of U) are not as enriched in U as the Permian intrusives, which could be most probably the source. Hydrothermal fluids interacting with this source of uranium circulated along LANFs and also at Novazza-Vedello Valley district, where U found favourable circumstances for precipitating, likely redox conditions in that part of the Orobic Basin, characterized by volcanites of Cabianca Volcanite and shales of the Pizzo del Diavolo Fm. Thus, the IOCG-type seems to be the most reliable genetic model.

6. CONCLUSIONS

The most relevant results of the present Ph.D. research project are here summarized:

- The combination of Low- and High-Angle Normal Faults (LANF-HANF) responsible for the opening of intracontinental Early Permian basins in the central Southern Alps (cSA) area is not an occasional feature, but so far it seems to be widespread along this entire sector of Alps. The same fault architecture has been recognized through the Orobic Basin, up to its western termination in the Gerola Valley area. Here, a LANF-HANF system extending for several kilometres has been identified and structurally characterized. This system is a typical expression of a stress regime with a vertical σ_1, suggesting a WNW-ESE direction of extension in present coordinates as a dominant mechanism during the Early Permian, controlling the opening of the Orobic Basin.
- Similarities with other Permian extensional systems in the cSA are also established based on the occurrence of syndepositional active tectonics, testified by the occurrence of growth faults and soft-sediment deformation, consistent with the strike of the Early Permian faults identified in the area. The synsedimentary tectonic structures are always in close relationships with LANFs and they formed at very shallow depth in sandy fine-grained units of the Lower Permian sedimentary succession of the Pizzo del Diavolo Formation. The recurrence of such common features suggests that the Permian basins experienced a similar/common tectonic-depositional evolution.
- This interpretation agrees with the thermal state inferred for the post-Variscan intermediate and lower crust during this period, with the LANF-HANF systems of the cSA that represent the shallow evidence of what was happening at deeper crustal levels.
- On the base of the presented results, it can be argued that the WNW-ESE oriented extension, all across the cSA, occurred before the important crustal reorganization affecting the entire Variscan belt including its forelands. This scenario is attributed by several authors to the transformation from Pangea B to Pangea A. Faults and shear zones formed during this stage may have been reactivated within and during the activity of the dextral mega-shear zone that caused the transformation from Pangea B to Pangea A. Regional tectonic response of this geodynamic process caused the tectonic inversion of Early Permian basins, testified by the Middle Permian sedimentary gap, later sealed by the Upper Permian successions.
- The structural architecture of the intra-continental Early Permian extensional basins of the cSA, strictly recalls the dynamics of the “Basin and Range Province”. For this reason, the Early Permian Orobic Basin could be considered as a fossil analogue of modern extensional

systems, where a combination of large-scale normal faulting at high and low angles dominates the tectonic scenario.

- Tourmalinites along the LANFs fault cores are genetically related to the ones from the Trompia Valley, occurring as hydrothermal veins related to intrusive bodies of 287-285 Ma age. According to the field-relationships, geochemical and isotopic data, with $\delta^{11}B$ ranging from an average of about -10.5‰ to -5‰ along the entire area, the boron-rich fluids are products of a calc-alkaline magmatic source, suitable with the Early Permian magmatism. This hydrothermal event was likely polyphasic, as suggested by the microstructural observations and the presence of different generation of tourmalines.
- Hydrothermal tourmaline-quartz veins of the Trompia Valley area are for the first time geochronologically constrained with U-Pb dating on newly formed rutile, which indicates a time interval that overlaps the intrusion age of magmatic bodies both in the Trompia Valley and Valsassina area. Tourmalinites replacing the LANF fault cores were not dated with direct analytical methods, but indirect stratigraphic and structural features support their formation between the Early and Middle Permian times. Thanks to the collected information and the obtained data, a geothermal model is proposed for the Orobic extensional system, fully consistent with the geological setting of the Southern Alps during the Early Permian.
- Some tourmalinites are spatially related to the uranium mineralization of the Novazza-Vedello Valley district, where uranium ores occur along the Aga-Vedello LANF. Geochemical data on tourmalinites support the hypothesis that boron-rich fluids were capable to mobilize uranium, as the higher uranium concentration in tourmalinites (up to 10 ppm) with respect to the average upper continental crust (2.7 ppm) demonstrates. This is the first direct evidence that tourmalinites and uranium mineralization of Novazza-Vedello district are genetically related.
- Boron-rich fluids transported uranium from a fertile source in the area and concentrated it along discontinuities with favourable conditions to precipitate uranium oxides. Despite the source of uranium is not well defined, a solid evidence is the genetic link between tourmalinites and magmatism. Lower Permian magmatic rocks of the cSA invariably display uranium contents higher than the upper continental crust and they likely acted as fertile source of uranium.
- Geochronological constrains on intrusive rocks, tourmalinites and uraninite indicate that they are broadly coeval, pointing to a strong interplay among the Early Permian tectonic, magmatic and hydrothermal activities.
- The wealth of presented data and observations is used to reconstruct a geological model for the formation of Early Permian basins and their relationships with magmatism and the

genesis of ore deposits. During the Early Permian evolution, crustal thinning is related to a combination of extensional tectonics, with the development of LANF-HANF system at shallow crustal levels, and magmatic activity occurring from the lower crust up to the surface. The Permian intrusives produced different expressions of hydrothermalism, one of which is characterized by boron-rich fluids precipitating tourmalinites. During their ascent, these fluids encountered as first discontinuities the faults of the LANF-HANF systems (Fig. 5.5), which worked as preferential channels for fluids, circulating for several kilometres. For these reasons, the LANFs can be identified as the best locations to see the interplay of different synchronous processes active during the Early Permian.

- According to this model, the temporal and spatial overlapping of processes further supports the hypothesis of a Permian magmatic source also for the uranium. In this context, the uranium ore-deposits of the Novazza-Vedello Valley district most likely formed as an IOCG (Iron Oxide Copper Gold) deposit rather than an U-unconformity type, as attested by several lines of evidence. To support this genetic model, there are different and coeval hydrothermal manifestations widespread in the cSA area, describing a complex scenario characterized by circulation of hydrothermal fluids, precipitating tourmalines and other mineral phases that point to medium-high temperatures. Furthermore, their boron isotopic compositions (δ^{11}B from -12‰ to 5‰) are lighter and are in contrast with a shallow water source as basinal brines, which are typical fluids responsible for the genesis of U-unconformity type deposits.
- By means of an interdisciplinary approach, the present study provides a new scenario for the complex interplay between tectonics and magmatism, that produced a geothermal and extensional system in the central Southern Alps during the Early Permian. The tectonic features analysed at different scale, starting from the fieldwork to the microstructural observations, exalt the importance of the structural control on channelling hydrothermal fluids along LANF fault planes, active during or immediately before the passage of boron-rich fluids. On the other hand, the petrographic, geochemical, isotopic and geochronological analysis was the only possible option to provide an accurate and thorough definition of the boron hydrothermalism that interacted with the evolution of the Early Permian Orobic Basin. Furthermore, the combination of structural geology and geochemistry of tourmalinites allowed for the comprehension of the origin of the uranium ore deposit of Novazza-Vedello district, which is for the first time demonstrated to be genetically linked to the same hydrothermal event.

7. ACKNOWLEDGMENTS

First of all, I would like to thank my supervisor Stefano Zanchetta and my tutor Andrea Zanchi for the professional support they gave me during these 3 years of Ph.D., and for their suggestions during the writing of the present thesis. I learnt many things on Geology and on the Lombardian tradition, especially thanks to the lessons of dialect from Bergamo provided by Zanchi's.

I also thank Marilena Moroni and Robert Trumbull, who transmitted to me the part of the knowledge coming from their expertise on ore deposits issues. In particular Robert was very supportive during the time of our collaboration in Potsdam and together with his wife Marion became my Nordic friends.

Of course, I warmly thank my friends of Bicocca, especially Chiara Montemario, Chiara Crippa Veleda, Martina and Silvia for giving me satisfaction in being stupid with me <3 you saw me in my best and worst moments of this experience, and I thank you so much for not killing me and for resisting during this long time together!!

I thank my family and my best friends which were cheering on me from Genoa. Last but not least, I want to thank Gregorio, who is the best discover of my Ph.D. experience!

8. REFERENCES

Angelier J., Colletta B., Chorowicz J., Ortlieb L., Rangin C. (1981). Fault tectonics of the Baja California Peninsula and the opening of the Sea of Cortez, Mexico. Journal of Structural Geology, 3(4), 347-357.

Arthaud F., Matte P. (1977). Late Paleozoic strike-slip faulting in southern Europe and northern Africa: Result of a right-lateral shear zone between the Appalachians and the Urals. Geological Society of America Bulletin, 88(9), 1305-1320.

Bachtadse V., Aubele K., Muttoni G., Ronchi A., Kirscher U., Kent D.V. (2018) - New early Permian paleopoles from Sardinia confirm intra-Pangea mobility. Tectonophysics, 749: 21-34.

Bakos F., Del Moro A., Visona D. (1990). The Hercynian volcano-phitonic association of Ganna (Lake Lugano, Central Southern Alps, Italy). European Journal of Mineralogy, 373-384.

Ballouard C., Poujol M., Boulvais P., Mercadier J., Tartese R., Venneman T., ... Cuney M. (2017). Magmatic and hydrothermal behavior of uranium in syntectonic leucogranites: The uranium mineralization associated with the Hercynian Guérande granite (Armorican Massif, France). Ore Geology Reviews, 80, 309-331.

Bates R. L., Jackson J. A. (1987). Glossary of geology.

Bergomi, M. A. (2004). Integrated study of the "Gneiss Chiari" in the framework of the Orobic basement of Southern Alps (filed relationships, mineral chemistry, geochemistry and geochronology). Eur. J. Miner. Plinius Ital. Supp. 30, 54–59.

Berra F., Siletto, G. B. (2006). Controllo litologico e stratigrafico sull'assetto strutturale delle Alpi meridionali lombarde: il ruolo degli orizzonti di scollamento. Rendiconti della Società Geologica Italiana, 2, 78-80.

Berra F., Carminati, E. (2010). Subsidence history from a backstripping analysis of the Permo-Mesozoic succession of the Central Southern Alps (Northern Italy). Basin Research, 22(6), 952-975.

Berra F., Felletti F. (2011) "Syndepositional tectonics recorded by soft-sediment deformation and liquefaction structures (continental Lower Permian sediments, Southern Alps, Northern Italy): stratigraphic significance." Sedimentary Geology 235.3-4 (2011): 249-263

Berra F., Tiepolo M., Caironi V., Siletto G. B. (2015). U–Pb zircon geochronology of volcanic deposits from the Permian basin of the Orobic Alps (Southern Alps, Lombardy): chronostratigraphic and geological implications. Geological Magazine, 152(3), 429-443.

Berra F., Felletti, F., Tessarollo, A. (2016). Stratigraphic architecture of a transtensional continental basin in low-latitude semiarid conditions: the Permian succession of the central Orobic Basin (Southern Alps, Italy). Journal of Sedimentary Research, 86(4), 408-429.

Berra F., Felletti F., Tessarollo A. (2019). Oncoids and groundwater calcrete in a continental siliciclastic succession in a fault-controlled basin (Early Permian, Northern Italy). Facies, 65(4), 1-19.

Bertotti, G., Siletto, G. B., Spalla, M. I. 1993. Deformation and metamorphism associated with crustal rifting: Permian to Liassic evolution of the Lake Lugano– Lake Como area (Southern Alps). Tectonophysics, 226, 271–284.

Blom J. C., Passchier C. W. (1997). Structures along the Orobic thrust, Central Orobic Alps, Italy. Geologische Rundschau, 86(3), 627-636.

Boriani A., Bini A., Beretta G. P., Bergomi M. A., Berra F., Cariboni M., ... Tognini P. (2012). Note Illustrative della Carta Geologica d'Italia alla scala 1: 50.000. Foglio 056-Sondrio.

Brack P. (1981). Structures in the southwestern border of the Adamello intrusion (Alpi Bresciane, Italy).

Brack P, Schaltegger U. (1999). Magmatism and extension in the Lower Permian of the Southern Alps: new age constraints from high-resolution U–Pb dating of zircons. In: International field conference ''The Permian of the Southern Alps and Sardinia (Italy)'', Brescia, 15–19 September 1999 (Abstr vol)

Brennecka G. A., Borg L. E., Hutcheon I. D., Sharp M. A., Anbar A. D. (2010). Natural variations in uranium isotope ratios of uranium ore concentrates: Understanding the 238U/235U fractionation mechanism. Earth and Planetary Science Letters, 291(1-4), 228-233.

Brennecka G. A., Wasylenki L. E., Bargar J. R., Weyer S., Anbar A. D. (2011). Uranium isotope fractionation during adsorption to Mn-oxyhydroxides. Environmental science & technology, 45(4), 1370-1375.

Brodie, K. H., Rutter, E. H., 1987. Deep crustal extensional faulting in the Ivrea Zone of Northern Italy. Tectonophysics, 140, 193-212.

Brodie, K.H., Rex, D., Rutter, E.H., 1989. On the age of deep crustal extensional faulting in the Ivrea zone, Northern Italy. Geol Soc London Spec Pub, 45, 203-210.

Brogi A., Novellino R. (2015). Low Angle Normal Fault (LANF)-zone architecture and permeability features in bedded carbonate from inner Northern Apennines (Rapolano Terme, Central Italy). Tectonophysics, 638, 126-146.

Brozzetti F., Cirillo D., Liberi F., Piluso E., Faraca E., De Nardis R., Lavecchia G. (2017). Structural style of Quaternary extension in the Crati Valley (Calabrian Arc): Evidence in support of an east-dipping detachment fault. Italian Journal of Geosciences, 136(3), 434-453.Bruce M., Kreuzer O., Wilde A., Buckingham A., Butera K., Bierlein, F. (2020). Unconformity-type uranium systems: A comparative review and predictive modelling of critical genetic factors. Minerals, 10(9), 738.

Brunet M. F., Le Pichon X. (1982). Subsidence of the Paris basin. Journal of Geophysical Research: Solid Earth, 87(B10), 8547-8560.

Byerlee J.D. (1978). Friction of rocks. Pure and Applied Geophysics 116, 615–626.Cadel G. (1986). Geology and uranium mineralization of the Collio Basin (central southern Alps, Italy). Uranium, 2, 2 15-240.

Cadel G., Fuchs Y., Meneghel L. (1987). Uranium mineralization associated with the evolution of a Permo-Carboniferous volcanic field. Examples from Novazza and Val Vedello (northern Italy). Uranium, 3, 407-42 1.

Cadel G., Cosi M., Pennacchioni G., Spalla M., I., (1996). A new map of the Permo-Carboniferous cover and Variscan metamorphic basement in the Central Orobic Alps, Southern Alps – Italy: structural and stratigraphical data. Mem. Sci. Geol., v. 48, pp 1-53.

Caine J. S., Evans J. P., Forster C. B. (1996). Fault zone architecture and permeability structure. Geology, 24(11), 1025-1028.

Caine J. S., Forster C. B. (1999). Fault zone architecture and fluid flow: Insights from field data and numerical modeling. Geophysical Monograph-American Geophysical Union, 113, 101-128.

Carminati E., Siletto G. B., Battaglia D. (1997). Thrust kinematics and internal deformation in basement-involved fold and thrust belts: The eastern Orobic Alps case (Central Southern Alps, northern Italy). Tectonics, 16(2), 259-271.

Carminati E., Siletto G.B. (2005) - The Central Southern Alps (N. Italy) paleoseismic zone: a comparison between field observations and predictions of fault mechanics. Tectonophysics, 401, 179-197.

Casati P., Gnaccolini M. (1967). Geologia delle Alpi Orobie occidentali. Rivista Italiana di Paleontologia e Stratigrafia, 73, 25-162.

Cassinis G., Dal Piaz G. V., Eusebio A., Gosso G., Martinotti G., Massari F., ... Zerbato M. (1986). Report on a structural and sedimentological analysis in the Uranium province of the Orobic Alps, Italy.

Cassinis G, Perotti C.R. (1993). Interazione strutturale permiana tra la Linea delle Giudicarie ed i Bacini di Collio, Tione e Tregiovo (Sudalpino centrale, N Italia). Boll Soc Geol It 112(1993):1021–1036.

Cassinis G., Frizzo P., Moroni M., Rodeghiero F. (1995). Le mineralizzazioni delle Alpi Bresciane: aspetti geologico-minerari e metallogenici. In Giornata di studio: Le vene delle montagne (pp. 97-119).

Cassinis G., Perotti C.R., Venturini C. (1997). Examples of late Hercynian transtensional tectonics in the Southern Alps (Italy). In: Dickins J.M., Yang Z.Y., Yin H.F., Lucas S.G. Acharyya S.K (eds.), Late Palaeozoic and Early Mesozoic

Circum-Pacific Events and Their Global Correlation. Cambridge Univ. Press, World and Regional Geol. Ser., 10, 41-50.

Cassinis G., Cortesogno L., Gaggero L., Perotti C. R., Buzzi L. (2008). Permian to Triassic geodynamic and magmatic evolution of the Brescian Prealps (eastern Lombardy, Italy). Bollettino della Società geologica italiana, 127(3), 501-518.

Cassinis G., Perotti C., Ronchi A. (2012) - Permian continental basins in the Southern Alps (Italy) and peri-mediterranean correlations. International Journal of Earth Sciences, 101, 129-157.

Castellarin A., Vai G. B., Cantelli L. (2006). The Alpine evolution of the Southern Alps around the Giudicarie faults: A Late Cretaceous to Early Eocene transfer zone. Tectonophysics, 414(1-4), 203-223.

Chernyshev, I. V., Dubinina, E. O., & Golubev, V. N. (2014). Fractionation factor of 238U and 235U isotopes in the process of hydrothermal pitchblende formation: A numerical estimate. Geology of Ore Deposits, 56(5), 315-321.

Cocherie A., Albarede F. (2001). An improved U-Th-Pb age calculation for electron microprobe dating of monazite. Geochimica et Cosmochimica Acta, 65(24), 4509-4522.

Colletta B., Angelier J. (1983). Fault tectonics in northwestern Mexico and opening of the Gulf of California: Bull. Centres Rech. Exlor.-Prod. Elf-Aquitaine, 7(1), 433-446.

Collettini, C. (2011). The mechanical paradox of low-angle normal faults: Current understanding and open questions. Tectonophysics, 510(3-4), 253-268.Corriveau L., Montreuil J. F., Potter E. G. (2016). Alteration facies linkages among iron oxide copper-gold, iron oxide-apatite, and affiliated deposits in the Great Bear magmatic zone, Northwest Territories, Canada. Economic Geology, 111(8), 2045-2072.

Crespi R. (1981). Metamorfismo tardo-alpino di grado bassissimo nel basamento a sud della Linea Insubrica.

Crippa C. (2017). Relazione tra il magmatismo Permiano e le strutture estensionali: caso di studio del Plutone della Val Biandino e Gressi detachment (Valsassina, LC). Unpublished master thesis.

Cuney, M. (2014). Felsic magmatism and uranium deposits. Bulletin de la Société Géologique de France, 185(2), 75-92.

Cuney M., Friedrich M., Blumenfeld P., Bourguignon A., Boiron M. C., Vigneresse J. L., Poty B. (1990). Metallogenesis in the French part of the Variscan orogen. Part I: U preconcentrations in pre-Variscan and Variscan formations—a comparison with Sn, W and Au. Tectonophysics, 177(1-3), 39-57.

D’Adda P., Zanchi A., Bergomi M., Berra F., Malusà M. G., Tunesi A., Zanchetta S. (2011). Polyphase thrusting and dyke emplacement in the central Southern Alps (Northern Italy). International Journal of Earth Sciences, 100(5), 1095-1113.

D'Adda P., Zanchetta S. (2015). Geological-structural map of the Orobic and Porcile thrust junction, central Southern Alps (N Italy). Journal of Maps, 11(1), 25-38.

Dadlez R., Narkiewicz M., Stephenson R. A., Visser M. T. M., Van Wees J. D. (1995). Tectonic evolution of the Mid-Polish Trough: modelling implications and significance for central European geology. Tectonophysics, 252(1-4), 179-195.

Dal Piaz, G.V.; Eusebio, A.; Gosso, G.; Martinotti, G.; Massari, F.; Milano, P.F.; Pennacchioni, G.; Perello, M.; Pessina, C.M.; Roman, E.; et al. (1986). Report on a structural and sedimentological analysis in the Uranium province of the Orobic alps, Italy. Uranium, 2, 241–260.

De Capitani L., Liborio G. (1988). Trace element abundance in the val Biandino pluton (Southern Alps, Italy). Memorie di Scienze Geologiche dell’Università di Padova, 40, 99–100.

De Capitani L., Delitala M. C., Liborio G., Mottana A., Nicoletti M., Petrucciani C. (1988). K-Ar dating of the val Biandino plutonic complex (Orobic Alps, Italy). Memorie di Scienze Geologiche dell’Università di Padova, 40, 285–294.

De Capitani L., Moroni M. (1992). Il microgabbro della Val Cavallina (Pezzaze, Prealpi Bresciane): caratteri chimici e mineralogici. Rend. Fis. Ace. Lincei, 3, 1 39- 149

De Capitani L., Delitala G., Liborio G., Mottana A., Rodeghiero F., Thoni M. (1994) The granitoid rocks of Val Navazze, Val Torgola and Val di Rango (Val Trompia, Lombardy, Italy). Mem. Sci. Geol., 46, 329-343

De Capitani L., Moroni M., Rodeghiero F. (1999). Geological and geochemical characteristics of Permian tourmalinization at Val Trompia (southern Alps, northern Italy) and relationship with the Orobic tourmalinites. Periodico di Mineralogia, 68, 185-212.

De Sitter L. U., De Sitter-Koomans C. M. (1949). The Geology of the Bergamasc Alps Lombardia Italy. Leidse Geologische Mededelingen, 14(2), 1-257.

Dewey J. F. (1988). Extensional collapse of orogens. Tectonics, 7(6), 1123-1139.

Diella, V., Spalla, M. I., Tunesi, A., 1992. Contrasting thermomechanical evolutions in the Southalpine metamorphic basement of the Orobic Alps (Central Alps, Italy). J Metam Geol, 10, 203-219.

Dini A., Mazzarini F., Musumeci G., Rocchi S. (2008). Multiple hydro-fracturing by boron-rich fluids in the Late Miocene contact aureole of eastern Elba Island (Tuscany, Italy). Terra Nova, 20(4), 318-326.Dill H. G. (1993). Die Antimonvorkommen der mitteleuropäischen Alpiden und Varisziden. Zeitschrift der deutschen geologischen Gesellschaft, 434-450.

Dyar M. D., Wiedenbeck M., Robertson D., Cross L. R., Delaney J. S., Ferguson K., ... & Yates M. (2001). Reference minerals for the microanalysis of light elements. Geostandards Newsletter, 25(2-3), 441-463.

Eaton G. P. (1982). The Basin and Range province: Origin and tectonic significance. Annual Review of Earth and Planetary Sciences, 10(1), 409-440.

Echtler H., Malavieille J. (1990). Extensional tectonics, basement uplift and Stephano-Permian collapse basin in a late Variscan metamorphic core complex (Montagne Noire, Southern Massif Central). Tectonophysics, 177(1-3), 125-138.

Ehrig K., McPhie J., Kamenetsky V. (2012). Geology and mineralogical zonation of the Olympic Dam iron oxide Cu-U-Au-Ag deposit, South Australia.

Evans J. P., Forster C. B., Goddard J. V. (1997). Permeability of fault-related rocks, and implications for hydraulic structure of fault zones. Journal of structural Geology, 19(11), 1393-1404.

Fantoni R., Bersezio R., Forcella F. (2004). Alpine structure and deformation chronology at the Southern Alps-Po Plain border in Lombardy. Bollettino della Società geologica italiana, 123(3), 463-476.

Filippi, M., Spalla, M. I., Pigazzini, N., Diella, V., Lardeaux, J. M., Zanoni, D. (2021). Cld-St-And-Bearing Assemblages in the Central Southalpine Basement: Markers of an Evolving Thermal Regime during Variscan Convergence. Minerals, 11(10), 1124.

Filippi M., Zanoni D., Rebay G., Roda M., Regorda A., Lardeaux J. M., Spalla M. I. (2022). Quantification of Alpine Metamorphism in the Edolo Diabase, Central Southern Alps. Geosciences, 12(8), 312.

Forcella F., Jadoul F. (1990). Deformazioni post-Adamello nelle Alpi Orobie. Stato dell'arte ed ipotesi di lavoro.

Forcella F., Jadoul F. (2000). Carta geologica della Provincia di Bergamo alla scala 1: 50.000 con relativa nota illustrativa. Provincia di Bergamo. Bergamo.

Friedmann, S. J., & Burbank, D. W. (1995). Rift basins and supradetachment basins: Intracontinental extensional end-members. Basin Research, 7(2), 109-127.

Frizzo P. (1995). Le mineralizzazioni a fluorite e solfuri polimetallici della Val Trompia. Atti della Giornata di Studio “Le vene delle montagne”, Brescia, 24, 149-163.

Froitzheim N., Derks J.F., Walter J.M., Sciunnach D. (2008). Evolution of an Early Permian extensional detachment fault from synintrusive, mylonitic flow to brittle faulting (Grassi Detachment Fault, Orobic Anticline, southern Alps, Italy). In: Tectonic Aspects of the Alpine-Dinaride-Carpathian System (Siegesmund S., Fugenshuh B. & Froitzheim N., eds). Geological Society, London, Special Publications, 298; 69-82 doi:10.1144/SP298.4.

Fuchs Y., Maury R. (1995). Borosilicate alteration associated with U-Mo-Zn and Ag-Au-Zn deposits in volcanic rocks. Mineralium Deposita, 30(6), 449-459.

Gans P. B., Mahood G. A., Schermeer E. (1989) Synextensional Magmatism in the Basin and Range Province: a Case Study from the Eastern Great Basin, Spec. Pap. geol. Soc. Am., 233.

Gallo L. C., Tomezzoli R. N., Cristallini E. O. (2017). A pure dipole analysis of the Gondwana apparent polar wander path: Paleogeographic implications in the evolution of Pangea. Geochemistry, Geophysics, Geosystems, 18, 1499–1519. https://doi.org/10.1002/2016GC006692

Giobbi Origoni E., Gregnanin A. (1983). The crystalline basement of the «Massiccio delle Tre Valli Bresciane»: new petrographic and chemical data. Mem. Soc. Geol. It., 26, 133- 144.

Giuseppetti G. (1959). Ricerche petrografiche sull'alta Val Trompia. Le formazioni eruttive di Val Navazze e di Val Torgola. Atti Ist. Geol. Univ. Pavia, vv. 9-10, pp 3-221, Pavia.

Gosso G., Siletto G.B., Spalla M.I. (1997). HT/LP metamorphism and structures in the South Alpine basement near Lake Coma, Orobic Alps; intracontinental imprints of the Permo- Triassic rifting. Ofioliti, 22, 133- 145.

Gretter N., Ronchi A., Langone A., Perotti C. R. (2013). The transition between the two major Permian tectono-stratigraphic cycles in the central Southern Alps: results from facies analysis and U/Pb geochronology. International Journal of Earth Sciences, 102(5), 1181-1202.

Hancock, P. L. (1985) Brittle microtectonics: principles and practices. Journal of Structural Geologv 7,431457.

Hawthorne, F.C.; Henry, D.J. (1999) Classification of the minerals of the tourmaline group. Eur. J. Miner. 11, 201–215.

Hayman N. W., Knott J. R., Cowan D. S., Nemser E., Sarna-Wojcicki A. M. (2003). Quaternary low-angle slip on detachment faults in Death Valley, California. Geology, 31(4), 343-346.

Henry D.J., Dutrow B.L. (1996) Metamorphic tourmaline and its petrologic applications. E.S. Grew, L.M. Anovitz (Eds.), Boron: Mineralogy, Petrology and Geochemistry, Reviews in Mineralogy, 33 (1996), pp. 503-557

Henry D.J., Guidotti C.V. (1985). Tourmaline as a petrogenetic indicator mineral: An example from the staurolite-grade metapelites of NW Maine. Am. Miner. 70, 1–15.

Hitzman M. W., Valenta, R. K. (2005). Uranium in iron oxide-copper-gold (IOCG) systems. Economic Geology, 100(8), 1657-1661.

Hoeve J., Sibbald T.I. (1978) On the genesis of Rabbit Lake and other unconformity-type uranium deposits in northern Saskatchewan, Canada. Economic Geology 73(8), 1450–1473.

Innocenti F., Serri G., Ferrara G., Manetti P., Tonarini S., 1992. Genesis and classification of the rocks of the Tuscan Magmatic Province: thirty years after Marinelli's model. Acta Vulcanol., 2, 247–265.Irving E., Parry L. G. (1963). The magnetism of some Permian rocks from New South Wales. Geophysical Journal International, 7(4), 395-411.

Irving E. (1977) - Drift of the major continental blocks since the Devonian. Nature, 270: 304-309.

Jadoul F., Gaetani M. (1986). L'assetto strutturale del settore lariano centro-meridionale. Memorie della Società Geologica Italiana, 32, 123-131.

Jiang S-Y., Yu J.-M., Lu J.-J. (2004). Trace and rare-earth element geochemistry in tourmaline and cassiterite from the Yunlong tin deposit, Yunnan, China: Implication for magmatitic-hydrothermal fluid evolution and ore genesis: Chemical Geology, v. 209, p. 193–213.

Jourde H., Cornaton F., Pistre S., Bidaux P. (2002). Flow behavior in a dual fracture network. Journal of hydrology, 266(1-2), 99-119.Kelly C. J., Davis W. J., Potter E. G., Corriveau L. (2020). Geochemistry of hydrothermal tourmaline from IOCG occurrences in the Great Bear magmatic zone: implications for fluid source (s) and fluid composition evolution. Ore Geology Reviews, 118, 103329.

Kent D. V., Muttoni G. (2020). Pangea B and the late paleozoic ice age. Palaeogeography, Palaeoclimatology, Palaeoecology, 553, 109753.

Kretschmar U., Scott S. D. (1976). Phase relations involving arsenopyrite in the system Fe-As-S and their application. Canadian mineralogist, 14(3), 364-386.

Krohe A., Eisbacher G. H. (1988). Oblique crustal detachment in the Variscan Schwarzwald, southwestern Germany. Geologische Rundschau, 77(1), 25-43.

Krosse S (1995) Hochdrucksyntheses, Stabilitat und Eigenschaften der Borsilikate Dravit und Kornerupin sowie Darstellung und Stabilitatsverhalten eines neuen Mg-Al-borates. Doctor thesis, Ruhr-Universitat, Bochum

Kyser K., Cuney M. 2009. Unconformity-related uranium deposits. Mineralogical Association of Canada Short Course Series, 39, 161–220.

Laubscher H. P. (1985). Large-scale, thin-skinned thrusting in the southern Alps: Kinematic models. Geological Society of America Bulletin, 96(6), 710-718.

Liotta D., Brogi A., Ruggieri G., Zucchi M. (2021). Fossil vs. active geothermal systems: A field and laboratory method to disclose the relationships between geothermal fluid flow and geological structures at depth. Energies, 14(4), 933.Lister G.S., Davis G.A. (1989). The origin of metamorphic core complexes and detachment faults formed during Tertiary continental extension in the northern Colorado River region, U.S.A. Journal of Structural Geology, 11, pp. 65-94.

Locchi S., Zanchetta S., Zanchi, A. (2022) Evidence of Early Permian extension during the post-Variscan evolution of the central Southern Alps (N Italy). Int J Earth Sci (Geol Rundsch) 111, 1717–1738. https://doi.org/10.1007/s00531-022-02220-2

Ludwig K. R. (2003). User's manual for IsoPlot 3.0. A geochronological toolkit for Microsoft Excel, 71.

Lynch G., Ortega S. (1997) Hydrothermal alteration and tourmaline–albite equilibria at the Coxheath porphyry Cu–Mo–Au deposit, Nova Scotia, The Canadian Mineralogist, 35, pp. 79-94

Marchetti L., Ronchi A., Santi G., Voigt S. (2015). The Gerola Valley site (Orobic Basin, Northern Italy): a key for understanding late early Permian tetrapod ichnofaunas. Palaeogeography, Palaeoclimatology, Palaeoecology, 439, 97-116.

Marchetti L. (2016). New occurrences of tetrapod ichnotaxa from the Permian Orobic Basin (Northern Italy) and critical discussion of the age of the ichnoassociation. Papers in Palaeontology, 2(3), 363-386.

Marotta A. M., Spalla M. I. (2007). Permian-Triassic high thermal regime in the Alps: Result of late Variscan collapse or continental rifting? Validation by numerical modeling. Tectonics, 26(4).

Marotta A. M., Spalla M. I., Gosso G. (2009). Upper and lower crustal evolution during lithospheric extension: numerical modelling and natural footprints from the European Alps. Geological Society, London, Special Publications, 321(1), 33-72.

Martin S., Toffolo L., Moroni M., Montorfano C., Secco L., Agnini C., Nimis P., Tumiati S. (2017). Siderite deposits in northern Italy: Early Permian to Early Triassic hydrothermalism in the Southern Alps. Lithos 284–285, 276–295.

Martina E. (1966). La granodiorite di V. Torgola-V. Navazze e la Linea della Val Trompia (Prealpi Bresciane). Rend. Ist. Lomb. Sci. Lett., s. A, V. 100, pp 366-404, Milano.

McCann T., Pascal C., Timmermann M. J., Krzywiec P., Lopez-Gomez J., Wetzel A., Krawczyk C. M., Rieke H., Lamarche J. (2006). Post-Variscan (end Carboniferous-Early Permian) basin evolution in Western and Central Europe. In: Gee D. G. & Stephenson R. A. (eds) 2006. European Lithosphere Dynamics. Geological Society, London, Memoirs, 32, 355-388.

McDonough W. F., Sun S. S. (1995). The composition of the Earth. Chemical geology, 120(3-4), 223-253.

Meijers M. J. M., Hamers M. F. van Hinsbergen D. J. J., van der Meer D. G., Kitchka A., Langereis C. G., Stephenson R. A. (2010). New Late Paleozoic paleopoles from the Donbas Foldbelt (Ukraine): Implications for the Pangea A vs. B controversy. Earth and Planetary Science Letters, 297(1-2), 18–33. https://doi.org/10.1016/j.epsl.2010.05.028

Ménard G., Molnar P. (1988). Collapse of a Hercynian Tibetan plateau into a late Palaeozoic European Basin and Range province. Nature, 334(6179), 235-237.

Meyer C., Wunder B., Meixner A., Romer R.L., Heinrich W. (2008). Boron-isotope fractionation between tourmaline and fluid: An experimental re-investigation. Contrib. Mineral. Petrol. 156, 259–267.

Milano P.F., Pennacchioni G., Spalla M.I. (1988). Alpine and pre- Alpine tectonics in the Central Orobic Alps (Southern Alps). Eclogae Geologicae Helvetiae, 81, 273-293.

Mittempergher S., Zanchi A., Zanchetta S., Fumagalli M., Gukov K., Bistacchi A. (2021). Fault reactivation and propagation in the northern Adamello pluton: The structure and kinematics of a kilometre-scale seismogenic source. Tectonophysics, 806, 228790.

Mittempergher S., Zanchetta S., Caldiroli F., Zanchi A., Bistacchi A., Hanchar J. M., Villa I. M. (2022). The timescale of solid-state deformation in the Northern Adamello igneous intrusive suite. Journal of the Geological Society, 179(4).

Mlynarczyk M.S.J., Williams-Jones A.E. (2006). Zoned tourmaline associated with cassiterite: Implications for fluid evolution and tin mineralization in the San Rafael Sn–Cu deposit, southeastern Peru: Canadian Mineralogist, v. 44, p. 347–365.

Montenat C., Barrier P., Hibsch C. (2007). Seismites: An attempt at critical analysis and classification. Sedimentary Geology, 196(1-4), 5-30.

Moroni, M. (1994). Identification of W-Sn mineralization associated with boron metasomatism in the crystalline basement of the Southern Italian Alps: Preliminary observations on a new finding. Chron. Rech. Min. 514, 38–43.

Muñoz-Barrera, J. M., Rotevatn, A., Gawthorpe, R. L., Henstra, G., Kristensen, T. B. (2022). Supradetachment basins in necking domains of rifted margins: Insights from the Norwegian Sea. Basin Research, 34(3), 991-1019.

Muttoni G., Kent D.V., Channell J.E.T. (1996). Evolution of Pangea: Paleomagnetic constraints from the Southern Alps, Italy. Earth Planet. Sci. Letters, 140: 97-112.

Muttoni G., Garzanti E., Alfonsi L., Cirilli S., Germani D., Lowrie W. (2001). Motion of Africa and Adria since the Permian: paleomagnetic and paleoclimatic constraints from northern Libya. Earth Planet. Sci. Letters, 192: 159-174.

Muttoni G., Kent D.V., Garzanti E., Brack P., Abrahamsen N., Gaetani M. (2003). Early Permian Pangaea ‘B’ to Late Permian Pangaea ‘A’. Earth Planet Science Letters, 215, 379-394.

Muttoni G., Mattei M., Balini M., Zanchi A., Gaetani M., Berra F. (2009). The drift history of Iran from the Ordovician to the Triassic. In: South Caspian to Central Iran Basins (Brunet M.-F., Wilmsen M. & Granath J.W., Eds.). Geological Society, London, Special Publications, 312, 7-29.

Muttoni G., Dallanave E., Channell J.E.T. (2013). The drift history of Adria and Africa from 280 Ma to Present, Jurassic true polar wander, and zonal climate control on Tethyan sedimentary facies. Palaeogeogr., Palaeoclimatol., Palaeoecol., 386: 415-435.

Muttoni G., Kent D. V. (2019). Adria as promontory of Africa and its conceptual role in the Tethys Twist and Pangea B to Pangea A Transformation in the Permian.

Muttoni G., Kent D. V. (2019). Jurassic monster polar shift confirmed by sequential paleopoles from Adria, promontory of Africa. Journal of Geophysical Research: Solid Earth, 124(4), 3288-3306.

Nayak B., Sindern S., Wagner T. (2021). Formation of late-stage hydrothermal mineralization in the Mesoarchean Boula-Nuasahi ultramafic complex, Odisha, India: Constraints from arsenopyrite geothermometry and trace element data. Ore Geology Reviews, 139, 104482.

Obermeier, S. F. (1996). Use of liquefaction-induced features for paleoseismic analysis—an overview of how seismic liquefaction features can be distinguished from other features and how their regional distribution and properties of source sediment can be used to infer the location and strength of Holocene paleo-earthquakes. Engineering Geology, 44(1-4), 1-76.

Ootes, L. U. K. E., Harris, J. E. F. F., Jackson, V. A., Azar, B. R. O. N. W. Y. N., & Corriveau, L. O. U. I. S. E. (2013). Uranium-enriched bedrock in the central Wopmay Orogen: implications for uranium mineralization. Exploration and Mining Geology, 21, 85-103.

Ota T., Kobayashi K., Katsura T., Nakamura E. (2008). Tourmaline breakdown in a pelitic system: implications for boron cycling through subduction zones. Contributions to Mineralogy and Petrology, 155(1), 19-32.

Palmer M.R., London D., Morgan G.B., Babb H.A. (1992). Experimental determination of fractionation of 11B/10B between tourmaline and aqueous vapor: A temperature- and pressure-dependent isotopic system. Chem. Geol. 101, 23–129.

Parrish R. R. (1989). U-Pb geochronology of the Cape Smith Belt and Sugluk block, northern Quebec. Geoscience Canada.

Pasquaré G. (1967). Analisi geologico-strutturale del complesso intrusivo di Val Biandino (Alpi Orobie Occidentali). Memorie della Società Geologica Italiana, 6, 343–357.

Petit J. P., Proust F., Tapponnier P. (1983). Criteres du sens du mouvement sur les miroirs de failles en roches non calcaires. Bulletin de la Societk geologique de France I, 589-608.

Petti F.M., Bernardi M., Ashley-Ross M.A., Berra F., Tessarollo A., Avanzini, M. (2014). Transition between terrestrial-submerged walking and swimming revealed by Early Permian amphibian trackways and a new proposal for the nomenclature of compound trace fossil. Palaeogeography, Palaeoclimatology, Palaeoecology, 410, 278-289.

Philippe S., Lang-Villemaire C., Lancelot J. R., Girod M., Mercadier H. (1987). Données minéralogiques et isotopiques sur deux gîtes hydrothermaux uranifères du bassin volcano-sédimentaire permien de Collio Orobico (Alpes Bergamasques): mise en évidence d'une phase de remobilisation crétacée. In: Bulletin de Minéralogie, volume 110, 2-3, 1987. Les mécanismes de concentration de l'uranium dans les environnements géologiques.

Pitra P., Burg J. P., Schulmann K., Ledru P. (1994). Late orogenic extension in the Bohemian Massif: petrostructural evidence in the Hlinsko region. Geodinamica Acta, 7(1), 15-30.

Pohl F., Froitzheim N., Obermüller G., Tomaschek F., Schröder O., Nagel T. J., Heuser, A. (2018). Kinematics and age of syn-intrusive detachment faulting in the Southern Alps: Evidence for Early Permian crustal extension and implications for the Pangea A versus B Controversy. Tectonics, 37(10), 3668-3689.

Pollard P.J., Pichavant M., Charoy B. (1987). Contrasting evolution of fluorine- and boron-rich tin systems: Mineralium Deposita, v. 22, p. 315–321.

Potter E. G., Kelly C. J., Davis W. J., Chi G., Jiang S. Y., Rabiei M., McEwan B. J. (2022). Fluid sources in basement-hosted unconformity–uranium ore systems: tourmaline chemistry and boron isotopes from the Patterson Lake corridor deposits, Canada. Geochemistry: Exploration, Environment, Analysis, 22(1).

Prijac C., Doin M. P., Gaulier J. M., Guillocheau F. (2000). Subsidence of the Paris Basin and its bearing on the late Variscan lithosphere evolution: a comparison between Plate and Chablis models. Tectonophysics, 323(1-2), 1-38.

Ravagnani D. (1974). I giacimenti uraniniferi italiani e i loro minerali. Gruppo Mineralogico Lombardo. Museo civico di storia naturale, Milano.

Rich R.A. (1976). Hydrothermal uranium deposits. Amsterdam: Elsevier, 284 p.

Rey P., Burg J. P., Caron J. M. (1992). Middle and Late Carboniferous extension in the Variscan Belt: structural and petrological evidence from the Vosges massif (Eastern France). Geodinamica Acta, 5(1-2), 17-36.

Roberts D. E., Hudson G. R. T. (1983). The Olympic Dam copper-uranium-gold deposit, Roxby Downs, South Australia. Economic Geology, 78(5), 799-822.

Roda M., Regorda A., Spalla M.I., Marotta A. (2019). What drives Alpine Tethys opening? clues from the review of geological data and model predictions. Geol. J., 54, 2646-2664.

Roger F., Teyssier C., Respaut J. P., Rey P. F., Jolivet M., Whitney D. L., ... Brunel M. (2015). Timing of formation and exhumation of the Montagne Noire double dome, French Massif Central. Tectonophysics, 640, 53-69.

Rose-Koga E. F., Sheppard S. M. F., Chaussidon M., Carignan, J. (2006). Boron isotopic composition of atmospheric precipitations and liquid–vapour fractionations. Geochimica et Cosmochimica Acta, 70(7), 1603-1615.

Rottura, A.; Bargossi, G.M.; Caggianelli, A.; Del Moro, A.; Visonà, D.; Tranne, C.A. (1998). Origin and significance of Permian high-K calc-alkaline magmatism in the central-eastern Southern Alps, Italy. Lithos 1998, 45, 329–348.

Rowland, J. V., & Sibson, R. H. (2004). Structural controls on hydrothermal flow in a segmented rift system, Taupo Volcanic Zone, New Zealand. Geofluids, 4(4), 259-283.Rudnick R. L., Gao S. (2003). Composition of the continental crust. The crust, 3, 1-64.

Schaltegger U. (1997). Magma pulses in the Central Variscan Belt: episodic melt generation and emplacement during lithospheric thinning. Terra Nova, 9(5-6), 242-245.

Schaltegger U., Brack P. (2007). Crustal-scale magmatic systems during intracontinental strike-slip tectonics: U, Pb and Hf isotopic constraints from Permian magmatic rocks of the Southern Alps. International Journal of Earth Sciences, 96(6), 1131-1151.

Schönborn G. (1992). Alpine tectonics and kinematic models of the central Southern Alps. Memorie di Scienze Geologiche, 44, 229-393.

Schuster R., Scharbert S., Abart R., Frank W. (2001). Permo-Triassic extension and related HT/LP metamorphism in the Austroalpine–Southalpine realm. Mitt. Ges. Geol. Bergbaustud. Österr, 45, 111-141.

Schuster R., Stüwe K. (2008). Permian metamorphic event in the Alps. Geology, 36(8), 603-606.

Sciunnach, D. (2001a). The Lower Permian in the Orobic Anticline (Southern Alps, Lombardy): A review based on new stratigraphic and petrographic data. Rivista Italiana di Paleontologia e Stratigrafia, 107, 47–68.

Sciunnach, D. (2001b). Early Permian palaeofaults at the western boundary of the Collio Basin (Valsassina, Lombardy). Natura Bresciana, 25, 37–43.

Selway J.B., Xiong, J. 2002. Tourmaline recalculation software (quoted in Tindle AG, Breaks, F.W., and Selway, J.B. 2002). Tourmaline in petalitesubtype granitic pegmatites: evidence of fractionation and contamination from the Pakeagama Lake and Separation Lake areas of northwestern Ontario, Canada. The Canadian Mineralogist, 40, 753–788, https://doi.org/10.2113/gscanmin.40.3.753

Shiel A. E., Laubach P. G., Johnson T. M., Lundstrom C. C., Long P. E., Williams K. H. (2013). No measurable changes in 238U/235U due to desorption–adsorption of U (VI) from groundwater at the Rifle, Colorado, integrated field research challenge site. Environmental science & technology, 47(6), 2535-2541.

Sibson, R. H. (1996). Structural permeability of fluid-driven fault-fracture meshes. Journal of Structural Geology, 18(8), 1031-1042.

Sibson, R. H. (2000). Fluid involvement in normal faulting. Journal of Geodynamics, 29(3-5), 469-499.Slack J. F. (1982). Tourmaline in Appalachian-Caledonian massive sulphide deposits and its exploration significance. Transactions of the Institution of Mining and Metallurgy, Section B: Applied Earth Science, 91(May), 81-89.

Slack J.F., Passchier C.W., Zhang J.S. (1996). Metasomatic tourmalinite formation along basement-cover décollements, Orobic Alps, Italy. Schweiz. Mineral. Petrogr. Mitt., 76, 193-207.

Spalla M. I., Carminati E., Ceriani S., Oliva A., Battaglia D. (1999). Influence of deformation partitioning and metamorphic re-equilibration on PT path reconstruction in the pre-Alpine basement of central southern Alps (northern Italy).

Spalla M.I., Gosso G. (1999). Pre-Alpine tectonometamorphic units in the central Southern Alps: structural and metamorphic memory. Memorie di Scienze Geologiche, 51, 221-229.

Spalla M. I., Zanoni D., Marotta A. M., Rebay G., Roda M., Zucali M., Gosso G. (2014). The transition from Variscan collision to continental break-up in the Alps: insights from the comparison between natural data and numerical model predictions. Geological Society, London, Special Publications, 405(1), 363-400.

Spiess, R., Langone, A., Caggianelli, A., Stuart, F. M., Zucchi, M., Bianco, C., ... & Liotta, D. (2021). Unveiling ductile deformation during fast exhumation of a granitic pluton in a transfer zone. Journal of Structural Geology, 147, 104326.Stampfli G. M., Kozur H. W. (2006). Europe from the Variscan to the Alpine cycles. Memoirs-Geological Society of London, 32, 57.

Stähle V., Frenzel G., Hess J. C. 2001. Permian metabasalt and Triassic alkaline dykes in the northern Ivrea zone: clues to the post-Variscan geodynamic evolution of the Southern Alps. Schweizerische Mineralogische und Petrographische Mitteilungen, 81, 1–21.

Taylor R.G. (1979) Geology of tin deposits: Development economic geology. Amsterdam: Elsevier, no 11, 543 p.

Thöni M., Mottana A., Delitala M. C., De Capitani L., Liborio G. (1992). The Val Biandino composite pluton: A late Hercynian intrusion into the South-Alpine metamorphic basement of the Alps (Italy). Neues Jahrbuch für Mineralogie Monatshefte, 12, 545–554.

Timmerman M. J., Heeremans M., Kirstein L. A., Larsen B. T., Spencer-Dunworth E. A., Sundvoll B. (2009). Linking changes in tectonic style with magmatism in northern Europe during the late Carboniferous to latest Permian. Tectonophysics, 473(3-4), 375-390.

Toffolo L., Nimis P., Martin S., Tumiati S., Bach W. (2017). The Cogne magnetite deposit (Western Alps, Italy): A Late Jurassic seafloor ultramafic-hosted hydrothermal system?. Ore Geology Reviews, 83, 103-126.

Trumbull R. B., Krienitz M. S., Gottesmann B., Wiedenbeck M. (2008). Chemical and boron-isotope variations in tourmalines from an S-type granite and its source rocks: the Erongo granite and tourmalinites in the Damara Belt, Namibia. Contributions to Mineralogy and Petrology, 155(1), 1-18.

Trumbull R. B., Codeço M. S., Jiang S. Y., Palmer M. R., Slack J. F. (2020). Boron isotope variations in tourmaline from hydrothermal ore deposits: a review of controlling factors and insights for mineralizing systems. Ore Geology Reviews, 125, 103682.

Umhoefer P. J., Plattner C., Malservisi R. (2020). Quantifying rates of “rifting while drifting” in the southern Gulf of California: The role of the southern Baja California microplate and its eastern boundary zone. Lithosphere, 12(1), 122-132.

Uvarova Y. A., Kyser T. K., Geagea M. L., Chipley D. (2014). Variations in the uranium isotopic compositions of uranium ores from different types of uranium deposits. Geochimica et cosmochimica acta, 146, 1-17.

Valoroso, L., Chiaraluce, L., Di Stefano, R., & Monachesi, G. (2017). Mixed‐mode slip behavior of the Altotiberina low‐angle normal fault system (Northern Apennines, Italy) through high‐resolution earthquake locations and repeating events. Journal of Geophysical Research: Solid Earth, 122(12), 10-220.Van Hinsberg V.J., Henry D.J., Marschall H.R. (2011) Tourmaline: an ideal indicator of its host environment The Canadian Mineralogist, 49, pp. 1-16

Van Wees J. D., Stephenson R. A., Ziegler P. A., Bayer U., McCann T., Dadlez R., ... Scheck M. (2000). On the origin of the southern Permian Basin, Central Europe. Marine and Petroleum Geology, 17(1), 43-59.

Voshage H., Hoffmann A. W., Mazzucchelli M., Rivalenti G., Sinigoi S., Raczek I., Demarchi G. (1990). Isotopic evidence from the Ivrea Zone for a hybrid lower crust formed by magmatic underplating. Nature, 347, 731–736.

Wernicke B., Axen G. J., Snow J. K. (1988). Basin and Range extensional tectonics at the latitude of Las Vegas, Nevada. Geological Society of America Bulletin, 100(11), 1738-1757.

Wernicke B. P., Snow J. K., Axen G. J., Burchfiel B. C., Hodges K. V., Walker J. D., Guth P. L. (1989). Extensional Tectonics in the Basin and Range Province between the southern Sierra Nevada and the Colorado Plateau. In 28th International Geological Congress Field Trip Guidebook (Vol. 138, p. 80).

Wickham S. M., Oxburgh E. R. (1987). Hercynian orogeny in the Pyrenees was not a rifting event. Nature, 325(6106), 740-740.

Yavuz F., Iskenderoglu A., Jiang S. Y. (1999a) Tourmaline composition from the Salikvan porphyry Cu–Mo deposit and vicinity, northeastern Turkey: Canadian Mineralogist, v. 37, p. 1007–1023.

Yavuz F., Fuchs Y., Karakaya N., Karakaya M.C. (2008). Chemical composition of tourmaline from the Asarcık Pb–Zn–Cu ^ U deposit, S¸ ebinkarahisar, Turkey: Mineralogy and Petrology, v. 94, p. 195–208.

Zanchetta S., D'Adda P., Zanchi A., Barberini V., Villa I. M. (2011). Cretaceous-Eocene compressions in the central Southern Alps (N Italy) inferred from 40Ar/39Ar dating of pseudotachylytes along regional thrust faults. Journal of Geodynamics, 51, 245-263, doi: 10.1016/j.jog.2010.09.004.

Zanchetta S., Garzanti E., Doglioni C., Zanchi A. (2012). The Alps in the Cretaceous: a doubly vergent pre-collisional orogen. Terra Nova, 24(5), 351-356.

Zanchetta S., Malusà M., Zanchi A. (2015). Precollisional development and Cenozoic evolution of the Southalpine retrobelt (European Alps). Lithosphere, 7, 662-681.0.

Zanchetta S., Locchi S., Carminati G., Mancuso M., Montemagni C., Zanchi A. (2022). Metasomatism by Boron-Rich Fluids along Permian Low-Angle Normal Faults (Central Southern Alps, N Italy). Minerals, 12(4), 404.

Zanchi A. (1994). The opening of the Gulf of California near Loreto, Baja California, Mexico: from basin and range extension to transtensional tectonics. Journal of Structural Geology, 16(12), 1619-1639.

Zanchi A., Zanchetta S., Berio L., Berra F., Felletti, F. (2019). Low-angle normal faults record Early Permian extensional tectonics in the Orobic Basin (Southern Alps, N Italy). Italian Journal of Geosciences, 138(2), 184-201.

Zanchi A., Locchi S., Zanchetta S. (2021). Early Permian syndepositional tectonics in the Orobic Basin, Southern Alps, Italy, EGU General Assembly 2021, online, 19–30 Apr 2021, EGU21-8056, https://doi.org/10.5194/egusphere-egu21-8056.

Zanoni D., Spalla M. I. (2018). The Variscan evolution in basement cobbles of the Permian Ponteranica Formation by microstructural and petrologic analysis. Italian Journal of Geosciences, 137(2), 254-271.

Zech J., Jeffries T., Faust D., Ullrich B., Linnemann U. (2010). U/Pb-dating and geochemical characterization of the Brocken and the Ramberg Pluton, Harz Mountains, Germany. Geologica Saxonica, 56, 9-24.

Zhang J.S., Passchier C.W., Slack J. F. (1994). Cryptocrystalline Permian tourmalinites of possible metasomatic origin in the Orobic Alps, Northern Italy. Economic Geology, 89, 391-396.

Ziegler P. A. (1986). Geodynamic model for the Palaeozoic crustal consolidation of Western and Central Europe. Tectonophysics, 126(2-4), 303-328.

Ziegler P. A. (1988). Hercynian Suturing of Pangea: Chapter 3.

Ziegler, P. A., Schumacher, M. E., Dèzes, P., Van Wees, J. D., & Cloetingh, S. A. P. L. (2006). Post-Variscan evolution of the lithosphere in the area of the European Cenozoic Rift System. Geological Society, London, Memoirs, 32(1), 97-112.

Zucchi, M., Brogi, A., Liotta, D., Caggianelli, A., Dini, A., Ventruti, G., ... & Matera, P. F. Fractures, fluid flow and inherited structures in geothermal systems: inputs from the Fe-ore deposits of eastern Elba Island (Northern Apennines, Italy). Geological Magazine, 1-24.

9. APPENDIX 1: SAMPLES OVERVIEW AND APPLIED METHODOLOGIES

SAMPLES	GPS COORDINATES	NOTE	THIN SECTION	SEM	SHORT DESCRIPTION	MICROPROBE	WHOLE ROCK ANALYSIS	SIMS
FC-1	46°03'35.2"N 9°54'28.4"E	Drill core from the basement at Forcellino Pass area	-	-	-	-	√	-
FC-2	46°03'35.2"N 9°54'28.4"E	Drill core from the basement at Forcellino Pass area	-	-	-	-	√	-
FC-3	46°03'35.2"N 9°54'28.4"E	Drill core from the basement at Forcellino Pass area	-	-	-	-	√	-
FC-4	46°03'35.2"N 9°54'28.4"E	Drill core from the basement at Forcellino Pass area	-	-	-	-	√	-
FC-5	46°03'35.2"N 9°54'28.4"E	Drill core from the basement at Forcellino Pass area	√	-	Orthogneiss in the footwall with fractures filled by new mineral phases, included few aggregates of tourmaline	-	√	-
FC-6	46°03'35.2"N 9°54'28.4"E	Drill core from the basement at Forcellino Pass area	√	-	Orthogneiss in the footwall with fractures filled by new mineral phases, included few aggregates of tourmaline	-	√	-
FC-7	46°03'35.2"N 9°54'28.4"E	Drill core from the basement at Forcellino Pass area	√	-	Orthogneiss in the footwall with fractures filled by new mineral phases, especially carbonates	-	√	-
FC-8	46°03'35.2"N 9°54'28.4"E	Drill core from the basement at Forcellino Pass area	√	-	Orthogneiss with cataclastic bands	-	√	-
FC-9	46°03'35.2"N 9°54'28.4"E	Drill core from the basement at Forcellino Pass area	√	-	Cataclasated orthogneiss closer to the fault core, the rock is interested by replacement of new mineral phases (sericite, chloritoide, white mica, oxides)	-	√	-
FC-10	46°03'35.2"N 9°54'28.4"E	Drill core from the basement at Forcellino Pass area	-	-	-	-	√	-
FC-11	46°03'35.2"N 9°54'28.4"E	Drill core from LANF fault zone	-	-	-	-	-	-
FC-12	46°03'35.2"N 9°54'28.4"E	Drill core from LANF fault zone	√	-	Cataclasite partially replace by aphanitic tourmaline in different bands, with dark to grey colour. Higher percentage of tourmaline occur in finer protions of the cataclasite	-	√	-
FC-13	46°03'35.2"N 9°54'28.4"E	Drill core from LANF fault zone	√	-	Cataclasite partially replace by aphanitic tourmaline in different bands, with dark to grey colour. Higher percentage of tourmaline occur in finer protions of the cataclasite	-	√	-
FC-14	46°03'35.2"N 9°54'28.4"E	Drill core from LANF fault zone	√	-	Cataclasite metasomatized	-	√	√
FC-15	46°03'35.2"N 9°54'28.4"E	Drill core from LANF fault zone	-	-	-	-	-	-
FC-16	46°03'35.2"N 9°54'28.4"E	Drill core from LANF fault zone	√	-	Cataclasite with clasts from the basement	-	√	-
FC-17	46°03'35.2"N 9°54'28.4"E	Drill core from LANF fault zone	-	-	-	-	-	-
FC-18	46°03'35.2"N 9°54'28.4"E	Drill core from LANF fault zone	√	-	Cataclasite with matrix replaced by tourmaline	-	√	-

SAMPLES	GPS COORDINATES	NOTE	THIN SECTION	SEM	SHORT DESCRIPTION	MICROPROBE	WHOLE ROCK ANALYSIS	SIMS
FC-19	46°03'35.2"N 9°54'28.4"E	Drill core from LANF fault zone	√	-	Big clast of basement in the Mt Aga conglomerate, there are also sparse tourmaline crystals	-	-	-
FC-21	46°03'35.2"N 9°54'28.4"E	Drill core from LANF fault zone	√	√	Factured conglomerate with cataclastic bands by new mineral phases. The relicts of clasts are altered (sericite). There are ehuedral cristals of tourmaline and carbonatic veins cutting the matrix	√	-	√
FC-22	46°03'35.2"N 9°54'28.4"E	Drill core from LANF fault zone	√	-	Cataclasite organized in bands with different grade of replacement by new fine grained mineral phases, aphanitic tourmaline. Ehuedral tourmaline occurs and it is pleochroic	-	√	-
PG-1	46°01'56.0"N 9°35'01.9"E	Sample from Gerola Valley area: PG 1.2 C (cataclasite), T1 (tormalinite 1), T2 (tormalinite 2)	√	-	Cataclasti and ultracataclastic bands alterned with dark layer enriched in fine-grained tourmaline. There is alpine crenulation cleavage in the finest portions	-	√	-
PG-2	46°01'56.0"N 9°35'01.9"E	Sample from Gerola Valley area	√	-	Foliated cataclasite composed of many clasts of quartz and the matrix is altered by new mineral phase	-	-	-
PG-3A	46°01'56.0"N 9°35'01.9"E	Sample from Gerola Valley area	√	√	Ultracataclasite with alterned layers of very fine grained tourmaline in different percentage, with carbonatic and oxides veins	√	√	√
PG-5A	46°01'37.4"N 9°35'00.6"E	Sample from Gerola Valley area	√	-	Conglomerate cut by cataclastic bands, the finer matrix is replaced by new fine grained minerals like sericite	-	-	-
PG-6	46°01'37.4"N 9°35'00.6"E	Sample from Gerola Valley area	√	-	Ultrcataclasite foliated with matrix replaced by a green mineral phase, too fine grained to be identified. There are many quartz veins	-	-	-
PG-7	46°01'37.4"N 9°35'00.6"E	Sample from Gerola Valley area - for bulk analysis:PG7-C (cataclasite) and PG7-T (tourmalinite)	√	-	Contact between fine grained tormalinite and foliated cataclasite. The tourmalinite is replaced by a green mineral phase, too fine grained to be identified, but related to more recent re-circulation of fluids	-	√	-
PG-8	46°01'37.4"N 9°35'00.6"E	Sample from Gerola Valley area	√	-	Tormalinite cut by quartzous and carbonatic veins. Also in this case the tourmalinite is replaced by a green mineral phase	-	√	-
PG-x	46°01'37.4"N 9°35'00.6"E	Sample from Gerola Valley area	-	-	-	-	-	-
PG-y	46°01'37.4"N 9°35'00.6"E	Sample from Gerola Valley area, Lake Pescegallo	-	-	-	-	-	-

SAMPLES	GPS COORDINATES	NOTE	THIN SECTION	SEM	SHORT DESCRIPTION	MICROPROBE	WHOLE ROCK ANALYSIS	SIMS
PG-10	46°02'14.1"N 9°35'04.4"E	Sample from Gerola Valley area, Lake Pescegallo	-	-	-	-	-	-
PG-11	46°02'14.1"N 9°35'04.4"E	Sample from Gerola Valley area, Lake Pescegallo	-	-	-	-	-	-
PG-12	46°02'14.1"N 9°35'04.4"E	Sample from Gerola Valley area, Lake Pescegallo	-	-	-	-	-	-
PG-13	46°02'14.1"N 9°35'04.4"E	Sample from Gerola Valley area, Lake Pescegallo	-	-	-	-	-	-
PG-14	46°01'56.0"N 9°35'01.9"E	Sample from Gerola Valley area	√	-	Cataclasite replaced by very fine grained tourmaline	-	-	-
PG-15	46°01'56.0"N 9°35'01.9"E	Sample from Gerola Valley area	√	-	Cataclasite replaced by very fine grained tourmaline	-	-	-
PG-16	46°01'56.0"N 9°35'01.9"E	Sample from Gerola Valley area	√	-	Cataclasite replaced by very fine grained tourmaline	-	-	-
PG-17	46°01'25.2"N 9°35'10.3"E	Sample from Gerola Valley area, close to Mt. Valletto	√	-	Cataclasite replaced by very fine grained tourmaline	-	-	-
PG-18	46°01'25.2"N 9°35'10.3"E	Sample from Gerola Valley area, close to Mt. Valletto	-	-	-	-	-	-
PG-19	46°01'25.2"N 9°35'10.3"E	Sample from Gerola Valley area, close to Mt. Valletto	√	-	Cataclasite replaced by cryptocrystalline tourmaline. There are also relict of first generation tourmalinites	-	-	-
PG-20	46°01'24.7"N 9°35'08.4"E	Sample from Gerola Valley area, close to Mt. Valletto	-	-	-	-	-	-
VM8	45°47'45.5"N 10°14'43.7"E	Sample from Trompia Valley	√	√	Tourmaline veins producing breccia texture in granitoid partially replaced with greisen alteration, with formation of new fine grained mineral phases. In the veins there are tourmaline, quartz and rutile and the cataclasated zones are interested by carbonatic veins	√	-	-
VM23	45°47'45.5"N 10°14'43.7"E	Sample from Trompia Valley	√	-	Paragneiss oblitarated by zoned acicular tormaline. In the cataclastic band there are fine grained crystals of tourmaline. Rutile occurs as well as idroxides veins	-	-	-
880	45°47'45.5"N 10°14'43.7"E	Sample from Trompia Valley	√	√	Tourmalinitic breccia with fragment of leucogranite. The tourmaline is microcristalline, there are veins of quartz associated with oxides and idroxides. The veins are well preserved and not deformed.	√	-	√

SAMPLES	GPS COORDINATES	NOTE	THIN SECTION	SEM	SHORT DESCRIPTION	MICROPROBE	WHOLE ROCK ANALYSIS	SIMS
VNE-1	45°48'26.3"N 10°17'18.8"E	Sample from Trompia Valley Granitoids of Val Navazze - VNE-1A VNE-1B	√	-	Granodiorite composed by quartz, feldpsar cloritized biotite and amphibole	-	√	-
VNE-2	45°48'26.3"N 10°17'18.8"E	Sample from Trompia Valley Granitoids of Val Navazze	√	-	Contact between two different grain size portions of granodiorite. The finest is enriched in amphibole and oxides, the other ha a porphiric texture with fenocrystals of quartz, feldspar and relicts of biotite	-	√	-
VNE-3	45°48'26.3"N 10°17'18.8"E	Sample from Trompia Valley Granitoids of Val Navazze	√	-	Granitoid with quartz, feldspar and biotite	-	√	-
VNE-4	45°48'26.3"N 10°17'18.8"E	Sample from Trompia Valley Granitoids of Val Navazze	√	-	Granodiorite with quartz, feldspar, amphibole and biotite	-	√	-
VNE-5	45°48'26.3"N 10°17'18.8"E	Sample from Trompia Valley Granitoids of Val Navazze	√	-	Porphiric granite with fenocrystals of quartz, plagioclase, k-feldspar (sericitized) and replaced femic mineral	-	√	-
VNE-6	45°48'26.3"N 10°17'18.8"E	Sample from Trompia Valley Granitoids of Val Navazze	√	-	Granodiorite with quartz, feldspar (sericitized), amphibole	-	√	-
MVN-1	45°48'26.3"N 10°17'18.8"E	Sample from Trompia Valley Granitoids of Val Navazze	√	-	Granite with quartz, feldsparto and altered biotite	-	√	-
MVN-2	45°48'26.3"N 10°17'18.8"E	Sample from Trompia Valley Granitoids of Val Navazze	√	-	Granite with quartz, feldsparto and altered biotite. Larger crystals with respect to MVN1	-	√	-
MVN-3	45°48'26.3"N 10°17'18.8"E	Sample from Trompia Valley Granitoids of Val Navazze	√	-	Granite with porphiric texture, with fenocrysts of quart, feldspar (sericitized) and biotite	-	√	-
AV-1	46°00'04.0"N 9°51'42.8"E	Sample from Lake Aviasco	√	-	Volcanoclastic sediments with new mineral phases as oxides and the quartz grans are absorbed	-	√	-
AV-2	46°00'04.0"N 9°51'42.8"E	Sample from Lake Aviasco	√	-	Volcanoclastic sediments in contact with a shear zone replaced by oxides and tourmaline	-	√	-
AV-3	46°00'04.0"N 9°51'42.8"E	Sample from Lake Aviasco	√	-	Volcanoclastic sediments with new mineral phases as oxides and the quartz grans are absorbed	-	-	-
AV-4	46°00'04.0"N 9°51'42.8"E	Sample from Lake Aviasco	√	-	Cataclasite of volcanoclastic sandstone replaced by arsenopyrite and tourmaline	-	-	-
AV-5	46°00'04.0"N 9°51'42.8"E	Sample from Lake Aviasco	√	-	Fine grained cataclasite replaced by oxides, arsenopyrite and tpurmaline, especially in the finest portions	-	-	√
AV-6	46°00'04.0"N 9°51'42.8"E	Sample from Lake Aviasco	√	-	Utracataclasite replaced by new mineral phases such as fine grained tourmaline and oxides and sulphides	-	√	√

SAMPLES	GPS COORDINATES	NOTE	THIN SECTION	SEM	SHORT DESCRIPTION	MICROPROBE	WHOLE ROCK ANALYSIS	SIMS
AV-7	46°00'04.0"N 9°51'42.8"E	Sample from Lake Aviasco	√	-	Utracataclasite replaced by new mineral phases such as fine grained tourmaline and oxides and sulphides	-	√	-
VSS 1	45°59'36.0"N 9°25'11.8"E	Sample from Valsassina	-	-	-	-	-	-
VSS 3	45°59'36.0"N 9°25'11.8"E	Sample from Valsassina	√	-	Cataclasite with clasts of metamorphic basement and granitoids strongly replaced by medium to fine-grained pleochroic tourmaline. There are relicts of first generation tourmalinites	-	√	√
LDC11B	45°48'15.5"N 10°16'13.8"E	Sample from Trompia Valley	-	-	-	-	-	-
LDC1	45°48'15.5"N 10°16'13.8"E	Sample from Trompia Valley	-	-	-	-	-	-
BV	45°47'45.5"N 10°14'43.7"E	Sample from Trompia Valley	√	-	Medium grained size tourmalinites compossed of acicular crystals, in equilibrium with quartz and pyrite	-	-	-
VV1	46°04'17.0"N 9°55'34.5"E	Sample from Vedello Valley mine	-	√	Preliminary identification at SEM-EDS of uraninite, brannerite, blende, calchopyrite, ankerite, aresenic-sulphide	√	-	-
X1 Z	46°02'57.7"N 9°52'29.4"E	Sample from Mt. Aga and Mt. Masoni Master thesis L. Berio	√	-	Cataclasite replaced by cryptocrystalline tourmaline	-	-	-
C1 Z	46°02'57.7"N 9°52'29.4"E	Sample from Mt. Aga and Mt. Masoni Master thesis L. Berio	√	-	Foliated cataclasite with basement-derived clasts	-	-	-
C2 Z	46°03'04.4"N 9°52'36.7"E	Sample from Mt. Aga and Mt. Masoni Master thesis L. Berio	√	-	Cataclasite replaced by cryptocrystalline tourmaline; sometimes can be recognized S-C fabric	-	-	-
C3	46°03'00.8"N 9°52'34.8"E	Sample from Mt. Aga and Mt. Masoni Master thesis L. Berio	√	-	Cataclasite with atrix replaced by new mineral phases. There are many quartzous veins subparallel oriented	-	-	-
C5	46°02'42.4"N 9°50'05.5"E	Sample from Mt. Aga and Mt. Masoni Master thesis L. Berio	√	√	Tormalinite in contact with foliated cataclasite replaced by fine-grained phyllosilicate	√	-	√
C5 Z	46°02'42.4"N 9°50'05.5"E	Sample from Mt. Aga and Mt. Masoni Master thesis L. Berio	√	-	Tormalinite cutting tha Mt Aga conglomerate	-	-	-
C6	46°02'42.4"N 9°50'05.5"E	Sample from Mt. Aga and Mt. Masoni Master thesis L. Berio	√	-	Fractured basement in contact with cataclasite	-	-	-

SAMPLES	GPS COORDINATES	NOTE	THIN SECTION	SEM	SHORT DESCRIPTION	MICROPROBE	WHOLE ROCK ANALYSIS	SIMS
C6 Z	46°02'42.4"N 9°50'05.5"E	Sample from Mt. Aga and Mt. Masoni Master thesis L. Berio	√	-	Tormalinite in contact with sandstone	-	-	-
C7 Z	46°02'50.4"N 9°52'32.2"E	Sample from Mt. Aga and Mt. Masoni Master thesis L. Berio	√	-	Tormalinite in contact with cataclastic band enriched in cryptocrystalline tourmaline especially in the finest portions	-	-	-
C8 Z	46°02'50.4"N 9°52'32.2"E	Sample from Mt. Aga and Mt. Masoni Master thesis L. Berio	√	-	Cataclasite with high percentage of matix replaced by aphanitic tourmaline. Clasts are characterized by iso-oriented strain shadows	-	-	-
C9	46°02'50.4"N 9°52'32.2"E	Sample from Mt. Aga and Mt. Masoni Master thesis L. Berio	√	-	Tormalinitic cataclasite with clasts of Mt Aga conglomerate	√	-	-
C9 Z	46°02'50.4"N 9°52'32.2"E	Sample from Mt. Aga and Mt. Masoni Master thesis L. Berio	√	-	Tormalinite organized in layers with different percentage of tourmaline	-	-	-
C11 Z	46°02'37.1"N 9°52'30.5"E	Sample from Mt. Aga and Mt. Masoni Master thesis L. Berio	√	-	Tormalinite/tourmalinitic cataclasite	-	-	-
C12	46°02'37.1"N 9°52'30.5"E	Sample from Mt. Aga and Mt. Masoni Master thesis L. Berio	√	-	Tourmalinitic vein cutting the sandstone	-	-	-
C12 Z	46°02'37.1"N 9°52'30.5"E	Sample from Mt. Aga and Mt. Masoni Master thesis L. Berio	√	-	Tormalinitic cataclasite	-	-	-
C13	46°02'42.5"N 9°52'31.2"E	Sample from Mt. Aga and Mt. Masoni Master thesis L. Berio	√	-	Metasomatized conglomerate with strain shadows along the clasts	-	-	-
C15	46°02'46.7"N 9°50'11.4"E	Sample from Mt. Aga and Mt. Masoni Master thesis L. Berio	√	-	Conglomerate with cataclastic bands	-	-	-
C16	46°02'46.7"N 9°50'11.4"E	Sample from Mt. Aga and Mt. Masoni Master thesis L. Berio	√	-	Contact between tourmalinite and sandstone	-	-	-
C20 A	46°03'04.4"N 9°52'36.7"E	Sample from Mt. Aga and Mt. Masoni Master thesis L. Berio	√	-	Cataclasite with matrix enriched in tourmaline, occurring sometimes as single euhedral crystal	-	-	-
C20 B	46°03'04.4"N 9°52'36.7"E	Sample from Mt. Aga and Mt. Masoni Master thesis L. Berio	√	-	Contact between tourmalinite and cataclasite with high percentage of tourmaline in the matrix	-	-	-

SAMPLES	GPS COORDINATES	NOTE	THIN SECTION	SEM	SHORT DESCRIPTION	MICROPROBE	WHOLE ROCK ANALYSIS	SIMS
C21	46°03'04.4"N 9°52'36.7"E	Sample from Mt. Aga and Mt. Masoni Master thesis L. Berio	√	-	Cataclasite with basement-derived clasts and matrix enriched in cryptocrystalline tourmaline	-	-	-
C23	46°02'49.4"N 9°50'14.7"E	Sample from Mt. Aga and Mt. Masoni Master thesis L. Berio	√	-	Cataclasite con clasti centimentrici e matrice ricca in tormalina	√	-	-
C25	46°02'49.4"N 9°50'14.7"E	Sample from Mt. Aga and Mt. Masoni Master thesis L. Berio	√	-	Metasomatic rock replaced by very fine grained tourmaline in contact with cataclasite enriched in euhedral tourmaline. This area is characterized by S-C fabric and is cut by quartzous veins	-	-	-
C27	46°02'49.4"N 9°50'14.7"E	Sample from Mt. Aga and Mt. Masoni Master thesis L. Berio	√	-	Tormalinite alternated with cataclastic bands and quartzous veins	-	-	-
C28	46°02'49.4"N 9°50'14.7"E	Sample from Mt. Aga and Mt. Masoni Master thesis L. Berio	√	-	Cataclasite enriched in fine grained tourmaline	-	-	-
RDC 3A	-	Powder of tourmalinites provided by De Capitani - from Trompia Valley	-	-	-	-	√	-
RDC 3B	-	Powder of tourmalinites provided by De Capitani - from Trompia Valley	-	-	-	-	√	-
RDC 8	-	Powder of tourmalinites provided by De Capitani - from Trompia Valley	-	-	-	-	√	-
RDC 11	-	Powder of tourmalinites provided by De Capitani - from Trompia Valley	-	-	-	-	√	-
T3A	-	Powder of tourmalinites provided by De Capitani - from Lake Diavolo	-	-	-	-	√	-

SAMPLES	GPS COORDINATES	NOTE	THIN SECTION	SEM	SHORT DESCRIPTION	MICROPROBE	WHOLE ROCK ANALYSIS	SIMS
T7	-	Powder of tourmalinites provided by De Capitani - from Lake Diavolo	-	-	-	-	√	-
T100C	-	Powder of tourmalinites provided by De Capitani - from Lake Diavolo	-	-	-	-	√	-
T106	-	Powder of tourmalinites provided by De Capitani - from Lake Diavolo	-	-	-	-	√	-
VBZ-1	-	Sample of granitoid from Valsassina Master thesis C. Crippa	-	-	-	-	√	-
VBZ-3	-	Sample of granitoid from Valsassina Master thesis C. Crippa	-	-	-	-	√	-
VBZ-35	-	Sample of granitoid from Valsassina Master thesis C. Crippa	-	-	-	-	√	-
VBZ-42	-	Sample of granitoid from Valsassina Master thesis C. Crippa	-	-	-	-	√	-
VBZ-43	-	Sample of granitoid from Valsassina Master thesis C. Crippa	-	-	-	-	√	-

SAMPLES	GPS COORDINATES	NOTE	LA-ICP-MS for U-Pb dating	LA-ICP-MS in situ on tourmaline for trace elements contents
FC-1	46°03'35.2"N 9°54'28.4"E	Drill core from the basement at Forcellino Pass area	-	-
FC-2	46°03'35.2"N 9°54'28.4"E	Drill core from the basement at Forcellino Pass area	-	-
FC-3	46°03'35.2"N 9°54'28.4"E	Drill core from the basement at Forcellino Pass area	-	-
FC-4	46°03'35.2"N 9°54'28.4"E	Drill core from the basement at Forcellino Pass area	-	-
FC-5	46°03'35.2"N 9°54'28.4"E	Drill core from the basement at Forcellino Pass area	-	-
FC-6	46°03'35.2"N 9°54'28.4"E	Drill core from the basement at Forcellino Pass area	-	-
FC-7	46°03'35.2"N 9°54'28.4"E	Drill core from the basement at Forcellino Pass area	-	-
FC-8	46°03'35.2"N 9°54'28.4"E	Drill core from the basement at Forcellino Pass area	-	-
FC-9	46°03'35.2"N 9°54'28.4"E	Drill core from the basement at Forcellino Pass area	-	-
FC-10	46°03'35.2"N 9°54'28.4"E	Drill core from the basement at Forcellino Pass area	-	-
FC-11	46°03'35.2"N 9°54'28.4"E	Drill core from LANF fault zone	-	-
FC-12	46°03'35.2"N 9°54'28.4"E	Drill core from LANF fault zone	-	-
FC-13	46°03'35.2"N 9°54'28.4"E	Drill core from LANF fault zone	-	-
FC-14	46°03'35.2"N 9°54'28.4"E	Drill core from LANF fault zone	-	-
FC-15	46°03'35.2"N 9°54'28.4"E	Drill core from LANF fault zone	-	-
FC-16	46°03'35.2"N 9°54'28.4"E	Drill core from LANF fault zone	-	-
FC-17	46°03'35.2"N 9°54'28.4"E	Drill core from LANF fault zone	-	-
FC-18	46°03'35.2"N 9°54'28.4"E	Drill core from LANF fault zone	-	-

SAMPLES	GPS COORDINATES	NOTE	LA-ICP-MS for U-Pb dating	LA-ICP-MS in situ on tourmaline for trace elements contents
FC-19	46°03'35.2"N 9°54'28.4"E	Drill core from LANF fault zone	-	-
FC-21	46°03'35.2"N 9°54'28.4"E	Drill core from LANF fault zone	-	√
FC-22	46°03'35.2"N 9°54'28.4"E	Drill core from LANF fault zone	-	-
PG-1	46°01'56.0"N 9°35'01.9"E	Sample from Gerola Valley area: PG 1.2 C (cataclasite), T1 (tormalinite 1), T2 (tormalinite 2)	-	-
PG-2	46°01'56.0"N 9°35'01.9"E	Sample from Gerola Valley area	-	-
PG-3A	46°01'56.0"N 9°35'01.9"E	Sample from Gerola Valley area	-	√
PG-5A	46°01'37.4"N 9°35'00.6"E	Sample from Gerola Valley area	-	-
PG-6	46°01'37.4"N 9°35'00.6"E	Sample from Gerola Valley area	-	-
PG-7	46°01'37.4"N 9°35'00.6"E	Sample from Gerola Valley area - for bulk analysis:PG7-C (cataclasite) and PG7-T (tourmalinite)	-	-
PG-8	46°01'37.4"N 9°35'00.6"E	Sample from Gerola Valley area	-	-
PG-x	46°01'37.4"N 9°35'00.6"E	Sample from Gerola Valley area	-	-
PG-y	46°01'37.4"N 9°35'00.6"E	Sample from Gerola Valley area, Lake Pescegallo	-	-

SAMPLES	GPS COORDINATES	NOTE	LA-ICP-MS for U-Pb dating	LA-ICP-MS in situ on tourmaline for trace elements contents
PG-10	46°02'14.1"N 9°35'04.4"E	Sample from Gerola Valley area, Lake Pescegallo	-	-
PG-11	46°02'14.1"N 9°35'04.4"E	Sample from Gerola Valley area, Lake Pescegallo	-	-
PG-12	46°02'14.1"N 9°35'04.4"E	Sample from Gerola Valley area, Lake Pescegallo	-	-
PG-13	46°02'14.1"N 9°35'04.4"E	Sample from Gerola Valley area, Lake Pescegallo	-	-
PG-14	46°01'56.0"N 9°35'01.9"E	Sample from Gerola Valley area	-	-
PG-15	46°01'56.0"N 9°35'01.9"E	Sample from Gerola Valley area	-	-
PG-16	46°01'56.0"N 9°35'01.9"E	Sample from Gerola Valley area	-	-
PG-17	46°01'25.2"N 9°35'10.3"E	Sample from Gerola Valley area, close to Mt. Valletto	-	-
PG-18	46°01'25.2"N 9°35'10.3"E	Sample from Gerola Valley area, close to Mt. Valletto	-	-
PG-19	46°01'25.2"N 9°35'10.3"E	Sample from Gerola Valley area, close to Mt. Valletto	-	-
PG-20	46°01'24.7"N 9°35'08.4"E	Sample from Gerola Valley area, close to Mt. Valletto	-	-
VM8	45°47'45.5"N 10°14'43.7"E	Sample from Trompia Valley	√	-
VM23	45°47'45.5"N 10°14'43.7"E	Sample from Trompia Valley	-	-
880	45°47'45.5"N 10°14'43.7"E	Sample from Trompia Valley	-	√

SAMPLES	GPS COORDINATES	NOTE	LA-ICP-MS for U-Pb dating	LA-ICP-MS in situ on tourmaline for trace elements contents
VNE-1	45°48'26.3"N 10°17'18.8"E	Sample from Trompia Valley Granitoids of Val Navazze - VNE-1A VNE-1B	-	-
VNE-2	45°48'26.3"N 10°17'18.8"E	Sample from Trompia Valley Granitoids of Val Navazze	-	-
VNE-3	45°48'26.3"N 10°17'18.8"E	Sample from Trompia Valley Granitoids of Val Navazze	√	-
VNE-4	45°48'26.3"N 10°17'18.8"E	Sample from Trompia Valley Granitoids of Val Navazze	√	-
VNE-5	45°48'26.3"N 10°17'18.8"E	Sample from Trompia Valley Granitoids of Val Navazze	-	-
VNE-6	45°48'26.3"N 10°17'18.8"E	Sample from Trompia Valley Granitoids of Val Navazze	-	-
MVN-1	45°48'26.3"N 10°17'18.8"E	Sample from Trompia Valley Granitoids of Val Navazze	-	-
MVN-2	45°48'26.3"N 10°17'18.8"E	Sample from Trompia Valley Granitoids of Val Navazze	-	-
MVN-3	45°48'26.3"N 10°17'18.8"E	Sample from Trompia Valley Granitoids of Val Navazze	√	-
AV-1	46°00'04.0"N 9°51'42.8"E	Sample from Lake Aviasco	-	-
AV-2	46°00'04.0"N 9°51'42.8"E	Sample from Lake Aviasco	-	-
AV-3	46°00'04.0"N 9°51'42.8"E	Sample from Lake Aviasco	-	-
AV-4	46°00'04.0"N 9°51'42.8"E	Sample from Lake Aviasco	-	-
AV-5	46°00'04.0"N 9°51'42.8"E	Sample from Lake Aviasco	-	√
AV-6	46°00'04.0"N 9°51'42.8"E	Sample from Lake Aviasco	-	-

SAMPLES	GPS COORDINATES	NOTE	LA-ICP-MS for U-Pb dating	LA-ICP-MS in situ on tourmaline for trace elements contents
AV-7	46°00'04.0"N 9°51'42.8"E	Sample from Lake Aviasco	-	-
VSS 1	45°59'36.0"N 9°25'11.8"E	Sample from Valsassina	-	-
VSS 3	45°59'36.0"N 9°25'11.8"E	Sample from Valsassina	-	√
LDC11B	45°48'15.5"N 10°16'13.8"E	Sample from Trompia Valley	-	√
LDC1	45°48'15.5"N 10°16'13.8"E	Sample from Trompia Valley	-	√
BV	45°47'45.5"N 10°14'43.7"E	Sample from Trompia Valley	-	-
VV1	46°04'17.0"N 9°55'34.5"E	Sample from Vedello Valley mine	-	-
X1 Z	46°02'57.7"N 9°52'29.4"E	Sample from Mt. Aga and Mt. Masoni Master thesis L. Berio	-	-
C1 Z	46°02'57.7"N 9°52'29.4"E	Sample from Mt. Aga and Mt. Masoni Master thesis L. Berio	-	-
C2 Z	46°03'04.4"N 9°52'36.7"E	Sample from Mt. Aga and Mt. Masoni Master thesis L. Berio	-	-
C3	46°03'00.8"N 9°52'34.8"E	Sample from Mt. Aga and Mt. Masoni Master thesis L. Berio	-	-
C5	46°02'42.4"N 9°50'05.5"E	Sample from Mt. Aga and Mt. Masoni Master thesis L. Berio	-	√
C5 Z	46°02'42.4"N 9°50'05.5"E	Sample from Mt. Aga and Mt. Masoni Master thesis L. Berio	-	-
C6	46°02'42.4"N 9°50'05.5"E	Sample from Mt. Aga and Mt. Masoni Master thesis L. Berio	-	-

SAMPLES	GPS COORDINATES	NOTE	LA-ICP-MS for U-Pb dating	LA-ICP-MS in situ on tourmaline for trace elements contents
C6 Z	46°02'42.4"N 9°50'05.5"E	Sample from Mt. Aga and Mt. Masoni Master thesis L. Berio	-	-
C7 Z	46°02'50.4"N 9°52'32.2"E	Sample from Mt. Aga and Mt. Masoni Master thesis L. Berio	-	-
C8 Z	46°02'50.4"N 9°52'32.2"E	Sample from Mt. Aga and Mt. Masoni Master thesis L. Berio	-	-
C9	46°02'50.4"N 9°52'32.2"E	Sample from Mt. Aga and Mt. Masoni Master thesis L. Berio	-	-
C9 Z	46°02'50.4"N 9°52'32.2"E	Sample from Mt. Aga and Mt. Masoni Master thesis L. Berio	-	-
C11 Z	46°02'37.1"N 9°52'30.5"E	Sample from Mt. Aga and Mt. Masoni Master thesis L. Berio	-	-
C12	46°02'37.1"N 9°52'30.5"E	Sample from Mt. Aga and Mt. Masoni Master thesis L. Berio	-	-
C12 Z	46°02'37.1"N 9°52'30.5"E	Sample from Mt. Aga and Mt. Masoni Master thesis L. Berio	-	-
C13	46°02'42.5"N 9°52'31.2"E	Sample from Mt. Aga and Mt. Masoni Master thesis L. Berio	-	-
C15	46°02'46.7"N 9°50'11.4"E	Sample from Mt. Aga and Mt. Masoni Master thesis L. Berio	-	-
C16	46°02'46.7"N 9°50'11.4"E	Sample from Mt. Aga and Mt. Masoni Master thesis L. Berio	-	-
C20 A	46°03'04.4"N 9°52'36.7"E	Sample from Mt. Aga and Mt. Masoni Master thesis L. Berio	-	-
C20 B	46°03'04.4"N 9°52'36.7"E	Sample from Mt. Aga and Mt. Masoni Master thesis L. Berio	-	-

SAMPLES	GPS COORDINATES	NOTE	LA-ICP-MS for U-Pb dating	LA-ICP-MS in situ on tourmaline for trace elements contents
C21	46°03'04.4"N 9°52'36.7"E	Sample from Mt. Aga and Mt. Masoni Master thesis L. Berio	-	-
C23	46°02'49.4"N 9°50'14.7"E	Sample from Mt. Aga and Mt. Masoni Master thesis L. Berio	-	-
C25	46°02'49.4"N 9°50'14.7"E	Sample from Mt. Aga and Mt. Masoni Master thesis L. Berio	-	-
C27	46°02'49.4"N 9°50'14.7"E	Sample from Mt. Aga and Mt. Masoni Master thesis L. Berio	-	-
C28	46°02'49.4"N 9°50'14.7"E	Sample from Mt. Aga and Mt. Masoni Master thesis L. Berio	-	-
RDC 3A	-	Powder of tourmalinites provided by De Capitani - from Trompia Valley	-	-
RDC 3B	-	Powder of tourmalinites provided by De Capitani - from Trompia Valley	-	-
RDC 8	-	Powder of tourmalinites provided by De Capitani - from Trompia Valley	-	-
RDC 11	-	Powder of tourmalinites provided by De Capitani - from Trompia Valley	-	-
T3A	-	Powder of tourmalinites provided by De Capitani - from Lake Diavolo	-	-

SAMPLES	GPS COORDINATES	NOTE	LA-ICP-MS for U-Pb dating	LA-ICP-MS in situ on tourmaline for trace elements contents
T7	-	Powder of tourmalinites provided by De Capitani - from Lake Diavolo	-	-
T100C	-	Powder of tourmalinites provided by De Capitani - from Lake Diavolo	-	-
T106	-	Powder of tourmalinites provided by De Capitani - from Lake Diavolo	-	-
VBZ-1	-	Sample of granitoid from Valsassina Master thesis C. Crippa	-	-
VBZ-3	-	Sample of granitoid from Valsassina Master thesis C. Crippa	-	-
VBZ-35	-	Sample of granitoid from Valsassina Master thesis C. Crippa	-	-
VBZ-42	-	Sample of granitoid from Valsassina Master thesis C. Crippa	-	-
VBZ-43	-	Sample of granitoid from Valsassina Master thesis C. Crippa	-	-

10. APPENDIX 2: WHOLE ROCK ANALYSIS

SAMPLE	FC-1	FC-2	FC-3	FC-4	FC-5	FC-6	FC-7	FC-8	FC-9	FC-10	FC-12	FC-14	FC-13/FC-16
Weight [gr]	19	20	20	25	18	25	23	20	20	18	8	6	4
Oxides wt%													
SiO_2	66.43	64.64	55.14	68.34	59.08	64.63	61.7	58.42	60.48	60.62	57.81	61.92	59.77
Al_2O_3	14.76	15.21	20.39	13.61	18.04	15.64	15.8	18.17	17.08	16.76	19.21	17.53	17.53
Fe_2O_3	5.43	6.07	8.18	5.6	7.3	6.35	7.06	7.96	7.96	8.06	6.52	6.61	6.47
MgO	2.43	2.74	3.63	2.43	3.13	2.59	3.03	3	2.85	2.92	2.72	2.33	2.6
CaO	0.99	1.22	0.61	0.9	0.84	0.72	1.28	0.76	0.63	0.6	0.29	0.24	0.31
Na_2O	3.75	3.24	3.41	2.84	4.22	3.8	3.63	4.73	3.94	3.73	1.95	3.05	1.66
K_2O	1.89	2	3.23	1.88	2.3	1.95	1.95	2.15	2.23	2.32	4.98	2.87	4.41
TiO_2	0.75	0.73	0.85	0.67	0.89	0.78	0.76	0.77	0.8	0.76	0.91	0.69	0.91
P_2O_5	0.19	0.19	0.17	0.22	0.2	0.21	0.2	0.19	0.11	0.19	0.17	0.11	0.18
MnO	0.08	0.13	0.08	0.09	0.09	0.07	0.18	0.1	0.1	0.08	0.05	0.04	0.05
Cr_2O_3	0.011	0.011	0.016	0.009	0.014	0.011	0.012	0.013	0.013	0.013	0.015	0.012	0.014
Ba [ppm]	441	489	802	428	543	403	451	363	449	405	660	467	563
Ni [ppm]	35	37	57	35	41	40	42	49	42	44	40	35	44
Sc [ppm]	12	13	19	11	16	13	15	16	16	16	19	15	18
LOI	3.1	3.6	4	3.2	3.7	3.1	4.2	3.5	3.6	3.7	5.1	4.4	5.8
Sum	99.82	99.85	99.82	99.86	99.84	99.86	99.84	99.84	99.8	99.83	99.8	99.84	99.8
Trace element [ppm]													
Be	2	2	<1	1	4	1	2	4	4	2	8	3	8
Co	15.2	13	24.3	13.8	16.3	18.8	18.7	23.4	16.4	20.4	21.8	13.6	20.2
Cs	3.8	3.6	6.3	3.1	4.9	4.3	4	6.3	7.2	6.9	14.5	5.5	12.8
Ga	16.9	18.2	26.2	16.6	21.8	18.6	20.6	22.5	22	21.9	28	22.4	27
Hf	6.4	5.7	4.4	6.2	5.4	5.7	5.2	4.7	5.5	5.7	6.7	5.6	7.2
Nb	12.2	11.3	14	10.5	14.1	12.4	12.3	11.9	14.1	12.6	15.8	15.2	18
Rb	78.4	71.8	111.4	71.8	91.5	80.4	77.5	107.3	107.7	114.7	281.5	140	245.4
Sn	3	3	4	2	3	2	3	3	4	3	5	4	5
Sr	174	154.2	181.3	146.7	162.4	151.3	153.3	158.8	125.9	121.5	53.8	95	49.6
Ta	1	0.9	1.1	0.7	1	0.9	0.9	0.8	1	0.9	1.2	1.3	1.4
Th	11.7	11.6	13.8	11.5	13.4	10.4	11.5	14.1	14.5	15.6	16.3	16	18
U	2.8	2.6	3.5	2.9	3.6	2.9	3	3.5	3.8	3.5	4.9	4.9	4.5
V	93	97	140	82	123	101	103	135	118	115	143	95	133

SAMPLE	FC-1	FC-2	FC-3	FC-4	FC-5	FC-6	FC-7	FC-8	FC-9	FC-10	FC-12	FC-14	FC-13/FC-16
W	2	4.1	2.7	1.4	1.8	1.4	1.4	1.5	2	1.8	3.2	2.8	4.1
Zr	230.1	213.9	159.4	226.5	199.9	214.7	204.5	173.4	198.6	203.5	229.2	188.6	243.4
Y	30.2	25.1	25.5	29.1	30.5	32.9	29.5	30.5	30.5	29.3	32.3	32.8	37.3
La	82.9	32.3	42.9	36.3	33	39.1	37.1	28.6	34.6	48	58.2	46.8	59.8
Ce	144.6	62.3	82.3	70.1	64.8	77.7	72.3	55.1	66.9	91.8	112.5	88.6	113.7
Pr	17.27	7.55	9.84	8.32	7.69	9.11	8.58	6.59	7.92	10.9	13.22	10.45	13.32
Nd	67	28.1	37	31.2	28.4	33.3	32.3	24.8	29.8	40	49.6	38.6	48.6
Sm	12.86	5.49	6.89	5.89	5.58	6.52	6.07	4.71	5.44	7.45	9.32	7.28	9.43
Eu	2.84	1.21	1.33	1.24	1.16	1.35	1.26	0.99	1.05	1.41	1.74	1.43	1.76
Gd	10.41	5.14	5.78	5.72	5.51	6.31	5.72	4.9	5.13	6.12	7.71	6.75	8.35
Tb	1.26	0.8	0.91	0.86	0.89	0.96	0.89	0.81	0.81	0.91	1.07	1.05	1.2
Dy	5.97	4.51	5	4.97	5.13	5.79	5.3	5.4	5.13	5.28	5.93	6.19	6.73
Ho	1.05	0.89	0.95	1.03	1.06	1.18	1.06	1.09	1.11	1.11	1.17	1.15	1.35
Er	2.8	2.61	2.81	3.05	3.27	3.4	3.02	3.52	3.25	3.15	3.54	3.56	4.04
Tm	0.39	0.37	0.42	0.45	0.45	0.48	0.45	0.47	0.46	0.45	0.51	0.52	0.58
Yb	2.51	2.51	2.67	2.85	2.9	3.16	3.01	3.06	2.99	3.02	3.52	3.49	4
Lu	0.38	0.39	0.41	0.43	0.44	0.48	0.45	0.47	0.46	0.43	0.56	0.53	0.61
Mo	0.7	0.1	0.1	0.4	0.4	0.4	0.8	0.5	0.4	0.7	6.3	15.5	2.7
Cu	105.6	68.3	64.1	50.8	39	30.1	58.3	58.1	73	36.8	127.7	155.8	84
Pb	26.1	18.6	8.8	7.3	6.6	5.3	15.4	12.8	9.9	9.6	26.8	19.2	17.6
Zn	57	71	84	88	78	62	78	102	403	188	71	82	97
Ni	31.2	33.2	53.6	29.2	43.6	37.7	44.4	47.8	40.7	42.3	33.4	29.5	40.5
As	13.6	15.9	34	20.6	29.6	32.9	33.4	52.8	35.5	40.7	95	106.9	73.7
Cd	<0.1	<0.1	<0.1	<0.1	<0.1	<0.1	<0.1	<0.1	0.7	0.1	<0.1	<0.1	<0.1
Sb	0.4	0.4	0.6	0.3	0.4	0.5	0.5	0.6	0.5	0.6	1	1.4	1.1
Bi	4.6	0.7	0.3	0.2	0.3	0.3	0.3	0.3	0.2	0.2	0.3	1	0.4
Ag	0.2	0.1	0.2	<0.1	0.1	<0.1	0.1	0.1	0.1	<0.1	0.1	0.2	<0.1
Au [ppb]	5.7	2.8	3.7	2.4	3.4	3	<0.5	2.9	<0.5	1	0.8	0.8	<0.5
Hg	0.02	0.03	0.03	0.08	0.02	0.03	0.04	0.07	0.97	0.29	0.08	0.13	0.06
Tl	0.1	<0.1	0.2	<0.1	<0.1	<0.1	0.1	0.1	<0.1	<0.1	0.4	0.2	0.5
Se	<0.5	0.6	<0.5	<0.5	<0.5	<0.5	<0.5	<0.5	<0.5	<0.5	<0.5	<0.5	<0.5

SAMPLE	PG7-C	PG7-T	PG8	FC-9	FC-22	PG1.2-C	PG1.2-T1	PG1.2-T2	PG 3A	AV-7	VSS-3	AV-1
Weight [gr]	20	20	20	20	19	27	26	22	23	20	25	25
Oxides wt%												
SiO_2	72.83	62.37	65.3	60.48	59.76	73.18	69.90	70.46	63.97	81.57	70.15	66.50
Al_2O_3	14.8	20.94	19.04	17.08	19.06	14.64	16.74	16.71	19.72	10.67	15.70	20.22
Fe_2O_3	4.45	7.99	7.13	7.96	6.87	2.46	3.72	3.86	5.90	0.56	6.32	1.24
MgO	1.87	3.34	3.1	2.85	2.43	0.68	1.05	1.45	2.51	0.40	2.58	0.64
CaO	0.26	0.24	0.34	0.63	0.19	0.30	0.22	0.14	0.24	<0.01	0.27	0.07
Na_2O	1.79	1.51	1.74	3.94	2.52	1.86	2.19	1.56	1.57	0.04	0.86	0.04
K_2O	0.75	0.08	0.11	2.23	3.88	3.86	2.76	2.69	1.91	3.69	0.33	7.25
TiO_2	0.31	0.25	0.26	0.8	0.80	0.30	0.41	0.47	0.69	0.27	0.48	0.18
P_2O_5	0.08	0.04	0.06	0.11	0.14	0.09	0.15	0.10	0.10	0.09	0.07	0.03
MnO	0.01	<0.01	0.01	0.1	0.04	0.05	0.06	0.03	0.02	<0.01	0.08	<0.01
Cr_2O_3	0.009	0.002	0.004	0.013	0.013	0.002	0.008	0.007	0.009	0.003	0.010	<0.002
Ba [ppm]	510	126	112	449	560	252	283	231	283	403	4107	949
Ni [ppm]	51	32	27	42	58	<20	26	21	46	<20	53	<20
Sc [ppm]	13	15	13	16	17	9	15	16	17	6	16	15
LOI	2.6	3.1	2.7	3.6	4.1	2.4	2.6	2.3	3.2	2.2	2.4	3.6
Sum	99.82	99.87	99.85	99.8	99.83	99.90	99.87	99.85	99.84	99.51	99.72	99.85
Trace element [ppm]												
Be	13	28	19	4	4	4	6	8	21	4	4	4
Co	26.2	8.5	7.2	16.4	38.3	7.5	19.1	12.3	30.7	<0.2	12.9	0.4
Cs	2.4	2.3	1.8	7.2	7.5	9.0	6.2	6.2	7.2	6.5	0.5	26.8
Ga	24.8	32	31.2	22	22.4	16.3	23.0	22.2	26.5	14.0	26.8	40.1
Hf	6.5	4.6	4.9	5.5	5.5	4.3	5.0	5.6	6.1	3.0	3.2	11.9
Nb	15	9.8	11.6	14.1	15.6	11.1	14.9	15.4	16.1	15.2	5.3	22.2
Rb	30.4	3.3	5.3	107.7	186.2	156.3	108.1	103.6	75.9	138.8	13.6	286.2
Sn	6	7	7	4	4	5	9	8	8	4	11	13
Sr	76.4	195	144.9	125.9	76.5	17.8	44.6	58.6	128.3	8.8	166.5	5.8
Ta	1.5	1	1	1	1.2	1.1	1.2	1.3	1.2	0.6	0.6	1.6
Th	19.1	16.2	13.9	14.5	16.7	15.9	17.4	19.9	18.6	11.0	7.4	26.2
U	7.9	5.2	4.6	3.8	3.2	6.6	7.5	6.7	8.7	6.7	3.1	9.8
V	35	38	41	118	112	39	60	72	116	28	107	<8

SAMPLE	PG7-C	PG7-T	PG8	FC-9	FC-22	PG1.2-C	PG1.2-T1	PG1.2-T2	PG 3A	AV-7	VSS-3	AV-1
W	3.7	3	2.4	2	3.5	3.6	6.7	5.1	6.7	9.2	4.5	4.6
Zr	180.1	143.7	153.6	198.6	190.1	140.6	164.7	179.6	206.0	90.1	116.7	328.7
Y	31	30.4	33.6	30.5	42.9	37.1	39.3	37.5	44.5	19.4	22.1	50.7
La	20.8	10.3	13.8	34.6	61.7	35.2	44.7	68.1	43.5	39.2	30.3	58.8
Ce	40.3	22.3	28.4	66.9	120.8	71.0	91.3	134.9	90.0	75.9	57.7	113.4
Pr	4.65	2.91	3.55	7.92	14.22	8.60	11.10	15.86	10.88	9.14	6.45	13.35
Nd	16.8	12.1	13.8	29.8	52.7	33.5	42.9	58.2	42.2	35.5	23.5	48.3
Sm	4	4.28	3.72	5.44	10.07	6.74	8.95	11.26	9.10	7.44	4.10	10.39
Eu	0.74	1.01	0.82	1.05	1.92	1.10	1.41	1.62	1.62	0.94	0.77	1.27
Gd	5.19	5.56	5.11	5.13	9.16	6.45	8.42	9.22	8.28	5.44	4.35	10.31
Tb	0.92	0.91	0.88	0.81	1.33	1.04	1.31	1.29	1.30	0.70	0.67	1.60
Dy	5.36	5.4	5.42	5.13	7.50	6.42	7.32	7.18	7.64	3.71	3.79	9.14
Ho	1.21	1.16	1.29	1.11	1.49	1.30	1.41	1.34	1.53	0.73	0.77	1.83
Er	3.66	3.7	4.1	3.25	4.32	3.70	3.93	3.97	4.56	1.99	2.51	5.52
Tm	0.58	0.59	0.61	0.46	0.62	0.55	0.58	0.56	0.63	0.30	0.39	0.88
Yb	3.81	3.54	3.95	2.99	3.82	3.41	3.70	3.75	4.04	2.00	2.99	5.79
Lu	0.56	0.57	0.58	0.46	0.58	0.51	0.55	0.58	0.61	0.28	0.51	0.92
Mo	168.9	3	24.5	0.4	1.6	1.9	5.4	1.1	0.5	14.9	6.4	0.8
Cu	312.8	15.8	165.9	73	169.1	27.4	37.1	64.5	17.3	9.2	33.4	21.4
Pb	23.5	1.7	4.3	9.9	20.8	15.9	32.9	32.9	23.7	3757.8	1247.9	27.6
Zn	4	5	8	403	54	5	10	6	5	187	20	18
Ni	16.6	4.7	6	40.7	55.6	9.2	19.5	8.4	18.5	0.6	13.9	1.3
As	58.2	16	16.6	35.5	89.4	37.8	105.4	75.6	82.6	121.3	27.8	42.7
Cd	0.2	<0.1	<0.1	0.7	<0.1	<0.1	<0.1	<0.1	<0.1	0.3	<0.1	<0.1
Sb	3.6	1.6	1.9	0.5	1.7	1.0	1.6	0.9	1.6	15.5	3.2	25.8
Bi	9.8	0.4	1.7	0.2	1.3	1.3	3.0	2.5	3.7	0.6	0.4	0.4
Ag	0.6	<0.1	0.1	0.1	0.3	0.2	0.7	0.4	0.4	1.6	35.9	0.4
Au [ppb]	4.4	0.6	0.6	<0.5	2.2	4.4	3.6	1.5	1.5	<0.5	2.2	<0.5
Hg	0.13	0.02	0.04	0.97	0.19	0.04	0.23	0.14	0.13			
Tl	0.2	<0.1	<0.1	<0.1	0.3	0.1	0.2	<0.1	<0.1			
Se	<0.5	<0.5	<0.5	<0.5	<0.5	<0.5	<0.5	<0.5	<0.5			

SAMPLE	AV-2	AV-6	RDC 3A	RDC 3B	RDC 8	RDC 11	T3A	T7	T100C	T106	VNE-1	VNE-2	VNE-3
Weight [gr]	24	28	23	23	22	22	20	22	23	22.00	20	26	24
Oxides wt%													
SiO_2	54.15	80.25	63.83	53.84	62.87	65.03	52.43	56.78	63.30	73.19	67.09	68.33	61.24
Al_2O_3	28.58	11.66	18.67	26.50	20.13	19.38	25.77	24.11	20.41	11.03	15.53	14.88	18.88
Fe_2O_3	1.31	0.69	9.18	6.28	8.71	5.88	8.09	6.67	6.00	8.26	2.28	3.83	3.96
MgO	0.67	0.45	3.32	6.70	3.75	2.56	3.05	4.08	2.48	1.18	1.03	0.92	2.27
CaO	<0.01	<0.01	0.36	0.86	0.43	0.39	0.11	0.20	0.10	0.02	2.74	1.75	2.84
Na_2O	0.07	0.03	1.39	1.68	1.51	4.09	1.32	1.53	1.17	0.44	6.58	2.87	4.84
K_2O	10.30	3.99	0.20	0.22	0.05	0.21	3.96	1.93	2.52	1.72	1.11	5.48	3.12
TiO_2	0.21	0.27	0.63	0.96	0.75	0.76	0.97	0.90	0.73	0.38	0.47	0.40	0.33
P_2O_5	0.03	0.07	0.08	0.08	0.04	0.11	0.12	0.13	0.07	0.09	0.16	0.14	0.16
MnO	<0.01	<0.01	0.05	<0.01	0.01	0.01	0.02	0.01	0.01	0.08	0.06	0.05	0.07
Cr_2O_3	<0.002	<0.002	0.010	0.015	0.011	0.010	0.014	0.013	0.011	0.006	0.010	0.002	0.003
Ba [ppm]	1428	424	15	12	5	18	201	179	149	102	115	716	388
Ni [ppm]	<20	<20	59	121	61	49	47	89	61	<20	<20	<20	<20
Sc [ppm]	21	6	19	36	17	15	23	20	17	13	13	11	12
LOI	4.4	2.2	2.1	2.7	1.6	1.4	3.9	3.4	3.0	3.4	2.8	1.2	2.1
Sum	99.86	99.65	99.86	99.86	99.88	99.85	99.79	99.81	99.84	99.84	99.87	99.87	99.89
Trace element [ppm]													
Be	8	5	7	7	2	3	20	15	21	3	2	5	2
Co	0.4	<0.2	12.5	14.0	13.8	24.2	11.8	27.3	32.6	13.5	2.4	6.0	6.0
Cs	30.3	6.6	0.6	0.3	<0.1	0.2	9.0	8.5	11.5	5.9	1.2	2.9	8.2
Ga	114.1	15.4	33.9	70.8	42.0	31.2	31.5	26.6	25.8	15.7	17.2	15.8	16.3
Hf	12.2	3.7	3.4	6.0	4.3	5.1	9.8	7.3	6.6	4.4	5.7	5.4	2.6
Nb	27.6	13.9	7.9	13.3	11.6	12.7	23.2	20.2	19.6	12.7	11.2	10.5	3.6
Rb	378.3	153.1	6.8	9.7	1.6	5.1	200.4	96.4	131.0	80.2	56.8	159.1	167.3
Sn	19	4	56	25	65	42	9	4	6	4	7	1	2
Sr	4.0	6.8	142.8	194.3	164.5	108.7	192.7	306.2	138.4	64.7	125.7	191.0	219.1
Ta	1.9	0.8	0.8	1.0	1.0	1.1	1.8	1.4	1.6	0.9	0.9	1.1	0.3
Th	31.0	11.3	10.8	17.0	14.1	18.5	27.4	20.3	18.9	12.5	16.4	12.7	5.5
U	13.3	6.7	1.3	3.2	1.4	2.7	20.7	11.4	6.7	5.9	4.2	4.3	1.2
V	21	28	116	163	125	90	139	138	97	50	33	43	69

SAMPLE	AV-2	AV-6	RDC 3A	RDC 3B	RDC 8	RDC 11	T3A	T7	T100C	T106	VNE-1	VNE-2	VNE-3
W	16.4	8.3	5.3	5.7	7.2	3.9	17.6	22.6	10.4	5.3	59.2	0.9	0.9
Zr	292.8	113.5	123.4	215.4	155.7	195.8	323.5	256.6	232.8	150.0	202.6	192.0	91.1
Y	49.8	19.1	27.7	33.1	26.6	48.4	40.4	37.7	39.5	25.1	39.3	32.3	19.2
La	20.2	41.7	65.7	7.3	2.5	41.5	59.7	42.8	32.2	33.1	40.7	31.0	18.9
Ce	40.3	80.7	135.1	15.4	4.8	95.1	126.8	61.3	68.5	63.5	80.0	60.5	36.7
Pr	4.91	9.53	15.42	1.91	0.55	11.92	14.65	6.30	7.84	7.42	9.91	7.42	4.65
Nd	18.1	34.7	57.8	7.3	2.2	47.2	54.2	23.2	29.8	27.8	36.5	27.9	17.3
Sm	3.73	7.08	9.35	1.96	0.57	8.87	9.24	4.69	6.57	5.12	7.58	6.00	3.76
Eu	0.46	0.81	1.76	0.67	0.24	2.65	1.88	1.14	1.12	0.82	1.19	1.15	1.10
Gd	4.88	4.16	5.03	3.05	0.91	8.31	7.46	6.16	6.76	4.73	7.22	5.84	3.75
Tb	1.10	0.59	0.54	0.61	0.25	1.27	1.10	1.00	1.15	0.75	1.14	0.92	0.56
Dy	7.79	3.48	3.41	4.46	2.63	7.66	6.96	6.22	7.02	4.50	6.84	5.57	3.31
Ho	1.86	0.69	0.95	1.14	0.89	1.64	1.43	1.29	1.48	0.96	1.40	1.20	0.67
Er	5.81	2.19	3.78	3.66	3.55	4.88	4.53	3.92	4.40	2.74	4.09	3.49	1.96
Tm	0.87	0.32	0.63	0.65	0.62	0.71	0.67	0.60	0.69	0.41	0.58	0.51	0.29
Yb	5.80	2.11	4.17	5.19	4.29	4.54	4.71	4.08	4.47	2.67	3.85	3.25	1.77
Lu	0.90	0.33	0.62	0.99	0.68	0.72	0.72	0.63	0.66	0.40	0.58	0.51	0.27
Mo	1.4	22.8	0.4	<0.1	<0.1	<0.1	4.7	0.5	0.6	47.4	0.3	0.4	0.3
Cu	25.0	12.8	2.9	0.6	15.7	38.4	64.6	3.2	1.9	355.0	0.7	1.0	0.6
Pb	35.6	1488.4	1.3	5.1	1.2	0.7	10.4	5.5	6.7	28.4	3.3	14.1	6.3
Zn	22	601	2	3	1	<1	4	4	3	9	21	37	27
Ni	0.6	0.5	1.9	2.2	1.3	5.1	5.3	9.7	4.5	13.1	1.9	2.2	3.2
As	80.8	152.5	2.9	2.1	5.0	0.7	23.4	36.3	10.8	1252.0	38.7	0.8	0.6
Cd	0.2	1.8	<0.1	<0.1	<0.1	<0.1	<0.1	<0.1	<0.1	<0.1	0.2	<0.1	<0.1
Sb	38.7	27.8	<0.1	0.2	0.1	<0.1	2.6	0.7	1.0	6.4	<0.1	<0.1	<0.1
Bi	0.4	0.6	0.3	0.1	2.4	0.3	1.2	1.5	1.2	8.6	0.3	<0.1	0.1
Ag	1.9	2.8	<0.1	<0.1	0.1	<0.1	0.1	<0.1	<0.1	0.8	<0.1	<0.1	<0.1
Au [ppb]	<0.5	<0.5	0.8	2.4	9.6	7.7	20.5	7.6	15.1	5.1	1.5	0.5	<0.5
Hg			0.01	<0.01	<0.01	0.02	0.05	0.02	0.03	0.07	<0.01	0.02	<0.01
Tl			<0.1	<0.1	<0.1	<0.1	<0.1	<0.1	<0.1	<0.1	<0.1	0.2	0.2
Se			<0.5	<0.5	<0.5	<0.5	<0.5	<0.5	<0.5	<0.5	<0.5	<0.5	<0.5

SAMPLE	VNE-4	VNE-5	VNE-6	MVN-1	MVN-2	MVN-3
Weight [gr]	20	25	24	26	25	23
Oxides wt%						
SiO_2	69.63	68.06	63.79	61.16	60.81	69.24
Al_2O_3	16.07	15.31	16.03	16.01	15.86	16.47
Fe_2O_3	1.66	3.50	5.25	7.42	7.12	1.68
MgO	0.36	1.09	2.01	1.42	2.16	0.39
CaO	1.65	1.63	2.43	3.62	3.19	1.76
Na_2O	3.81	3.11	3.99	3.06	3.00	3.52
K_2O	5.11	5.04	3.62	4.16	4.21	5.39
TiO_2	0.16	0.44	0.71	0.65	0.92	0.16
P_2O_5	0.09	0.16	0.21	0.22	0.22	0.07
MnO	0.03	0.04	0.07	0.13	0.15	0.03
Cr_2O_3	<0.002	<0.002	<0.002	<0.002	<0.002	<0.002
Ba [ppm]	557	689	580	527	584	602
Ni [ppm]	<20	<20	<20	<20	<20	<20
Sc [ppm]	5	11	15	19	23	5
LOI	1.3	1.4	1.7	1.9	2.1	1.1
Sum	99.90	99.86	99.86	99.87	99.84	99.90
Trace element [ppm]						
Be	3	2	4	5	3	3
Co	2.5	5.9	8.7	10.2	12.2	2.3
Cs	3.1	3.3	5.7	6.8	6.0	2.1
Ga	15.0	16.3	17.4	17.7	18.2	15.5
Hf	2.8	5.7	5.5	5.5	4.9	2.9
Nb	4.9	10.6	10.5	10.0	9.8	4.9
Rb	185.3	155.0	164.2	159.6	179.7	165.4
Sn	<1	<1	2	1	1	<1
Sr	162.0	183.4	198.4	159.9	206.8	202.7
Ta	0.5	1.0	1.0	0.7	0.8	0.5
Th	10.0	13.9	13.8	10.7	11.2	8.4
U	2.9	3.7	4.3	2.4	3.0	2.5
V	19	38	88	70	149	16

SAMPLE	VNE-4	VNE-5	VNE-6	MVN-1	MVN-2	MVN-3
W	8.9	0.7	1.0	0.8	2.4	3.6
Zr	96.6	209.5	196.3	195.8	166.8	103.7
Y	23.3	27.1	43.8	36.4	47.6	17.8
La	27.8	39.5	36.5	33.7	36.6	22.2
Ce	54.7	77.2	72.2	68.5	75.1	43.8
Pr	6.33	9.11	8.81	8.52	9.44	5.08
Nd	24.0	34.0	34.8	33.7	37.6	19.3
Sm	4.66	6.47	7.33	6.92	7.92	3.93
Eu	1.05	1.22	1.28	1.41	1.56	1.21
Gd	4.30	5.64	7.23	6.80	8.15	3.61
Tb	0.68	0.85	1.22	1.07	1.33	0.54
Dy	4.04	5.04	7.46	6.55	8.10	3.10
Ho	0.83	0.96	1.54	1.34	1.65	0.64
Er	2.36	2.80	4.59	4.01	5.00	1.81
Tm	0.35	0.39	0.69	0.57	0.72	0.25
Yb	2.28	2.63	4.31	3.88	4.46	1.75
Lu	0.34	0.40	0.67	0.59	0.65	0.26
Mo	0.2	1.1	0.7	0.4	0.3	0.1
Cu	2.3	2.1	1.4	4.0	5.0	1.4
Pb	15.8	20.3	19.6	4.0	18.2	14.9
Zn	24	40	56	82	101	25
Ni	0.9	2.2	4.7	0.5	0.8	1.0
As	4.9	0.8	1.5	1.0	2.2	2.4
Cd	<0.1	<0.1	<0.1	0.3	0.2	<0.1
Sb	<0.1	<0.1	<0.1	0.2	0.3	0.1
Bi	<0.1	0.2	<0.1	<0.1	<0.1	<0.1
Ag	<0.1	<0.1	<0.1	<0.1	<0.1	<0.1
Au [ppb]	<0.5	<0.5	<0.5	<0.5	<0.5	<0.5
Hg	<0.01	0.02	0.02	<0.01	0.02	<0.01
Tl	<0.1	0.2	0.4	0.3	0.3	<0.1
Se	<0.5	<0.5	<0.5	<0.5	<0.5	<0.5

SAMPLE FC18					
Weight [gr]	2				
Trace element [ppm]					
Mo	2.19	W	<0.1	Ho	0.31
Cu	121.84	Cs	8.75	Er	0.78
Pb	10.7	Sc	8.7	Tm	0.13
Zn	73.6	Tl	0.51	Yb	0.84
Ag [ppb]	154	S [%]	0.07	Lu [ppm]	0.09
Ni	36.8	Hg [ppb]	43	Pd [ppb]	<10
Co	16.1	Se	<0.1	Pt [ppb]	<2
Mn	381	Te	0.04		
Fe [%]	3.73	Ga	14.7		
As	41.5	Ge	0.2		
U	3.1	Hf	<0.02		
Au [ppb]	3.7	Nb	0.1		
Th	14.9	Rb	111.4		
Sr	26.2	Sn	2		
Cd	0.02	Ta	<0.05		
Sb	1.13	Zr	0.8		
Bi	0.46	Y	8.26		
V	49	Ce	77.7		
Ca [%]	0.2	In	0.04		
P [%]	0.043	Re [ppb]	<1		
La	42.3	Be	3.8		
Cr	47	Li	48.9		
Mg [%]	1.02	Pr	9.44		
Ba	346.4	Nd	30.04		
Ti	0.014	Sm	6.07		
B	125	Eu	1.04		
Al [%]	5.1	Gd	4.09		
Na [%]	0.146	Tb	0.55		
K [%]	2.04	Dy	2.13		

SAMPLE (De Capitani et al. 1999)	VT1	VT2	VT3	VN1	VN2	VN3	VN4F	VN4C	VN11	VNE2	VNE3	VNE4	VNE5	VNE6	ZVN1	ZVN2	ZVN3	ZVN4	ZVN5	ZVN6	VR4	VR5	VR6
Oxides wt%																							
SiO_2	66.92	69.34	69.56	63.92	62.38	68.66	66.9	67.95	63.72	68.4	63.43	69.41	68.12	64.46	68.97	69.97	62.56	67.53	62.88	62.73	60.15	59.51	65.11
Al_2O_3	16.8	14.66	14.48	14.06	15.4	14.88	13.81	14.91	13.71	14.23	12.55	13.7	14.65	14.45	14.61	14.02	15.98	14.68	15.04	13.76	16.01	14.73	15.47
Fe_2O_3	0.67	0.64	0.69	2.26	1.07	0.82	1.07	0	2.28	0.84	1.23	0.7	0.82	0.81	0.84	0.85	1.58	0.87	1.52	2.17	0.78	2.38	1.3
MgO	0.63	0.64	0.7	1.99	2	0.78	1.25	0.91	2.2	0.85	2.83	0.63	0.89	1.87	0.81	0.67	2.22	0.88	1.64	2.48	4.24	4.43	2.98
CaO	1.35	1.82	1.82	3.21	3.39	2	2.01	2.2	3.22	2.04	2.64	1.79	1.79	2.58	1.79	0.98	2.32	2.33	3.69	3.58	5.13	6.22	4.82
Na_2O	2.35	2.92	3.31	2.76	3.6	3.04	2.78	3.04	2.62	3.17	3.93	3.15	3.17	3.69	2.82	3.13	3.49	2.58	3.29	2.49	3.57	3.23	3
K_2O	5.86	5.14	4.68	3.86	3.57	5.23	5.27	5.19	3.87	5.19	3.02	5.3	5.06	3.75	5.49	5.52	3.68	5.55	4.19	4.23	1.58	1.17	1.36
TiO_2	0.36	0.37	0.43	0.8	0.9	0.41	0.52	0.46	0.87	0.43	0.91	0.4	0.49	0.81	0.42	0.4	0.8	0.43	0.72	0.85	0.68	0.82	0.62
P_2O_5	0.14	0.13	0.16	0.25	0.24	0.16	0.13	0.18	0.25	0.18	0.2	0.17	0.19	0.27	0.15	0.16	0.23	0.16	0.24	0.26	0.24	0.22	0.21
MnO	0.05	0.05	0.04	0.09	0.14	0.05	0.06	0.05	0.09	0.05	0.09	0.06	0.05	0.08	0.06	0.04	0.11	0.08	0.12	0.08	0.09	0.1	0.05
FeO(tot)	2.27	2.47	2.69	3.93	4.96	2.65	3.65	2.82	4.17	2.66	4.98	2.71	2.79	4.22	2.65	2.41	4.65	2.91	4.31	4.19	1.96	4.15	2.84
H2O+	2.3	1.99	1.94	2.27	2.27	1.94	1.88	1.55	2.25	1.65	2.8	1.56	1.7	1.92	1.67	1.49	2.25	2.91	2.77	2.5	6.84	3.46	2.57
Total	99.7	100.17	100.5	99.4	99.92	100.62	99.33	99.26	99.25	99.69	99.61	99.58	99.72	99.01	100.28	99.64	99.87	100.91	100.41	99.32	101.27	100.42	100.33
[ppm]																							
Cr	5	3	4	7	7	8	14	7	6	5	17	5	6	13	5	5	7	5	5	6	15	25	14
Ba	606	626	637	532	475	785	584	609	527	697	377	494	627	546	552	663	478	605	420	575	170	313	266
Ni	5	4	5	8	6	5	8	5	7	5	11	6	6	8	6	6	9	6	7	7	2	9	6
Sc	5	6	8	13	12	7	7	7	14	7	13	7	7	11	6	5	14	7	12	16	10	20	10
Co	0	8	9	19	17	10	13	8	18	10	21	7	9	13	9	9	21	9	15	20	0	11	12
Nb	10	12	11	10	11	9	9	11	1	10	10	9	10	11	10	9	11	10	14	10	10	10	7
Rb	205	181	167	154	157	148	197	172	154	159	172	191	160	179	154	168	159	178	174	168	59	56	59
Sr	92	92	114	173	225	141	176	201	173	188	170	116	189	196	114	155	163	158	166	176	446	403	453
Y	21	21	22	22	23	22	21	22	23	22	23	22	22	23	22	22	22	22	22	23	19	22	22
Th	10	11	9	5	9	11	9	7	7	10	7	12	6	7	10	9	5	13	8	3	4	11	5
Pb	22	19	19	8	11	10	14	16	7	20	1	22	11	6	23	21	19	32	13	3	3	32	0
V	28	22	27	57	75	32	59	35	64	39	108	31	44	90	31	34	62	39	59	72	134	156	97
Zr	161	203	198	174	181	165	189	173	160	171	148	140	182	169	157	177	217	159	245	195	171	154	174
Zn	646	20	28	69	94	32	52	48	68	38	58	49	45	69	36	49	66	54	85	55	362	303	71

SAMPLE (Crippa. master thesis 2017)	VBZ-42	VBZ-43	VBZ-35	VBZ-1	VBZ-3
Oxides wt%					
SiO_2	68.51	73.49	74.96	73.33	73.06
Al_2O_3	15.61	14.08	13.02	14.7	14.87
Fe_2O_3	2.77	1.76	1.41	1.34	1.49
MgO	0.46	0.35	0.44	0.47	0.47
CaO	1.68	0.09	0.65	1.38	1.9
Na_2O	3.66	2.41	2.29	3.02	3.2
K_2O	4.86	5.5	5.25	4.22	4.02
TiO_2	0.341	0.234	0.214	0.192	0.229
P_2O_5	0.07	0.04	0.22	0.06	0.05
MnO	0.052	0.066	0.031	0.033	0.029
Cr [ppm]	< 20	< 20	< 20	< 20	< 20
Total	98.01	98.02	98.49	98.74	99.32
[ppm]					
Be	3	3	2	3	4
Sc	15	6	5	4	4
V	21	16	21	12	15
Co	3	3	4	2	2
Ni	< 20	< 20	< 20	< 20	< 20
Cu	< 10	< 10	< 10	< 10	< 10
Zn	60	< 30	40	40	40
Ga	23	17	12	17	18
As	< 5	6	< 5	< 5	< 5
Rb	107	168	126	185	161
Sr	149	45	211	150	229
Y	33	24	12	13	11
Zr	346	170	76	97	105
Nb	14	10	6	6	6
Mo	< 2	< 2	< 2	< 2	< 2
Cs	3.3	10.1	3.8	6	4.7
Ba	1701	499	873	469	574

	VBZ-42	VBZ-43	VBZ-35	VBZ-1	VBZ-3
[ppm]					
La	83.3	32.8	12.3	34.9	35.3
Ce	163	66.3	23.7	66.2	67.9
Pr	17.6	7.21	2.66	7.01	7.36
Nd	65.6	26.6	10.1	25.7	26
Sm	11.7	5.5	2.1	4.9	4.8
Eu	2.26	0.76	1.28	0.83	0.99
Gd	8.9	4.6	1.9	3.5	3.4
Tb	1.3	0.8	0.4	0.5	0.5
Dy	7	4.6	2.2	2.4	2.3
Ho	1.3	0.9	0.4	0.4	0.4
Er	3.5	2.5	1.3	1.2	1
Tm	0.45	0.38	0.21	0.17	0.15
Yb	3	2.7	1.5	1.1	0.9
Lu	0.47	0.39	0.24	0.16	0.14
Hf	7.6	4.1	1.6	2.4	2.4
Ta	0.7	1.2	1.2	0.8	0.6
W	< 1	3	1	2	< 1
Tl	0.5	0.9	0.6	0.7	0.8
Pb	16	21	47	25	26
Sb	< 0.5	2	< 0.5	< 0.5	< 0.5
Th	14.5	19.7	3.6	15.6	14.5
U	1.6	4.9	1.4	3.1	2.8

11. APPENDIX 3: EMPA DATASET

SAMPLE	**PG19A**										
Spot analysis	PG19A-C1-1	PG19A-C1-2	PG19A-C1-3-1	PG19A-C1-3-2	PG19A-C1-3-3	PG19A-C1-4-1	PG19A-C1-4-2	PG19A-C1-5	PG19A-C2-1	PG19A-C2-2-1	PG19A-C2-2-2
Oxides wt%											
SiO_2	38.27	37.42	36.99	39.05	37.13	38.17	37.66	36.17	34.96	37.00	36.98
TiO_2	0.23	0.19	0.22	0.17	0.20	0.23	0.23	0.16	0.29	0.13	0.17
Al_2O_3	32.36	32.20	32.38	31.88	32.81	32.09	32.43	32.54	30.48	33.34	32.72
Cr_2O_3	0.03	0.05	0.03	0.00	0.00	0.00	0.00	0.01	0.06	0.06	0.02
FeO	10.79	11.18	10.69	9.72	10.52	10.37	10.45	11.80	11.40	9.98	10.21
MgO	4.01	3.94	4.38	4.26	4.24	4.64	4.69	3.44	3.61	4.37	4.60
CaO	0.16	0.22	0.20	0.13	0.14	0.19	0.17	0.26	0.21	0.18	0.15
MnO	0.00	0.00	0.00	0.06	0.03	0.05	0.00	0.01	0.00	0.01	0.03
Na_2O	2.05	1.97	2.21	1.93	2.13	2.06	2.20	1.92	1.95	1.92	1.93
K_2O	0.03	0.10	0.01	0.70	0.03	0.30	0.21	0.00	0.23	0.02	0.02
F	0.00	0.06	0.00	0.09	0.00	0.08	0.00	0.00	0.00	0.00	0.01
Cl	0.00	0.00	0.02	0.01	0.06	0.00	0.00	0.00	0.02	0.03	0.02
H_2O*	3.70	3.63	3.65	3.67	3.65	3.67	3.70	3.60	3.46	3.67	3.65
B_2O_3*	10.73	10.61	10.60	10.76	10.64	10.74	10.72	10.45	10.04	10.65	10.61
Li_2O*	0.00	0.00	0.00	0.00	0.00	0.00	0.00	0.00	0.00	0.00	0.00
Total	102.37	101.58	101.38	102.43	101.58	102.60	102.46	100.37	96.71	101.36	101.13
O=F	0.00	0.03	0.00	0.04	0.00	0.03	0.00	0.00	0.00	0.00	0.00
Total*	102.37	101.55	101.38	102.39	101.58	102.56	102.46	100.37	96.71	101.36	101.12
Cation apfu											
Si	6.20	6.13	6.07	6.31	6.07	6.17	6.10	6.02	6.05	6.04	6.06
Ti	0.03	0.02	0.03	0.02	0.02	0.03	0.03	0.02	0.04	0.02	0.02
Cr	0.00	0.01	0.00	0.00	0.00	0.00	0.00	0.00	0.01	0.01	0.00
Al	6.18	6.22	6.26	6.07	6.32	6.12	6.19	6.38	6.22	6.41	6.32
Fe^{2+}	1.46	1.53	1.47	1.31	1.44	1.40	1.42	1.64	1.65	1.36	1.40
Mg	0.97	0.96	1.07	1.03	1.03	1.12	1.13	0.85	0.93	1.06	1.12
Mn	0.00	0.00	0.00	0.01	0.00	0.01	0.00	0.00	0.00	0.00	0.00
Ca	0.03	0.04	0.04	0.02	0.02	0.03	0.03	0.05	0.04	0.03	0.03
Na	0.64	0.63	0.70	0.60	0.67	0.65	0.69	0.62	0.65	0.61	0.61
K	0.01	0.02	0.00	0.14	0.01	0.06	0.04	0.00	0.05	0.00	0.01
B	3.00	3.00	3.00	3.00	3.00	3.00	3.00	3.00	3.00	3.00	3.00
F	0.00	0.03	0.00	0.04	0.00	0.04	0.00	0.00	0.00	0.00	0.00
Cl	0.00	0.00	0.01	0.00	0.02	0.00	0.00	0.00	0.01	0.01	0.00
H	4.00	3.97	3.99	3.95	3.98	3.96	4.00	4.00	3.99	3.99	3.99
CatSum	18.51	18.56	18.63	18.51	18.59	18.59	18.64	18.58	18.65	18.54	18.57

SAMPLE	**PG19A**								
Spot analysis	PG19A-C2-3-1	PG19A-C2-3-2	PG19A-C2-3-3	PG19A-C2-MARTIX-1	PG19A-C2-MARTIX-2	PG19A-C3-1	PG19A-C3-2	PG19A-C4-1-1	PG19A-C4-1-2
Oxides wt%									
SiO_2	35.83	36.19	37.49	53.98	79.45	47.45	36.70	36.13	37.18
TiO_2	0.30	0.31	0.26	0.27	0.12	0.28	0.61	1.18	0.11
Al_2O_3	31.93	31.41	31.37	25.53	9.77	26.58	32.52	31.10	32.08
Cr_2O_3	0.00	0.00	0.00	0.00	0.03	0.00	0.01	0.02	0.00
FeO	10.77	10.58	10.70	7.23	3.02	8.39	6.47	9.87	8.60
MgO	5.02	4.99	5.02	3.82	1.68	4.39	7.06	5.55	5.83
CaO	0.32	0.37	0.40	0.12	0.08	0.18	0.71	0.65	0.11
MnO	0.00	0.00	0.05	0.02	0.00	0.02	0.00	0.06	0.04
Na_2O	2.29	2.36	2.26	4.02	0.87	2.74	1.94	2.16	2.45
K_2O	0.04	0.04	0.17	0.22	0.17	0.41	0.02	0.01	0.15
F	0.00	0.00	0.00	0.00	0.00	0.00	0.10	0.07	0.00
Cl	0.03	0.01	0.00	0.00	0.01	0.00	0.02	0.00	0.02
H_2O*	3.61	3.60	3.67	4.15	4.46	3.89	3.63	3.60	3.66
B_2O_3*	10.47	10.45	10.64	12.02	12.94	11.28	10.67	10.53	10.62
Li_2O*	0.00	0.00	0.00	0.00	0.00	0.00	0.00	0.00	0.00
Total	100.61	100.32	102.03	111.37	112.61	105.61	100.45	100.93	100.85
O=F	0.00	0.00	0.00	0.00	0.00	0.00	0.04	0.03	0.00
Total*	100.61	100.32	102.03	111.37	112.61	105.61	100.41	100.90	100.85
Cation apfu									
Si	5.95	6.02	6.12	7.81	10.67	7.31	5.98	5.96	6.08
Ti	0.04	0.04	0.03	0.03	0.01	0.03	0.07	0.15	0.01
Cr	0.00	0.00	0.00	0.00	0.00	0.00	0.00	0.00	0.00
Al	6.24	6.15	6.04	4.35	1.55	4.83	6.24	6.05	6.19
Fe^{2+}	1.49	1.47	1.46	0.87	0.34	1.08	0.88	1.36	1.18
Mg	1.24	1.24	1.22	0.82	0.34	1.01	1.71	1.37	1.42
Mn	0.00	0.00	0.01	0.00	0.00	0.00	0.00	0.01	0.01
Ca	0.06	0.07	0.07	0.02	0.01	0.03	0.12	0.12	0.02
Na	0.74	0.76	0.72	1.13	0.23	0.82	0.61	0.69	0.78
K	0.01	0.01	0.04	0.04	0.03	0.08	0.01	0.00	0.03
B	3.00	3.00	3.00	3.00	3.00	3.00	3.00	3.00	3.00
F	0.00	0.00	0.00	0.00	0.00	0.00	0.05	0.04	0.00
Cl	0.01	0.00	0.00	0.00	0.00	0.00	0.00	0.00	0.01
H	3.99	4.00	4.00	4.00	4.00	4.00	3.95	3.96	3.99
CatSum	18.77	18.75	18.70	18.07	16.17	18.19	18.63	18.71	18.71

SAMPLE	**PG19A**								
Spot analysis	PG19A-C5-1-1	PG19A-C5-1-2	PG19A-C5-MATRIX-1	PG19A-C5-MATRIX-2	PG19A-C2-4-1	PG19A-C2-4-2	PG19A-C2-4-3	PG19A-C2-5-1	PG19A-C2-5-2
Oxides wt%									
SiO_2	34.46	34.41	56.59	45.48	51.54	44.20	39.39	34.40	38.06
TiO_2	0.82	0.81	0.31	0.29	0.12	0.28	0.24	0.28	0.24
Al_2O_3	30.25	31.18	21.82	27.18	23.98	28.10	30.21	33.00	31.29
Cr_2O_3	0.05	0.06	0.00	0.00	0.00	0.00	0.03	0.00	0.00
FeO	9.43	9.04	6.64	9.17	7.97	9.92	9.94	10.33	9.74
MgO	6.10	6.09	3.39	4.45	3.83	4.18	4.46	4.68	4.29
CaO	0.54	0.67	0.14	0.38	0.18	0.18	0.24	0.22	0.21
MnO	0.04	0.02	0.00	0.03	0.01	0.03	0.02	0.00	0.06
Na_2O	2.43	2.25	1.57	1.93	1.72	1.93	2.01	2.31	2.20
K_2O	0.01	0.00	0.46	0.02	0.09	0.04	0.16	0.01	0.01
F	0.13	0.18	0.00	0.00	0.00	0.00	0.00	0.06	0.00
Cl	0.02	0.00	0.00	0.03	0.00	0.00	0.02	0.01	0.00
H_2O*	3.45	3.46	4.03	3.81	3.92	3.80	3.66	3.53	3.64
B_2O_3*	10.19	10.27	11.69	11.07	11.35	11.01	10.63	10.33	10.55
Li_2O*	0.00	0.00	0.00	0.00	0.00	0.00	0.00	0.00	0.00
Total	97.93	98.45	106.64	103.83	104.70	103.67	101.01	99.16	100.29
O=F	0.05	0.08	0.00	0.00	0.00	0.00	0.00	0.03	0.00
Total*	97.87	98.37	106.64	103.83	104.70	103.67	101.01	99.13	100.29
Cation apfu									
Si	5.88	5.82	8.41	7.14	7.89	6.98	6.44	5.79	6.27
Ti	0.11	0.10	0.03	0.03	0.01	0.03	0.03	0.04	0.03
Cr	0.01	0.01	0.00	0.00	0.00	0.00	0.00	0.00	0.00
Al	6.08	6.22	3.82	5.03	4.33	5.23	5.82	6.54	6.07
Fe^{2+}	1.34	1.28	0.83	1.20	1.02	1.31	1.36	1.45	1.34
Mg	1.55	1.54	0.75	1.04	0.87	0.98	1.09	1.17	1.05
Mn	0.01	0.00	0.00	0.00	0.00	0.00	0.00	0.00	0.01
Ca	0.10	0.12	0.02	0.06	0.03	0.03	0.04	0.04	0.04
Na	0.80	0.74	0.45	0.59	0.51	0.59	0.64	0.75	0.70
K	0.00	0.00	0.09	0.00	0.02	0.01	0.03	0.00	0.00
B	3.00	3.00	3.00	3.00	3.00	3.00	3.00	3.00	3.00
F	0.07	0.10	0.00	0.00	0.00	0.00	0.00	0.03	0.00
Cl	0.01	0.00	0.00	0.01	0.00	0.00	0.01	0.00	0.00
H	3.93	3.90	4.00	3.99	4.00	4.00	3.99	3.96	4.00
CatSum	18.88	18.83	17.41	18.11	17.69	18.17	18.45	18.78	18.52

SAMPLE	**PG19A**				**PG3A**					
Spot analysis	PG19A-C2-6-1	PG19A-C2-6-2	PG19A-C3-MATRIX-1	PG19A-C3-MATRIX-2	PG3A-T5-70	PG3A-T5-71	PG3A-T5-72	PG3A-T4-73	PG3A-T4-74	PG3A-T3-75
Oxides wt%										
SiO_2	38.21	73.51	50.31	45.96	37.39	37.93	36.89	35.41	35.84	36.45
TiO_2	0.31	0.16	0.25	0.28	0.77	0.68	0.70	0.88	0.74	0.46
Al_2O_3	30.46	15.16	25.74	28.17	32.35	33.75	30.89	29.99	31.06	30.71
Cr_2O_3	0.00	0.00	0.00	0.05	0.09	0.10	0.04	0.02	0.09	0.00
FeO	10.96	5.19	7.70	8.96	7.34	6.61	8.88	10.44	8.19	11.26
MgO	5.08	2.61	4.01	4.61	6.92	7.10	6.43	5.27	5.90	5.06
CaO	0.25	0.15	0.11	0.15	0.18	0.27	0.14	0.33	0.42	0.57
MnO	0.03	0.00	0.00	0.00	0.01	0.01	0.00	0.03	0.00	0.00
Na_2O	2.61	1.23	2.15	1.96	2.65	2.51	2.46	2.35	2.15	2.28
K_2O	0.01	0.05	1.09	1.22	0.04	0.04	0.03	0.03	0.04	0.02
F	0.05	0.00	0.00	0.00	0.15	0.02	0.08	0.03	0.00	0.03
Cl	0.00	0.01	0.00	0.00	0.00	0.00	0.00	0.01	0.00	0.05
H_2O*	3.65	4.49	3.96	3.90	3.66	3.80	3.61	3.52	3.57	3.59
B_2O_3*	10.66	13.03	11.48	11.31	10.82	11.03	10.57	10.25	10.36	10.48
Li_2O*	0.00	0.00	0.00	0.00	0.00	0.00	0.00	0.00	0.00	0.00
Total	102.28	115.59	106.81	106.58	102.36	103.85	100.72	98.55	98.35	100.96
O=F	0.02	0.00	0.00	0.00	0.06	0.01	0.03	0.01	0.00	0.01
Total*	102.26	115.59	106.81	106.58	102.29	103.84	100.69	98.54	98.35	100.95
Cation apfu										
Si	6.23	9.81	7.62	7.06	6.01	5.97	6.06	6.01	6.01	6.05
Ti	0.04	0.02	0.03	0.03	0.09	0.08	0.09	0.11	0.09	0.06
Cr	0.00	0.00	0.00	0.01	0.01	0.01	0.01	0.00	0.01	0.00
Al	5.85	2.38	4.59	5.10	6.13	6.27	5.98	6.00	6.14	6.00
Fe^{2+}	1.49	0.58	0.97	1.15	0.99	0.87	1.22	1.48	1.15	1.56
Mg	1.23	0.52	0.91	1.06	1.66	1.67	1.58	1.33	1.48	1.25
Mn	0.00	0.00	0.00	0.00	0.00	0.00	0.00	0.00	0.00	0.00
Ca	0.04	0.02	0.02	0.03	0.03	0.05	0.03	0.06	0.07	0.10
Na	0.82	0.32	0.63	0.58	0.83	0.77	0.78	0.77	0.70	0.73
K	0.00	0.01	0.21	0.24	0.01	0.01	0.01	0.01	0.01	0.00
B	3.00	3.00	3.00	3.00	3.00	3.00	3.00	3.00	3.00	3.00
F	0.03	0.00	0.00	0.00	0.08	0.01	0.04	0.01	0.00	0.02
Cl	0.00	0.00	0.00	0.00	0.00	0.00	0.00	0.00	0.00	0.01
H	3.97	4.00	4.00	4.00	3.92	3.99	3.96	3.98	4.00	3.97
CatSum	18.72	16.65	17.98	18.26	18.75	18.69	18.75	18.77	18.67	18.76

SAMPLE	**PG3A**							**AV5**				
Spot analysis	PG3A-T3-76	PG3A-T2-77	PG3A-T2-78	PG3A-T2-79	PG3A-T2-80	PG3A-T6-81	PG3A-T6-82	AV5-C3-2-1	AV5-C3-2-2	AV5-C3-3	AV5-C3-4-1	AV5-C3-4-2
Oxides wt%												
SiO_2	36.10	0.13	36.39	36.42	36.97	37.21	72.70	36.75	37.28	36.26	36.53	37.12
TiO_2	0.47	0.01	0.63	0.62	0.66	0.73	0.12	0.68	0.43	0.18	0.39	0.50
Al_2O_3	31.08	0.04	33.41	33.80	34.07	34.54	18.48	32.13	32.34	33.95	32.77	32.60
Cr_2O_3	0.00	0.00	0.02	0.10	0.06	0.02	0.04	0.03	0.00	0.00	0.03	0.02
FeO	11.36	9.65	9.24	8.81	8.85	5.92	0.88	10.99	9.32	11.61	9.36	12.08
MgO	5.06	16.47	5.36	5.40	5.25	6.30	0.95	3.89	5.50	2.81	5.53	3.55
CaO	0.63	29.60	0.86	0.76	0.62	0.33	0.03	0.02	0.05	0.01	0.17	0.00
MnO	0.00	1.29	0.03	0.02	0.00	0.00	0.01	0.02	0.00	0.01	0.01	0.00
Na_2O	2.25	0.01	1.88	1.82	1.88	1.81	0.20	2.65	2.30	1.69	2.32	2.41
K_2O	0.03	0.02	0.02	0.02	0.04	0.06	6.29	0.06	0.07	0.07	0.04	0.06
F	0.00	0.00	0.07	0.00	0.03	0.00	0.00	0.24	0.01	0.00	0.05	0.13
Cl	0.03	0.10	0.00	0.00	0.01	0.00	0.01	0.02	0.00	0.00	0.00	0.00
H_2O*	3.61	1.59	3.67	3.71	3.73	3.75	4.52	3.53	3.68	3.63	3.65	3.62
B_2O_3*	10.48	4.67	10.73	10.76	10.85	10.86	13.10	10.57	10.69	10.53	10.65	10.67
Li_2O*	0.00	0.00	0.00	0.00	0.00	0.00	0.00	0.00	0.00	0.00	0.00	0.00
Total	101.10	63.57	102.32	102.24	103.01	101.53	117.32	101.57	101.68	100.77	101.51	102.76
O=F	0.00	0.00	0.03	0.00	0.01	0.00	0.00	0.10	0.00	0.00	0.02	0.06
Total*	101.10	63.57	102.29	102.24	103.00	101.53	117.32	101.47	101.67	100.77	101.49	102.71
Cation apfu												
Si	5.99	0.05	5.89	5.88	5.92	5.95	9.64	6.04	6.06	5.99	5.96	6.05
Ti	0.06	0.00	0.08	0.08	0.08	0.09	0.01	0.08	0.05	0.02	0.05	0.06
Cr	0.00	0.00	0.00	0.01	0.01	0.00	0.00	0.00	0.00	0.00	0.00	0.00
Al	6.07	0.02	6.38	6.43	6.43	6.51	2.89	6.23	6.20	6.60	6.30	6.26
Fe^{2+}	1.58	3.00	1.25	1.19	1.19	0.79	0.10	1.51	1.27	1.60	1.28	1.65
Mg	1.25	9.14	1.29	1.30	1.25	1.50	0.19	0.95	1.33	0.69	1.35	0.86
Mn	0.00	0.41	0.00	0.00	0.00	0.00	0.00	0.00	0.00	0.00	0.00	0.00
Ca	0.11	11.81	0.15	0.13	0.11	0.06	0.00	0.00	0.01	0.00	0.03	0.00
Na	0.72	0.01	0.59	0.57	0.58	0.56	0.05	0.84	0.72	0.54	0.73	0.76
K	0.01	0.01	0.01	0.01	0.01	0.01	1.06	0.01	0.01	0.02	0.01	0.01
B	3.00	3.00	3.00	3.00	3.00	3.00	3.00	3.00	3.00	3.00	3.00	3.00
F	0.00	0.00	0.04	0.00	0.02	0.00	0.00	0.12	0.01	0.00	0.03	0.07
Cl	0.01	0.06	0.00	0.00	0.00	0.00	0.00	0.01	0.00	0.00	0.00	0.00
H	3.99	3.94	3.96	4.00	3.98	4.00	4.00	3.87	3.99	4.00	3.97	3.93
CatSum	18.78	27.45	18.64	18.61	18.58	18.49	16.96	18.69	18.66	18.47	18.71	18.65

SAMPLE	**AV5**									
Spot analysis	AV5-C3-5-1	AV5-C3-5-2	AV5-C3-MATRIX-1	AV5-C3-MATRIX-2	AV5-C6-1	AV5-C8-1-1	AV5-C8-1-2	AV5-C8-2	AV5-C8-MATRIX-1	AV5-C8-MATRIX-2
Oxides wt%										
SiO_2	37.20	36.39	59.61	49.54	34.82	36.57	36.26	51.39	48.09	56.25
TiO_2	0.41	0.23	0.22	0.34	0.68	0.49	0.49	0.32	0.27	0.15
Al_2O_3	32.35	34.23	26.50	31.00	31.71	32.71	32.34	32.02	31.20	29.15
Cr_2O_3	0.04	0.00	0.00	0.02	0.00	0.05	0.03	0.03	0.03	0.01
FeO	10.92	11.44	1.20	1.66	11.15	9.56	11.14	2.24	1.41	1.28
MgO	3.97	2.97	1.12	1.19	3.47	5.72	3.77	1.54	1.15	1.33
CaO	0.01	0.01	0.05	0.04	0.09	0.18	0.01	0.01	0.02	0.00
MnO	0.00	0.01	0.00	0.05	0.01	0.02	0.00	0.00	0.00	0.01
Na_2O	2.58	1.93	0.11	0.20	2.35	2.59	2.47	0.07	0.06	0.03
K_2O	0.05	0.08	10.28	10.72	0.17	0.04	0.08	10.98	10.71	9.99
F	0.12	0.03	0.22	0.25	0.23	0.11	0.09	0.37	0.15	0.30
Cl	0.01	0.01	0.02	0.01	0.02	0.00	0.01	0.01	0.02	0.03
H_2O*	3.61	3.65	4.19	3.91	3.40	3.65	3.57	4.01	3.88	4.10
B_2O_3*	10.63	10.61	12.47	11.68	10.19	10.71	10.49	12.14	11.46	12.32
Li_2O*	0.00	0.00	0.00	0.00	0.00	0.00	0.00	0.00	0.00	0.00
Total	101.89	101.57	116.01	110.61	98.30	102.40	100.76	115.12	108.45	114.96
O=F	0.05	0.01	0.09	0.11	0.10	0.04	0.04	0.16	0.06	0.13
Total*	101.84	101.56	115.91	110.50	98.20	102.35	100.73	114.97	108.39	114.83
Cation apfu										
Si	6.08	5.96	8.31	7.37	5.94	5.93	6.01	7.36	7.29	7.93
Ti	0.05	0.03	0.02	0.04	0.09	0.06	0.06	0.03	0.03	0.02
Cr	0.01	0.00	0.00	0.00	0.00	0.01	0.00	0.00	0.00	0.00
Al	6.23	6.61	4.35	5.44	6.37	6.25	6.32	5.40	5.58	4.84
Fe^{2+}	1.49	1.57	0.14	0.21	1.59	1.30	1.54	0.27	0.18	0.15
Mg	0.97	0.73	0.23	0.26	0.88	1.38	0.93	0.33	0.26	0.28
Mn	0.00	0.00	0.00	0.01	0.00	0.00	0.00	0.00	0.00	0.00
Ca	0.00	0.00	0.01	0.01	0.02	0.03	0.00	0.00	0.00	0.00
Na	0.82	0.61	0.03	0.06	0.78	0.81	0.79	0.02	0.02	0.01
K	0.01	0.02	1.83	2.03	0.04	0.01	0.02	2.01	2.07	1.80
B	3.00	3.00	3.00	3.00	3.00	3.00	3.00	3.00	3.00	3.00
F	0.06	0.01	0.10	0.12	0.12	0.05	0.05	0.17	0.07	0.14
Cl	0.00	0.00	0.00	0.00	0.01	0.00	0.00	0.00	0.01	0.01
H	3.93	3.98	3.90	3.88	3.87	3.94	3.95	3.83	3.92	3.86
CatSum	18.66	18.52	17.92	18.42	18.70	18.79	18.68	18.42	18.43	18.03

SAMPLE	**AV5**									
Spot analysis	AV5-C8-MATRIX-3	AV5-C8-MATRIX-4	AV5-C11-1-1	AV5-C11-1-2	AV5-C11-1-3	AV5-C11-1-4	AV5-C11-1-5	AV5-C11-1-6	AV5-C11-1-7	AV5-C11-1-8
Oxides wt%										
SiO_2	52.28	50.90	35.65	35.85	35.85	36.29	36.29	36.45	36.59	36.63
TiO_2	0.25	0.25	0.31	0.28	0.68	0.94	0.87	0.94	0.86	0.87
Al_2O_3	31.34	33.68	33.16	32.88	32.51	32.61	33.16	33.26	32.80	32.67
Cr_2O_3	0.01	0.01	0.00	0.00	0.00	0.00	0.00	0.00	0.00	0.01
FeO	1.51	1.45	12.02	12.14	10.93	5.95	5.86	5.86	5.49	5.65
MgO	1.25	1.32	2.98	2.93	3.58	7.54	7.52	7.42	8.12	7.73
CaO	0.01	0.03	0.00	0.01	0.00	0.57	0.58	0.60	0.47	0.49
MnO	0.02	0.00	0.01	0.00	0.03	0.00	0.00	0.00	0.01	0.01
Na_2O	0.11	0.07	1.92	1.98	2.34	2.36	2.46	2.44	2.56	2.47
K_2O	10.43	10.78	0.03	0.02	0.03	0.02	0.01	0.03	0.01	0.03
F	0.40	0.21	0.03	0.06	0.27	0.08	0.00	0.10	0.00	0.00
Cl	0.00	0.02	0.02	0.00	0.02	0.00	0.01	0.00	0.02	0.00
H_2O*	3.98	4.10	3.57	3.56	3.46	3.65	3.71	3.68	3.72	3.71
B_2O_3*	12.08	12.19	10.41	10.41	10.43	10.70	10.76	10.79	10.79	10.75
Li_2O*	0.00	0.00	0.00	0.00	0.00	0.00	0.00	0.00	0.00	0.00
Total	113.67	115.01	100.11	100.13	100.14	100.71	101.24	101.57	101.44	101.02
O=F	0.17	0.09	0.01	0.03	0.12	0.03	0.00	0.04	0.00	0.00
Total*	113.50	114.92	100.10	100.11	100.02	100.68	101.24	101.53	101.44	101.02
Cation apfu										
Si	7.52	7.26	5.95	5.99	5.98	5.90	5.86	5.87	5.89	5.92
Ti	0.03	0.03	0.04	0.04	0.09	0.11	0.11	0.11	0.10	0.11
Cr	0.00	0.00	0.00	0.00	0.00	0.00	0.00	0.00	0.00	0.00
Al	5.31	5.66	6.52	6.47	6.39	6.25	6.31	6.31	6.22	6.23
Fe^{2+}	0.18	0.17	1.68	1.70	1.52	0.81	0.79	0.79	0.74	0.76
Mg	0.27	0.28	0.74	0.73	0.89	1.83	1.81	1.78	1.95	1.86
Mn	0.00	0.00	0.00	0.00	0.00	0.00	0.00	0.00	0.00	0.00
Ca	0.00	0.00	0.00	0.00	0.00	0.10	0.10	0.10	0.08	0.09
Na	0.03	0.02	0.62	0.64	0.76	0.74	0.77	0.76	0.80	0.77
K	1.91	1.96	0.01	0.00	0.01	0.00	0.00	0.01	0.00	0.01
B	3.00	3.00	3.00	3.00	3.00	3.00	3.00	3.00	3.00	3.00
F	0.18	0.09	0.01	0.03	0.14	0.04	0.00	0.05	0.00	0.00
Cl	0.00	0.00	0.01	0.00	0.01	0.00	0.00	0.00	0.01	0.00
H	3.82	3.90	3.98	3.97	3.85	3.96	4.00	3.95	3.99	4.00
CatSum	18.27	18.38	18.56	18.57	18.63	18.74	18.76	18.74	18.79	18.75

SAMPLE	**AV5**		**VSS3A**								
Spot analysis	AV5-C11-1-9	AV5-C11-1-10	VSS3A-C1-1	VSS3A-C1-2	VSS3A-C1-3	VSS3A-C1-4-1	VSS3A-C1-4-2	VSS3A-C1-5-1	VSS3A-C1-5-2	VSS3A-C1-6-1	VSS3A-C1-6-2
Oxides wt%											
SiO_2	36.54	36.58	36.94	38.50	37.25	35.76	36.03	37.07	36.73	36.40	36.72
TiO_2	0.84	1.14	0.54	0.83	0.36	1.41	0.53	0.61	0.44	0.62	0.50
Al_2O_3	32.51	32.52	33.59	31.72	33.20	30.71	34.53	32.73	33.20	33.62	33.43
Cr_2O_3	0.00	0.00	0.03	0.02	0.04	0.08	0.05	0.04	0.00	0.04	0.02
FeO	5.39	9.95	8.36	10.49	8.58	9.46	7.79	8.25	7.94	7.73	8.13
MgO	7.86	3.79	5.84	4.01	5.37	6.05	5.45	5.83	5.77	5.87	5.61
CaO	0.52	0.01	0.59	0.46	0.37	0.83	0.42	0.40	0.43	0.55	0.41
MnO	0.02	0.00	0.08	0.15	0.04	0.10	0.07	0.04	0.06	0.04	0.09
Na_2O	2.46	2.89	2.02	1.80	1.75	2.28	2.33	2.46	2.34	2.14	2.11
K_2O	0.03	0.03	0.02	1.14	0.03	0.01	0.03	0.03	0.02	0.03	0.02
F	0.06	0.69	0.07	0.11	0.01	0.31	0.13	0.17	0.10	0.20	0.25
Cl	0.02	0.00	0.00	0.00	0.03	0.00	0.00	0.00	0.00	0.01	0.00
H_2O*	3.66	3.33	3.70	3.67	3.69	3.48	3.65	3.63	3.64	3.60	3.58
B_2O_3*	10.71	10.58	10.82	10.80	10.72	10.51	10.74	10.74	10.70	10.72	10.72
Li_2O*	0.00	0.00	0.00	0.00	0.00	0.00	0.00	0.00	0.00	0.00	0.00
Total	100.63	101.50	102.59	103.70	101.43	100.98	101.74	101.99	101.39	101.58	101.58
O=F	0.03	0.29	0.03	0.05	0.00	0.13	0.05	0.07	0.04	0.09	0.10
Total*	100.60	101.21	102.57	103.65	101.43	100.85	101.69	101.92	101.35	101.49	101.47
Cation apfu											
Si	5.93	6.01	5.94	6.20	6.04	5.91	5.83	6.00	5.96	5.90	5.96
Ti	0.10	0.14	0.07	0.10	0.04	0.17	0.06	0.07	0.05	0.08	0.06
Cr	0.00	0.00	0.00	0.00	0.00	0.01	0.01	0.00	0.00	0.00	0.00
Al	6.22	6.30	6.36	6.02	6.34	5.99	6.59	6.24	6.35	6.42	6.39
Fe^{2+}	0.73	1.37	1.12	1.41	1.16	1.31	1.05	1.12	1.08	1.05	1.10
Mg	1.90	0.93	1.40	0.96	1.30	1.49	1.31	1.41	1.40	1.42	1.36
Mn	0.00	0.00	0.01	0.02	0.01	0.01	0.01	0.00	0.01	0.01	0.01
Ca	0.09	0.00	0.10	0.08	0.07	0.15	0.07	0.07	0.08	0.10	0.07
Na	0.77	0.92	0.63	0.56	0.55	0.73	0.73	0.77	0.74	0.67	0.66
K	0.01	0.01	0.00	0.23	0.01	0.00	0.01	0.01	0.00	0.01	0.00
B	3.00	3.00	3.00	3.00	3.00	3.00	3.00	3.00	3.00	3.00	3.00
F	0.03	0.36	0.04	0.06	0.00	0.16	0.07	0.09	0.05	0.10	0.13
Cl	0.00	0.00	0.00	0.00	0.01	0.00	0.00	0.00	0.00	0.00	0.00
H	3.96	3.64	3.96	3.94	3.99	3.84	3.93	3.91	3.95	3.89	3.87
CatSum	18.75	18.67	18.63	18.59	18.52	18.78	18.68	18.69	18.67	18.65	18.62

SAMPLE	**VSS3A**							
Spot analysis	VSS3A-C1-MATRIX-1	VSS3A-C1-MATRIX-2	VSS3A-C4-1-1	VSS3A-C4-1-2	VSS3A-C4-MATRIX-1	VSS3A-C4-MATRIX-2	VSS3A-C5-1-1	VSS3A-C5-1-2
Oxides wt%								
SiO_2	36.95	38.35	37.20	37.11	35.85	35.98	36.56	36.08
TiO_2	0.78	0.46	0.33	0.54	0.83	0.53	0.60	0.61
Al_2O_3	32.75	32.24	34.07	33.19	32.56	33.52	32.62	32.16
Cr_2O_3	0.04	0.00	0.03	0.00	0.00	0.02	0.03	0.00
FeO	8.88	8.07	8.86	8.41	8.53	8.53	7.88	9.26
MgO	5.27	5.79	5.10	5.77	5.70	5.03	5.86	5.14
CaO	0.58	0.37	0.18	0.37	0.71	0.52	0.47	0.39
MnO	0.00	0.02	0.05	0.07	0.06	0.03	0.05	0.03
Na_2O	1.99	2.19	2.02	2.21	2.09	2.06	2.00	1.88
K_2O	0.02	0.26	0.01	0.04	0.03	0.02	0.03	0.03
F	0.06	0.00	0.00	0.01	0.00	0.00	0.00	0.18
Cl	0.01	0.01	0.00	0.00	0.01	0.00	0.00	0.03
H_2O*	3.66	3.73	3.73	3.71	3.64	3.65	3.66	3.52
B_2O_3*	10.70	10.82	10.81	10.78	10.57	10.59	10.61	10.47
Li_2O*	0.00	0.00	0.00	0.00	0.00	0.00	0.00	0.00
Total	101.70	102.32	102.40	102.22	100.58	100.49	100.37	99.79
O=F	0.03	0.00	0.00	0.00	0.00	0.00	0.00	0.07
Total*	101.67	102.32	102.40	102.22	100.57	100.49	100.37	99.72
Cation apfu								
Si	6.00	6.16	5.98	5.98	5.90	5.91	5.99	5.99
Ti	0.10	0.06	0.04	0.07	0.10	0.07	0.07	0.08
Cr	0.00	0.00	0.00	0.00	0.00	0.00	0.00	0.00
Al	6.27	6.11	6.46	6.31	6.31	6.48	6.30	6.29
Fe^{2+}	1.21	1.08	1.19	1.13	1.17	1.17	1.08	1.29
Mg	1.28	1.39	1.22	1.39	1.40	1.23	1.43	1.27
Mn	0.00	0.00	0.01	0.01	0.01	0.00	0.01	0.00
Ca	0.10	0.06	0.03	0.06	0.13	0.09	0.08	0.07
Na	0.63	0.68	0.63	0.69	0.67	0.66	0.64	0.60
K	0.00	0.05	0.00	0.01	0.01	0.00	0.01	0.01
B	3.00	3.00	3.00	3.00	3.00	3.00	3.00	3.00
F	0.03	0.00	0.00	0.00	0.00	0.00	0.00	0.09
Cl	0.00	0.00	0.00	0.00	0.00	0.00	0.00	0.01
H	3.96	4.00	4.00	3.99	4.00	4.00	4.00	3.90
CatSum	18.58	18.60	18.56	18.65	18.68	18.62	18.61	18.60

SAMPLE	**VSS3A**							
Spot analysis	VSS3A-C5-MATRIX-1	VSS3A-C5-MATRIX-2	VSS3A-C6-1-1	VSS3A-C6-1-2	VSS3A-C6-2	VSS3A-C6-3	VSS3A-C6-MATRIX-1	VSS3A-C6-MATRIX-2
Oxides wt%								
SiO_2	42.79	49.90	37.11	37.45	36.88	36.81	40.32	36.32
TiO_2	0.32	0.89	0.53	0.33	0.24	0.54	0.83	1.65
Al_2O_3	33.37	26.56	33.13	33.77	33.61	32.85	29.74	29.63
Cr_2O_3	0.00	0.00	0.02	0.00	0.01	0.07	0.00	0.06
FeO	7.62	8.52	8.26	8.27	8.39	7.78	9.02	8.96
MgO	4.15	4.75	5.37	5.34	5.18	5.57	5.64	6.62
CaO	0.29	0.66	0.34	0.28	0.18	0.41	0.48	1.31
MnO	0.01	0.04	0.06	0.08	0.05	0.05	0.00	0.04
Na_2O	1.29	1.76	1.94	1.93	1.91	2.07	1.93	1.98
K_2O	3.12	0.01	0.01	0.02	0.00	0.03	0.02	0.02
F	0.00	0.17	0.01	0.00	0.00	0.00	0.35	0.29
Cl	0.01	0.00	0.01	0.00	0.04	0.01	0.00	0.00
H_2O*	3.94	3.95	3.68	3.73	3.67	3.67	3.57	3.49
B_2O_3*	11.43	11.69	10.70	10.80	10.67	10.63	10.84	10.52
Li_2O*	0.00	0.00	0.00	0.00	0.00	0.00	0.00	0.00
Total	108.36	108.90	101.19	101.99	100.83	100.48	102.74	100.90
O=F	0.00	0.07	0.01	0.00	0.00	0.00	0.15	0.12
Total*	108.36	108.83	101.18	101.99	100.83	100.48	102.59	100.78
Cation apfu								
Si	6.50	7.42	6.03	6.03	6.01	6.02	6.46	6.00
Ti	0.04	0.10	0.06	0.04	0.03	0.07	0.10	0.21
Cr	0.00	0.00	0.00	0.00	0.00	0.01	0.00	0.01
Al	5.98	4.66	6.34	6.41	6.45	6.33	5.62	5.77
Fe^{2+}	0.97	1.06	1.12	1.11	1.14	1.06	1.21	1.24
Mg	0.94	1.05	1.30	1.28	1.26	1.36	1.35	1.63
Mn	0.00	0.01	0.01	0.01	0.01	0.01	0.00	0.01
Ca	0.05	0.10	0.06	0.05	0.03	0.07	0.08	0.23
Na	0.38	0.51	0.61	0.60	0.60	0.66	0.60	0.63
K	0.60	0.00	0.00	0.00	0.00	0.01	0.00	0.00
B	3.00	3.00	3.00	3.00	3.00	3.00	3.00	3.00
F	0.00	0.08	0.01	0.00	0.00	0.00	0.18	0.15
Cl	0.00	0.00	0.00	0.00	0.01	0.00	0.00	0.00
H	4.00	3.92	3.99	4.00	3.99	4.00	3.82	3.85
CatSum	18.46	17.91	18.54	18.53	18.54	18.58	18.43	18.73

SAMPLE	**VSS3A**							
Spot analysis	VSS3A-C7-1-1	VSS3A-C7-1-2	VSS3A-C7-2-1	VSS3A-C7-2-2	VSS3A-C7-2-3	VSS3A-C1-MATRIX-3	VSS3A-C1-MATRIX-4	VSS3A-C1-MATRIX-5
Oxides wt%								
SiO_2	50.32	36.91	37.04	36.78	36.59	37.55	37.16	36.67
TiO_2	0.33	0.41	0.35	0.62	0.76	1.03	0.39	0.99
Al_2O_3	24.91	33.20	34.16	32.64	33.27	30.93	33.56	31.64
Cr_2O_3	0.07	0.01	0.00	0.10	0.05	0.01	0.00	0.02
FeO	6.01	9.14	8.34	8.05	7.84	8.89	7.43	8.53
MgO	4.53	5.17	4.81	5.85	5.44	6.03	5.67	6.19
CaO	0.46	0.29	0.13	0.42	0.39	0.88	0.49	0.85
MnO	0.04	0.07	0.07	0.03	0.00	0.04	0.10	0.01
Na_2O	1.71	2.00	1.75	2.00	2.08	2.13	2.16	1.89
K_2O	0.01	0.01	0.01	0.01	0.02	0.02	0.02	0.06
F	0.00	0.00	0.00	0.00	0.15	0.24	0.14	0.27
Cl	0.00	0.01	0.00	0.00	0.01	0.01	0.00	0.02
H_2O*	3.90	3.69	3.70	3.68	3.61	3.57	3.64	3.54
B_2O_3*	11.30	10.70	10.71	10.65	10.66	10.70	10.76	10.64
Li_2O*	0.00	0.00	0.00	0.00	0.00	0.00	0.00	0.00
Total	103.58	101.61	101.07	100.83	100.88	102.04	101.53	101.31
O=F	0.00	0.00	0.00	0.00	0.06	0.10	0.06	0.11
Total*	103.58	101.61	101.07	100.83	100.81	101.94	101.47	101.19
Cation apfu								
Si	7.74	6.00	6.01	6.00	5.96	6.10	6.00	5.99
Ti	0.04	0.05	0.04	0.08	0.09	0.13	0.05	0.12
Cr	0.01	0.00	0.00	0.01	0.01	0.00	0.00	0.00
Al	4.52	6.36	6.53	6.28	6.39	5.92	6.39	6.09
Fe^{2+}	0.77	1.24	1.13	1.10	1.07	1.21	1.00	1.17
Mg	1.04	1.25	1.16	1.42	1.32	1.46	1.37	1.51
Mn	0.01	0.01	0.01	0.00	0.00	0.01	0.01	0.00
Ca	0.08	0.05	0.02	0.07	0.07	0.15	0.09	0.15
Na	0.51	0.63	0.55	0.63	0.66	0.67	0.68	0.60
K	0.00	0.00	0.00	0.00	0.00	0.00	0.00	0.01
B	3.00	3.00	3.00	3.00	3.00	3.00	3.00	3.00
F	0.00	0.00	0.00	0.00	0.08	0.12	0.07	0.14
Cl	0.00	0.00	0.00	0.00	0.00	0.00	0.00	0.00
H	4.00	4.00	4.00	4.00	3.92	3.87	3.93	3.86
CatSum	17.71	18.59	18.46	18.60	18.57	18.65	18.59	18.64

SAMPLE	**VSS3A**			**FC21.1**					
Spot analysis	VSS3A-C1-MATRIX-6	VSS3A-C1-7-1	VSS3A-C1-7-2	FC21.1-T2B-1	FC21.1-T2B-2	FC21.1-T2B-3	FC21.1-T2B-4	FC21.1-T2B-5	FC21.1-T2A-6
Oxides wt%									
SiO_2	36.81	36.94	37.90	37.00	36.71	37.50	37.00	37.31	37.59
TiO_2	0.86	0.41	0.32	0.62	0.20	0.69	0.32	0.36	0.78
Al_2O_3	31.93	33.16	34.56	31.81	32.17	31.40	31.31	32.03	31.75
Cr_2O_3	0.03	0.00	0.01	0.05	0.00	0.04	0.06	0.03	0.03
FeO	8.73	10.26	10.46	5.34	10.12	5.92	10.21	9.63	5.36
MgO	6.13	4.12	4.10	8.13	5.30	8.36	5.48	5.33	8.34
CaO	0.77	0.38	0.27	0.81	0.03	0.46	0.05	0.10	0.69
MnO	0.00	0.03	0.06	0.00	0.06	0.04	0.03	0.09	0.01
Na_2O	2.10	2.11	2.27	2.17	2.51	2.58	2.60	2.31	2.41
K_2O	0.04	0.02	0.02	0.02	0.03	0.03	0.02	0.02	0.04
F	0.33	0.00	0.00	0.00	0.00	0.03	0.00	0.00	0.00
Cl	0.00	0.06	0.02	0.00	0.01	0.00	0.00	0.02	0.00
H_2O*	3.53	3.67	3.78	3.69	3.66	3.71	3.65	3.67	3.73
B_2O_3*	10.69	10.66	10.98	10.70	10.60	10.79	10.59	10.66	10.82
Li_2O*	0.00	0.00	0.00	0.00	0.00	0.00	0.00	0.00	0.00
Total	101.95	101.82	104.76	100.34	101.40	101.54	101.31	101.56	101.56
O=F	0.14	0.00	0.00	0.00	0.00	0.01	0.00	0.00	0.00
Total*	101.81	101.82	104.76	100.34	101.40	101.53	101.31	101.56	101.56
Cation apfu									
Si	5.98	6.02	6.00	6.01	6.02	6.04	6.08	6.08	6.04
Ti	0.10	0.05	0.04	0.08	0.03	0.08	0.04	0.04	0.09
Cr	0.00	0.00	0.00	0.01	0.00	0.01	0.01	0.00	0.00
Al	6.12	6.37	6.45	6.09	6.21	5.96	6.06	6.16	6.01
Fe^{2+}	1.19	1.40	1.38	0.73	1.39	0.80	1.40	1.31	0.72
Mg	1.49	1.00	0.97	1.97	1.29	2.01	1.34	1.30	2.00
Mn	0.00	0.00	0.01	0.00	0.01	0.00	0.00	0.01	0.00
Ca	0.13	0.07	0.05	0.14	0.01	0.08	0.01	0.02	0.12
Na	0.66	0.67	0.70	0.68	0.80	0.81	0.83	0.73	0.75
K	0.01	0.00	0.00	0.00	0.01	0.01	0.00	0.00	0.01
B	3.00	3.00	3.00	3.00	3.00	3.00	3.00	3.00	3.00
F	0.17	0.00	0.00	0.00	0.00	0.02	0.00	0.00	0.00
Cl	0.00	0.02	0.00	0.00	0.00	0.00	0.00	0.00	0.00
H	3.83	3.98	4.00	4.00	4.00	3.98	4.00	4.00	4.00
CatSum	18.69	18.58	18.59	18.71	18.75	18.80	18.77	18.66	18.74

SAMPLE	**FC21.1**									
Spot analysis	FC21.1-T2A-7	FC21.1-T2A-8	FC21.1-T2A-9	FC21.1-T2A-10	FC21.1-T2A-11	FC21.1-T2A-12	FC21.1-T2A-13	FC21.1-T5-14	FC21.1-T5-15	FC21.1-T5-16
Oxides wt%										
SiO_2	37.30	37.51	36.29	37.67	37.07	37.31	37.20	36.89	35.48	0.58
TiO_2	0.46	0.73	0.13	0.46	0.99	0.56	0.15	0.72	0.14	95.10
Al_2O_3	31.30	32.14	30.30	31.83	30.75	32.14	32.04	31.74	30.31	0.83
Cr_2O_3	0.01	0.00	0.00	0.00	0.00	0.04	0.01	0.03	0.04	0.00
FeO	10.16	5.26	12.27	6.19	10.23	5.13	10.03	4.98	10.83	0.58
MgO	5.68	8.24	5.16	8.04	5.74	8.16	5.20	8.10	5.01	0.04
CaO	0.04	0.77	0.05	0.33	0.08	0.71	0.03	0.81	0.06	0.07
MnO	0.02	0.06	0.02	0.06	0.02	0.00	0.01	0.00	0.06	0.04
Na_2O	2.46	2.17	2.34	2.51	2.66	2.25	2.33	2.29	2.08	0.06
K_2O	0.02	0.01	0.01	0.00	0.01	0.01	0.02	0.05	0.07	0.37
F	0.00	0.00	0.00	0.00	0.32	0.05	0.00	0.00	0.00	0.00
Cl	0.00	0.01	0.03	0.01	0.00	0.01	0.01	0.07	0.01	0.01
H_2O*	3.67	3.73	3.58	3.73	3.52	3.69	3.66	3.66	3.51	3.59
B_2O_3*	10.64	10.83	10.40	10.80	10.63	10.76	10.62	10.67	10.18	10.40
Li_2O*	0.00	0.00	0.00	0.00	0.00	0.00	0.00	0.00	0.00	0.00
Total	101.76	101.47	100.58	101.62	102.02	100.82	101.30	100.00	97.78	111.64
O=F	0.00	0.00	0.00	0.00	0.13	0.02	0.00	0.00	0.00	0.00
Total*	101.76	101.47	100.58	101.62	101.89	100.80	101.30	100.00	97.78	111.64
Cation apfu										
Si	6.09	6.02	6.06	6.06	6.06	6.02	6.09	6.01	6.06	0.10
Ti	0.06	0.09	0.02	0.06	0.12	0.07	0.02	0.09	0.02	11.95
Cr	0.00	0.00	0.00	0.00	0.00	0.00	0.00	0.00	0.01	0.00
Al	6.02	6.08	5.97	6.03	5.93	6.12	6.18	6.10	6.10	0.16
Fe^{2+}	1.39	0.71	1.71	0.83	1.40	0.69	1.37	0.68	1.55	0.08
Mg	1.38	1.97	1.29	1.93	1.40	1.96	1.27	1.97	1.28	0.01
Mn	0.00	0.01	0.00	0.01	0.00	0.00	0.00	0.00	0.01	0.01
Ca	0.01	0.13	0.01	0.06	0.01	0.12	0.01	0.14	0.01	0.01
Na	0.78	0.68	0.76	0.78	0.84	0.70	0.74	0.72	0.69	0.02
K	0.00	0.00	0.00	0.00	0.00	0.00	0.00	0.01	0.02	0.08
B	3.00	3.00	3.00	3.00	3.00	3.00	3.00	3.00	3.00	3.00
F	0.00	0.00	0.00	0.00	0.16	0.02	0.00	0.00	0.00	0.00
Cl	0.00	0.00	0.01	0.00	0.00	0.00	0.00	0.02	0.00	0.00
H	4.00	4.00	3.99	4.00	3.84	3.97	4.00	3.98	4.00	4.00
CatSum	18.73	18.69	18.82	18.76	18.77	18.70	18.68	18.72	18.72	15.42

SAMPLE	**FC21.1**				**880**								
Spot analysis	FC21.1-T5-17	FC21.1-T10-18	FC21.1-T11-19	FC21.1-T11-20	880-T1-21	880-T1-22	880-T1-23	880-T1-24	880-T1-25	880-T1-26	880-T1-27	880-T1-28	880-T3-29
Oxides wt%													
SiO_2	0.13	71.37	37.05	35.81	37.25	38.07	67.27	36.74	34.61	36.54	37.10	36.53	37.07
TiO_2	95.78	0.00	0.73	0.14	0.56	0.45	0.00	0.49	0.27	0.63	0.43	0.44	0.44
Al_2O_3	0.04	20.10	33.21	31.02	31.75	26.20	18.61	30.34	26.79	25.88	30.84	30.90	32.52
Cr_2O_3	0.00	0.00	0.01	0.00	0.00	0.05	0.00	0.00	0.00	0.01	0.03	0.04	0.28
FeO	0.34	0.19	8.13	11.49	8.03	18.68	0.59	10.96	19.72	18.66	9.15	10.43	6.11
MgO	0.00	0.01	5.45	4.21	6.69	3.78	0.07	5.68	2.75	3.72	6.59	5.98	6.92
CaO	0.04	0.11	0.43	0.02	0.76	0.49	0.01	0.56	0.12	0.55	0.64	0.65	0.74
MnO	0.01	0.02	0.00	0.02	0.01	0.04	0.03	0.03	0.04	0.03	0.06	0.04	0.00
Na_2O	0.06	10.73	1.90	2.10	2.25	2.57	0.14	2.56	2.69	2.55	2.38	2.37	2.37
K_2O	0.16	0.08	0.03	0.06	0.06	0.77	16.28	0.04	0.06	0.31	0.03	0.02	0.02
F	0.00	0.00	0.00	0.00	0.00	0.01	0.00	0.00	0.00	0.00	0.00	0.00	0.00
Cl	0.12	0.00	0.00	0.01	0.00	0.01	0.00	0.02	0.00	0.00	0.01	0.01	0.00
H_2O*	3.52	4.63	3.70	3.54	3.70	3.62	4.37	3.63	3.44	3.53	3.67	3.65	3.70
B_2O_3*	10.28	13.41	10.72	10.26	10.73	10.50	12.67	10.54	9.96	10.23	10.64	10.58	10.72
Li_2O*	0.00	0.00	0.00	0.00	0.00	0.00	0.00	0.00	0.00	0.00	0.00	0.00	0.00
Total	110.50	120.66	101.37	98.69	101.79	105.24	120.04	101.59	100.44	102.64	101.57	101.64	100.90
O=F	0.00	0.00	0.00	0.00	0.00	0.00	0.00	0.00	0.00	0.00	0.00	0.00	0.00
Total*	110.50	120.66	101.37	98.69	101.79	105.23	120.04	101.59	100.44	102.64	101.57	101.64	100.90
Cation apfu													
Si	0.02	9.25	6.00	6.06	6.04	6.30	9.23	6.06	6.04	6.21	6.06	6.00	6.01
Ti	12.18	0.00	0.09	0.02	0.07	0.06	0.00	0.06	0.04	0.08	0.05	0.05	0.05
Cr	0.00	0.00	0.00	0.00	0.00	0.01	0.00	0.00	0.00	0.00	0.00	0.01	0.04
Al	0.01	3.07	6.34	6.19	6.06	5.11	3.01	5.90	5.51	5.18	5.94	5.98	6.21
Fe^{2+}	0.05	0.02	1.10	1.63	1.09	2.59	0.07	1.51	2.88	2.65	1.25	1.43	0.83
Mg	0.00	0.00	1.32	1.06	1.62	0.93	0.01	1.40	0.72	0.94	1.61	1.47	1.67
Mn	0.00	0.00	0.00	0.00	0.00	0.01	0.00	0.00	0.01	0.00	0.01	0.01	0.00
Ca	0.01	0.02	0.07	0.00	0.13	0.09	0.00	0.10	0.02	0.10	0.11	0.11	0.13
Na	0.02	2.70	0.60	0.69	0.71	0.82	0.04	0.82	0.91	0.84	0.75	0.76	0.74
K	0.04	0.01	0.01	0.01	0.01	0.16	2.85	0.01	0.01	0.07	0.01	0.00	0.00
B	3.00	3.00	3.00	3.00	3.00	3.00	3.00	3.00	3.00	3.00	3.00	3.00	3.00
F	0.00	0.00	0.00	0.00	0.00	0.01	0.00	0.00	0.00	0.00	0.00	0.00	0.00
Cl	0.03	0.00	0.00	0.00	0.00	0.00	0.00	0.01	0.00	0.00	0.00	0.00	0.00
H	3.97	4.00	4.00	4.00	4.00	3.99	4.00	3.99	4.00	4.00	4.00	4.00	4.00
CatSum	15.32	18.07	18.54	18.67	18.72	19.08	18.21	18.85	19.13	19.07	18.79	18.83	18.69

SAMPLE	**880**													
Spot analysis	880-T3-30	880-T3-31	880-T3-32	880-T3-33	880-T2-34	880-T2-35	880-T2-36	880-T2-37	880-T2-38	880-T2-39	880-R1-40	880-R1-41	880-R1-42	880-R1-43
Oxides wt%														
SiO_2	37.10	37.18	36.92	37.88	35.60	37.09	37.19	36.84	37.21	37.31	0.03	0.05	0.10	0.09
TiO_2	0.60	0.32	0.48	0.38	0.68	0.27	0.38	0.59	0.21	0.72	98.75	99.38	96.75	97.07
Al_2O_3	31.50	31.26	30.46	33.00	26.21	30.91	32.19	32.15	33.01	31.14	0.00	0.02	0.16	0.07
Cr_2O_3	0.06	0.03	0.04	0.00	0.10	0.05	0.11	0.03	0.04	0.60	0.01	0.00	0.04	0.03
FeO	10.22	10.96	10.54	5.96	18.24	8.85	8.33	8.75	8.88	8.33	0.38	0.30	0.48	0.80
MgO	5.32	5.47	5.89	7.09	3.79	6.98	6.21	5.83	5.56	6.20	0.01	0.00	0.02	0.01
CaO	0.32	0.22	0.32	0.26	0.53	0.79	0.64	0.36	0.20	0.87	0.04	0.03	0.03	0.02
MnO	0.00	0.01	0.02	0.03	0.00	0.00	0.00	0.00	0.03	0.02	0.03	0.00	0.03	0.00
Na_2O	2.21	2.44	2.60	2.26	2.56	2.44	2.39	2.17	2.14	2.21	0.00	0.02	0.02	0.02
K_2O	0.02	0.00	0.02	0.04	0.14	0.12	0.09	0.04	0.03	0.04	0.01	0.02	0.02	0.03
F	0.03	0.00	0.00	0.00	0.00	0.00	0.00	0.02	0.02	0.00	0.00	0.00	0.00	0.00
Cl	0.01	0.01	0.00	0.02	0.01	0.01	0.00	0.02	0.00	0.00	0.00	0.00	0.00	0.00
H_2O*	3.65	3.67	3.65	3.73	3.49	3.68	3.70	3.66	3.69	3.69	3.65	3.67	3.59	3.60
B_2O_3*	10.63	10.64	10.57	10.84	10.13	10.67	10.73	10.64	10.72	10.70	10.57	10.64	10.40	10.43
Li_2O*	0.00	0.00	0.00	0.00	0.00	0.00	0.00	0.00	0.00	0.00	0.00	0.00	0.00	0.00
Total	101.67	102.20	101.50	101.49	101.48	101.85	101.97	101.10	101.74	101.82	113.49	114.13	111.63	112.18
O=F	0.01	0.00	0.00	0.00	0.00	0.00	0.00	0.01	0.01	0.00	0.00	0.00	0.00	0.00
Total*	101.66	102.20	101.50	101.49	101.48	101.85	101.97	101.09	101.73	101.82	113.49	114.13	111.63	112.18
Cation apfu														
Si	6.07	6.07	6.07	6.08	6.11	6.04	6.02	6.02	6.03	6.06	0.01	0.01	0.02	0.01
Ti	0.07	0.04	0.06	0.05	0.09	0.03	0.05	0.07	0.03	0.09	12.21	12.21	12.16	12.16
Cr	0.01	0.00	0.01	0.00	0.01	0.01	0.01	0.00	0.01	0.08	0.00	0.00	0.01	0.00
Al	6.07	6.02	5.91	6.24	5.30	5.94	6.14	6.19	6.30	5.96	0.00	0.00	0.03	0.01
Fe^{2+}	1.40	1.50	1.45	0.80	2.62	1.21	1.13	1.20	1.20	1.13	0.05	0.04	0.07	0.11
Mg	1.30	1.33	1.44	1.70	0.97	1.70	1.50	1.42	1.34	1.50	0.00	0.00	0.00	0.00
Mn	0.00	0.00	0.00	0.00	0.00	0.00	0.00	0.00	0.00	0.00	0.00	0.00	0.00	0.00
Ca	0.06	0.04	0.06	0.04	0.10	0.14	0.11	0.06	0.03	0.15	0.01	0.00	0.01	0.00
Na	0.70	0.77	0.83	0.70	0.85	0.77	0.75	0.69	0.67	0.70	0.00	0.01	0.01	0.01
K	0.00	0.00	0.00	0.01	0.03	0.02	0.02	0.01	0.01	0.01	0.00	0.00	0.00	0.01
B	3.00	3.00	3.00	3.00	3.00	3.00	3.00	3.00	3.00	3.00	3.00	3.00	3.00	3.00
F	0.02	0.00	0.00	0.00	0.00	0.00	0.00	0.01	0.01	0.00	0.00	0.00	0.00	0.00
Cl	0.00	0.00	0.00	0.00	0.00	0.00	0.00	0.00	0.00	0.00	0.00	0.00	0.00	0.00
H	3.98	4.00	4.00	4.00	4.00	4.00	4.00	3.99	3.99	4.00	4.00	4.00	4.00	4.00
CatSum	18.67	18.77	18.83	18.61	19.08	18.85	18.74	18.66	18.63	18.68	15.29	15.28	15.31	15.32

SAMPLE	**880**										
Spot analysis	880-T6-44	880-T6-45	880-T6-46	880-T6-47	880-T6-48	880-T6-49	Line 1 880-T7-L1	Line 2 880-T7-L1	Line 3 880-T7-L1	Line 4 880-T7-L1	Line 5 880-T7-L1
Oxides wt%											
SiO_2	36.56	37.54	37.37	36.65	70.92	70.95	37.51	37.51	37.22	36.89	37.21
TiO_2	0.50	0.19	0.72	0.92	0.00	0.09	0.28	0.29	0.60	0.53	0.26
Al_2O_3	28.05	31.51	30.13	29.56	20.41	20.66	34.09	32.17	32.20	32.05	32.78
Cr_2O_3	0.00	0.06	0.03	0.09	0.00	0.02	0.00	0.23	0.08	0.02	0.06
FeO	15.39	8.15	9.22	9.19	0.06	0.45	5.42	7.94	8.03	8.35	8.26
MgO	4.41	6.94	7.14	7.02	0.01	0.07	6.83	6.51	6.53	6.46	6.15
CaO	0.55	0.95	0.79	1.03	0.55	0.04	0.78	0.60	0.52	0.48	0.32
MnO	0.03	0.02	0.00	0.01	0.05	0.02	0.02	0.03	0.00	0.00	0.03
Na_2O	2.50	2.30	2.27	2.23	10.95	10.88	2.16	2.15	2.26	2.19	2.18
K_2O	0.08	0.04	0.03	0.05	0.10	0.12	0.04	0.13	0.03	0.02	0.02
F	0.00	0.00	0.00	0.00	0.00	0.00	0.00	0.00	0.13	0.15	0.06
Cl	0.01	0.01	0.00	0.01	0.03	0.01	0.01	0.02	0.03	0.05	0.05
H_2O*	3.57	3.71	3.68	3.63	4.62	4.64	3.75	3.71	3.64	3.60	3.66
B_2O_3*	10.36	10.75	10.68	10.54	13.43	13.46	10.88	10.77	10.75	10.68	10.74
Li_2O*	0.00	0.00	0.00	0.00	0.00	0.00	0.00	0.00	0.00	0.00	0.00
Total	102.01	102.18	102.07	100.94	121.14	121.41	101.78	102.06	102.03	101.48	101.77
O=F	0.00	0.00	0.00	0.00	0.00	0.00	0.00	0.00	0.05	0.06	0.03
Total*	102.01	102.18	102.07	100.94	121.14	121.41	101.78	102.06	101.98	101.41	101.75
Cation apfu											
Si	6.14	6.07	6.08	6.05	9.18	9.16	5.99	6.05	6.02	6.00	6.02
Ti	0.06	0.02	0.09	0.11	0.00	0.01	0.03	0.04	0.07	0.06	0.03
Cr	0.00	0.01	0.00	0.01	0.00	0.00	0.00	0.03	0.01	0.00	0.01
Al	5.55	6.00	5.78	5.75	3.11	3.14	6.42	6.12	6.13	6.15	6.25
Fe^{2+}	2.16	1.10	1.25	1.27	0.01	0.05	0.72	1.07	1.09	1.14	1.12
Mg	1.10	1.67	1.73	1.73	0.00	0.01	1.63	1.57	1.57	1.57	1.48
Mn	0.00	0.00	0.00	0.00	0.01	0.00	0.00	0.00	0.00	0.00	0.00
Ca	0.10	0.17	0.14	0.18	0.08	0.01	0.13	0.10	0.09	0.08	0.06
Na	0.81	0.72	0.72	0.71	2.75	2.72	0.67	0.67	0.71	0.69	0.68
K	0.02	0.01	0.01	0.01	0.02	0.02	0.01	0.03	0.01	0.00	0.00
B	3.00	3.00	3.00	3.00	3.00	3.00	3.00	3.00	3.00	3.00	3.00
F	0.00	0.00	0.00	0.00	0.00	0.00	0.00	0.00	0.06	0.08	0.03
Cl	0.00	0.00	0.00	0.00	0.01	0.00	0.00	0.01	0.01	0.01	0.01
H	4.00	4.00	4.00	4.00	3.99	4.00	4.00	3.99	3.93	3.91	3.96
CatSum	18.94	18.77	18.80	18.82	18.15	18.13	18.60	18.69	18.70	18.70	18.66

SAMPLE **880**

Spot analysis	Line 6 880-T7-L1	Line 7 880-T7-L1	Line 8 880-T7-L1	Line 9 880-T7-L1	Line 10 880-T7-L1	Line 11 880-T7-L1	Line 12 880-T7-L1	Line 13 880-T7-L1
Oxides wt%								
SiO_2	37.04	37.23	37.46	37.49	37.05	37.07	37.45	37.46
TiO_2	0.33	0.40	0.19	0.30	0.49	0.60	0.58	0.55
Al_2O_3	32.15	32.37	32.42	32.22	32.36	31.86	32.41	33.16
Cr_2O_3	0.01	0.07	0.03	0.00	0.08	0.00	0.03	0.02
FeO	8.37	8.53	8.72	9.42	8.18	8.12	7.66	7.71
MgO	6.15	6.25	6.02	6.01	6.32	6.54	6.59	6.31
CaO	0.38	0.35	0.36	0.39	0.39	0.58	0.47	0.48
MnO	0.05	0.00	0.04	0.00	0.00	0.00	0.00	0.04
Na_2O	2.25	2.16	2.19	2.26	2.20	2.19	2.33	2.11
K_2O	0.09	0.05	0.05	0.03	0.02	0.05	0.02	0.02
F	0.08	0.14	0.01	0.03	0.00	0.13	0.03	0.03
Cl	0.34	0.10	0.03	0.02	0.01	0.04	0.02	0.01
H_2O*	3.55	3.61	3.69	3.70	3.69	3.62	3.70	3.72
B_2O_3*	10.66	10.73	10.74	10.77	10.71	10.69	10.79	10.84
Li_2O*	0.00	0.00	0.00	0.00	0.00	0.00	0.00	0.00
Total	101.45	102.00	101.97	102.64	101.50	101.48	102.09	102.45
O=F	0.04	0.06	0.01	0.01	0.00	0.05	0.01	0.01
Total*	101.41	101.94	101.96	102.63	101.50	101.43	102.08	102.44
Cation apfu								
Si	6.04	6.03	6.06	6.05	6.01	6.03	6.03	6.00
Ti	0.04	0.05	0.02	0.04	0.06	0.07	0.07	0.07
Cr	0.00	0.01	0.00	0.00	0.01	0.00	0.00	0.00
Al	6.18	6.18	6.18	6.13	6.19	6.11	6.15	6.26
Fe^{2+}	1.14	1.15	1.18	1.27	1.11	1.10	1.03	1.03
Mg	1.49	1.51	1.45	1.45	1.53	1.59	1.58	1.51
Mn	0.01	0.00	0.01	0.00	0.00	0.00	0.00	0.01
Ca	0.07	0.06	0.06	0.07	0.07	0.10	0.08	0.08
Na	0.71	0.68	0.69	0.71	0.69	0.69	0.73	0.66
K	0.02	0.01	0.01	0.01	0.00	0.01	0.00	0.00
B	3.00	3.00	3.00	3.00	3.00	3.00	3.00	3.00
F	0.04	0.07	0.01	0.01	0.00	0.06	0.02	0.02
Cl	0.09	0.03	0.01	0.01	0.00	0.01	0.01	0.00
H	3.86	3.90	3.98	3.98	4.00	3.93	3.98	3.98
CatSum	18.70	18.67	18.67	18.71	18.68	18.70	18.69	18.63

SAMPLE	**880**							**C23**		
Spot analysis	Line 14 880-T7-L1	Line 15 880-T7-L1	Line 15 880-R2-65	Line 15 880-R2-66	Line 15 880-R3-67	Line 15 880-R3-68	Line 15 880-R3-69	C23-1	C23-2	C23-3
Oxides wt%										
SiO_2	38.44	37.13	0.03	0.05	0.50	0.15	0.04	37.02	37.27	37.27
TiO_2	0.54	0.36	98.26	98.74	96.54	94.83	98.85	0.45	0.50	0.67
Al_2O_3	33.85	33.52	0.02	0.05	0.32	0.06	0.03	32.11	32.22	31.86
Cr_2O_3	0.03	0.00	0.00	0.00	0.04	0.00	0.00	0.01	0.00	0.00
FeO	7.83	6.49	0.38	0.39	0.64	1.79	0.56	8.07	8.18	8.36
MgO	6.64	6.55	0.00	0.00	0.01	0.00	0.00	6.57	6.64	6.98
CaO	0.85	1.11	0.02	0.02	0.07	0.03	0.05	0.25	0.26	0.42
MnO	0.03	0.00	0.02	0.03	0.01	0.02	0.03	0.00	0.00	0.00
Na_2O	2.32	1.90	0.02	0.03	0.00	0.04	0.06	2.50	2.57	2.51
K_2O	0.06	0.04	0.01	0.01	0.04	0.03	0.01	0.03	0.02	0.03
F	0.00	0.00	0.00	0.00	0.00	0.00	0.00	0.18	0.09	0.09
Cl	0.01	0.01	0.00	0.00	0.00	0.01	0.02	0.00	0.01	0.00
H_2O*	3.85	3.72	3.63	3.65	3.61	3.54	3.65	3.60	3.67	3.68
B_2O_3*	11.16	10.80	10.52	10.58	10.46	10.26	10.60	10.69	10.77	10.80
Li_2O*	0.00	0.00	0.00	0.00	0.00	0.00	0.00	0.00	0.00	0.00
Total	105.61	101.64	112.90	113.56	112.24	110.77	113.89	101.48	102.20	102.68
O=F	0.00	0.00	0.00	0.00	0.00	0.00	0.00	0.08	0.04	0.04
Total*	105.61	101.64	112.90	113.56	112.24	110.77	113.89	101.40	102.16	102.64
Cation apfu										
Si	5.99	5.97	0.01	0.01	0.08	0.03	0.01	6.02	6.02	6.00
Ti	0.06	0.04	12.21	12.20	12.06	12.08	12.19	0.05	0.06	0.08
Cr	0.00	0.00	0.00	0.00	0.01	0.00	0.00	0.00	0.00	0.00
Al	6.22	6.35	0.00	0.01	0.06	0.01	0.01	6.15	6.13	6.05
Fe^{2+}	1.02	0.87	0.05	0.05	0.09	0.25	0.08	1.10	1.10	1.13
Mg	1.54	1.57	0.00	0.00	0.00	0.00	0.00	1.59	1.60	1.68
Mn	0.00	0.00	0.00	0.00	0.00	0.00	0.00	0.00	0.00	0.00
Ca	0.14	0.19	0.00	0.00	0.01	0.01	0.01	0.04	0.05	0.07
Na	0.70	0.59	0.01	0.01	0.00	0.01	0.02	0.79	0.80	0.78
K	0.01	0.01	0.00	0.00	0.01	0.01	0.00	0.01	0.00	0.01
B	3.00	3.00	3.00	3.00	3.00	3.00	3.00	3.00	3.00	3.00
F	0.00	0.00	0.00	0.00	0.00	0.00	0.00	0.09	0.05	0.04
Cl	0.00	0.00	0.00	0.00	0.00	0.00	0.01	0.00	0.00	0.00
H	4.00	4.00	4.00	4.00	4.00	4.00	3.99	3.91	3.95	3.95
CatSum	18.69	18.61	15.29	15.29	15.33	15.40	15.31	18.75	18.76	18.79

SAMPLE									**C20**							**C9**				
Spot analysis	C23-4	C23-5	C23-6	C23-7	C23-8	C23-9	C23-10	C23-11	C20a-12	C20a-13	C20a-16	C20a-17	C20a-18	C20a-19	C23-22	C9-24	C9-26	C9-27	C9-28	C9-29
Oxides wt%																				
SiO_2	36.76	37.05	36.79	32.77	37.29	37.12	36.78	34.09	36.80	37.14	37.06	36.59	37.58	37.38	37.79	45.11	49.10	53.82	52.55	48.33
TiO_2	0.79	0.27	0.78	0.17	0.43	0.87	0.82	0.08	1.03	0.84	0.91	0.92	0.73	0.63	0.64	0.52	0.49	0.38	0.44	0.58
Al_2O_3	31.61	32.30	31.36	28.83	31.92	31.00	31.33	27.88	30.84	32.91	31.23	31.01	32.60	34.29	30.86	30.53	30.55	31.99	30.75	30.37
Cr_2O_3	0.03	0.04	0.00	0.04	0.05	0.03	0.05	0.00	0.06	0.06	0.01	0.05	0.27	0.27	0.00	0.00	0.00	0.00	0.00	0.00
FeO	8.37	8.17	8.04	15.99	8.50	7.81	8.26	17.06	10.03	6.04	10.87	9.91	7.09	5.99	10.97	10.40	7.64	4.21	6.57	8.01
MgO	6.69	6.28	6.82	4.30	6.58	6.86	6.85	4.04	6.00	7.89	5.45	5.83	6.88	6.50	3.89	4.15	3.23	2.05	2.94	3.44
CaO	0.30	0.16	0.42	0.12	0.10	0.21	0.33	0.04	0.38	1.03	0.18	0.35	0.45	0.40	0.11	0.11	0.08	0.05	0.05	0.08
MnO	0.01	0.01	0.02	0.06	0.06	0.00	0.00	0.08	0.03	0.02	0.00	0.01	0.00	0.00	0.00	0.01	0.05	0.01	0.00	0.04
Na_2O	2.56	2.46	2.50	2.99	2.48	2.64	2.49	2.74	2.62	1.93	2.58	2.49	2.21	1.84	1.97	2.05	1.33	0.89	1.23	1.45
K_2O	0.01	0.02	0.03	0.02	0.03	0.02	0.02	0.02	0.03	0.04	0.03	0.03	0.03	0.05	1.65	1.99	3.77	6.59	4.74	3.29
F	0.10	0.04	0.10	0.00	0.02	0.19	0.18	0.00	0.14	0.17	0.00	0.00	0.02	0.00	0.20	0.19	0.26	0.02	0.08	0.18
Cl	0.03	0.00	0.01	0.00	0.00	0.00	0.00	0.01	0.00	0.01	0.00	0.00	0.02	0.02	0.00	0.01	0.04	0.00	0.00	0.01
H_2O*	3.63	3.66	3.62	3.42	3.69	3.58	3.59	3.44	3.60	3.68	3.69	3.65	3.73	3.76	3.55	3.90	3.98	4.31	4.23	3.99
B_2O_3*	10.67	10.67	10.64	9.91	10.73	10.64	10.65	9.98	10.65	10.90	10.69	10.59	10.86	10.90	10.58	11.58	11.92	12.52	12.36	11.82
Li_2O*	0.00	0.00	0.00	0.00	0.00	0.00	0.00	0.00	0.00	0.00	0.00	0.00	0.00	0.00	0.00	0.00	0.00	0.00	0.00	0.00
Total	101.55	101.14	101.13	98.61	101.87	100.97	101.35	99.46	102.23	102.64	102.70	101.42	102.46	102.01	102.22	110.57	112.43	116.84	115.95	111.60
O=F	0.04	0.02	0.04	0.00	0.01	0.08	0.08	0.00	0.06	0.07	0.00	0.00	0.01	0.00	0.09	0.08	0.11	0.01	0.03	0.08
Total*	101.51	101.12	101.09	98.61	101.86	100.89	101.27	99.46	102.17	102.57	102.70	101.42	102.45	102.01	102.13	110.48	112.32	116.83	115.92	111.52
Cation apfu																				
Si	5.99	6.03	6.01	5.75	6.04	6.07	6.00	5.94	6.01	5.92	6.03	6.01	6.02	5.96	6.21	6.77	7.16	7.47	7.39	7.10
Ti	0.10	0.03	0.10	0.02	0.05	0.11	0.10	0.01	0.13	0.10	0.11	0.11	0.09	0.08	0.08	0.06	0.05	0.04	0.05	0.06
Cr	0.00	0.01	0.00	0.01	0.01	0.00	0.01	0.00	0.01	0.01	0.00	0.01	0.03	0.03	0.00	0.00	0.00	0.00	0.00	0.00
Al	6.07	6.20	6.04	5.96	6.10	5.97	6.03	5.72	5.93	6.19	5.99	6.00	6.15	6.45	5.97	5.40	5.25	5.23	5.09	5.26
Fe^{2+}	1.14	1.11	1.10	2.35	1.15	1.07	1.13	2.49	1.37	0.81	1.48	1.36	0.95	0.80	1.51	1.31	0.93	0.49	0.77	0.98
Mg	1.62	1.52	1.66	1.12	1.59	1.67	1.67	1.05	1.46	1.88	1.32	1.43	1.64	1.55	0.95	0.93	0.70	0.42	0.62	0.75
Mn	0.00	0.00	0.00	0.01	0.01	0.00	0.00	0.01	0.00	0.00	0.00	0.00	0.00	0.00	0.00	0.00	0.01	0.00	0.00	0.01
Ca	0.05	0.03	0.07	0.02	0.02	0.04	0.06	0.01	0.07	0.18	0.03	0.06	0.08	0.07	0.02	0.02	0.01	0.01	0.01	0.01
Na	0.81	0.78	0.79	1.02	0.78	0.84	0.79	0.93	0.83	0.60	0.81	0.79	0.69	0.57	0.63	0.60	0.38	0.24	0.34	0.41
K	0.00	0.00	0.01	0.00	0.01	0.00	0.00	0.01	0.01	0.01	0.01	0.01	0.01	0.01	0.35	0.38	0.70	1.17	0.85	0.62
B	3.00	3.00	3.00	3.00	3.00	3.00	3.00	3.00	3.00	3.00	3.00	3.00	3.00	3.00	3.00	3.00	3.00	3.00	3.00	3.00
F	0.05	0.02	0.05	0.00	0.01	0.10	0.09	0.00	0.07	0.09	0.00	0.00	0.01	0.00	0.11	0.09	0.12	0.01	0.04	0.08
Cl	0.01	0.00	0.00	0.00	0.00	0.00	0.00	0.00	0.00	0.00	0.00	0.00	0.00	0.00	0.00	0.00	0.01	0.00	0.00	0.00
H	3.94	3.98	3.95	4.00	3.99	3.90	3.91	4.00	3.93	3.91	4.00	4.00	3.98	4.00	3.89	3.90	3.87	3.99	3.96	3.91
CatSum	18.79	18.72	18.77	19.26	18.75	18.76	18.78	19.16	18.81	18.68	18.78	18.78	18.65	18.51	18.71	18.46	18.20	18.07	18.11	18.22

SAMPLE	**C9**											**C17**
Spot analysis	C9-30	C9-31	C9-32	C9-33	C9-34	C9-35	C9-36	C9-37	C9-38	C9-39	C9-40	C17
Oxides wt%												
SiO_2	51.55	44.28	44.00	55.38	65.65	45.13	41.75	95.76	54.75	47.92	45.44	37.22
TiO_2	0.49	0.52	0.51	0.41	0.46	0.61	0.60	0.15	0.41	0.43	0.55	0.51
Al_2O_3	28.71	29.98	30.17	25.50	22.24	33.70	30.06	7.40	27.76	28.69	29.66	32.43
Cr_2O_3	0.00	0.00	0.00	0.00	0.00	0.00	0.00	0.00	0.00	0.00	0.00	0.00
FeO	8.28	11.14	10.91	9.66	10.22	7.60	8.03	1.73	8.03	7.98	10.52	9.00
MgO	3.53	4.24	4.27	3.84	3.60	7.50	6.77	0.92	3.18	3.13	4.10	6.15
CaO	0.11	0.15	0.14	0.13	0.12	0.67	0.38	0.04	0.09	0.11	0.15	0.53
MnO	0.04	0.04	0.02	0.01	0.06	0.06	0.05	0.01	0.00	0.03	0.04	0.03
Na_2O	1.51	2.10	2.07	2.02	1.85	2.44	2.44	0.41	1.63	1.49	2.15	2.18
K_2O	3.26	1.26	1.35	1.00	0.42	0.03	0.05	0.89	3.16	2.94	1.82	0.02
F	0.00	0.18	0.14	0.00	0.04	0.03	0.09	0.00	0.02	0.15	0.10	0.00
Cl	0.00	0.01	0.02	0.00	0.02	0.00	0.00	0.01	0.01	0.00	0.02	0.00
H_2O*	4.17	3.86	3.86	4.23	4.56	4.18	3.80	5.10	4.25	3.89	3.93	3.72
B_2O_3*	12.09	11.42	11.39	12.27	13.30	12.16	11.15	14.80	12.37	11.49	11.53	10.78
Li_2O*	0.00	0.00	0.00	0.00	0.00	0.00	0.00	0.00	0.00	0.00	0.00	0.00
Total	113.76	109.18	108.86	114.47	122.55	114.11	105.18	127.23	115.66	108.26	110.00	102.57
O=F	0.00	0.07	0.06	0.00	0.02	0.01	0.04	0.00	0.01	0.07	0.04	0.00
Total*	113.76	109.10	108.80	114.47	122.53	114.10	105.14	127.23	115.65	108.19	109.96	102.57
Cation apfu												
Si	7.41	6.74	6.71	7.84	8.58	6.45	6.51	11.24	7.69	7.25	6.85	6.00
Ti	0.05	0.06	0.06	0.04	0.05	0.07	0.07	0.01	0.04	0.05	0.06	0.06
Cr	0.00	0.00	0.00	0.00	0.00	0.00	0.00	0.00	0.00	0.00	0.00	0.00
Al	4.86	5.38	5.42	4.26	3.43	5.68	5.52	1.02	4.60	5.11	5.27	6.16
Fe^{2+}	1.00	1.42	1.39	1.14	1.12	0.91	1.05	0.17	0.94	1.01	1.33	1.21
Mg	0.76	0.96	0.97	0.81	0.70	1.60	1.57	0.16	0.67	0.71	0.92	1.48
Mn	0.01	0.01	0.00	0.00	0.01	0.01	0.01	0.00	0.00	0.00	0.01	0.00
Ca	0.02	0.02	0.02	0.02	0.02	0.10	0.06	0.01	0.01	0.02	0.02	0.09
Na	0.42	0.62	0.61	0.55	0.47	0.68	0.74	0.09	0.44	0.44	0.63	0.68
K	0.60	0.24	0.26	0.18	0.07	0.01	0.01	0.13	0.57	0.57	0.35	0.00
B	3.00	3.00	3.00	3.00	3.00	3.00	3.00	3.00	3.00	3.00	3.00	3.00
F	0.00	0.08	0.07	0.00	0.02	0.01	0.05	0.00	0.01	0.07	0.05	0.00
Cl	0.00	0.00	0.01	0.00	0.00	0.00	0.00	0.00	0.00	0.00	0.01	0.00
H	4.00	3.91	3.92	4.00	3.98	3.99	3.95	4.00	3.99	3.93	3.95	4.00
CatSum	18.12	18.45	18.46	17.85	17.43	18.49	18.54	15.84	17.97	18.15	18.44	18.70

12: APPENDIX 4: LA-ICP-MS DATASET - TRACE ELEMENTS

	Element [ppm]															
Spot analysis	Li7	1se Li7	Be9	1se Be9	Na23	1se Na23	Mg25	1se Mg25	Si29	1se Si29	K39	1se K39	Ca43	1se Ca43	Ca44	1se Ca44
NIST612	42.35	1.96	38.77	1.75	106131.77	4319.55	78.33	3.55	71.86	2.27	67.57	3.84	87365.32	3653.82	87461.63	3894.88
NIST612(Copy1)	39.53	1.83	36.9	1.66	101961.37	4150.5	75.8	3.43	71.86	2.27	61.95	3.54	82046.03	3431.05	81716.89	3638.52
NIST612(Copy2)	42.48	1.96	38.16	1.72	104305.46	4247.79	79.07	3.59	71.86	2.27	67.08	3.82	86336.31	3611.72	87615.67	3901.91
BCR2g	8.85	0.43	1.99	0.17	20570.95	838.41	22855.29	963.38	54.4	1.72	10934.57	601	42999.11	1808	46261.92	2061.79
BCR2g(Copy1)	9.08	0.44	1.72	0.15	21155.84	863.06	23080.16	974.05	54.4	1.72	11028.48	606.88	42758.89	1799.37	47583.96	2122.39
FC21.1_torm1	16.98	0.83	4.27	0.38	14178.93	579.51	44418.09	1878.45	37	1.17	113.45	6.55	2416.26	196.17	1895.64	88.59
FC21.1_torm2	25.65	1.23	5.33	0.43	13692.97	560.45	44715.98	1894.33	37	1.17	143.69	8.18	2228.91	191.47	2040.43	95
FC21.1_matrice1	91.58	4.26	5.4	0.41	4656.19	190.96	19148.14	813.01	41.3	1.31	38514.71	2132.12	1606.13	140.32	1395.08	65.49
FC21.1_matrice2	86.46	4.04	5.52	0.45	2602.89	107.11	17729.94	754.82	41.3	1.31	37798.99	2098.27	887.99	128.82	857.03	42.88
FC21.1_torm_matrice3	96.5	4.66	6.36	0.84	2880.93	119.39	21117.41	904.87	37	1.18	35451.61	1976.06	36076.15	1628.28	40717.37	1841.1
FC21.1_matrice4	91.62	4.33	5.86	0.55	3056.12	126.42	21133.02	905.14	39.1	1.24	36579.54	2044.16	1484.13	163.07	1073.16	54
FC21.1_matrice5	45.77	2.18	8.98	0.62	14406.62	596.14	43250.79	1855.98	37	1.17	199.94	11.38	2102.93	179.56	1869.09	88.16
FC21.1_matrice6	38.98	1.87	1.66	0.22	32258.36	1338.37	6893.21	297.39	46.2	1.46	15928.09	896.91	1279.55	156.47	1473.13	70.88
FC21.1_torm_matrice7	76.83	3.65	5.37	0.45	12730.09	529.95	27386.14	1183.58	41.3	1.31	17271.02	976.88	1480.44	165.48	1494.17	72.19
FC21.1_torm_matrice8	86.07	4.09	3.99	0.35	11519.16	481.12	23014.23	998.34	37	1.17	22155.88	1259.06	1161.28	144.81	1061.65	52.6
FC21.1_matrice9	118.32	5.65	3.85	0.4	9547.69	400.34	24571.37	1070.7	41.3	1.31	27280.95	1558.3	932.22	153.99	977.38	50.44
AV5_1_torm_matrice1	602.96	28.67	2.61	0.33	11152.02	469.39	16676.73	730.18	48.1	1.52	13313.79	764.58	944.54	197.66	307.33	29.63
AV5_1_matrice2	214.16	10.29	11.86	0.92	385.08	18.67	6949.4	306.65	48.1	1.53	60125.66	3472.55	711.54	190.94	479.44	34.2
AV5_4_torm_matrice3	784.74	37.81	5.96	0.87	13374.75	568.58	20769.56	920.9	48.1	1.53	17948.81	1043.57	938.9	296	495.73	46.33
AV5_4_matrice4	180.71	8.74	9.85	0.68	534.73	24.2	6168.56	274.27	48.1	1.52	49936.79	2918.56	<366.99	165.51	335.67	27.17
AV5_4_matrice5	197.76	9.65	11.65	0.91	252.83	14.33	7387.75	330.74	48.1	1.53	60355.34	3550.94	<352.28	187.92	344.88	30.7
AV5_5_torm_matrice6	441.4	21.63	2.08	0.43	11453.38	493.55	19147.36	861.41	37	1.18	17622.9	1044.44	1429.52	247.1	1003.54	58.98
NIST612(Copy3)	41.52	2.04	36.79	1.73	101936.79	4404.07	75.56	3.63	71.86	2.27	66.87	4.1	84982.84	3769.08	83940.14	3986.17
NIST612(Copy4)	42.29	2.09	38.16	1.8	103636.13	4500.74	77.28	3.74	71.86	2.27	68.96	4.25	85204.48	3799.12	85641.99	4090.55
BCR2g(Copy2)	8.9	0.46	1.68	0.15	21392.45	934.11	23503.37	1071.42	54.4	1.72	11307	683.92	43874.71	1974.63	47177.34	2267.29
BCR2g(Copy3)	9.09	0.47	1.98	0.17	21851.82	959.45	22925.14	1051.48	54.4	1.72	11135.11	678.62	42837.66	1938.9	47018.61	2273.57
AV5_5_matrice7	206.09	10.38	10.22	0.73	442.55	21.12	6745.63	312.21	48.1	1.52	57742.55	3547.05	686.86	161.61	455.15	31.16
AV5_5_matrice8	227.5	11.54	11.28	0.84	352.02	17.68	6663.55	310.69	48.1	1.53	61096.02	3783.12	580.82	170.25	497.04	33.59
AV5_6_torm1	300.82	15.39	1.92	0.37	7774.13	348.05	11188.79	525.43	36.6	1.16	13106.76	818.55	1013.67	208.51	390.6	33.59
AV5_6_torm2	403.46	20.71	2.26	0.34	8000.49	360.16	11239.43	530.69	36.6	1.16	15706.07	988.75	781.57	181.14	500.32	34.68
AV5_8_torm3	548.97	28.37	1.06	0.26	15154.12	686.48	32639.22	1550.09	36.6	1.16	1182.83	75.2	1710.03	225.17	1345.87	74.51
AV5_8_torm4	62.68	3.35	0.56	0.19	14295	651.72	34674.14	1658.24	36.6	1.16	2265.81	145.17	1659.87	229.78	1607.34	87.67
AV5_3_torm_matrice9	386.1	20.33	1.98	0.45	6868.24	315.68	11645.59	563.28	36.6	1.17	14955.35	966.36	320.4	225.9	265.11	33.19
AV5_3_matrice10	189.07	9.98	11.04	0.71	<16.10	8.26	6699.04	325.02	48.1	1.52	56073.69	3651.8	524.15	143.26	313.46	24.37
AV5_3_matrice11	141.14	7.5	8.89	0.57	82.38	6.54	5362.08	262.08	36.6	1.16	42790.26	2811.56	281.63	108.3	279.18	20.29
880_1_torm1	7.85	0.49	7.68	0.68	15424.39	722.07	43876.14	2159.61	37.2	1.18	152.24	10.57	5053.64	367.67	4870.88	256.72
880_1_torm2	7.63	0.49	6	0.63	15261.25	719.47	36719.46	1821.76	37.2	1.18	214.77	14.65	3271.4	283.47	3184.03	171.06
880_1_torm3	6.29	0.4	4.94	0.48	12958.72	615.02	21701.46	1084.82	37.2	1.18	12856	868.18	2254.18	220.49	2256.49	122.54
880_3_torm4	19.07	1.08	3.98	0.37	16808.33	803.19	32543.03	1638.57	37.2	1.18	139.08	9.67	1806.96	179.51	1511.81	83.47
880_3_torm5	20.31	1.16	4.89	0.43	15072.58	725.53	32733.89	1661.44	37.2	1.18	177.05	12.36	2527.25	212.81	2313.29	126.61
880_q1_qtz1	107.38	14.13	<4.43	1.37	2023.51	632.72	<16.08	19.81	99	4.6	<167.84	152.57	<13357.76	12216.17	<1705.74	1553.63
880_q1_qtz2	88.32	5.31	2.75	0.85	213.39	23.77	4.32	1.74	99	3.15	275.15	20.22	<435.26	398.36	493.42	64.7
880_6_torm6	27.42	1.6	4.56	0.46	13860.39	682.32	34760.39	1808.14	37.2	1.18	148.83	10.86	2986.09	267.04	2630.53	147.96
NIST612(Copy5)	41.46	2.37	37.42	1.95	105773.45	5242.22	79.04	4.36	71.86	2.27	64.62	4.72	86010.84	4380.18	86530.74	4775.07

	Element [ppm]															
Spot analysis	Li7	1se Li7	Be9	1se Be9	Na23	1se Na23	Mg25	1se Mg25	Si29	1se Si29	K39	1se K39	Ca43	1se Ca43	Ca44	1se Ca44
NIST612(Copy6)	42.03	2.42	37.95	2	103113.37	5149.41	78.49	4.37	71.86	2.27	67.81	4.98	86854.72	4457.02	85302.46	4745.77
BCR2g(Copy4)	9.33	0.56	1.57	0.15	21511.71	1082.63	24226.51	1291.11	54.4	1.72	11051.62	804.47	42058.52	2181.85	45892.06	2574.58
BCR2g(Copy5)	9.11	0.55	1.8	0.17	20343.38	1031.76	23264.06	1250.34	54.4	1.72	11106.71	816.26	43604.71	2279.15	45855.02	2593.71
880_6_torm7	9.2	0.6	3.7	0.42	15379.78	786.64	39424.11	2138.42	37.2	1.18	302.64	22.62	3860.14	300.28	3779.3	218.71
880_7_torm8	17.49	1.07	1.51	0.21	13103.81	675.32	36973.57	2022.06	37.2	1.18	106.3	8.22	2436.85	215.74	2236.32	131.28
880_7_torm9	16.55	1.02	1.68	0.22	11109.47	577.06	35668.98	1967.48	37.2	1.18	95.64	7.5	2224.92	205.13	2017.66	119.65
VSS3a_1_torm1	12.18	0.77	4.2	0.38	9465.9	495.59	31037.06	1726.84	37	1.17	2514.05	192.07	2784.56	218.55	2567.92	152.25
VSS3a_1_torm2	11.71	0.75	4.11	0.42	10828.47	571.48	35233.29	1977.6	38.5	1.22	1910.99	147.43	2817.39	229.63	2402.7	144.3
VSS3a_3a_matrice1	23.48	1.47	1.93	0.22	3834.72	204.07	7094.44	401.95	35.9	1.14	94.47	7.52	754.43	128.51	1058.81	65.51
VSS3a_4_torm3	12.98	0.86	6.47	0.65	10989.95	589.51	35296.23	2016.69	37.2	1.18	3779.21	297.24	2055.58	223.05	2289.05	141.02
VSS3a_4_qtz1	44.05	3.51	0.64	0.64	<63.16	103.14	1589.3	105.09	99	3.2	7194.82	572.75	2586.46	1081.03	2175.97	201.78
VSS3a_4_torm4	8.8	0.58	5.99	0.48	6955.46	379.01	24817.83	1442.3	37.1	1.18	1835.17	147.12	2082.96	194.05	2041.67	126.71
VSS3a_4_torm_matrice2	22.83	1.52	4.45	0.57	5743.74	315.78	18327.32	1075.82	42.8	1.36	161.19	13.27	1860.94	221.97	1598.96	103.07
VSS3a_7_qtz2	<14.68	13.38	<0.00	<0.00	<2267.59	2503.63	<80.27	56.9	99	8.7	<501.85	418.28	<40817.21	33705.92	<4963.78	4068.35
VSS3a_7_qtz3	22.91	4.71	<1.46	0.45	<340.68	331.43	7.01	10.71	99	3.71	200.12	76.07	<6129.28	5966.89	<742.15	724.29
VSS3a_7_qtz4	50.14	8.1	<0.00	<0.00	188453.55	11156.48	475.43	87.35	99	4.03	607.72	118.8	11732	8766.13	2482.33	1077.04
VSS3a_5_torm5	15.47	1.04	5.05	0.44	8973.41	509.04	29943.43	1818.38	36.6	1.16	141.66	12.02	2388.64	196.13	2259.19	145.32
VSS3a_5_torm6	11.56	0.79	5.71	0.49	10510.03	601.06	35680.85	2186.05	36	1.14	2808.18	238.36	2878.8	224.44	2905.67	187.94
VSS3a_4_matrice3	14.85	1.01	3.98	0.36	4054.37	233.81	13699.66	846.95	35.9	1.14	100.67	8.74	1101.63	132.01	1219.3	80.67
VSS3a_4_matrice4	13.17	0.93	5.38	0.53	5123.26	297.92	16996.04	1060.44	35.9	1.14	103.15	9.08	1292.84	160.85	1376.35	92.44
BCR2g(Copy6)	8.49	0.59	1.84	0.19	19758.6	1157.44	22516.64	1416.25	54.4	1.72	10531.21	919.3	39584.19	2386.08	42720.87	2808.02
BCR2g(Copy7)	8.76	0.61	1.66	0.18	19847.03	1172.08	22310.11	1415.68	54.4	1.72	10206.56	899.32	37974	2307.58	42826.96	2838.36
NIST612(Copy9)	40.59	2.8	37.63	2.28	101184.1	6023.74	76.09	5.07	71.86	2.27	65.48	5.91	84063.61	5133.58	83919.16	5607.1
NIST612(Copy10)	42.01	2.92	38.28	2.33	106690.44	6403.18	75.97	5.1	71.86	2.27	66	6	84078.87	5175.07	85200.42	5739.79
NIST612(Copy11)	41.46	2.91	37.61	2.31	103220.52	6245.25	79.23	5.35	71.86	2.27	66.05	6.07	86204.69	5347.92	86098.8	5848.17
VSS3a_4_qtz1	272.94	19.44	0.53	0.31	82.89	23.34	88.17	8.63	99	3.15	1712.09	156.82	<621.27	422.36	1285.28	107.42
VSS3a_7_qtz2	20.19	1.57	<0.203	0.062	85.36	24.88	10.83	2.11	99	3.14	82.68	9.44	<873.70	460.58	1252.08	105.87
VSS3a_7_qtz3	79.38	5.82	<0.120	0.037	<27.67	18.58	25.71	3.37	99	3.14	364.14	34.24	<525.11	329.76	1492.68	115.34
VSS3a_7_qtz4	40.56	3.05	<0.00	<0.00	<38.26	23.13	14.69	2.4	99	3.14	266.71	25.58	<719.11	386.96	1357.14	109.49

Spot analysis	Sc45	1se Sc45	Ti49	1se Ti49	V51	1se V51	Cr53	1se Cr53	Mn55	1se Mn55	Co59	1se Co59	Ni60	1se Ni60	Cu65	1se Cu65	Zn66	1se Zn66
NIST612	42.13	1.76	47.98	2.04	40.37	1.76	40.71	2.88	39.39	1.93	35.88	1.57	38.22	1.83	37.26	1.64	38.16	1.66
NIST612(Copy1)	40.27	1.68	48.83	2.05	38.85	1.69	38.72	2.74	37.46	1.83	35.21	1.54	38.63	1.85	36.82	1.61	37.3	1.62
NIST612(Copy2)	41.65	1.74	47.13	2.01	39.18	1.71	40.35	2.86	39.22	1.92	35.28	1.55	39.24	1.88	37.43	1.65	38.81	1.69
BCR2g	27.93	1.18	14307.17	506.07	381.81	16.55	15.34	1.21	1315.39	64.08	33.69	1.48	10.01	0.55	15.68	0.83	134.9	5.54
BCR2g(Copy1)	27.55	1.16	14243.52	504.14	371.87	16.13	16.12	1.27	1343.85	65.54	34	1.5	10.8	0.58	15.75	0.83	138.35	5.69
FC21.1_torm1	12.8	0.58	2412.66	86.5	145.22	6.35	128.58	9.07	75.88	3.74	31.57	1.42	90.19	4.39	3.7	0.72	191.28	7.96
FC21.1_torm2	16.89	0.75	2820.69	101.01	163.49	7.15	136.14	9.59	127.92	6.29	26.8	1.21	87.01	4.24	7.66	0.8	195.28	8.12
FC21.1_matrice1	14.5	0.64	4086.71	145.87	130.76	5.73	97.03	6.89	382.73	18.79	18.06	0.83	44.36	2.23	56.03	2.52	152.86	6.37
FC21.1_matrice2	14.25	0.64	4501.98	161.07	124.23	5.47	101.64	7.29	314.55	15.49	12.06	0.58	34.37	1.81	21.22	1.18	134.24	5.67
FC21.1_torm_matrice3	15.42	0.8	3765.12	138.38	138.53	6.23	124.57	9.71	429.72	21.32	16.19	0.88	46.96	2.9	4.82	1.01	173.7	7.82
FC21.1_matrice4	13.83	0.65	4928.85	177.45	140.7	6.25	163.96	11.82	407.52	20.2	19.41	0.93	50.06	2.67	7.18	0.8	166.54	7.11
FC21.1_matrice5	36.01	1.56	3182.23	114.71	240.51	10.64	62.48	4.66	275.96	13.72	17.56	0.82	75.54	3.78	13.63	0.96	192.41	8.08
FC21.1_matrice6	8.3	0.4	405.22	15.55	40.31	1.82	17.29	1.57	136.94	6.85	1.046	0.085	10.64	0.69	4.15	0.71	40.36	1.97
FC21.1_torm_matrice7	15.85	0.72	2943.6	106.64	163.68	7.31	90.88	6.7	326.83	16.37	20.38	0.96	63.36	3.24	70.45	3.23	329.72	13.74
FC21.1_torm_matrice8	15.13	0.68	3315.2	119.97	127.77	5.72	74.88	5.54	378.86	19.05	24.5	1.13	69	3.48	91.98	4.09	366.23	15.23
FC21.1_matrice9	11.78	0.56	3691.79	134.33	114.82	5.19	88.85	6.7	571.5	28.87	32.95	1.54	102.56	5.2	120.46	5.4	507.96	21.21
AV5_1_torm_matrice1	13.22	0.64	3105.85	113.6	37.09	1.72	14.94	1.56	16.44	0.88	<0.070	0.033	1.08	0.25	8.4	1.03	313.19	13.25
AV5_1_matrice2	18.45	0.88	1421.18	53.4	30.34	1.44	11.19	1.41	7.06	0.42	<0.066	0.033	<0.31	0.19	39.61	2.16	64.62	3.13
AV5_4_torm_matrice3	28.5	1.41	5252.78	195.55	42.9	2.12	22.62	2.77	105.29	5.52	0.4	0.1	2.55	0.53	13.62	1.69	384.54	16.88
AV5_4_matrice4	16.72	0.77	1246.18	46.42	26.36	1.24	17.48	1.65	6.96	0.4	0.065	0.034	0.39	0.17	24.32	1.43	47.51	2.31
AV5_4_matrice5	17.71	0.85	1464.08	55.39	29.75	1.44	18	1.9	6.8	0.41	0.085	0.044	0.49	0.19	26.64	1.69	56.99	2.85
AV5_5_torm_matrice6	13.25	0.71	4971.24	185.67	78.72	3.76	58.56	5.22	43.32	2.35	4.38	0.32	7.51	0.8	11.29	1.32	254.44	11.35
NIST612(Copy3)	39.94	1.78	47.65	2.07	37.55	1.75	39.88	3.06	37.88	2	34.57	1.62	36.88	1.91	35.35	1.65	36.71	1.65
NIST612(Copy4)	41.13	1.84	48.92	2.14	39.98	1.88	40.14	3.11	38.54	2.04	35.01	1.65	39.58	2.07	36.03	1.69	38.06	1.72
BCR2g(Copy2)	27.86	1.26	14489.65	535.97	394.53	18.51	15.36	1.31	1365.59	72.61	35.26	1.68	11.82	0.68	14.91	0.86	138.89	6.02
BCR2g(Copy3)	27.48	1.25	14840.12	550.93	400.54	18.91	15.68	1.35	1305.09	69.88	34.92	1.67	11.02	0.64	15.38	0.87	140.54	6.11
AV5_5_matrice7	16.08	0.78	1459.86	55.61	29.95	1.47	12.91	1.4	7.05	0.42	0.13	0.039	0.55	0.17	31.96	1.77	62.14	2.97
AV5_5_matrice8	15.43	0.77	1440.41	55.44	28.08	1.4	10.91	1.35	6.58	0.4	<0.076	0.037	0.34	0.17	33.79	1.93	59.57	2.94
AV5_6_torm1	13.52	0.72	2941.46	113.13	32.72	1.67	17.96	2.09	11.81	0.72	5.11	0.34	12.26	1.02	7.79	1.1	173.8	8.05
AV5_6_torm2	10.55	0.56	2651.36	101.88	34.22	1.73	10.09	1.35	13.9	0.82	0.382	0.063	0.83	0.24	11.53	1.1	208.38	9.46
AV5_8_torm3	10.24	0.57	6714.64	256.88	121.82	6.03	115.74	9.83	137.69	7.72	13.95	0.78	40.14	2.54	2.6	0.91	246.98	11.3
AV5_8_torm4	5.26	0.34	3508.5	135.9	137.81	6.86	155.82	13.13	97.74	5.54	31.35	1.64	71.84	4.27	2.6	0.96	246.39	11.33
AV5_3_torm_matrice9	8.74	0.55	1803.59	72.67	20.56	1.15	4.33	1.18	11.14	0.73	<0.066	0.048	0.41	0.26	4.28	1.16	212.09	10.1
AV5_3_matrice10	16.37	0.81	1286.12	50.15	25.52	1.3	9.59	1.07	6.13	0.38	0.071	0.034	0.53	0.14	26.28	1.51	46.67	2.3
AV5_3_matrice11	13.24	0.66	1038.36	40.65	20.96	1.08	9.3	0.99	5.06	0.31	<0.048	0.023	0.35	0.11	24.48	1.36	38.32	1.89
880_1_torm1	22.14	1.14	7959.67	310.18	635.53	32.26	356.86	30.24	82.89	4.84	19.65	1.07	149.02	8.59	<2.47	1.13	10.77	1.32
880_1_torm2	37.43	1.89	2937.79	116.41	522.23	26.74	199.43	17.33	93.82	5.53	14.34	0.81	110.04	6.53	<1.76	0.95	10.45	1.18
880_1_torm3	18.32	0.95	2790.88	110.51	315.4	16.28	98.74	8.76	82.64	4.9	8.29	0.48	65.04	3.92	<1.69	0.82	10.62	1.02
880_3_torm4	62.17	3.09	1918.29	76.33	265.13	13.78	232.24	20.22	89.45	5.34	42.25	2.23	75.19	4.46	2.79	0.72	175.78	8.28
880_3_torm5	64.46	3.23	2698.37	107.62	264.18	13.85	219.92	19.37	92.17	5.55	41.86	2.23	86.42	5.16	1.73	0.75	169.6	8.06
880_q1_qtz1	<9.25	8.73	<26.63	32.8	<2.64	2.52	<53.33	52.27	<7.76	6.59	<2.84	2.28	<9.97	6.54	80.73	60.74	<59.74	54.75
880_q1_qtz2	11.65	0.9	1.65	1.34	0.2	0.11	3.59	1.95	0.58	0.26	<0.088	0.087	<0.35	0.3	<2.02	1.97	8.31	2.16
880_6_torm6	31.43	1.64	2804.19	113.85	268.13	14.41	155.9	14.29	67.69	4.2	20.24	1.14	36.21	2.37	3.45	1.01	155.98	7.63
NIST612(Copy5)	41.57	2.13	47.97	2.26	39.52	2.15	40.91	3.79	37.92	2.36	35.03	1.91	37.75	2.32	36.36	1.94	38.24	1.9

Spot analysis	Sc45	1se Sc45	Ti49	1se Ti49	V51	1se V51	Cr53	1se Cr53	Mn55	1se Mn55	Co59	1se Co59	Ni60	1se Ni60	Cu65	1se Cu65	Zn66	1se Zn66
NIST612(Copy6)	40.56	2.1	48.65	2.3	39.21	2.15	38.66	3.63	38.22	2.4	35.92	1.97	38.29	2.38	37.33	2	38.77	1.94
BCR2g(Copy4)	25.95	1.36	14324.43	584.55	397.56	21.85	15.46	1.56	1401.32	88.59	35.34	1.96	11.58	0.78	15.56	0.97	137.32	6.69
BCR2g(Copy5)	26.67	1.41	14482.32	594.31	398.34	22.08	15.39	1.57	1348.99	86.06	35.73	2	11.34	0.77	16.36	1.02	135.61	6.66
880_6_torm7	30.55	1.66	3225.68	134.5	582.12	32.58	176.09	16.93	528.26	34.05	15.68	0.93	151.8	9.69	9.72	1.14	37.45	2.21
880_7_torm8	5.91	0.36	2722.71	113.9	201.61	11.4	147.15	14.24	44.34	2.9	24.47	1.42	103.78	6.68	<1.65	0.74	172.56	8.66
880_7_torm9	6.59	0.4	2346.76	98.82	153.95	8.78	168.13	16.39	50.16	3.31	22.01	1.29	61.75	4.07	<1.71	0.74	169.02	8.53
VSS3a_1_torm1	11.73	0.67	3399.74	143.57	138.42	7.97	90.49	9	213.53	14.15	6.37	0.4	44.83	3.02	3.65	0.73	76.58	4
VSS3a_1_torm2	12.95	0.75	3358.78	142.97	163.96	9.52	114.84	11.54	324.75	21.71	7.46	0.47	42.91	2.96	5.22	0.79	86.38	4.55
VSS3a_3a_matrice1	7.06	0.42	3823.82	163.16	85.27	5	55.9	5.73	55.07	3.73	5.39	0.34	32.57	2.25	6.03	0.69	34.94	1.94
VSS3a_4_torm3	16.47	0.98	4008.5	173.05	194.32	11.5	124.78	12.89	279.49	19.05	4.57	0.33	30.61	2.29	2.58	0.87	96.91	5.24
VSS3a_4_qtz1	16.84	1.68	158.33	18.93	5.21	0.78	18.58	6.11	9.1	1.15	0.69	0.35	10.2	2.5	9.56	5.19	45.84	6.37
VSS3a_4_torm4	13.68	0.8	2788.09	121.36	153.57	9.22	87.06	9.09	182.79	12.68	6.46	0.42	43.77	3.07	5.81	0.82	64.17	3.48
VSS3a_4_torm_matrice2	11.01	0.7	2274.34	101.1	120.64	7.36	47.43	5.38	100.92	7.1	7.47	0.53	44.16	3.33	6.22	0.99	52.54	3.12
VSS3a_7_qtz2	<27.50	22.25	<98.77	89.88	<6.43	5.99	<156.98	104.38	<24.24	19.36	<9.36	4.45	<37.05	24.76	<194.75	161.5	<168.26	137.88
VSS3a_7_qtz3	<4.26	4.09	<14.01	13	<1.05	0.67	<24.46	21.82	<3.32	3.06	<1.04	1.19	<4.29	4.69	<28.99	27.69	<26.40	26.75
VSS3a_7_qtz4	9.04	6.33	1312.8	159.45	<1.87	1.44	<36.16	26.81	12.98	5.54	<2.10	1.39	11.12	9.7	2038.7	153.13	<41.10	37.39
VSS3a_5_torm5	13.24	0.81	3334.59	149.55	126.65	7.95	84.18	9.22	217.87	15.81	8.06	0.53	55.45	4.04	<1.29	0.59	65.85	3.67
VSS3a_5_torm6	18.01	1.1	3722.14	167.99	189.72	12	236.47	25.86	272.68	19.96	6.87	0.47	53.03	3.92	2.77	0.67	85.42	4.75
VSS3a_4_matrice3	8.86	0.56	1714.03	78.13	78.17	5	46.51	5.26	80	5.92	4.85	0.33	36.51	2.74	7.01	0.71	39.6	2.29
VSS3a_4_matrice4	9.8	0.63	2199.78	101.24	94.44	6.11	58.59	6.75	89	6.65	6.44	0.46	42.99	3.32	9.55	0.94	48.91	2.89
BCR2g(Copy6)	26.48	1.63	14253.33	652.75	370.76	24.04	14.51	1.74	1250.15	93.95	32.65	2.13	10.27	0.83	15.15	1.06	134.11	7.45
BCR2g(Copy7)	26.16	1.62	13752.54	633.86	373.51	24.43	13.98	1.71	1250.16	94.8	33.08	2.18	11.2	0.9	14.22	1.04	131.63	7.36
NIST612(Copy9)	40.34	2.51	48.51	2.56	38.89	2.57	37.05	4.3	37.05	2.84	33.92	2.25	37.51	2.87	37.05	2.36	37.74	2.18
NIST612(Copy10)	41.1	2.57	47.68	2.52	38.99	2.6	39.77	4.65	38.54	2.98	35.33	2.36	39.49	3.04	37.21	2.39	37.9	2.2
NIST612(Copy11)	42.04	2.66	47.82	2.54	39.95	2.69	43.12	5.08	40.34	3.15	36.61	2.47	39.03	3.04	36.43	2.36	37.72	2.2
VSS3a_4_qtz1	13.54	1.07	2.7	1.47	0.31	0.11	<2.31	1.43	1.03	0.28	<0.130	0.1	3.19	0.76	<2.93	2.01	8.6	1.96
VSS3a_7_qtz2	9.83	0.8	2.99	1.45	<0.162	0.089	5.18	1.88	0.59	0.27	<0.165	0.085	1.78	0.5	<4.01	2.14	<3.37	1.76
VSS3a_7_qtz3	10.36	0.81	3.95	1.36	<0.084	0.063	<1.75	1.16	1.8	0.28	<0.111	0.068	1.15	0.43	<2.41	1.54	<1.99	1.28
VSS3a_7_qtz4	11.36	0.88	<1.64	1.02	0.133	0.075	<2.48	1.42	<0.40	0.23	<0.164	0.074	0.78	0.42	<3.37	1.88	<2.74	1.5

Spot analysis	Ga71	1se Ga71	Rb85	1 Rb85	Sr88	1se Sr88	Y89	1se Y89	Zr90	1se Zr90	Nb93	1se Nb93	Mo95	1se Mo95	Cd111	1se Cd111	In115	1se In115
NIST612	36.82	2.27	32.38	1.3	77.69	2.63	38.12	1.38	35.27	1.29	38.47	1.5	38.41	1.69	28.19	1.7	43.38	1.85
NIST612(Copy1)	34.11	2.11	30.59	1.23	75.14	2.54	37.61	1.36	35.61	1.3	36.96	1.44	38.48	1.69	27.9	1.67	42.03	1.79
NIST612(Copy2)	37.39	2.31	31.94	1.28	76.4	2.59	38.92	1.4	36.64	1.34	38.76	1.51	37.65	1.66	27.76	1.67	42.62	1.82
BCR2g	19.49	1.21	43.65	1.75	261.95	8.84	23.59	0.86	122.31	4.44	10.35	0.42	237.23	10.17	0.23	0.058	0.098	0.0091
BCR2g(Copy1)	19.41	1.21	43.93	1.76	264.2	8.92	24.51	0.89	126.69	4.6	10.63	0.43	248.74	10.67	0.229	0.052	0.1056	0.0095
FC21.1_torm1	27.56	1.73	0.113	0.039	106.81	3.64	2.41	0.12	0.082	0.022	0.12	0.019	<0.075	0.03	<0.121	0.042	0.0255	0.007
FC21.1_torm2	27.66	1.74	0.337	0.046	153.16	5.2	3.27	0.15	0.115	0.023	0.136	0.02	<0.077	0.03	<0.167	0.055	0.0319	0.0076
FC21.1_matrice1	30.49	1.92	283.49	11.36	20.59	0.72	5.2	0.21	19.19	0.75	15.74	0.64	3.56	0.25	0.75	0.12	0.106	0.013
FC21.1_matrice2	29.93	1.9	280.89	11.28	18.06	0.64	3.33	0.15	27.57	1.07	16.4	0.68	4.21	0.3	0.72	0.13	0.101	0.014
FC21.1_torm_matrice3	27.51	1.85	251.81	10.25	120.33	4.2	24	0.99	13.25	0.69	15.08	0.71	1.22	0.26	2.23	0.43	0.067	0.021
FC21.1_matrice4	33.14	2.13	254.07	10.27	24.74	0.89	22.4	0.86	26.24	1.06	20.15	0.84	5.45	0.42	1.27	0.21	0.101	0.017
FC21.1_matrice5	31.14	1.99	0.602	0.054	192.44	6.56	4.93	0.21	0.732	0.066	0.236	0.027	<0.059	0.026	0.039	0.028	0.073	0.012
FC21.1_matrice6	12.88	0.85	122.47	4.98	107.74	3.69	0.104	0.017	0.066	0.019	0.167	0.023	0.061	0.037	<0.084	0.043	0.0382	0.0085
FC21.1_torm_matrice7	25.4	1.65	117.19	4.78	71.89	2.48	4.81	0.21	6.55	0.3	6.56	0.29	0.64	0.1	0.071	0.043	0.073	0.012
FC21.1_torm_matrice8	27.48	1.78	172.33	7.03	56.84	1.96	5.13	0.21	10.18	0.43	9.11	0.39	1.95	0.17	<0.130	0.052	0.0635	0.0098
FC21.1_matrice9	27.17	1.79	183.53	7.52	21.48	0.77	11.14	0.45	17.88	0.74	11.55	0.5	0.99	0.14	<0.078	0.056	0.093	0.015
AV5_1_torm_matrice1	29.06	1.92	97.11	4.02	48.96	1.72	15.29	0.61	109.13	4.11	3.35	0.17	19.2	1.04	<0.112	0.059	0.085	0.015
AV5_1_matrice2	49.65	3.28	464.23	19.1	2.12	0.12	13.06	0.54	90.98	3.48	8.52	0.4	2.39	0.27	<0.108	0.033	0.24	0.029
AV5_4_torm_matrice3	49.41	3.37	131.52	5.56	153.78	5.42	1705.27	62.86	4639.02	172.52	4.16	0.28	0.4	0.16	0.13	0.12	0.161	0.035
AV5_4_matrice4	39.5	2.63	377.34	15.62	5.8	0.23	13.74	0.54	87.92	3.34	7.25	0.33	2.16	0.2	<0.084	0.038	0.203	0.021
AV5_4_matrice5	44.21	2.99	432.61	18.01	2.37	0.13	12.66	0.53	84.35	3.27	8.03	0.38	0.49	0.12	<0.132	0.054	0.28	0.032
AV5_5_torm_matrice6	34.42	2.4	134.86	5.73	107.48	3.81	17.23	0.74	95.36	3.78	4.94	0.29	1.14	0.23	<0.093	0.068	0.119	0.026
NIST612(Copy3)	34.93	2.35	31.29	1.32	76.46	2.65	38.72	1.45	36.25	1.38	37.51	1.54	37.76	1.76	28.15	1.81	43.02	1.94
NIST612(Copy4)	38.34	2.6	32.15	1.36	75.48	2.62	38.58	1.45	36.55	1.4	38.58	1.59	39.64	1.85	29.65	1.92	43.11	1.95
BCR2g(Copy2)	20.46	1.41	44	1.87	263.85	9.17	23.51	0.89	123.64	4.7	10.78	0.46	251.56	11.58	0.262	0.054	0.0933	0.009
BCR2g(Copy3)	19.53	1.36	43.36	1.85	264.07	9.21	23.61	0.9	125.02	4.77	10.81	0.46	245.53	11.37	0.215	0.056	0.0993	0.0095
AV5_5_matrice7	48.67	3.41	444.76	19.01	2.4	0.11	5.16	0.23	38.82	1.55	7.59	0.35	0.8	0.12	<0.094	0.029	0.265	0.026
AV5_5_matrice8	49.22	3.49	447.81	19.25	2.31	0.12	12.99	0.54	80.57	3.18	8.34	0.4	0.94	0.15	<0.122	0.063	0.257	0.028
AV5_6_torm1	25.36	1.87	92.31	4.06	67.06	2.43	15.86	0.68	76.3	3.09	9.34	0.47	1.63	0.25	0.079	0.069	0.081	0.019
AV5_6_torm2	24.9	1.83	106.63	4.68	39.99	1.46	11.16	0.48	76.28	3.06	7.2	0.36	2.53	0.28	<0.069	0.021	0.148	0.022
AV5_8_torm3	19.67	1.48	5.61	0.31	187.65	6.7	9.16	0.42	48.06	2.01	5.04	0.28	0.197	0.084	<0.094	0.029	0.069	0.017
AV5_8_torm4	20.13	1.53	14.42	0.7	106.93	3.86	0.67	0.068	6	0.35	0.232	0.039	<0.071	0.038	<0.142	0.087	0.044	0.014
AV5_3_torm_matrice9	18.53	1.46	89.44	4.06	42.04	1.6	2.95	0.2	20.56	1.01	2	0.16	0.098	0.07	<0.084	0.026	0.085	0.023
AV5_3_matrice10	43.22	3.21	420.97	18.68	2.44	0.11	7.55	0.32	48.34	1.95	7.31	0.34	0.614	0.088	<0.075	0.038	0.204	0.019
AV5_3_matrice11	34.56	2.59	333.45	14.89	2.054	0.09	9.09	0.37	58.4	2.35	5.83	0.27	0.381	0.061	<0.090	0.033	0.162	0.015
880_1_torm1	74.76	5.67	0.139	0.054	183.07	6.62	0.684	0.06	0.304	0.051	0.654	0.061	0.071	0.049	<0.085	0.041	0.692	0.054
880_1_torm2	85.9	6.58	0.111	0.049	139.33	5.08	15.35	0.67	1.73	0.15	1.5	0.11	<0.082	0.059	<0.082	0.07	1.89	0.12
880_1_torm3	47.75	3.7	64.2	2.96	120.11	4.38	6.65	0.3	1.076	0.095	0.899	0.07	<0.058	0.025	<0.100	0.047	2.16	0.13
880_3_torm4	34.03	2.66	0.139	0.036	90.67	3.32	34.52	1.4	0.279	0.038	0.347	0.033	<0.035	0.021	0.036	0.025	0.715	0.048
880_3_torm5	34.91	2.76	0.252	0.042	232.76	8.5	28.13	1.16	0.308	0.041	0.809	0.06	<0.040	0.018	0.098	0.051	0.432	0.034
880_q1_qtz1	<0.77	0.24	<2.70	2.63	1.77	1.02	<0.304	0.094	<0.59	0.18	<0.79	0.25	<2.28	0.7	<4.53	1.41	<0.33	0.1
880_q1_qtz2	0.156	0.09	1.48	0.22	2.88	0.26	<0.0095	0.0029	<0.00	<0.00	<0.0101	0.0031	<0.101	0.031	<0.100	0.031	0.015	0.015
880_6_torm6	45.09	3.66	<0.101	0.047	168.68	6.25	34.7	1.45	0.155	0.032	0.502	0.048	<0.053	0.03	<0.130	0.053	0.546	0.044
NIST612(Copy5)	37.03	3.02	32.04	1.52	75.82	2.81	38.07	1.56	36.29	1.53	38.56	1.79	38.4	2.05	28.66	2.18	44.15	2.28

Spot analysis	Ga71	1se Ga71	Rb85	1 Rb85	Sr88	1se Sr88	Y89	1se Y89	Zr90	1se Zr90	Nb93	1se Nb93	Mo95	1se Mo95	Cd111	1se Cd111	In115	1se In115
NIST612(Copy6)	36.79	3.03	31.28	1.5	75.26	2.8	37.38	1.55	35.6	1.51	38.16	1.79	37.9	2.04	29.45	2.26	43.8	2.28
BCR2g(Copy4)	19.4	1.62	44	2.12	262.53	9.79	23.48	0.98	124.64	5.25	11.02	0.53	252.63	13.47	0.268	0.055	0.0961	0.0097
BCR2g(Copy5)	19.8	1.67	42.41	2.06	263.9	9.88	23.51	0.99	122.27	5.18	10.91	0.53	247.55	13.3	0.185	0.05	0.0897	0.0091
880_6_torm7	84.8	7.21	0.288	0.052	142.07	5.38	4.59	0.23	2.02	0.15	1.012	0.079	0.75	0.13	<0.167	0.074	1.65	0.11
880_7_torm8	26.7	2.31	<0.070	0.033	211.59	8.01	0.359	0.033	0.182	0.031	0.475	0.042	<0.058	0.029	<0.082	0.04	0.146	0.017
880_7_torm9	23.98	2.09	<0.072	0.03	149.65	5.69	0.707	0.05	<0.016	0.01	0.062	0.014	<0.075	0.034	<0.061	0.039	0.095	0.013
VSS3a_1_torm1	45.35	3.98	12.58	0.65	42.28	1.63	0.806	0.055	0.499	0.052	1.72	0.11	<0.068	0.034	<0.077	0.041	0.234	0.022
VSS3a_1_torm2	52.8	4.68	9.74	0.52	39.68	1.55	2.57	0.14	1.104	0.094	2.55	0.15	0.147	0.059	0.132	0.055	0.347	0.032
VSS3a_3a_matrice1	18	1.62	0.292	0.036	12.9	0.52	0.688	0.047	1.334	0.093	10.6	0.54	0.21	0.05	<0.056	0.023	0.151	0.016
VSS3a_4_torm3	50.96	4.62	20.19	1.07	42.86	1.7	0.65	0.061	0.584	0.076	1.249	0.099	0.154	0.065	<0.083	0.042	0.277	0.032
VSS3a_4_qtz1	1.41	0.42	17.48	1.4	1.15	0.24	<0.00	<0.00	0.1	0.12	<0.040	0.012	0.57	0.47	<0.00	<0.00	<0.00	<0.00
VSS3a_4_torm4	33.56	3.09	6.98	0.38	37.19	1.47	1.135	0.069	2.36	0.14	0.678	0.052	<0.062	0.025	<0.122	0.041	0.193	0.019
VSS3a_4_torm_matrice2	29.24	2.76	0.328	0.059	32.06	1.31	1.42	0.11	3.68	0.26	0.754	0.078	<0.00	<0.00	<0.068	0.063	0.16	0.026
VSS3a_7_qtz2	4.09	5.01	<7.25	6.3	1.54	1.55	<0.00	<0.00	<0.00	<0.00	<0.00	<0.00	<5.28	1.63	<7.31	2.26	<1.22	0.38
VSS3a_7_qtz3	<0.57	0.72	<1.30	1.39	2.22	0.84	<0.200	0.062	<0.00	<0.00	<0.151	0.046	<1.30	0.4	2.55	2.89	<0.150	0.046
VSS3a_7_qtz4	8.18	2.88	<2.00	2.01	12.09	2.3	<0.33	0.1	<0.00	<0.00	0.55	0.55	3.57	3.95	2.73	3.85	0.23	0.32
VSS3a_5_torm5	43.08	4.16	0.059	0.027	42.73	1.72	1.356	0.081	0.398	0.044	0.89	0.065	<0.066	0.02	<0.079	0.033	0.228	0.022
VSS3a_5_torm6	49.26	4.81	12.22	0.68	44.85	1.81	1.229	0.077	0.462	0.051	1.202	0.084	0.051	0.03	<0.104	0.033	0.253	0.024
VSS3a_4_matrice3	20.47	2.03	0.209	0.031	26.19	1.07	3.84	0.2	2.17	0.14	0.48	0.04	<0.065	0.038	0.057	0.034	0.138	0.015
VSS3a_4_matrice4	24.86	2.49	0.216	0.038	33.51	1.38	1.71	0.11	5.27	0.31	0.653	0.06	<0.054	0.024	<0.043	0.013	0.161	0.021
BCR2g(Copy6)	19.12	1.92	42.14	2.32	247.55	10.03	22.34	1.05	116.38	5.53	10.47	0.58	241.97	15.05	0.211	0.053	0.091	0.01
BCR2g(Copy7)	19.12	1.94	40.65	2.25	239.47	9.75	21.24	1	113.6	5.43	10.29	0.57	232.68	14.59	0.233	0.054	0.099	0.01
NIST612(Copy9)	35.56	3.63	31.88	1.78	76.56	3.14	38.16	1.8	35.48	1.72	37.72	2.07	37.11	2.38	26.45	2.47	41.19	2.53
NIST612(Copy10)	35.64	3.67	31.44	1.77	76.41	3.15	38.56	1.82	35.96	1.75	37.55	2.08	38.3	2.47	28.22	2.65	43.11	2.67
NIST612(Copy11)	36.41	3.79	31.5	1.78	76.47	3.16	38.44	1.83	36.25	1.78	38.51	2.15	39.41	2.56	28.98	2.75	43.01	2.68
VSS3a_4_qtz1	0.28	0.1	4.97	0.42	1.89	0.18	<0.0237	0.0073	<0.00	<0.00	<0.00	<0.00	<0.125	0.039	<0.197	0.062	<0.0083	0.0026
VSS3a_7_qtz2	2.68	0.37	0.25	0.1	1.9	0.15	0.011	0.011	0.054	0.04	<0.021	0.013	<0.146	0.074	0.08	0.08	<0.0119	0.0037
VSS3a_7_qtz3	0.063	0.043	0.79	0.13	1.41	0.13	<0.012	0.012	<0.00	<0.00	0.025	0.017	<0.086	0.027	<0.187	0.059	<0.0099	0.0031
VSS3a_7_qtz4	0.7	0.14	0.54	0.11	0.96	0.099	0.011	0.011	0.021	0.021	0.011	0.011	<0.122	0.038	<0.24	0.11	<0.014	0.01

Spot analysis	1se Sn118	Sn118	Cs133	1se Cs133	Ba137	1se Ba137	La139	1se La139	Ce140	1se Ce140	Pr141	1se Pr141	Nd146	1se Nd146	Sm149	1se Sm149	Eu151
NIST612	38.61	1.67	41.74	2.02	37.93	1.64	36.32	1.31	38.5	1.77	37.72	1.72	35.15	1.3	37.1	1.44	34.45
NIST612(Copy1)	37.05	1.6	40.27	1.94	36.8	1.59	35.43	1.28	37.67	1.73	36.3	1.65	34.52	1.27	35.75	1.39	34.16
NIST612(Copy2)	38.43	1.66	43.47	2.1	38.41	1.66	35.73	1.29	38.53	1.77	37.93	1.73	36.11	1.33	37.32	1.45	34.97
BCR2g	1.91	0.11	1.018	0.055	529.18	22.21	18.79	0.68	42.61	1.96	5	0.23	22.27	0.84	5.03	0.23	1.451
BCR2g(Copy1)	2.09	0.12	1.087	0.058	557.46	23.4	19.04	0.69	43.92	2.02	5.13	0.24	22.15	0.83	4.99	0.23	1.588
FC21.1_torm1	1.26	0.11	0.107	0.017	8.53	0.48	0.366	0.028	1.148	0.067	0.136	0.014	0.397	0.055	0.275	0.052	0.073
FC21.1_torm2	1.56	0.12	0.418	0.032	11.39	0.6	0.431	0.031	1.431	0.08	0.132	0.013	0.607	0.068	0.237	0.046	0.096
FC21.1_matrice1	5.33	0.28	10.29	0.51	623.8	26.31	2.073	0.092	6.25	0.3	0.632	0.038	2.41	0.15	0.768	0.08	0.279
FC21.1_matrice2	5.16	0.28	9.69	0.49	686.63	29.03	2.17	0.1	6.55	0.32	0.561	0.037	2.07	0.15	0.417	0.064	0.165
FC21.1_torm_matrice3	4.52	0.36	11.42	0.61	723.15	31.06	2.83	0.17	12.07	0.62	1.63	0.11	8.38	0.57	4.57	0.43	1.39
FC21.1_matrice4	5.01	0.3	11.04	0.56	604.07	25.74	89.19	3.26	267.11	12.41	21.22	0.99	72.11	2.76	11.83	0.61	1.557
FC21.1_matrice5	3.19	0.2	0.829	0.054	20.52	1	0.694	0.043	2.05	0.11	0.23	0.02	0.924	0.089	0.575	0.076	0.194
FC21.1_matrice6	1.75	0.13	3.72	0.2	307.65	13.19	0.122	0.015	0.315	0.026	0.0324	0.0065	0.154	0.034	0.027	0.016	0.089
FC21.1_torm_matrice7	3.1	0.19	4.37	0.23	250.53	10.8	3.66	0.16	11.36	0.55	1.117	0.064	4.5	0.25	1.11	0.11	0.323
FC21.1_torm_matrice8	3.72	0.21	5.64	0.29	375.43	16.13	12.83	0.49	33.71	1.6	3.39	0.17	10.79	0.47	2	0.15	0.397
FC21.1_matrice9	4.41	0.26	7.68	0.4	442.63	19.13	4.51	0.19	14.52	0.7	1.232	0.072	4.6	0.27	1.29	0.13	0.394
AV5_1_torm_matrice1	3.04	0.21	7.24	0.38	432.68	18.78	0.145	0.02	0.514	0.041	0.0561	0.01	0.244	0.051	0.367	0.07	0.133
AV5_1_matrice2	18.51	0.92	24.61	1.26	1935.11	83.69	0.188	0.026	0.494	0.044	0.068	0.013	0.295	0.064	0.502	0.094	0.221
AV5_4_torm_matrice3	5.29	0.44	8.59	0.49	581.55	25.79	0.733	0.079	2.76	0.19	0.561	0.06	9.22	0.64	74.69	3.37	27.4
AV5_4_matrice4	15.66	0.76	23.12	1.18	1800.58	78.36	15.44	0.59	31.73	1.54	2.58	0.13	8.19	0.39	1.2	0.12	0.261
AV5_4_matrice5	13.05	0.69	21.55	1.12	2306.36	100.91	0.634	0.051	1.434	0.093	0.134	0.018	0.559	0.089	0.407	0.085	0.124
AV5_5_torm_matrice6	5.04	0.39	8.97	0.5	438.39	19.66	0.62	0.063	1.62	0.12	0.145	0.024	0.61	0.12	0.54	0.13	0.306
NIST612(Copy3)	37.19	1.69	40.36	2.07	36.99	1.67	35.23	1.31	37.46	1.83	36.35	1.75	35.11	1.33	37.01	1.49	34.64
NIST612(Copy4)	38.24	1.75	42.2	2.18	38.74	1.76	36.39	1.36	39.49	1.94	37.11	1.8	35.26	1.34	36.63	1.48	33.95
BCR2g(Copy2)	2	0.12	1.083	0.062	547.92	24.41	18.59	0.7	43.01	2.13	5.09	0.25	21.93	0.86	4.73	0.23	1.452
BCR2g(Copy3)	2.01	0.12	1.036	0.06	554.9	24.85	18.84	0.72	43.14	2.15	4.99	0.25	21.85	0.86	4.78	0.23	1.509
AV5_5_matrice7	26.11	1.26	22.88	1.22	2014.83	90.68	0.215	0.022	0.339	0.03	0.0556	0.0094	0.19	0.043	0.137	0.038	0.184
AV5_5_matrice8	12.81	0.68	26	1.4	2058.35	93.2	0.889	0.059	2.28	0.13	0.201	0.021	0.81	0.098	0.419	0.077	0.249
AV5_6_torm1	2.61	0.26	7.24	0.42	345.41	16.02	1.44	0.096	4.35	0.25	0.303	0.033	1.06	0.14	0.65	0.12	0.17
AV5_6_torm2	21.35	1.1	8.55	0.48	447.75	20.7	6.93	0.3	58.95	3.03	7.07	0.38	31.61	1.36	7.01	0.44	0.634
AV5_8_torm3	1.06	0.17	0.443	0.047	16.14	0.99	2.02	0.12	11.46	0.62	1.72	0.11	7.38	0.45	2.08	0.22	0.314
AV5_8_torm4	5.52	0.38	1.086	0.085	43.74	2.3	0.0237	0.0097	0.079	0.017	0.0106	0.0053	0.016	0.016	<0.00	<0.00	0.0152
AV5_3_torm_matrice9	2.38	0.27	7	0.43	378.03	18.06	10.25	0.47	28.09	1.51	2.48	0.16	6.02	0.46	0.81	0.17	0.081
AV5_3_matrice10	11.38	0.59	23.02	1.28	2088.89	97.85	0.904	0.05	2	0.12	0.252	0.02	0.679	0.068	0.284	0.046	0.131
AV5_3_matrice11	9.36	0.49	17.33	0.97	1643.81	77.49	1.123	0.056	3.11	0.17	0.264	0.02	0.913	0.073	0.301	0.043	0.132
880_1_torm1	43.77	2.22	0.024	0.013	0.62	0.11	0.197	0.025	0.472	0.042	0.0229	0.0067	0.084	0.035	<0.040	0.019	0.044
880_1_torm2	159.04	7.89	0.045	0.017	3.72	0.34	0.253	0.031	0.669	0.057	0.068	0.013	0.231	0.059	0.035	0.025	0.039
880_1_torm3	161.96	8.05	0.246	0.028	63.59	3.21	0.693	0.048	1.414	0.093	0.139	0.016	0.393	0.063	0.129	0.039	0.077
880_3_torm4	66.58	3.35	0.037	0.011	2.04	0.18	0.353	0.028	1.058	0.069	0.12	0.013	0.409	0.054	0.142	0.036	0.054
880_3_torm5	15.68	0.84	0.035	0.012	1.94	0.18	0.449	0.033	1.094	0.072	0.105	0.013	0.465	0.061	0.143	0.036	0.054
880_q1_qtz1	<6.09	4.44	<0.90	0.96	9.49	5.76	<0.00	<0.00	0.41	0.42	<0.137	0.042	<0.00	<0.00	<0.00	<0.00	<0.00
880_q1_qtz2	0.3	0.2	0.221	0.061	2.8	0.58	<0.00	<0.00	0.028	0.02	<0.00	<0.00	<0.00	<0.00	<0.00	<0.00	<0.0082
880_6_torm6	36.12	1.91	<0.027	0.013	2.93	0.26	1.193	0.071	3.45	0.21	0.348	0.03	1.43	0.13	0.389	0.071	0.125
NIST612(Copy5)	38.12	1.98	41.26	2.47	37.23	1.9	35.3	1.44	39.27	2.22	38.02	2.12	35.63	1.47	37.08	1.65	34.72

Spot analysis	1se Sn118	Sn118	Cs133	1se Cs133	Ba137	1se Ba137	La139	1se La139	Ce140	1se Ce140	Pr141	1se Pr141	Nd146	1se Nd146	Sm149	1se Sm149	Eu151
NIST612(Copy6)	38.73	2.02	42.98	2.59	38.67	1.99	35.84	1.47	38.51	2.2	37.2	2.09	35.23	1.46	36.24	1.63	34.06
BCR2g(Copy4)	2.1	0.13	1.041	0.068	549.23	27.9	18.81	0.78	44.3	2.55	5.19	0.3	21.78	0.92	5.1	0.26	1.47
BCR2g(Copy5)	2.07	0.13	1.048	0.069	549.7	28.12	19.15	0.8	44.51	2.58	5.28	0.3	21.51	0.92	4.87	0.25	1.471
880_6_torm7	138.87	7.43	0.033	0.014	6.78	0.48	0.265	0.028	0.983	0.073	0.087	0.013	0.337	0.059	0.1	0.036	0.075
880_7_torm8	12.75	0.73	<0.0225	0.0096	1.34	0.14	0.067	0.011	0.216	0.022	0.0185	0.0049	0.087	0.024	0.025	0.015	0.0189
880_7_torm9	8.19	0.48	0.0237	0.0092	0.644	0.089	0.0456	0.0087	0.142	0.016	0.0177	0.0044	0.026	0.013	<0.028	0.014	0.036
VSS3a_1_torm1	19.73	1.11	0.502	0.041	3.77	0.28	0.831	0.05	2.06	0.13	0.153	0.015	0.578	0.065	0.172	0.037	0.216
VSS3a_1_torm2	29.09	1.64	0.413	0.038	3.65	0.29	0.838	0.054	2.02	0.13	0.152	0.017	0.465	0.065	0.164	0.042	0.187
VSS3a_3a_matrice1	5.75	0.35	0.074	0.013	4.15	0.29	0.217	0.019	0.797	0.057	0.0482	0.0071	0.259	0.039	0.135	0.031	0.067
VSS3a_4_torm3	27.25	1.59	0.749	0.066	5.78	0.46	1.004	0.07	2.69	0.18	0.212	0.024	0.74	0.1	0.155	0.049	0.262
VSS3a_4_qtz1	1.51	0.57	0.33	0.12	2.73	0.89	<0.00	<0.00	0.174	0.079	<0.00	<0.00	<0.00	<0.00	<0.00	<0.00	<0.00
VSS3a_4_torm4	13.24	0.78	0.282	0.027	4.49	0.32	0.87	0.051	1.93	0.13	0.151	0.015	0.445	0.054	0.142	0.032	0.203
VSS3a_4_torm_matrice2	7.73	0.53	0.088	0.02	6.63	0.55	0.323	0.038	1.013	0.086	0.066	0.014	0.291	0.069	0.236	0.069	0.13
VSS3a_7_qtz2	<16.09	12.12	<2.16	1.26	17.12	12.18	<0.00	<0.00	<0.00	<0.00	<0.62	0.19	<0.00	<0.00	<0.00	<0.00	<0.00
VSS3a_7_qtz3	8.55	3.3	<0.37	0.45	3.31	2.49	<0.095	0.029	<0.00	<0.00	<0.088	0.027	<0.38	0.12	<0.00	<0.00	<0.00
VSS3a_7_qtz4	8.04	3.99	<0.58	0.53	9.22	4.64	497.3	27.19	<0.00	<0.00	<0.00	<0.00	<0.63	0.19	<0.00	<0.00	<0.00
VSS3a_5_torm5	18.94	1.14	0.0298	0.0076	3.39	0.26	0.68	0.043	1.49	0.11	0.142	0.015	0.452	0.055	0.128	0.031	0.203
VSS3a_5_torm6	26.53	1.6	0.63	0.053	3.65	0.28	1.286	0.073	2.87	0.2	0.252	0.023	0.987	0.09	0.198	0.041	0.26
VSS3a_4_matrice3	5.71	0.37	0.068	0.011	4.25	0.31	0.354	0.027	0.864	0.065	0.0815	0.0099	0.401	0.049	0.188	0.036	0.15
VSS3a_4_matrice4	7.15	0.48	0.061	0.013	4.87	0.39	0.32	0.03	0.907	0.073	0.088	0.013	0.252	0.049	0.148	0.042	0.139
BCR2g(Copy6)	1.93	0.14	1.017	0.077	521.74	30.4	17.94	0.83	41.63	2.79	4.79	0.32	20.45	0.96	4.57	0.27	1.53
BCR2g(Copy7)	1.91	0.14	0.939	0.072	512.58	30.08	18.29	0.85	42.08	2.85	4.89	0.33	20.73	0.97	4.48	0.26	1.395
NIST612(Copy9)	36.65	2.26	41.61	3.01	37.08	2.22	35.47	1.64	36.7	2.5	35.73	2.38	34.99	1.62	37.39	1.91	34.42
NIST612(Copy10)	38.09	2.36	41.69	3.04	37.96	2.29	36.45	1.7	39.07	2.68	37.34	2.51	34.85	1.62	36.16	1.86	34.58
NIST612(Copy11)	38.67	2.41	41.29	3.03	37.82	2.3	35.66	1.67	38.49	2.67	38.11	2.58	35.63	1.67	36.68	1.9	34.49
VSS3a_4_qtz1	0.34	0.17	0.442	0.076	3.16	0.52	<0.00	<0.00	<0.00	<0.00	<0.00	<0.00	<0.052	0.016	<0.00	<0.00	<0.0115
VSS3a_7_qtz2	<0.33	0.16	0.157	0.04	2.2	0.35	<0.0130	0.004	0.0124	0.0088	<0.00	<0.00	<0.074	0.023	<0.00	<0.00	<0.00
VSS3a_7_qtz3	<0.18	0.13	0.187	0.04	0.71	0.2	0.0077	0.0077	0.0064	0.0065	0.0101	0.0071	0.031	0.031	<0.00	<0.00	<0.010
VSS3a_7_qtz4	0.75	0.18	0.159	0.037	0.65	0.18	<0.00	<0.00	0.0059	0.0059	0.0046	0.0046	<0.062	0.019	<0.00	<0.00	<0.0137

Spot analysis	1se Eu151	Gd157	1se Gd157	Tb159	1 Tb159	Dy163	1se Dy163	Ho165	1se Ho165	Er167	1se Er167	Tm169	1se Tm169	Yb173	1se Yb173	Lu175	1se Lu175
NIST612	1.15	37.42	1.78	36.92	1.74	36.19	1.42	37.05	1.55	36.36	1.66	37.48	1.37	39.78	1.77	37.62	1.44
NIST612(Copy1)	1.14	35.44	1.69	34.4	1.62	35.19	1.38	37.23	1.56	37.08	1.69	36.89	1.34	38.66	1.71	36.57	1.4
NIST612(Copy2)	1.17	38.11	1.81	36.89	1.74	36.99	1.45	38.83	1.63	38.3	1.75	38.15	1.39	41.5	1.84	38.77	1.49
BCR2g	0.06	4.74	0.26	0.737	0.04	4.72	0.21	0.914	0.044	2.42	0.13	0.397	0.021	2.68	0.15	0.359	0.02
BCR2g(Copy1)	0.065	4.76	0.26	0.738	0.04	4.82	0.21	0.946	0.046	2.61	0.14	0.364	0.019	2.64	0.15	0.376	0.02
FC21.1_torm1	0.013	0.296	0.053	0.079	0.011	0.358	0.047	0.093	0.012	0.264	0.042	0.071	0.01	0.626	0.076	0.126	0.014
FC21.1_torm2	0.015	0.44	0.066	0.091	0.011	0.617	0.062	0.109	0.013	0.449	0.055	0.088	0.011	0.895	0.092	0.184	0.017
FC21.1_matrice1	0.025	1.025	0.1	0.141	0.014	1.009	0.078	0.18	0.016	0.396	0.047	0.0661	0.0089	0.652	0.072	0.168	0.015
FC21.1_matrice2	0.02	0.565	0.078	0.117	0.014	0.63	0.065	0.132	0.015	0.562	0.064	0.068	0.01	0.548	0.072	0.086	0.012
FC21.1_torm_matrice3	0.12	5.94	0.54	0.925	0.081	5.7	0.41	1.053	0.087	2.99	0.29	0.349	0.045	2.33	0.29	0.253	0.038
FC21.1_matrice4	0.091	9.58	0.59	1.075	0.07	5.24	0.3	0.787	0.053	2.06	0.17	0.282	0.027	1.72	0.17	0.303	0.028
FC21.1_matrice5	0.022	0.797	0.094	0.169	0.017	1.053	0.087	0.226	0.02	0.686	0.071	0.166	0.016	1.39	0.12	0.248	0.021
FC21.1_matrice6	0.015	0.046	0.021	0.004	0.0023	0.051	0.017	<0.0049	0.0025	<0.0147	0.0045	0.0014	0.0014	0.0083	0.0083	0.0042	0.0024
FC21.1_torm_matrice7	0.03	1.06	0.11	0.16	0.017	1.088	0.091	0.192	0.019	0.586	0.066	0.097	0.012	0.775	0.089	0.118	0.014
FC21.1_torm_matrice8	0.03	1.5	0.13	0.187	0.017	1.208	0.089	0.164	0.016	0.517	0.056	0.0784	0.0099	0.556	0.067	0.101	0.011
FC21.1_matrice9	0.036	1.49	0.15	0.296	0.027	1.93	0.14	0.361	0.03	1.17	0.11	0.164	0.018	1.06	0.12	0.174	0.019
AV5_1_torm_matrice1	0.021	1.17	0.13	0.264	0.025	2.49	0.17	0.577	0.042	1.95	0.16	0.276	0.025	2.11	0.18	0.309	0.027
AV5_1_matrice2	0.031	1.05	0.14	0.251	0.028	2.15	0.17	0.411	0.037	1.6	0.15	0.248	0.027	1.68	0.18	0.31	0.031
AV5_4_torm_matrice3	1.06	272.61	13.66	50.9	2.55	428.08	17.19	67.48	2.98	186.25	8.96	23.87	0.96	144.24	6.9	17.23	0.75
AV5_4_matrice4	0.026	1.36	0.13	0.277	0.024	2.26	0.14	0.492	0.034	1.51	0.12	0.281	0.022	1.8	0.15	0.299	0.024
AV5_4_matrice5	0.023	1.09	0.15	0.228	0.026	2.09	0.17	0.454	0.039	1.37	0.14	0.218	0.025	1.63	0.17	0.249	0.027
AV5_5_torm_matrice6	0.048	1.21	0.2	0.359	0.042	2.65	0.24	0.588	0.057	1.76	0.2	0.243	0.034	1.81	0.23	0.308	0.039
NIST612(Copy3)	1.18	37.28	1.88	36.13	1.81	35.67	1.44	37.47	1.65	37.01	1.78	37.16	1.4	39.33	1.84	37.76	1.51
NIST612(Copy4)	1.16	36.77	1.86	36.08	1.81	36.22	1.47	39.29	1.73	38.59	1.86	38.33	1.45	40.96	1.92	38.35	1.54
BCR2g(Copy2)	0.061	4.83	0.28	0.72	0.041	4.53	0.21	0.924	0.047	2.59	0.15	0.343	0.019	2.62	0.15	0.352	0.02
BCR2g(Copy3)	0.063	4.51	0.26	0.69	0.04	4.6	0.21	0.922	0.047	2.46	0.14	0.376	0.02	2.71	0.16	0.376	0.021
AV5_5_matrice7	0.023	0.418	0.071	0.114	0.014	0.792	0.079	0.202	0.02	0.557	0.067	0.101	0.013	0.591	0.08	0.088	0.013
AV5_5_matrice8	0.03	1.19	0.14	0.289	0.028	1.81	0.14	0.493	0.039	1.43	0.13	0.196	0.021	1.52	0.15	0.209	0.022
AV5_6_torm1	0.031	1.22	0.18	0.316	0.036	2.45	0.21	0.546	0.049	1.68	0.18	0.214	0.028	1.57	0.19	0.301	0.034
AV5_6_torm2	0.055	3.06	0.27	0.355	0.034	2.01	0.16	0.419	0.037	1.32	0.13	0.234	0.025	1.48	0.16	0.194	0.023
AV5_8_torm3	0.042	1.53	0.19	0.206	0.027	1.44	0.15	0.341	0.036	0.94	0.12	0.136	0.021	1.18	0.16	0.167	0.024
AV5_8_torm4	0.0088	0.021	0.021	0.0176	0.0072	0.075	0.031	0.0269	0.0095	<0.015	0.014	0.0061	0.0043	0.14	0.053	0.0092	0.0054
AV5_3_torm_matrice9	0.026	0.59	0.14	0.056	0.016	0.53	0.11	0.109	0.024	0.336	0.086	0.072	0.019	0.49	0.12	0.054	0.016
AV5_3_matrice10	0.016	0.816	0.088	0.143	0.014	1.282	0.092	0.273	0.021	0.875	0.077	0.127	0.013	0.999	0.094	0.158	0.015
AV5_3_matrice11	0.015	0.929	0.088	0.195	0.016	1.583	0.099	0.295	0.021	0.923	0.075	0.152	0.013	1.083	0.091	0.153	0.013
880_1_torm1	0.013	0.044	0.026	<0.0057	0.0041	0.046	0.023	0.0295	0.0087	0.078	0.03	0.0109	0.0049	0.212	0.054	0.071	0.013
880_1_torm2	0.013	0.212	0.062	0.059	0.013	0.97	0.11	0.446	0.041	2.01	0.18	0.567	0.045	5.07	0.38	1.313	0.081
880_1_torm3	0.016	0.213	0.052	0.0338	0.0078	0.553	0.068	0.218	0.022	0.799	0.088	0.146	0.017	1.82	0.17	0.376	0.03
880_3_torm4	0.011	0.501	0.07	0.16	0.016	2.7	0.16	0.946	0.057	4.44	0.28	0.961	0.052	8.85	0.52	1.771	0.089
880_3_torm5	0.011	0.451	0.069	0.135	0.015	1.85	0.13	0.866	0.054	3.63	0.24	0.799	0.046	7.76	0.47	1.676	0.087
880_q1_qtz1	<0.00	<0.00	<0.00	<0.00	<0.00	<0.00	<0.00	<0.00	<0.00	<0.00	<0.00	<0.222	0.068	<0.00	<0.00	<0.00	<0.00
880_q1_qtz2	0.0025	<0.00	<0.00	<0.00	<0.00	0.046	0.052	<0.0050	0.0015	<0.00	<0.00	<0.00	<0.00	<0.0298	0.0092	<0.00	<0.00
880_6_torm6	0.019	1.11	0.13	0.315	0.029	3.83	0.23	1.141	0.072	3.99	0.28	0.786	0.049	6.48	0.43	0.959	0.059
NIST612(Copy5)	1.25	38.07	2.22	35.83	2.08	35.85	1.6	38.09	1.89	37.56	2.06	37.72	1.55	39.77	2.12	37.63	1.67

Spot analysis	1se Eu151	Gd157	1se Gd157	Tb159	1 Tb159	Dy163	1se Dy163	Ho165	1se Ho165	Er167	1se Er167	Tm169	1se Tm169	Yb173	1se Yb173	Lu175	1se Lu175
NIST612(Copy6)	1.23	35.87	2.11	34.75	2.03	35.33	1.59	37.68	1.89	38.01	2.1	37.4	1.54	40	2.15	37.48	1.67
BCR2g(Copy4)	0.065	4.45	0.29	0.688	0.045	4.58	0.23	0.878	0.049	2.44	0.16	0.368	0.021	2.5	0.16	0.368	0.022
BCR2g(Copy5)	0.065	4.69	0.31	0.692	0.045	4.48	0.23	0.91	0.051	2.48	0.16	0.35	0.02	2.44	0.16	0.332	0.02
880_6_torm7	0.016	0.201	0.052	0.0447	0.0093	0.505	0.066	0.144	0.018	0.626	0.079	0.133	0.017	1.95	0.18	0.385	0.032
880_7_torm8	0.007	<0.038	0.017	0.0072	0.003	0.051	0.018	0.0128	0.0041	0.049	0.016	0.0137	0.0042	0.083	0.025	0.0356	0.0069
880_7_torm9	0.0086	<0.028	0.014	0.0092	0.0033	0.039	0.014	0.0183	0.0048	0.196	0.034	0.0405	0.0072	0.528	0.068	0.09	0.011
VSS3a_1_torm1	0.022	0.173	0.038	0.0224	0.0054	0.099	0.022	0.0213	0.0054	0.121	0.026	0.0289	0.0061	0.246	0.044	0.0425	0.0074
VSS3a_1_torm2	0.023	0.134	0.038	0.0235	0.0061	0.198	0.036	0.088	0.013	0.356	0.053	0.076	0.011	0.711	0.09	0.129	0.015
VSS3a_3a_matrice1	0.011	0.15	0.033	0.0174	0.0043	0.242	0.034	0.0595	0.0084	0.152	0.027	0.029	0.0055	0.476	0.061	0.0513	0.0077
VSS3a_4_torm3	0.033	0.093	0.039	0.0087	0.0053	0.121	0.034	0.0258	0.0079	0.139	0.038	0.059	0.012	0.437	0.083	0.075	0.014
VSS3a_4_qtz1	<0.00	<0.090	0.028	<0.0129	0.004	<0.00	<0.00	<0.00	<0.00	<0.058	0.018	<0.00	<0.00	<0.00	<0.00	<0.00	<0.00
VSS3a_4_torm4	0.02	0.228	0.043	0.0304	0.0059	0.209	0.032	0.0504	0.0078	0.159	0.028	0.0375	0.0067	0.292	0.047	0.0761	0.0097
VSS3a_4_torm_matrice2	0.026	0.138	0.053	0.0253	0.0086	0.213	0.051	0.079	0.016	0.277	0.061	0.032	0.0097	0.72	0.12	0.131	0.021
VSS3a_7_qtz2	<0.00	<0.00	<0.00	<0.69	0.21	<0.00	<0.00	<0.00	<0.00	<0.00	<0.00	<0.00	<0.00	<0.00	<0.00	<0.52	0.16
VSS3a_7_qtz3	<0.00	<0.00	<0.00	<0.069	0.021	<0.00	<0.00	<0.073	0.022	<0.00	<0.00	<0.00	<0.00	<0.00	<0.00	<0.073	0.022
VSS3a_7_qtz4	<0.00	<0.00	<0.00	<0.00	<0.00	<0.00	<0.00	0.76	0.46	1.12	1.13	<0.00	<0.00	<0.00	<0.00	<0.119	0.037
VSS3a_5_torm5	0.02	0.157	0.035	0.0234	0.0051	0.171	0.029	0.0472	0.0076	0.241	0.037	0.0546	0.0081	0.587	0.071	0.147	0.015
VSS3a_5_torm6	0.025	0.167	0.038	0.0227	0.0053	0.162	0.029	0.0361	0.007	0.198	0.035	0.0456	0.0076	0.526	0.069	0.109	0.013
VSS3a_4_matrice3	0.017	0.443	0.062	0.126	0.014	0.623	0.058	0.124	0.013	0.397	0.048	0.0784	0.0094	0.879	0.089	0.136	0.013
VSS3a_4_matrice4	0.02	0.183	0.047	0.0309	0.0074	0.266	0.045	0.069	0.012	0.261	0.047	0.071	0.011	0.632	0.089	0.131	0.016
BCR2g(Copy6)	0.072	4.26	0.32	0.661	0.05	4.22	0.24	0.794	0.051	2.39	0.17	0.354	0.022	2.53	0.18	0.342	0.023
BCR2g(Copy7)	0.066	4.27	0.32	0.642	0.048	3.94	0.22	0.811	0.052	2.23	0.16	0.347	0.021	2.41	0.18	0.335	0.022
NIST612(Copy9)	1.35	36.82	2.57	35.73	2.49	35.71	1.83	37.4	2.18	36.19	2.35	37.14	1.72	39.58	2.5	37.57	1.92
NIST612(Copy10)	1.36	36.97	2.6	36.24	2.54	36.08	1.86	37.62	2.21	37.17	2.43	37.23	1.74	39.74	2.53	37.71	1.94
NIST612(Copy11)	1.36	37	2.62	36.5	2.58	36.61	1.9	38.17	2.26	38.15	2.52	38.11	1.79	40.45	2.59	37.78	1.95
VSS3a_4_qtz1	0.0035	<0.00	<0.00	<0.0066	0.002	<0.00	<0.00	<0.0069	0.0021	<0.0293	0.009	<0.00	<0.00	<0.00	<0.00	<0.00	<0.00
VSS3a_7_qtz2	<0.00	<0.00	<0.00	<0.0133	0.0041	<0.00	<0.00	<0.0141	0.0043	0.024	0.024	<0.00	<0.00	<0.00	<0.00	<0.00	<0.00
VSS3a_7_qtz3	0.01	<0.00	<0.00	<0.00	<0.00	0.023	0.023	<0.00	<0.00	<0.0248	0.0077	0.0057	0.0057	<0.00	<0.00	<0.00	<0.00
VSS3a_7_qtz4	0.0042	<0.00	<0.00	<0.0079	0.0024	<0.047	0.014	<0.00	<0.00	<0.035	0.011	<0.00	<0.00	<0.00	<0.00	<0.00	<0.00

Spot analysis	Hf177	1se Hf177	Ta181	1se Ta181	W182	1se W182	Pb208	1se Pb208	Th232	1se Th232	U238	1se U238
NIST612	34.46	1.34	39.71	1.34	40.56	2.04	38.64	1.47	36.23	1.42	37.2	1.59
NIST612(Copy1)	33.95	1.31	39.33	1.33	38.53	1.93	38.76	1.47	37.34	1.46	36.25	1.55
NIST612(Copy2)	35.87	1.39	40.51	1.37	40.38	2.02	39.62	1.51	37.55	1.47	37.49	1.6
BCR2g	3.31	0.16	0.629	0.028	0.496	0.04	9.09	0.36	4.6	0.19	1.526	0.069
BCR2g(Copy1)	3.43	0.16	0.645	0.029	0.455	0.037	9.7	0.38	4.56	0.18	1.568	0.071
FC21.1_torm1	0.0122	0.0087	0.0069	0.0031	<0.019	0.012	8.82	0.36	0.304	0.024	0.0877	0.0099
FC21.1_torm2	0.0059	0.0059	0.0147	0.0048	<0.0136	0.0076	9.94	0.4	0.494	0.032	0.098	0.01
FC21.1_matrice1	0.668	0.063	1.213	0.055	1.89	0.13	8.22	0.34	4.15	0.18	2.29	0.11
FC21.1_matrice2	0.778	0.077	1.407	0.066	1.97	0.14	6.77	0.29	4.18	0.18	3	0.14
FC21.1_torm_matrice3	0.359	0.094	0.912	0.077	3.44	0.3	11.24	0.53	11.92	0.53	3.79	0.2
FC21.1_matrice4	1.06	0.11	1.658	0.083	2.95	0.21	12.74	0.53	26.41	1.06	7.62	0.34
FC21.1_matrice5	0.032	0.014	0.0229	0.0058	0.034	0.013	7.23	0.31	0.997	0.054	0.183	0.016
FC21.1_matrice6	0.0126	0.0089	0.077	0.011	0.034	0.013	1.82	0.1	0.0354	0.0072	0.11	0.011
FC21.1_torm_matrice7	0.297	0.047	0.495	0.032	1.211	0.099	5.81	0.25	2.11	0.1	1.234	0.064
FC21.1_torm_matrice8	0.381	0.047	0.761	0.04	1.41	0.1	7.99	0.33	3.83	0.17	1.538	0.075
FC21.1_matrice9	0.584	0.072	1.056	0.057	1.74	0.14	10.73	0.45	3.04	0.14	2.29	0.11
AV5_1_torm_matrice1	4.48	0.26	0.385	0.031	1.78	0.14	22.3	0.9	3.69	0.17	11.67	0.52
AV5_1_matrice2	3.82	0.26	1.004	0.062	6.14	0.39	88.84	3.47	3.18	0.16	16.04	0.72
AV5_4_torm_matrice3	149.1	6.14	1.048	0.088	2.56	0.26	29.71	1.27	61.78	2.55	70.2	3.12
AV5_4_matrice4	3.83	0.22	0.809	0.044	4.52	0.28	92.08	3.59	6.79	0.29	8.86	0.4
AV5_4_matrice5	3.77	0.25	0.788	0.053	4.67	0.32	8.76	0.39	4.28	0.2	10.17	0.47
AV5_5_torm_matrice6	4.53	0.35	0.929	0.072	3.72	0.31	32.15	1.34	3.73	0.2	15.08	0.7
NIST612(Copy3)	34.83	1.4	39.63	1.37	39.41	2.1	38.11	1.5	37.1	1.51	36.5	1.62
NIST612(Copy4)	35.01	1.41	39.92	1.38	38.93	2.09	39.43	1.56	38.17	1.56	38.71	1.73
BCR2g(Copy2)	3.22	0.16	0.64	0.029	0.495	0.04	9.41	0.38	4.35	0.18	1.492	0.071
BCR2g(Copy3)	3.17	0.15	0.658	0.03	0.462	0.039	9.82	0.4	4.47	0.19	1.524	0.073
AV5_5_matrice7	1.73	0.13	0.944	0.051	5.27	0.33	43.68	1.76	1.671	0.086	8.3	0.39
AV5_5_matrice8	3.6	0.23	1.082	0.061	5.51	0.36	48.81	1.98	3.61	0.17	14.22	0.66
AV5_6_torm1	3.26	0.26	1.191	0.076	3.56	0.28	11.71	0.53	3.5	0.18	10.41	0.5
AV5_6_torm2	3.16	0.23	1.056	0.063	2.6	0.21	15.48	0.67	21.48	0.93	10.26	0.49
AV5_8_torm3	1.8	0.18	0.787	0.057	1.88	0.18	6.71	0.33	5.92	0.28	4.7	0.24
AV5_8_torm4	0.222	0.056	0.053	0.013	0.207	0.049	22.33	0.96	0.357	0.036	0.962	0.064
AV5_3_torm_matrice9	1.15	0.17	0.305	0.041	1.41	0.17	2.9	0.2	2.35	0.15	2.1	0.13
AV5_3_matrice10	2.41	0.15	0.634	0.035	5.08	0.32	17.09	0.72	2.95	0.14	5.72	0.28
AV5_3_matrice11	2.59	0.15	0.65	0.033	3.77	0.24	23.14	0.97	3.54	0.16	6.48	0.31
880_1_torm1	<0.00	<0.00	0.0204	0.0068	0.076	0.024	0.456	0.071	0.0424	0.0099	0.0215	0.0058
880_1_torm2	0.114	0.039	0.046	0.011	0.282	0.054	0.618	0.074	0.219	0.026	0.181	0.02
880_1_torm3	0.032	0.016	0.056	0.01	0.227	0.04	0.826	0.071	0.235	0.023	0.104	0.012
880_3_torm4	0.028	0.013	0.0128	0.0041	0.198	0.032	11.96	0.52	0.454	0.031	0.195	0.016
880_3_torm5	0.018	0.011	0.077	0.011	0.134	0.026	16.46	0.72	0.751	0.046	0.176	0.015
880_q1_qtz1	<0.72	0.22	<0.00	<0.00	1.3	1.3	<3.19	2.84	<0.00	<0.00	<0.00	<0.00
880_q1_qtz2	<0.0225	0.0069	<0.00	<0.00	<0.0171	0.0053	0.61	0.15	<0.00	<0.00	<0.00	<0.00
880_6_torm6	0.0078	0.0078	0.0158	0.0053	0.254	0.042	16.92	0.76	0.195	0.02	0.906	0.056
NIST612(Copy5)	34.6	1.53	39.33	1.44	39.52	2.45	39.25	1.69	37.97	1.71	37.14	1.85

Spot analysis	Hf177	1se Hf177	Ta181	1se Ta181	W182	1se W182	Pb208	1se Pb208	Th232	1se Th232	U238	1se U238
NIST612(Copy6)	34.85	1.55	39.77	1.46	39.28	2.46	39.37	1.71	36.71	1.66	37.54	1.88
BCR2g(Copy4)	3.3	0.17	0.649	0.031	0.489	0.044	9.91	0.44	4.41	0.21	1.491	0.079
BCR2g(Copy5)	3.23	0.17	0.59	0.028	0.501	0.044	9.52	0.43	4.55	0.21	1.539	0.082
880_6_torm7	0.076	0.026	0.0459	0.0095	0.572	0.071	3.81	0.2	0.789	0.053	0.169	0.017
880_7_torm8	<0.0183	0.008	0.0683	0.0097	0.074	0.019	22.35	1.01	0.043	0.0076	0.0216	0.0045
880_7_torm9	<0.00	<0.00	0.0098	0.0039	0.054	0.015	17.21	0.79	0.0157	0.0044	0.0066	0.0024
VSS3a_1_torm1	0.0106	0.0075	0.29	0.022	0.334	0.043	37.87	1.71	0.421	0.03	0.0513	0.0069
VSS3a_1_torm2	0.028	0.014	0.398	0.029	0.642	0.072	116.36	5.25	0.326	0.027	0.117	0.013
VSS3a_3a_matrice1	0.019	0.011	0.715	0.038	11.57	0.8	415.18	18.76	0.563	0.036	1.195	0.069
VSS3a_4_torm3	0.01	0.01	0.204	0.023	0.294	0.052	27.74	1.3	0.281	0.029	0.15	0.017
VSS3a_4_qtz1	<0.00	<0.00	0.032	0.032	<0.00	<0.00	52.7	2.91	0.095	0.055	1.01	0.16
VSS3a_4_torm4	0.048	0.015	0.102	0.011	0.188	0.03	62.4	2.88	0.662	0.042	0.124	0.012
VSS3a_4_torm_matrice2	0.146	0.045	0.089	0.017	0.273	0.056	60.67	2.85	0.509	0.046	0.338	0.032
VSS3a_7_qtz2	<0.00	<0.00	<0.00	<0.00	<0.00	<0.00	<9.12	7.99	<0.00	<0.00	1.33	0.94
VSS3a_7_qtz3	<0.00	<0.00	<0.00	<0.00	<0.248	0.076	3.26	1.62	<0.00	<0.00	0.14	0.14
VSS3a_7_qtz4	<0.00	<0.00	<0.00	<0.00	0.9	0.91	90.91	7.84	<0.00	<0.00	12.84	1.69
VSS3a_5_torm5	0.0192	0.0096	0.168	0.015	0.346	0.043	16.29	0.79	0.461	0.032	0.0539	0.0069
VSS3a_5_torm6	0.0054	0.0054	0.192	0.017	0.313	0.042	45.54	2.18	0.655	0.043	0.108	0.011
VSS3a_4_matrice3	0.07	0.018	0.0791	0.0094	0.219	0.031	96.05	4.6	1.012	0.06	0.469	0.032
VSS3a_4_matrice4	0.054	0.02	0.09	0.013	0.344	0.051	86.95	4.21	0.747	0.052	0.318	0.026
BCR2g(Copy6)	3.03	0.18	0.621	0.032	0.476	0.048	9.27	0.46	4.24	0.22	1.372	0.082
BCR2g(Copy7)	3.17	0.18	0.595	0.03	0.482	0.048	9.17	0.46	4.21	0.22	1.411	0.084
NIST612(Copy9)	35.05	1.77	39.36	1.57	37.75	2.83	38.2	1.87	37.23	1.93	36.52	2.11
NIST612(Copy10)	34.97	1.78	40.09	1.61	40.41	3.05	38.67	1.91	36.64	1.91	36.82	2.14
NIST612(Copy11)	34.25	1.75	40.12	1.62	40.97	3.11	39.65	1.97	37.39	1.96	37.54	2.2
VSS3a_4_qtz1	<0.00	<0.00	<0.0070	0.0022	<0.00	<0.00	5.6	0.4	0.0085	0.0086	0.0058	0.0058
VSS3a_7_qtz2	<0.00	<0.00	<0.00	<0.00	0.057	0.033	0.96	0.14	1476.35	78.17	0.116	0.022
VSS3a_7_qtz3	<0.00	<0.00	<0.00	<0.00	<0.00	<0.00	3.21	0.24	<0.00	<0.00	0.0156	0.0078
VSS3a_7_qtz4	<0.00	<0.00	<0.00	<0.00	<0.00	<0.00	0.64	0.11	0.0053	0.0053	0.043	0.013

	Element [ppm]													
Spot analysis	Li7	1se Li7	Be9	1se Be9	Na23	1se Na23	Mg25	1se Mg25	Si29	1se Si29	K39	1se K39	Ca43	1se Ca43
NIST612	40.62	1.8	35.97	1.99	100629.02	4112.4	75.62	4.05	335916.84	10627.35	65.02	2.82	82875.26	3329.46
NIST612(Copy1)	42.48	1.88	39.62	2.18	106964.86	4371.93	77.5	4.14	335916.84	10627.24	67.39	2.91	86609.82	3479.79
NIST612(Copy2)	41.99	1.86	38.04	2.1	103488.69	4233.09	78.76	4.2	335916.84	10627.09	65.66	2.85	85539.91	3439.77
BCR2g	11.17	0.53	2.5	0.29	24869.69	1169.29	28226.9	1796.54	322145.09	21232.16	12459.06	490.77	50029.05	1628.14
BCR2g(Copy1)	10.7	0.51	1.95	0.25	25011.93	1180.43	27821.91	1778.65	327561.31	21623.5	13196.19	522.02	50029.05	1639.9
PG3A_5_torm1	26.73	1.25	5.33	0.52	9976.73	411.09	37671.71	1915.2	170147.94	5399.19	5124.3	210.56	2394.02	208.45
PG3A_5_matrice1	43.71	1.99	10.67	0.78	12015.82	496.37	10517.12	537.56	252417.3	7995.48	27680.65	1140.64	1304.36	184.24
PG3A_4_torm2	4.8	0.25	1.33	0.18	13191.26	547.01	41573.12	2135.23	170147.95	5391.37	232.18	9.78	1990.42	167.86
PG3A_5_matrice2	55.49	2.54	22.25	1.44	8587.38	357.7	16209.55	838.43	252417.27	7995.61	5100.42	212.16	1262.1	163.46
PG3A_matrice3	41.59	1.91	11.72	0.79	7675.68	321.27	9925.45	517.12	252417.27	7991.73	2132.48	89.2	598.95	160.72
PG3A_2_matrice4	56.63	2.6	21.86	1.35	8452.37	355.66	16273.33	854.27	252417.27	7990.77	4850.36	204.02	968.24	149.77
C5_2_matrice1	80.71	3.73	14.6	0.96	7396.32	313.21	16121.93	853.84	179496.72	5686.72	6647.97	281.5	546.27	171.01
C5_4_matrice2	83.98	3.9	19.26	1.22	8042.94	342.72	17127.59	915.45	176692.06	5596.34	4527.82	193.06	928.92	134.89
C5_3_matrice3	77.28	3.64	17.88	1.22	9095.09	390.33	20070.05	1083.65	180899.05	5733.37	6692.82	287.57	1057.52	147.41
LDC11b_1_torm1	8.87	0.47	0.73	0.15	11561.57	499.92	39428.75	2150.86	172485.13	5469.17	87.61	4.3	2994.64	225.39
LDC11b_1_torm2	20.9	1.03	0.97	0.15	12442.53	542.14	43376.8	2391.96	172485.13	5466.29	92.82	4.51	3867.73	248.63
LDC11b_1_torm3	12.14	0.63	4.01	0.42	13978.28	614.21	42954.4	2396.52	172485.13	5470.23	126.71	5.96	2888.87	226.68
LDC11b_1_torm4	17.98	0.91	2.19	0.27	16515.07	731.81	20932.66	1182.03	172485.13	5467.31	10788.61	479.75	2036.97	191.47
LDC11b_2_torm5	12.87	0.67	2.77	0.3	14305.36	639.63	37587.87	2148.48	172485.13	5467.25	208.98	9.6	2620.78	210.76
LDC11b_2_torm6	16.36	0.85	3.52	0.37	11578.82	522.65	46934.46	2717.19	172485.13	5468.76	426.83	19.51	4350.57	279.8
NIST612(Copy3)	40.52	2.03	37.05	2.35	103600.85	4718.14	75.68	4.65	335916.81	10627.22	66.28	3.18	85931.72	3842.86
NIST612(Copy4)	41.7	2.12	37.93	2.43	104672.97	4814.6	80.18	4.97	335916.81	10627.07	67.74	3.27	86270.84	3895.62
BCR2g(Copy2)	11.29	0.6	2.33	0.3	26936.25	1444.15	29221.33	2236.63	328414.94	22735.27	13209.13	575.48	50029.06	1639.45
BCR2g(Copy3)	10.61	0.57	1.99	0.26	24826.07	1345.26	27949.57	2170.03	317045.81	22043.52	13215.57	580.49	50029.06	1638.6
LDC11b_3_torm7	42.26	2.24	1.23	0.19	11027.59	523.71	39016.45	2418.69	172485.13	5466.72	66.56	3.68	2223.88	197.1
LDC11b_3_torm8	11.27	0.63	2.82	0.32	13276.19	637.39	41937.44	2637.47	172485.13	5467.03	102.47	5.34	2428.62	212.98
LDC11b_4_torm9	7.86	0.45	1.63	0.21	13553.33	657.92	41240.07	2631.6	172485.13	5466.07	84.21	4.56	2616.64	216.67
LDC11b_4_torm10	10.8	0.62	2.94	0.32	13791.77	677.06	36060.91	2335.25	172485.13	5465.56	1185.21	58.86	2347.69	205.81
LDC11b_4_torm11	10.16	0.59	1.91	0.24	13642.24	677.42	38582.43	2535.97	172485.13	5466.16	201.61	10.32	1944.09	197.44
LDC11b_4_torm12	41.23	2.32	2.16	0.23	7668.77	385.21	14445.46	963.85	172485.13	5462.53	153.73	7.98	1239.38	153.05
LDC11b_4_qtz1	113.78	11.15	7.19	5.62	48542.52	2606.64	8659.12	671.99	462764.97	17784.19	466.25	88.26	<9120.51	7200.56
LDC11b_4_qtz2	189.59	11.07	0.47	0.29	464.73	28.1	896.09	64.73	462764.97	14709.35	629.88	33.3	<366.28	308.74
LDC11b_5_torm13	11.18	0.68	2.5	0.29	14701.43	765.06	40034.3	2794.85	172485.13	5466.55	170.39	9.25	2966.25	243.08
LDC1_1_qtz1	185.09	10.97	0.16	0.12	1533.28	81.11	129.77	10.62	462764.94	14670.41	710.8	38.19	280.94	135.94
LDC1_1_qtz2	750.18	47.78	2.03	2.03	332.55	126.31	930.47	97.74	462764.91	15718.23	130.1	31.95	<2460.11	2641.65
LDC1_2_torm1	7.27	0.48	1.18	0.2	13529.97	730.01	37091.25	2710.46	172952.55	5483.93	75.82	4.61	1571.79	197.27
LDC1_2_torm2	3.96	0.31	3.36	0.49	12666.77	692.02	39835	2956.39	172952.53	5493.73	151.5	8.7	3339.6	269.6
LDC1_2_torm3	19.75	1.26	2.43	0.32	7442.52	411.46	18497.61	1393.64	172952.55	5483.17	117.47	6.85	1508.17	174.43
BCR2g(Copy6)	10.83	0.68	2.52	0.33	23948.71	1551.38	27194.51	2651.92	323270.81	24391.59	13460.16	684.3	50029.07	1636.37
BCR2g(Copy7)	11.47	0.73	2.3	0.31	25571.7	1677.48	28833.71	2855.3	335486.13	25476.98	13732.25	705.84	50029.07	1638.57
NIST612(Copy9)	42.21	2.73	38.18	3.19	105342.46	6037.21	80.38	6.51	335916.78	10627.42	64.14	3.89	83414.97	4689.98
NIST612(Copy10)	42.54	2.79	38.11	3.23	101870.8	5909.82	74.6	6.13	335916.78	10627.25	66.41	4.07	87137.38	4958.98
NIST612(Copy11)	40.4	2.68	37.17	3.19	103646.94	6086.52	77.13	6.42	335916.78	10627.23	67.3	4.17	84326.21	4858.53

	Element [ppm]														
Spot analysis	Ca44	1se Ca44	Sc45	1se Sc45	Ti49	1se Ti49	V51	1se V51	Cr53	1se Cr53	Mn55	1se Mn55	Co59	1se Co59	Ni60
NIST612	82758.57	3061.89	39.81	1.66	46.45	3.55	36.96	2.27	39.11	2.56	38.09	1.49	34.91	1.27	36.84
NIST612(Copy1)	86946.91	3216.77	41.4	1.67	46.12	3.53	39.19	2.41	37.94	2.48	38.36	1.5	35.47	1.29	39.57
NIST612(Copy2)	85659.23	3170.59	41.64	1.68	50.68	3.85	40.46	2.49	41.83	2.72	38.71	1.52	35.3	1.28	38.82
BCR2g	53569.58	1962.63	32.51	1.48	17507.12	1449.99	460.22	28.35	16.76	1.37	1604.39	79.69	41.91	1.99	13.5
BCR2g(Copy1)	52740.07	1939.89	32.08	1.47	16500.56	1371.64	457.37	28.3	17.6	1.48	1676.27	83.65	43.76	2.09	12.4
PG3A_5_torm1	2436.68	95.22	10.99	0.51	3036.72	220.93	182.57	11.35	164.76	10.8	43.87	1.77	4.57	0.24	10.3
PG3A_5_matrice1	1345.48	55.32	13.28	0.59	13717.96	1000.03	134.19	8.38	110.09	7.29	17.06	0.71	4.43	0.21	10.85
PG3A_4_torm2	1432.39	57.15	4.47	0.23	3867.61	283.99	186.74	11.72	288.32	18.57	3.46	0.18	49.26	1.83	179.9
PG3A_5_matrice2	1094.09	46.19	13.56	0.61	2162.69	160.27	76.95	4.89	35.79	2.65	31.42	1.28	7.87	0.34	17.99
PG3A_matrice3	886.81	38.84	10.42	0.47	2953.91	220.25	45.54	2.92	24	1.85	15.73	0.66	19.63	0.76	19.47
PG3A_2_matrice4	913.46	38.96	12.62	0.55	2539.81	191.09	75.11	4.84	32.36	2.36	24.76	1.01	25.82	0.98	25.97
C5_2_matrice1	683.62	32.73	11	0.5	3108.63	236.13	93.99	6.11	72.65	5.03	34.19	1.4	5.33	0.24	36.58
C5_4_matrice2	705.78	31.23	11.11	0.5	3072.25	235.79	86.26	5.66	60.01	4.21	51.25	2.09	10.2	0.41	45.87
C5_3_matrice3	1005.05	42.84	11.06	0.51	4471.31	347.05	93.54	6.22	81.94	5.84	48.55	2.01	11.11	0.47	55.42
LDC11b_1_torm1	2438.32	97.78	29.27	1.29	2023.25	159.22	223.04	14.96	151.46	10.66	166.46	6.85	6.4	0.3	10.69
LDC11b_1_torm2	3760.48	148.42	5.52	0.29	2950.36	234.67	178.17	12.09	117.48	8.37	156.11	6.47	9.65	0.41	13.09
LDC11b_1_torm3	2622.84	106.15	36.82	1.63	2459.61	198.42	231.37	15.9	299.46	21.31	78.24	3.29	7.7	0.35	22.04
LDC11b_1_torm4	2000.5	82.06	18.37	0.84	2210.11	180.63	132.89	9.26	210.87	15.25	56.82	2.41	9.28	0.4	38.39
LDC11b_2_torm5	2322.47	95.13	46.1	2.05	2143.81	177.64	288.19	20.33	143.13	10.58	86.11	3.67	6.21	0.29	12.8
LDC11b_2_torm6	4338.72	175.67	90.21	4.01	2744.3	230.56	515.79	36.88	243.64	18.1	141.36	6.06	7.39	0.34	30.61
NIST612(Copy3)	85272.05	3418.98	40.73	1.82	48.41	4.3	39.41	2.87	40.62	3.13	38.54	1.67	35.47	1.39	38.79
NIST612(Copy4)	86419.88	3491.56	42.07	1.9	50.31	4.51	41.49	3.06	40.69	3.18	38.48	1.68	35.19	1.39	38.4
BCR2g(Copy2)	53151.2	2090.2	33.24	1.73	17214.23	1740.31	468.28	34.77	16.77	1.65	1649.47	96.83	43.69	2.39	14.13
BCR2g(Copy3)	53650.09	2122.2	32.43	1.7	16376.29	1681.27	448.09	33.75	18.62	1.82	1622.04	96.48	41.26	2.29	13.24
LDC11b_3_torm7	1833.11	79.26	4.62	0.27	1082.7	98.25	83.07	6.41	116.88	9.48	179.46	8.06	7.93	0.36	13.27
LDC11b_3_torm8	2379.18	102.47	27.54	1.32	1946.74	179.1	187.92	14.7	162.78	13.31	96.04	4.37	4.86	0.24	14.78
LDC11b_4_torm9	1979.42	86.55	21.52	1.05	1029.99	96.4	125.43	9.97	170.12	14.1	66.4	3.06	30.74	1.29	15.34
LDC11b_4_torm10	1820.44	80.58	26.63	1.3	1176.43	111.77	168.54	13.6	192.68	16.19	71.15	3.31	4.75	0.24	4.9
LDC11b_4_torm11	1792.52	80.12	20.78	1.04	2422.98	233.55	182.57	14.97	95.71	8.3	67.33	3.17	5.64	0.28	8.52
LDC11b_4_torm12	1434.14	64.6	11.47	0.59	2505.89	245.26	90.88	7.57	20.25	1.92	56.7	2.69	9.66	0.43	26.91
LDC11b_4_qtz1	6628.85	923.21	16.86	5.33	163.09	50.03	77.97	9.52	94.53	36.38	<4.85	4.17	<1.76	1.62	179.04
LDC11b_4_qtz2	1752.17	93.34	13.3	0.89	2.63	1.4	<0.059	0.062	<1.37	1.08	1.94	0.27	0.084	0.073	2.45
LDC11b_5_torm13	2605.2	118.82	15.76	0.83	2338.03	240.08	117.68	10.28	228.49	20.8	73.59	3.62	3.67	0.2	4.14
LDC1_1_qtz1	1432.54	70.67	13.22	0.79	18.84	2.95	2.86	0.31	2.52	0.75	1.91	0.18	0.124	0.05	14.07
LDC1_1_qtz2	1224.48	314.9	17.34	2.93	7.16	8.95	<0.37	0.43	46.88	16.11	<1.30	1.39	<0.47	0.52	2.04
LDC1_2_torm1	1001.13	50.76	46.6	2.48	2804.01	301.85	389.91	35.69	221.87	21.27	50.82	2.6	19.99	0.93	65.97
LDC1_2_torm2	2824.85	134.99	10.07	0.61	5840.81	638.54	100.57	9.38	125.38	12.51	49.51	2.59	18.05	0.9	99.9
LDC1_2_torm3	1562.8	76.22	6.43	0.39	2092.97	232.49	64.55	6.11	3.27	0.68	52.5	2.75	10.87	0.54	52.67
BCR2g(Copy6)	50783.76	2237.26	30.95	1.93	15803.91	2055.95	433.03	40.96	18.98	2.25	1564.29	115.14	40.76	2.73	13.4
BCR2g(Copy7)	52684.44	2340.57	33.44	2.11	17294.7	2284.78	465.92	44.75	19.06	2.31	1627.37	121.54	44.01	2.99	14.6
NIST612(Copy9)	84691.55	4082	41.12	2.29	50.48	6	39.63	3.92	41.38	4.35	39.77	2.15	36.18	1.69	38.47
NIST612(Copy10)	85053.05	4141.16	40.32	2.28	45.41	5.48	37.73	3.79	39.72	4.24	38.19	2.09	35.09	1.66	39.28
NIST612(Copy11)	85338.83	4197.51	41.31	2.36	47.52	5.81	39.1	3.99	37.97	4.12	37.42	2.07	34.55	1.65	37.45

	Element [ppm]															
Spot analysis	1se Ni60	Cu65	1se Cu65	Zn66	1se Zn66	Ga71	1se Ga71	Rb85	1se Rb85	Sr88	1se Sr88	Y89	1se Y89	Zr90	1se Zr90	Nb93
NIST612	1.76	36.12	2.14	37.1	2.14	34.44	1.77	30.42	1.29	73.93	2.69	37.04	1.45	35.27	1.29	37.08
NIST612(Copy1)	1.89	38.43	2.27	39.01	2.24	37.79	1.95	32.18	1.37	76.99	2.81	38.7	1.51	36.46	1.33	38.18
NIST612(Copy2)	1.85	35.28	2.1	36.87	2.12	36.8	1.9	32.41	1.38	76.95	2.81	38.48	1.5	35.78	1.31	38.41
BCR2g	0.66	19.25	1.24	165.19	9.94	23.14	1.13	51.6	2.04	317.44	11.63	28.34	1.12	148.91	6.13	13.03
BCR2g(Copy1)	0.65	19.87	1.3	163.72	9.91	23.3	1.14	53.53	2.12	318.01	11.71	27.86	1.11	146.09	6.05	12.85
PG3A_5_torm1	0.73	2.92	0.74	121.14	7.01	24.85	1.34	33.03	1.44	78.17	2.89	1.191	0.081	8.99	0.41	2.52
PG3A_5_matrice1	0.7	13.25	1.14	36.49	2.27	26.66	1.43	178.14	7.61	63.39	2.35	10.02	0.42	31.19	1.19	34.04
PG3A_4_torm2	8.58	<1.35	0.57	227.22	12.98	25.4	1.36	0.583	0.049	92.74	3.42	0.0454	0.0098	0.202	0.03	0.09
PG3A_5_matrice2	1.05	7.18	0.83	65.88	3.93	24.89	1.35	32.63	1.43	74.89	2.79	13.07	0.55	31.62	1.22	6.05
PG3A_matrice3	1.07	25.76	1.75	41.63	2.54	16.16	0.88	12.18	0.55	51.18	1.91	16.67	0.68	169.84	6.21	12.01
PG3A_2_matrice4	1.37	9.46	0.87	59.16	3.54	23.35	1.27	28.83	1.27	93.92	3.5	13.78	0.57	39.25	1.47	8.82
C5_2_matrice1	1.91	10.2	0.97	80.89	4.84	19.6	1.08	52.02	2.3	89.8	3.36	5.87	0.26	9.6	0.4	7.39
C5_4_matrice2	2.36	8.42	0.79	100.01	5.98	20.84	1.16	34.45	1.54	117.79	4.42	14.41	0.6	115.81	4.29	8.65
C5_3_matrice3	2.92	1.84	0.58	113.27	6.87	23.86	1.35	50.05	2.25	122.05	4.62	15.84	0.67	42.02	1.62	16.81
LDC11b_1_torm1	0.72	<1.69	0.73	44.57	2.86	38.83	2.19	<0.069	0.032	32.7	1.26	0.652	0.05	0.137	0.028	5.09
LDC11b_1_torm2	0.81	<1.75	0.7	176.14	10.79	23.55	1.35	<0.073	0.029	68.53	2.63	0.271	0.026	0.025	0.01	0.163
LDC11b_1_torm3	1.33	<1.68	0.76	17.04	1.3	62.59	3.59	0.173	0.036	59.07	2.29	19.81	0.85	0.571	0.062	5.15
LDC11b_1_torm4	2.15	1.79	0.7	6.77	0.74	37.43	2.18	28.79	1.35	96.02	3.72	5.21	0.24	0.84	0.071	2.38
LDC11b_2_torm5	0.83	2.93	0.73	10.33	0.91	71.43	4.17	0.638	0.058	32.3	1.28	4.99	0.24	0.859	0.072	16.74
LDC11b_2_torm6	1.8	2.13	0.77	91.22	5.94	52.9	3.14	1.79	0.11	71.11	2.8	1.397	0.084	0.536	0.056	1.75
NIST612(Copy3)	2.13	36.53	2.55	37.63	2.48	35.9	2.15	31.14	1.48	76.68	3.02	39.09	1.67	36.73	1.43	38.22
NIST612(Copy4)	2.13	37.69	2.66	39.9	2.66	36.38	2.2	32.03	1.54	76.93	3.05	38.48	1.66	36.21	1.42	38.99
BCR2g(Copy2)	0.76	19.01	1.44	164.72	11.7	23.94	1.36	52.93	2.32	324	12.93	29.1	1.26	152.98	7.02	13.5
BCR2g(Copy3)	0.72	18.15	1.4	159.37	11.47	22.66	1.3	53.17	2.35	323.89	13.01	29.07	1.27	149.83	6.94	13.02
LDC11b_3_torm7	0.9	2.74	0.71	215.87	14.77	17.01	1.1	<0.070	0.028	28.04	1.16	0.503	0.041	0.036	0.015	0.149
LDC11b_3_torm8	1	<1.70	0.71	11.87	1.06	80.33	5.15	<0.072	0.032	24.77	1.03	3.55	0.18	3.57	0.19	11.34
LDC11b_4_torm9	1.03	16.4	1.47	9.08	0.88	49.6	3.23	<0.072	0.029	19.21	0.81	3.59	0.18	0.278	0.036	7.18
LDC11b_4_torm10	0.42	<1.77	0.71	8.28	0.84	47.35	3.13	4.3	0.24	23.13	0.98	3.89	0.2	2.5	0.14	8.92
LDC11b_4_torm11	0.65	<1.69	0.69	7.51	0.8	51.46	3.45	0.669	0.059	20.84	0.89	3.67	0.19	0.559	0.055	11.61
LDC11b_4_torm12	1.72	1.8	0.58	6.55	0.67	28.68	1.95	0.267	0.032	68.52	2.91	6.03	0.29	0.614	0.049	2.9
LDC11b_4_qtz1	26.84	54.25	34.07	66.45	26.63	<0.91	0.73	4.75	1.94	6.65	1.48	0.32	0.4	1.55	1.1	<0.236
LDC11b_4_qtz2	0.64	<1.54	1.28	2.56	1.07	0.072	0.05	2.47	0.25	2.58	0.22	0.016	0.016	0.033	0.033	<0.013
LDC11b_5_torm13	0.39	<1.95	0.78	9.08	0.94	40.57	2.89	0.557	0.053	29.97	1.32	1.96	0.11	1.049	0.08	5.56
LDC1_1_qtz1	1.33	2.45	0.67	23.02	2.1	0.62	0.1	1.49	0.14	1.7	0.13	0.015	0.012	0.03	0.023	0.0079
LDC1_1_qtz2	2.37	18.88	12.29	29.88	10	2.03	0.86	<0.44	0.43	0.49	0.28	<0.00	<0.00	<0.00	<0.00	<0.00
LDC1_2_torm1	4.52	<1.64	0.71	4.24	0.65	52.84	3.93	<0.068	0.031	8.2	0.39	0.61	0.051	0.691	0.068	10.34
LDC1_2_torm2	6.99	3.81	0.85	10.67	1.13	67.58	5.12	<0.051	0.031	113.09	5.16	6.03	0.35	4.79	0.3	2.03
LDC1_2_torm3	3.75	2.13	0.64	8.16	0.87	36	2.77	0.108	0.03	72.78	3.35	2.09	0.13	0.78	0.074	3.1
BCR2g(Copy6)	0.79	17.87	1.63	152.39	13.52	22.93	1.6	51.5	2.64	310.9	14.17	27.03	1.36	141.05	7.61	12.19
BCR2g(Copy7)	0.87	18.18	1.69	162.25	14.6	23.85	1.69	53.2	2.76	324.77	14.94	28.39	1.44	145.15	7.92	12.8
NIST612(Copy9)	2.8	35.02	3.32	37.33	3.23	35.76	2.85	31.57	1.91	75.5	3.56	38.44	2.01	36.02	1.64	37.94
NIST612(Copy10)	2.89	36.79	3.53	36.72	3.22	35.81	2.9	31.8	1.94	75.73	3.6	38.09	2.02	35.54	1.64	37.26
NIST612(Copy11)	2.8	37.85	3.69	38.89	3.46	37.16	3.05	31.5	1.95	76.45	3.68	37.7	2.02	35.95	1.67	38.4

	Element [ppm]														
Spot analysis	1se Nb93	Mo95	1se Mo95	Cd111	1se Cd111	In115	1se In115	Sn118	1se Sn118	Cs133	1se Cs133	Ba137	1se Ba137	La139	1se La139
NIST612	1.44	36.79	1.64	27.59	1.69	41.95	1.5	37	1.52	40.21	1.74	35.55	1.98	34.41	1.42
NIST612(Copy1)	1.49	39.1	1.73	27.79	1.7	43.4	1.55	37.85	1.56	42.14	1.83	38.92	2.16	36.16	1.49
NIST612(Copy2)	1.5	38.47	1.7	28.38	1.73	43.25	1.54	38.12	1.57	42.16	1.83	37.76	2.1	36.27	1.49
BCR2g	0.59	289.38	11.88	0.247	0.061	0.124	0.012	2.14	0.12	1.299	0.065	671.23	30	22.7	0.97
BCR2g(Copy1)	0.59	291.63	12.04	0.257	0.068	0.113	0.012	2.25	0.13	1.295	0.067	648.92	29.14	22.2	0.95
PG3A_5_torm1	0.14	<0.073	0.048	<0.109	0.048	0.0426	0.0098	3.35	0.21	2.2	0.12	53.57	3.09	2.33	0.12
PG3A_5_matrice1	1.36	0.298	0.068	<0.127	0.066	0.114	0.014	12.68	0.58	10.47	0.47	612.51	33.94	4.64	0.21
PG3A_4_torm2	0.015	<0.068	0.03	0.053	0.035	0.0352	0.0068	0.778	0.076	0.065	0.011	0.634	0.083	0.136	0.015
PG3A_5_matrice2	0.27	0.161	0.055	<0.091	0.047	0.103	0.014	5.38	0.28	3.63	0.18	57.46	3.32	14.26	0.62
PG3A_matrice3	0.5	0.076	0.027	<0.065	0.034	0.0732	0.0094	3.68	0.19	2.16	0.11	35.18	2.05	15.71	0.67
PG3A_2_matrice4	0.37	0.324	0.06	<0.057	0.031	0.117	0.011	5.85	0.28	4.45	0.21	58.06	3.36	12.1	0.52
C5_2_matrice1	0.32	<0.101	0.043	<0.076	0.039	0.111	0.012	2.97	0.17	3.52	0.17	62.48	3.65	1.988	0.098
C5_4_matrice2	0.37	<0.067	0.026	<0.071	0.034	0.0678	0.0087	2.95	0.16	2.12	0.11	50.79	3	17.6	0.76
C5_3_matrice3	0.71	0.094	0.036	0.035	0.025	0.092	0.012	3.63	0.21	2.7	0.14	71.35	4.26	7.58	0.34
LDC11b_1_torm1	0.24	<0.071	0.022	0.056	0.032	0.522	0.035	9.87	0.48	<0.0181	0.0086	0.63	0.095	2.73	0.14
LDC11b_1_torm2	0.021	<0.082	0.028	<0.107	0.033	0.0327	0.0074	2.08	0.14	0.0277	0.0082	1	0.11	0.071	0.01
LDC11b_1_torm3	0.25	0.046	0.027	<0.109	0.039	0.479	0.034	34.38	1.56	0.045	0.011	6.5	0.49	2.02	0.11
LDC11b_1_torm4	0.13	0.012	0.012	<0.088	0.036	0.713	0.041	39.19	1.77	0.2	0.019	170.46	10.48	0.775	0.049
LDC11b_2_torm5	0.73	<0.048	0.023	<0.089	0.027	0.822	0.046	28.86	1.33	0.0347	0.008	3.61	0.3	4.29	0.21
LDC11b_2_torm6	0.1	0.04	0.023	<0.099	0.035	0.18	0.018	10.78	0.53	0.083	0.014	4.16	0.34	1.426	0.081
NIST612(Copy3)	1.63	38.59	1.9	29.45	2.11	43.09	1.65	38.53	1.76	41.14	2	38.59	2.48	36.3	1.66
NIST612(Copy4)	1.68	39.27	1.95	29.55	2.14	43.17	1.66	39.27	1.81	43.14	2.12	39.18	2.55	36.26	1.67
BCR2g(Copy2)	0.7	294.59	13.52	0.306	0.075	0.115	0.012	2.46	0.15	1.299	0.074	694.8	35.65	23.13	1.12
BCR2g(Copy3)	0.68	288.13	13.34	0.301	0.071	0.11	0.012	2.22	0.14	1.284	0.074	650.94	33.78	22.73	1.11
LDC11b_3_torm7	0.02	0.012	0.012	<0.086	0.031	0.0106	0.0038	0.847	0.083	<0.0200	0.0073	0.413	0.07	0.0226	0.0065
LDC11b_3_torm8	0.53	<0.050	0.031	<0.065	0.037	0.672	0.04	17.47	0.87	<0.0194	0.0085	3.33	0.29	3.16	0.17
LDC11b_4_torm9	0.35	0.156	0.046	0.099	0.038	0.375	0.026	19.03	0.95	<0.0192	0.0075	0.92	0.11	3.79	0.2
LDC11b_4_torm10	0.43	<0.055	0.025	<0.103	0.042	0.388	0.026	14.97	0.76	0.125	0.014	14.55	1.08	2.69	0.14
LDC11b_4_torm11	0.56	<0.085	0.034	<0.064	0.025	0.312	0.023	18.27	0.94	0.0358	0.0089	1.85	0.19	2.59	0.14
LDC11b_4_torm12	0.15	<0.046	0.014	0.02	0.014	0.699	0.038	36.71	1.85	0.073	0.01	1.54	0.15	0.421	0.029
LDC11b_4_qtz1	0.073	1.66	2.03	<1.46	0.45	0.19	0.23	12.81	3.69	<0.37	0.11	227.59	26.03	<0.00	<0.00
LDC11b_4_qtz2	0.018	<0.093	0.029	<0.055	0.017	<0.0095	0.0029	<0.109	0.096	0.444	0.068	2.95	0.51	<0.00	<0.00
LDC11b_5_torm13	0.29	0.033	0.019	<0.078	0.041	0.364	0.026	12.16	0.66	0.0257	0.0074	1.4	0.16	11.4	0.61
LDC1_1_qtz1	0.009	0.037	0.042	0.049	0.056	0.0136	0.0082	2.15	0.21	0.582	0.06	3.1	0.41	<0.00207	0.00064
LDC1_1_qtz2	<0.00	<0.282	0.087	<0.37	0.12	0.09	0.12	1.37	1.12	0.3	0.22	2.63	1.53	<0.00	<0.00
LDC1_2_torm1	0.54	0.028	0.02	<0.061	0.033	0.0564	0.0098	2.37	0.17	<0.0145	0.0078	1.32	0.16	0.98	0.068
LDC1_2_torm2	0.15	0.041	0.038	<0.065	0.02	0.513	0.045	36.82	2.07	<0.0120	0.0071	1.84	0.25	0.393	0.042
LDC1_2_torm3	0.18	<0.051	0.025	<0.048	0.015	0.898	0.055	56.08	3.11	0.02	0.0082	1.18	0.15	0.102	0.015
BCR2g(Copy6)	0.75	266.89	14.42	0.23	0.063	0.106	0.012	2.17	0.15	1.24	0.082	638.69	39.81	22.24	1.28
BCR2g(Copy7)	0.8	282.32	15.43	0.297	0.07	0.109	0.012	2.31	0.16	1.284	0.086	669.25	42.25	22.46	1.31
NIST612(Copy9)	1.99	38.01	2.35	29.44	2.85	43.26	1.96	37.43	2.14	41.71	2.59	37.51	3.2	35.98	2.06
NIST612(Copy10)	1.98	37.72	2.36	27.28	2.68	42.15	1.93	37.51	2.17	41.03	2.58	37.37	3.23	35.16	2.04
NIST612(Copy11)	2.06	38.48	2.44	27.3	2.73	43.18	1.99	37.96	2.22	41.64	2.65	37.18	3.26	35.64	2.09

	Element [ppm]														
Spot analysis	Ce140	1se Ce140	Pr141	1se Pr141	Nd146	1se Nd146	Sm149	1se Sm149	Eu151	1se Eu151	Gd157	1se Gd157	Tb159	1se Tb159	Dy163
NIST612	36.42	1.84	35.54	1.64	33.79	1.61	36.14	1.39	33.72	1.35	36.15	1.59	35.18	1.38	35.64
NIST612(Copy1)	38.1	1.93	37.4	1.72	35.33	1.68	37.39	1.43	34.98	1.4	37.87	1.67	36.41	1.43	36.94
NIST612(Copy2)	39.77	2.01	38.31	1.77	36.53	1.74	36.25	1.39	34.42	1.38	37.27	1.64	36.38	1.43	35.16
BCR2g	52.32	2.4	6.2	0.27	26.19	1.26	5.67	0.29	1.756	0.093	5.49	0.33	0.872	0.049	5.59
BCR2g(Copy1)	52.12	2.41	6.26	0.28	26.26	1.28	5.8	0.31	1.817	0.099	5.84	0.36	0.827	0.049	5.49
PG3A_5_torm1	4.01	0.22	0.325	0.027	1.03	0.11	0.182	0.048	0.102	0.018	0.246	0.056	0.0328	0.0076	0.174
PG3A_5_matrice1	15.74	0.82	1.766	0.094	7.46	0.42	1.86	0.15	0.463	0.037	2.18	0.17	0.316	0.023	2.29
PG3A_4_torm2	0.401	0.03	0.0311	0.0055	0.104	0.024	0.0068	0.0068	0.071	0.012	<0.025	0.014	0.0019	0.0014	<0.0150
PG3A_5_matrice2	37.58	1.96	3.87	0.19	14.78	0.78	3.7	0.23	0.643	0.046	3.42	0.23	0.418	0.029	2.86
PG3A_matrice3	55.05	2.88	5.68	0.28	23.02	1.16	4.95	0.26	0.918	0.053	3.88	0.23	0.501	0.029	3.05
PG3A_2_matrice4	37.63	1.98	4.02	0.2	15.8	0.81	3.59	0.2	0.651	0.04	2.89	0.18	0.443	0.026	2.62
C5_2_matrice1	7.47	0.4	0.898	0.051	3.96	0.24	1.111	0.093	0.258	0.023	1.129	0.098	0.171	0.014	1.015
C5_4_matrice2	44.55	2.39	4.02	0.2	13.58	0.71	1.93	0.13	0.41	0.029	1.86	0.13	0.348	0.022	2.46
C5_3_matrice3	23.61	1.29	2.16	0.12	7.34	0.43	1.72	0.14	0.386	0.033	2.07	0.16	0.418	0.028	2.34
LDC11b_1_torm1	6.17	0.35	0.528	0.036	1.52	0.13	0.137	0.038	0.269	0.027	0.093	0.03	0.013	0.0041	0.099
LDC11b_1_torm2	0.201	0.019	0.012	0.0034	0.085	0.022	0.021	0.012	0.0139	0.005	0.021	0.012	0.002	0.0014	0.038
LDC11b_1_torm3	4.75	0.28	0.453	0.033	1.46	0.13	0.387	0.064	0.159	0.021	0.83	0.1	0.265	0.022	2.43
LDC11b_1_torm4	1.68	0.11	0.151	0.015	0.565	0.067	0.076	0.033	0.083	0.013	0.138	0.034	0.026	0.0055	0.401
LDC11b_2_torm5	10.57	0.61	0.875	0.054	2.86	0.2	0.387	0.057	0.218	0.023	0.423	0.061	0.0791	0.01	0.645
LDC11b_2_torm6	3.12	0.19	0.258	0.022	0.784	0.085	0.12	0.033	0.136	0.018	0.078	0.026	0.0146	0.0043	0.19
NIST612(Copy3)	39.36	2.3	36.99	1.95	34.69	1.87	36.75	1.52	34.07	1.51	35.93	1.77	35.45	1.52	35.76
NIST612(Copy4)	39.14	2.32	38.05	2.03	36.18	1.97	37.49	1.56	35.2	1.57	37.21	1.85	36	1.56	36.57
BCR2g(Copy2)	52.93	2.81	6.25	0.31	26.78	1.48	5.86	0.34	1.8	0.11	5.63	0.39	0.859	0.056	5.82
BCR2g(Copy3)	52.77	2.84	6.19	0.31	26.16	1.47	5.77	0.34	1.68	0.1	5.71	0.4	0.849	0.056	5.35
LDC11b_3_torm7	0.0597	0.0094	0.0107	0.0037	0.061	0.02	0.031	0.015	0.0038	0.0027	0.062	0.022	0.0043	0.0022	0.05
LDC11b_3_torm8	8.06	0.51	0.684	0.046	2.07	0.16	0.3	0.05	0.244	0.024	0.303	0.051	0.0552	0.0081	0.417
LDC11b_4_torm9	10.09	0.65	0.786	0.052	2.41	0.18	0.348	0.051	0.235	0.023	0.148	0.033	0.0411	0.0066	0.298
LDC11b_4_torm10	6.81	0.44	0.551	0.038	1.58	0.13	0.283	0.045	0.227	0.022	0.186	0.037	0.0436	0.0067	0.495
LDC11b_4_torm11	6.13	0.41	0.515	0.037	1.52	0.13	0.254	0.046	0.144	0.018	0.238	0.043	0.0613	0.0083	0.485
LDC11b_4_torm12	1.017	0.073	0.118	0.011	0.298	0.038	0.049	0.016	0.0486	0.009	0.159	0.029	0.0414	0.0057	0.438
LDC11b_4_qtz1	1.04	0.49	0.34	0.24	1.04	1.04	<0.71	0.22	<0.00	<0.00	<0.00	<0.00	<0.00	<0.00	0.77
LDC11b_4_qtz2	<0.00	<0.00	<0.00	<0.00	<0.00	<0.00	<0.00	<0.00	<0.00	<0.00	<0.00	<0.00	<0.00	<0.00	<0.00
LDC11b_5_torm13	29.98	2.07	2.34	0.15	7.27	0.5	0.767	0.081	0.34	0.03	0.441	0.063	0.0473	0.0075	0.318
LDC1_1_qtz1	0.0045	0.0045	<0.00	<0.00	<0.00	<0.00	<0.00	<0.00	<0.00	<0.00	<0.00	<0.00	<0.00	<0.00	<0.00
LDC1_1_qtz2	0.11	0.11	<0.0239	0.0074	0.53	0.53	<0.183	0.056	<0.00	<0.00	<0.00	<0.00	<0.00	<0.00	<0.00
LDC1_2_torm1	2.63	0.2	0.228	0.022	0.706	0.085	0.157	0.039	0.061	0.012	0.14	0.037	0.0104	0.0041	0.071
LDC1_2_torm2	0.942	0.086	0.091	0.015	0.293	0.065	0.134	0.048	0.089	0.02	0.135	0.048	0.046	0.011	0.557
LDC1_2_torm3	0.265	0.028	0.0407	0.0075	0.19	0.039	0.037	0.018	0.063	0.012	0.102	0.031	0.017	0.005	0.12
BCR2g(Copy6)	51.09	3.33	6.17	0.37	25.39	1.71	6.08	0.41	1.77	0.13	5.26	0.44	0.747	0.058	4.82
BCR2g(Copy7)	51.82	3.42	6.17	0.37	26.99	1.84	6.3	0.43	1.81	0.13	5.97	0.51	0.815	0.064	5.47
NIST612(Copy9)	37.89	2.93	36.57	2.51	35.12	2.45	37.03	1.83	35.26	1.94	37.88	2.37	36.87	1.95	36.46
NIST612(Copy10)	37.99	2.98	36.88	2.56	34.88	2.46	36.11	1.81	33.92	1.89	36.18	2.29	35.22	1.88	35.94
NIST612(Copy11)	38.2	3.04	37.56	2.64	35.44	2.54	36.65	1.85	34.01	1.92	37.21	2.39	35.92	1.94	35.38

	Element [ppm]													
Spot analysis	1se Dy163	Ho165	1se Ho165	Er167	1se Er167	Tm169	1se Tm169	Yb173	1se Yb173	Lu175	1se Lu175	Hf177	1se Hf177	Ta181
NIST612	1.42	37.13	1.39	36.67	1.76	36.39	1.69	38.47	1.86	37.26	1.29	33.94	1.36	38.49
NIST612(Copy1)	1.48	37.83	1.41	37.51	1.79	38.07	1.77	40.39	1.95	38.37	1.33	35.7	1.43	40.76
NIST612(Copy2)	1.41	38.19	1.43	37.26	1.78	37.37	1.74	39.98	1.93	37.21	1.29	34.39	1.37	39.77
BCR2g	0.27	1.007	0.049	3.08	0.2	0.429	0.027	3.2	0.2	0.442	0.025	3.89	0.2	0.732
BCR2g(Copy1)	0.28	1.116	0.056	3.04	0.2	0.418	0.028	2.91	0.19	0.412	0.026	3.94	0.21	0.798
PG3A_5_torm1	0.036	0.056	0.01	0.147	0.034	0.0331	0.0078	0.255	0.053	0.0447	0.0091	0.302	0.051	0.175
PG3A_5_matrice1	0.14	0.399	0.027	1.128	0.096	0.162	0.016	0.96	0.098	0.172	0.016	1.025	0.087	1.917
PG3A_4_torm2	0.0085	<0.0037	0.0023	0.0087	0.0062	<0.00	<0.00	0.0119	0.0084	0.003	0.0017	0.0137	0.0079	0.0052
PG3A_5_matrice2	0.17	0.564	0.035	1.53	0.12	0.23	0.021	1.52	0.13	0.208	0.018	1.24	0.1	0.54
PG3A_matrice3	0.16	0.649	0.035	1.95	0.13	0.277	0.02	2.13	0.15	0.279	0.019	4.04	0.21	1.038
PG3A_2_matrice4	0.14	0.535	0.029	1.66	0.11	0.252	0.019	1.46	0.11	0.206	0.015	1.415	0.092	0.944
C5_2_matrice1	0.074	0.229	0.017	0.709	0.063	0.114	0.012	0.794	0.077	0.138	0.012	0.38	0.042	0.578
C5_4_matrice2	0.14	0.503	0.028	1.69	0.11	0.258	0.019	2.13	0.15	0.296	0.019	3.18	0.17	0.668
C5_3_matrice3	0.15	0.489	0.031	1.37	0.11	0.26	0.022	1.86	0.15	0.25	0.02	1.36	0.1	1.164
LDC11b_1_torm1	0.024	0.0149	0.0045	0.087	0.023	0.0184	0.005	0.183	0.039	0.0322	0.0067	<0.00	<0.00	0.352
LDC11b_1_torm2	0.013	0.0084	0.003	0.045	0.014	0.0111	0.0034	0.067	0.021	0.0124	0.0036	0.0047	0.0047	0.014
LDC11b_1_torm3	0.16	0.714	0.043	2.7	0.19	0.539	0.039	4.29	0.29	0.682	0.04	<0.021	0.015	0.205
LDC11b_1_torm4	0.048	0.161	0.015	0.904	0.083	0.198	0.018	1.53	0.13	0.321	0.023	0.026	0.012	0.0584
LDC11b_2_torm5	0.062	0.189	0.017	0.585	0.062	0.141	0.015	0.846	0.089	0.159	0.015	0.052	0.017	0.705
LDC11b_2_torm6	0.032	0.0395	0.0073	0.228	0.038	0.0664	0.0097	0.574	0.072	0.093	0.011	0.0057	0.0057	0.217
NIST612(Copy3)	1.57	37.67	1.53	37.45	2.04	37.71	1.99	40.88	2.23	38.06	1.4	34.76	1.51	39.49
NIST612(Copy4)	1.62	39.04	1.59	39.12	2.15	39.1	2.09	41.12	2.27	37.96	1.4	35.41	1.55	40.77
BCR2g(Copy2)	0.32	1.153	0.063	3.1	0.23	0.444	0.032	3.21	0.23	0.413	0.027	3.84	0.22	0.799
BCR2g(Copy3)	0.3	1.076	0.059	3.04	0.23	0.401	0.03	3.13	0.23	0.411	0.027	3.92	0.23	0.802
LDC11b_3_torm7	0.015	0.0124	0.0038	0.063	0.018	0.0129	0.0042	0.132	0.03	0.0155	0.0042	0.005	0.005	0.0058
LDC11b_3_torm8	0.048	0.142	0.014	0.583	0.063	0.098	0.012	1.06	0.1	0.166	0.015	0.101	0.023	0.609
LDC11b_4_torm9	0.038	0.115	0.012	0.404	0.048	0.094	0.011	0.9	0.09	0.163	0.014	<0.022	0.011	0.405
LDC11b_4_torm10	0.05	0.12	0.012	0.566	0.059	0.123	0.013	0.846	0.085	0.097	0.01	0.095	0.021	0.518
LDC11b_4_torm11	0.051	0.123	0.013	0.582	0.062	0.092	0.011	0.861	0.089	0.122	0.012	0.028	0.011	0.77
LDC11b_4_torm12	0.041	0.202	0.015	1.001	0.082	0.222	0.018	1.85	0.14	0.332	0.02	0.057	0.014	0.0946
LDC11b_4_qtz1	0.78	<0.00	<0.00	<0.45	0.14	<0.00	<0.00	<0.00	<0.00	<0.00	<0.00	<0.00	<0.00	0.2
LDC11b_4_qtz2	<0.00	<0.00	<0.00	<0.00	<0.00	<0.00	<0.00	<0.0234	0.0072	<0.00	<0.00	<0.00	<0.00	<0.00
LDC11b_5_torm13	0.04	0.084	0.01	0.197	0.032	0.0354	0.0064	0.308	0.049	0.0442	0.007	<0.025	0.011	0.618
LDC1_1_qtz1	<0.00	<0.00	<0.00	<0.00	<0.00	<0.00	<0.00	<0.00	<0.00	<0.00150	0.00046	<0.00	<0.00	<0.00
LDC1_1_qtz2	<0.00	<0.00	<0.00	<0.00	<0.00	<0.00	<0.00	<0.00	<0.00	<0.00	<0.00	4.32	1.38	<0.00
LDC1_2_torm1	0.02	0.0327	0.0068	0.128	0.029	0.0223	0.0056	0.269	0.049	0.0412	0.0076	<0.019	0.01	0.867
LDC1_2_torm2	0.08	0.18	0.023	1.04	0.13	0.257	0.03	1.81	0.2	0.217	0.025	0.238	0.052	0.211
LDC1_2_torm3	0.026	0.0623	0.0096	0.272	0.044	0.076	0.011	0.536	0.075	0.111	0.013	0.102	0.026	0.565
BCR2g(Copy6)	0.32	1.033	0.065	2.95	0.27	0.402	0.034	2.9	0.25	0.411	0.029	3.72	0.24	0.73
BCR2g(Copy7)	0.36	1.053	0.067	3.07	0.28	0.442	0.038	2.95	0.25	0.452	0.032	3.99	0.26	0.713
NIST612(Copy9)	1.97	37.86	1.85	38.15	2.7	38.05	2.6	40.36	2.85	37.99	1.6	35.08	1.84	39.79
NIST612(Copy10)	1.96	37.46	1.85	36.01	2.58	36.41	2.52	38.52	2.75	37.28	1.58	34.25	1.82	39.59
NIST612(Copy11)	1.96	37.78	1.88	37.38	2.71	37.39	2.63	39.99	2.9	37.6	1.61	34.68	1.86	39.54

	Element [ppm]								
Spot analysis	1se Ta181	W182	1se W182	Pb208	1se Pb208	Th232	1se Th232	U238	1se U238
NIST612	1.56	37.72	2.12	37.23	2.02	35.79	1.65	35.29	1.76
NIST612(Copy1)	1.66	40.61	2.29	38.82	2.1	37.72	1.74	37.74	1.89
NIST612(Copy2)	1.62	40.07	2.26	39.7	2.15	37.74	1.74	37.83	1.89
BCR2g	0.036	0.512	0.044	11.43	0.63	5.28	0.27	1.764	0.085
BCR2g(Copy1)	0.041	0.53	0.048	11.26	0.63	5.39	0.27	1.73	0.085
PG3A_5_torm1	0.019	1.27	0.11	12.94	0.73	1.292	0.077	1.03	0.062
PG3A_5_matrice1	0.093	9.09	0.55	32.8	1.81	7.24	0.35	7.55	0.39
PG3A_4_torm2	0.0023	0.0133	0.0067	11.47	0.64	0.0407	0.0066	0.0406	0.0057
PG3A_5_matrice2	0.035	1.24	0.1	13.98	0.79	8.04	0.39	4.98	0.26
PG3A_matrice3	0.053	4.91	0.31	11.18	0.63	9.05	0.44	8.74	0.45
PG3A_2_matrice4	0.048	1.43	0.1	13	0.74	6.97	0.34	5.52	0.29
C5_2_matrice1	0.034	3.45	0.23	24.86	1.42	6.67	0.33	1.278	0.072
C5_4_matrice2	0.037	3.92	0.26	14.89	0.86	8.82	0.43	4.47	0.24
C5_3_matrice3	0.063	5.15	0.34	8.05	0.48	8.07	0.4	3.24	0.18
LDC11b_1_torm1	0.027	0.419	0.051	3.44	0.22	0.166	0.017	0.0167	0.0039
LDC11b_1_torm2	0.0039	0.189	0.028	14.9	0.89	0.0174	0.0043	0.0041	0.0017
LDC11b_1_torm3	0.02	0.738	0.075	0.667	0.063	0.65	0.045	0.358	0.027
LDC11b_1_torm4	0.0088	0.132	0.024	0.875	0.07	0.355	0.027	0.0529	0.007
LDC11b_2_torm5	0.043	0.483	0.053	0.221	0.037	0.46	0.033	0.118	0.011
LDC11b_2_torm6	0.019	0.134	0.025	7.77	0.5	0.093	0.012	0.0312	0.0054
NIST612(Copy3)	1.77	38.72	2.54	39.29	2.46	37.1	1.93	37.02	2.12
NIST612(Copy4)	1.85	41.31	2.74	41.08	2.6	38.33	2.02	38.71	2.25
BCR2g(Copy2)	0.043	0.582	0.055	11.45	0.75	5.41	0.32	1.723	0.095
BCR2g(Copy3)	0.043	0.572	0.054	11.34	0.75	5.34	0.32	1.721	0.096
LDC11b_3_torm7	0.0026	0.0185	0.0084	5.91	0.4	0.446	0.033	0.0073	0.0023
LDC11b_3_torm8	0.039	0.958	0.09	0.441	0.048	0.624	0.043	0.459	0.033
LDC11b_4_torm9	0.028	0.204	0.031	1.88	0.14	4.63	0.27	0.0656	0.0077
LDC11b_4_torm10	0.034	0.303	0.038	0.59	0.057	0.293	0.024	0.133	0.012
LDC11b_4_torm11	0.047	0.162	0.026	0.245	0.035	0.267	0.023	0.1	0.01
LDC11b_4_torm12	0.0096	0.164	0.023	0.33	0.036	0.358	0.026	0.049	0.0057
LDC11b_4_qtz1	0.2	<0.00	<0.00	8.45	1.98	3.73	0.87	0.25	0.18
LDC11b_4_qtz2	<0.00	0.234	0.081	0.81	0.12	0.0078	0.0079	<0.00	<0.00
LDC11b_5_torm13	0.041	0.322	0.043	0.171	0.037	0.791	0.056	0.0776	0.0089
LDC1_1_qtz1	<0.00	0.039	0.023	1.13	0.12	0.0194	0.0088	0.0051	0.0037
LDC1_1_qtz2	<0.00	<0.00	<0.00	0.76	0.51	0.38	0.19	<0.00	<0.00
LDC1_2_torm1	0.057	0.089	0.023	0.206	0.036	0.252	0.024	0.13	0.014
LDC1_2_torm2	0.026	0.169	0.04	1.15	0.11	3	0.21	0.124	0.017
LDC1_2_torm3	0.041	0.088	0.021	0.45	0.051	1.18	0.086	0.0304	0.0056
BCR2g(Copy6)	0.043	0.473	0.051	11.05	0.9	5.14	0.37	1.75	0.12
BCR2g(Copy7)	0.043	0.486	0.054	11.11	0.92	5.42	0.4	1.85	0.12
NIST612(Copy9)	2.21	38.84	3.39	39.14	3.24	37.99	2.55	37.16	2.79
NIST612(Copy10)	2.23	38.58	3.42	37.7	3.17	36.27	2.47	36.6	2.79
NIST612(Copy11)	2.25	40.69	3.66	38.84	3.31	36.99	2.55	36.94	2.85

13. APPENDIX 5: SIMS DATASET

Sample	Locality	Analysis	Beam Current nA	^{11}B/^{10}B measured	int. precision percent	^{11}B/^{10}B cor IMF-corrected	δ^{11}B	Int. Precision permil	^{11}B/Coeff H'2	Avarage δ^{11}B	Sd	N analysis	Min	Max
880	Val Trompia	880-2-Area1@1	6.03	3.94	0.01	4.03	-2.3	0.12	12967390	-5.1	1.6	15	-9.4	-2.3
		880-2-Area1@2	5.41	3.93	0.01	4.03	-3.7	0.09	13666440					
		880-2-Area1@5	5.51	3.93	0.01	4.02	-5.1	0.10	16452360					
		880-2-Area1@6	5.56	3.93	0.01	4.03	-3.6	0.12	14208340					
		880-2-Area1@7	5.49	3.93	0.01	4.02	-5.1	0.10	14761760					
		880-2-Area1@8	6.54	3.93	0.01	4.02	-5.7	0.10	18962680					
		880-2-Area2@1	8.82	3.93	0.01	4.02	-5.8	0.08	23944820					
		880-2-Area2@2	8.81	3.93	0.01	4.02	-5.6	0.07	24223140					
		880-2-Area2@3	8.81	3.91	0.01	4.01	-9.4	0.06	23998050					
		880-2-Area2@4	8.75	3.93	0.01	4.02	-5.8	0.07	23908970					
		880-2-Area2@5	8.76	3.92	0.01	4.02	-6.8	0.07	24021030					
		880-2-Area3@2	8.50	3.93	0.01	4.03	-4.3	0.07	22526200					
		880-2-Area3@3	8.16	3.93	0.01	4.03	-3.9	0.06	21165780					
		880-2-Area3@4b	7.06	3.93	0.01	4.02	-5.4	0.08	19217070					
		880-2-Area3@1b	6.68	3.93	0.01	4.03	-4.4	0.11	17778520					
VSS3A	Valsassina	VSS3A-Area2@1	5.31	3.90	0.01	4.00	-11.5	0.09	14226940	-10.5	1.2	13	-12.9	-8.8
		VSS3A-Area2@2	5.32	3.91	0.01	4.00	-10.1	0.09	14144130					
		VSS3A-Area2@4	5.35	3.91	0.01	4.00	-9.7	0.10	13775080					
		VSS3A-Area2@5	5.38	3.91	0.01	4.00	-10.6	0.11	14516770					
		VSS3A-Area3@1	5.37	3.91	0.01	4.00	-9.6	0.08	14313170					
		VSS3A-Area3@2	5.38	3.91	0.01	4.00	-9.7	0.11	14326260					
		VSS3A-Area3@3	5.31	3.91	0.01	4.01	-9.5	0.09	14143550					
		VSS3A-Area3@4	5.30	3.91	0.01	4.00	-10.9	0.10	12690430					
		VSS3A-Area3@5	5.21	3.91	0.01	4.00	-11.0	0.10	13210160					
		VSS3A-Area4@1	5.13	3.90	0.02	3.99	-12.9	0.15	10327900					
		VSS3A-Area4@2	5.12	3.90	0.01	3.99	-12.5	0.12	12403180					
		VSS3A-Area1@3	6.31	3.91	0.01	4.01	-8.8	0.10	11566500					
		VSS3A-Area1@5	6.20	3.91	0.02	4.00	-9.9	0.17	13483950					
FC21.1	Forcellino Pass	FC21-1-Area1@T1-4	6.34	3.92	0.01	4.01	-7.8	0.06	15625900	-5.7	1.0	7	-7.8	4.4
		FC21-1-Area1@T1-5	6.35	3.93	0.01	4.02	-5.4	0.13	14195170					
		FC21-1-Area1@T1-6	6.31	3.92	0.01	4.02	-6.5	0.09	15489470					
		FC21-1-Area1@T2-4	6.25	3.93	0.01	4.02	-5.4	0.09	15171050					
		FC21-1-Area1@T2-5	6.25	3.93	0.01	4.03	-4.4	0.12	11616200					
		FC21-1-Area2@T3-4	6.23	3.93	0.01	4.02	-5.2	0.11	11246990					
		FC21-1-Area2@T3-5	6.20	3.93	0.01	4.02	-5.1	0.14	12426750					

Sample	Locality	Analysis	Beam Current nA	$^{11}B/^{10}B$ measured	int. precision percent	$^{11}B/^{10}B$ cor IMF-corrected	$\delta^{11}B$	Int. Precision permil	^{11}B/Coeff H'2	Avarage $\delta^{11}B$	Sd	N analysis	Min	Max
FC14	Forcellino Pass	FC14-Area3@1	6.07	3.92	0.01	4.02	-6.7	0.09	13184980	-8.2	2.7	15	-10.6	-2.2
		FC14-Area3@2	6.04	3.92	0.01	4.01	-8.2	0.10	15236730					
		FC14-Area2@1	6.02	3.92	0.01	4.02	-7.0	0.09	16276750					
		FC14-Area2@2	5.83	3.93	0.01	4.03	-4.0	0.12	12962620					
		FC14-Area2@3	5.82	3.94	0.01	4.03	-2.2	0.09	15226060					
		FC14-Area2.1@1	6.17	3.91	0.01	4.00	-10.6	0.10	14907760					
		FC14-Area1@1	5.89	3.91	0.01	4.00	-10.4	0.11	13195760					
		FC14-Area1@2	5.83	3.91	0.01	4.00	-10.6	0.08	15058600					
		FC14-Area1@3	5.83	3.92	0.01	4.01	-7.1	0.13	14823430					
		FC14-Area4@1	5.50	3.92	0.01	4.02	-6.6	0.12	11947780					
		FC14-Area4@2	6.04	3.92	0.01	4.01	-8.3	0.09	12466320					
		FC14-Area5@1	5.51	3.90	0.01	3.99	-13.3	0.12	14224240					
		FC14-Area5@2	6.07	3.92	0.01	4.01	-7.3	0.10	13834080					
		FC14-Area6@1	5.34	3.91	0.01	4.00	-10.6	0.08	12655900					
		FC14-Area6@2	5.21	3.91	0.01	4.00	-10.3	0.13	12349500					
C5	Monte Aga	C5-Area1@2	6.05	3.92	0.02	4.01	-8.2	0.15	10747200	-7.0	2.6	9	-10.1	-2.0
		C5-Area4@1	6.08	3.92	0.01	4.02	-6.5	0.13	11738480					
		C5-Area4@2	6.09	3.92	0.01	4.02	-7.1	0.12	10597360					
		C5-Area3@1	5.97	3.93	0.01	4.03	-3.5	0.10	14181940					
		C5-Area3@2	5.95	3.94	0.01	4.04	-2.0	0.09	17338420					
		C5-Area2-1@1	5.56	3.91	0.01	4.01	-9.5	0.11	14704820					
		C5-Area2-1@2	6.08	3.91	0.01	4.00	-10.1	0.10	13993910					
		C5-Area2-2@1	6.00	3.92	0.01	4.02	-6.7	0.08	16403490					
		C5-Area2-2@3	5.88	3.91	0.01	4.01	-9.2	0.10	11698610					
PG3A	Gerola Valley	PG3A-Area1@1	6.02	3.93	0.01	4.02	-5.3	0.09	10778820	-3.6	1.5	9	-5.5	-2.0
	Lake Pescegallo	PG3A-area2@1	6.15	3.93	0.02	4.02	-5.5	0.17	10603850					
		PG3A-Area3-Clast@1	6.17	3.94	0.01	4.04	-1.9	0.12	12476360					
		PG3A-Area3-Clast@2	6.27	3.94	0.01	4.03	-2.6	0.11	13868920					
		PG3A-Area3-Clast@3	6.37	3.94	0.01	4.04	-2.0	0.11	14126240					
		PG3A-Area3-tourm@1	6.39	3.93	0.01	4.02	-4.6	0.12	10463090					
		PG3A-Area3-1@1	6.28	3.93	0.01	4.03	-4.2	0.11	14196600					
		PG3A-Area4@1	6.21	3.93	0.02	4.02	-4.7	0.16	10750820					
		PG3A-Area4@2	6.14	3.93	0.01	4.02	-4.6	0.13	11596850					

			Beam Current	**$^{11}B/^{10}B$**	**int. precision**	**$^{11}B/^{10}B$ cor**		**Int. Precision**	**^{11}B/Coeff**	**Avarage**				
Sample	**Locality**	**Analysis**	**nA**	**measured**	**percent**	**IMF-corrected**	**$\delta^{11}B$**	**permil**	**H'2**	**$\delta^{11}B$**	**Sd**	**N analysis**	**Min**	**Max**
AV6	Lake Aviasco	AV6-Area1@1	6.94	3.91	0.01	4.01	-8.6	0.10	15052780	-10.7	1.5	10	-13.3	-8.6
		AV6-Area1@2	7.04	3.90	0.01	3.99	-12.5	0.08	16936570					
		AV6-Area2@1	7.02	3.91	0.01	4.00	-10.2	0.09	16591840					
		AV6-Area3@1	6.72	3.90	0.01	3.99	-13.3	0.08	18057990					
		AV6-Area3@2	6.67	3.91	0.01	4.00	-10.4	0.11	18408870					
		AV6-Area6@1	6.52	3.90	0.01	3.99	-12.8	0.09	14084040					
		AV6-Area6@2	6.36	3.91	0.01	4.00	-10.1	0.11	16666250					
		AV6-Area6@3	6.21	3.91	0.01	4.01	-9.5	0.07	15873030					
		AV6-Area7@1	6.06	3.91	0.01	4.00	-10.6	0.09	16343680					
		AV6-Area5@1	5.99	3.91	0.01	4.01	-9.2	0.07	16139210					

14. APPENDIX 6: ARSENOPYRITE COMPOSITION

	Weight%				Arsenic Atom%		
Spot analysis	Fe	As	S	Total	Fe	As	S
AV5-SOLF-4	34.68	45.38	20.98	101.04	33.01	32.20	34.79
AV5-SOLF-6	34.75	44.05	20.66	99.46	33.55	31.70	34.75
AV5-SOLF-8	34.90	45.55	21.16	101.61	33.01	32.12	34.87
AV5-SOLF-9	35.00	44.83	21.48	101.31	33.07	31.57	35.35
AV5-SOLF-10	35.17	45.20	21.58	101.95	33.04	31.65	35.31
AV5-SOLF-11	34.48	44.86	21.32	100.66	32.82	31.83	35.35
AV5-SOLF-12	34.85	44.36	21.02	100.23	33.34	31.63	35.03
AV5-SOLF-13	35.01	44.08	21.49	100.58	33.25	31.20	35.55
AV5-SOLF-14	34.73	44.69	21.46	100.88	32.94	31.60	35.46
AV5-SOLF-15	33.91	43.21	20.74	97.86	33.16	31.50	35.33
AV5-SOLF-20	35.04	45.97	20.68	101.69	33.27	32.53	34.20
AV5-SOLF-21	34.87	43.97	21.60	100.44	33.12	31.13	35.74
AV5-SOLF-22	34.52	43.32	21.45	99.29	33.14	31.00	35.87
AV5-SOLF-23	35.19	44.53	21.31	101.03	33.35	31.46	35.18
AV5-SOLF-24	34.96	44.17	21.64	100.77	33.11	31.18	35.70
AV5-SOLF-25	34.86	43.67	21.91	100.44	33.02	30.83	36.15
AV5-SOLF-26	35.27	43.28	21.36	99.91	33.67	30.80	35.52
AV5-SOLF-27	35.28	44.07	21.14	100.49	33.61	31.30	35.09
AV5-SOLF-28	35.45	44.13	21.08	100.66	33.74	31.31	34.95
AV5-SOLF-29	35.69	44.08	21.83	101.60	33.49	30.83	35.68
AV5-SOLF-31	35.01	45.50	20.89	101.40	33.24	32.20	34.55
AV5-SOLF-33	35.45	44.52	20.74	100.71	33.84	31.68	34.49
AV5-SOLF-35	35.41	44.07	21.68	101.16	33.40	30.98	35.62
AV5-SOLF-36	35.05	44.67	21.06	100.78	33.37	31.70	34.93
AV5-SOLF-37	34.86	44.01	21.60	100.47	33.11	31.16	35.74
AV5-SOLF-38	35.02	44.33	21.62	100.97	33.12	31.25	35.62
AV5-SOLF-39	35.02	44.62	20.85	100.49	33.48	31.80	34.72
AV5-SOLF-41	35.30	44.32	21.07	100.69	33.61	31.45	34.94
AV5-SOLF-43	34.97	46.12	20.45	101.54	33.31	32.75	33.94
AV5-SOLF-45	35.48	44.03	22.51	102.02	33.00	30.53	36.47

15. APPENDIX 7: LA-ICP-MS U-Pb DATING

7.1 U-Pb DATING ON ZIRCONS

SAMPLE	**VNE3**								**SAMPLE**	**VNE3**		
Spot analysis	Pb_{207}/Pb_{206}	1se Pb_{207}/Pb_{206}	Pb_{206}/U_{238}	1se Pb_{206}/U_{238}	Pb_{207}/U_{235}	1se Pb_{207}/U_{235}	Pb_{208}/Th_{232}	1se Pb_{208}/Th_{232}	AGE Pb_{206}/U_{238} (Ma)	1se (Ma)	AGE Pb_{207}/U_{235} (Ma)	1se (Ma)
91500	0.0754	0.0022	0.1784	0.0026	1.8535	0.0545	0.0558	0.0014	1058.1	14.1	1064.7	19.4
91500(Copy1)	0.0758	0.0021	0.1787	0.0025	1.8652	0.0518	0.0550	0.0013	1059.7	13.8	1068.8	18.4
91500(Copy2)	0.0757	0.0020	0.1803	0.0025	1.8796	0.0502	0.0518	0.0012	1068.4	13.9	1073.9	17.7
91500(Copy3)	0.0737	0.0019	0.1799	0.0025	1.8251	0.0476	0.0533	0.0012	1066.3	13.7	1054.5	17.1
Plesovice	0.0544	0.0015	0.0559	0.0008	0.4188	0.0118	0.0184	0.0007	350.8	4.8	355.2	8.5
VNE3_z4_rim1	0.0515	0.0018	0.0463	0.0007	0.3280	0.0114	0.0134	0.0004	291.5	4.3	288.0	8.7
VNE3_z4_rim2	0.0511	0.0016	0.0450	0.0007	0.3166	0.0098	0.0133	0.0004	283.6	4.0	279.3	7.5
VNE3_z4_core	0.0484	0.0047	0.0515	0.0011	0.3430	0.0328	0.0140	0.0009	323.7	6.6	299.4	24.8
VNE3_z5_rim	0.0523	0.0014	0.0446	0.0006	0.3217	0.0087	0.0129	0.0003	281.5	3.9	283.2	6.7
VNE3_z5_core1	0.0604	0.0020	0.0453	0.0007	0.3771	0.0128	0.0148	0.0004	285.5	4.1	324.9	9.4
VNE3_z5_core2	0.0580	0.0022	0.0445	0.0007	0.3554	0.0132	0.0128	0.0004	280.8	4.2	308.8	9.9
VNE3_z2_core	0.0773	0.0017	0.0249	0.0003	0.2648	0.0059	0.0078	0.0001	158.3	2.1	238.5	4.8
VNE3_z3_rim	0.0541	0.0014	0.0652	0.0009	0.4863	0.0132	0.0241	0.0008	407.4	5.5	402.4	9.0
VNE3_z3_core	0.0559	0.0018	0.0778	0.0012	0.5989	0.0199	0.0261	0.0008	482.8	7.0	476.6	12.7
VNE3_z1_core	0.0519	0.0021	0.0538	0.0009	0.3845	0.0152	0.0156	0.0005	338.0	5.2	330.3	11.1
VNE3_z1_rim	0.0517	0.0024	0.0461	0.0008	0.3283	0.0149	0.0157	0.0005	290.4	4.7	288.3	11.4

SAMPLE	**VNE4**								**SAMPLE**	**VNE4**		
Spot analysis	Pb_{207}/Pb_{206}	1se Pb_{207}/Pb_{206}	Pb_{206}/U_{238}	1se Pb_{206}/U_{238}	Pb_{207}/U_{235}	1se Pb_{207}/U_{235}	Pb_{208}/Th_{232}	1se Pb_{208}/Th_{232}	AGE Pb_{206}/U_{238} (Ma)	1se (Ma)	AGE Pb_{207}/U_{235} (Ma)	1se (Ma)
VNE4_z1_rim	0.0519	0.0025	0.0451	0.0008	0.3223	0.0152	0.0125	0.0005	284.4	4.8	283.7	11.7
VNE4_z1_core	0.0527	0.0024	0.0441	0.0007	0.3201	0.0146	0.0122	0.0004	278.1	4.5	282.0	11.2
VNE4_z2_rim	0.0672	0.0028	0.0488	0.0008	0.4511	0.0187	0.0157	0.0005	306.9	5.0	378.1	13.1
VNE4_z3_rim	0.0521	0.0017	0.0445	0.0007	0.3193	0.0106	0.0120	0.0003	280.8	4.1	281.4	8.2
VNE4_z3_core	0.0529	0.0020	0.0463	0.0007	0.3374	0.0129	0.0133	0.0004	291.8	4.4	295.2	9.8
VNE4_z4_rim	0.0523	0.0031	0.0436	0.0008	0.3142	0.0183	0.0117	0.0005	275.2	5.2	277.4	14.2
VNE4_z5_rim	0.0526	0.0019	0.0458	0.0007	0.3321	0.0120	0.0125	0.0004	288.8	4.4	291.1	9.1
VNE4_z5_core	0.0515	0.0018	0.0446	0.0007	0.3164	0.0108	0.0123	0.0004	281.3	4.2	279.1	8.4
VNE4_z6_rim1	0.0526	0.0022	0.0455	0.0007	0.3300	0.0135	0.0119	0.0004	287.1	4.6	289.6	10.3
VNE4_z6_rim2	0.0516	0.0021	0.0451	0.0007	0.3211	0.0132	0.0119	0.0004	284.6	4.5	282.8	10.2
91500(Copy4)	0.0755	0.0031	0.1768	0.0029	1.8395	0.0740	0.0518	0.0018	1049.3	15.7	1059.7	26.5
91500(Copy5)	0.0775	0.0033	0.1799	0.0030	1.9211	0.0810	0.0538	0.0020	1066.5	16.4	1088.5	28.1
91500(Copy6)	0.0739	0.0032	0.1784	0.0030	1.8175	0.0787	0.0547	0.0021	1058.4	16.4	1051.8	28.4
91500(Copy7)	0.0741	0.0034	0.1792	0.0031	1.8303	0.0819	0.0534	0.0021	1062.4	16.7	1056.4	29.4
Plesovice(Copy2)	0.0521	0.0024	0.0536	0.0009	0.3847	0.0176	0.0174	0.0008	336.3	5.6	330.5	12.9
VNE4_z7_rim	0.0522	0.0025	0.0447	0.0008	0.3216	0.0150	0.0124	0.0005	282.0	4.8	283.2	11.5
VNE4_z8_core	0.0532	0.0024	0.0468	0.0008	0.3425	0.0151	0.0127	0.0005	294.7	4.9	299.1	11.4
VNE4_z9_rim	0.0575	0.0036	0.0476	0.0010	0.3770	0.0235	0.0118	0.0006	299.7	6.1	324.8	17.3
VNE4_z10_core	0.0528	0.0048	0.0446	0.0010	0.3241	0.0292	0.0121	0.0007	281.0	6.2	285.1	22.4
VNE4_z11_rim	0.0518	0.0028	0.0446	0.0008	0.3179	0.0172	0.0128	0.0006	281.0	5.2	280.3	13.2
VNE4_z12_rim	0.0618	0.0031	0.0437	0.0008	0.3723	0.0184	0.0105	0.0005	275.9	4.8	321.3	13.6
VNE4_z13_rim	0.1762	0.0149	0.0435	0.0012	1.0547	0.0885	0.0261	0.0018	274.4	7.2	731.2	43.7

SAMPLE	**VNE4**								**SAMPLE**	**VNE4**		
Spot analysis	Pb_{207}/Pb_{206}	1se Pb_{207}/Pb_{206}	Pb_{206}/U_{238}	1se Pb_{206}/U_{238}	Pb_{207}/U_{235}	1se Pb_{207}/U_{235}	Pb_{208}/Th_{232}	1se Pb_{208}/Th_{232}	AGE Pb_{206}/U_{238} (Ma)	1se (Ma)	AGE Pb_{207}/U_{235} (Ma)	1se (Ma)
VNE4_z13_core	0.0516	0.0039	0.0425	0.0010	0.3020	0.0223	0.0117	0.0008	268.2	6.2	268.0	17.4
VNE4_z14_core	0.0521	0.0028	0.0377	0.0007	0.2703	0.0145	0.0126	0.0006	238.5	4.4	243.0	11.6
VNE4_z14_rim	0.0514	0.0035	0.0449	0.0010	0.3180	0.0215	0.0124	0.0007	283.4	6.1	280.4	16.6
VNE4_z16_core	0.0572	0.0046	0.0777	0.0019	0.6126	0.0484	0.0269	0.0019	482.5	11.3	485.2	30.5
VNE4_z16_rim	0.0522	0.0056	0.0465	0.0015	0.3346	0.0354	0.0123	0.0011	293.1	9.2	293.1	26.9
VNE4_z18_rim	0.0529	0.0045	0.0454	0.0012	0.3309	0.0275	0.0145	0.0011	285.9	7.2	290.2	21.0
VNE4_z18_core	0.0513	0.0033	0.0453	0.0009	0.3199	0.0204	0.0127	0.0007	285.7	5.8	281.9	15.7
VNE4_z20_rim	0.0520	0.0052	0.0446	0.0013	0.3194	0.0317	0.0117	0.0009	281.1	7.9	281.4	24.4
VNE4_z22_rim	0.0586	0.0076	0.0434	0.0016	0.3496	0.0437	0.0125	0.0013	273.9	9.7	304.4	32.9
VNE4_z23_core	0.0512	0.0037	0.0443	0.0010	0.3127	0.0225	0.0117	0.0007	279.5	6.1	276.2	17.4
VNE4_z23_rim	0.0507	0.0061	0.0399	0.0014	0.2786	0.0333	0.0111	0.0012	252.2	8.9	249.5	26.4
VNE4_z25_rim	0.0522	0.0045	0.0403	0.0011	0.2896	0.0245	0.0127	0.0010	254.7	6.5	258.2	19.3
VNE4_z25_core	0.0528	0.0042	0.0472	0.0011	0.3431	0.0268	0.0120	0.0008	297.4	7.0	299.5	20.2
VNE4_z34_rim	0.0524	0.0079	0.0466	0.0020	0.3364	0.0499	0.0142	0.0019	293.5	12.6	294.4	37.9
VNE4_z35_rim	0.0584	0.0048	0.0436	0.0011	0.3503	0.0285	0.0137	0.0010	275.0	6.7	305.0	21.5
VNE4_z37_rim	0.0522	0.0069	0.0389	0.0015	0.2795	0.0361	0.0107	0.0012	245.7	9.2	250.2	28.6
Plesovice(Copy1)	0.0539	0.0046	0.0561	0.0014	0.4168	0.0349	0.0176	0.0014	351.8	8.7	353.7	25.0
91500(Copy8)	0.0718	0.0063	0.1802	0.0047	1.7817	0.1541	0.0531	0.0040	1067.8	25.7	1038.8	56.3
91500(Copy9)	0.0740	0.0067	0.1807	0.0048	1.8427	0.1630	0.0528	0.0041	1070.9	26.3	1060.8	58.2
91500(Copy10)	0.0758	0.0071	0.1779	0.0049	1.8585	0.1703	0.0539	0.0044	1055.4	26.8	1066.4	60.5
91500(Copy11)	0.0750	0.0070	0.1802	0.0049	1.8607	0.1696	0.0545	0.0044	1067.9	26.9	1067.2	60.2

SAMPLE	**MVN3**								**SAMPLE**	**MVN3**		
Spot analysis	Pb_{207}/Pb_{206}	1se Pb_{207}/Pb_{206}	Pb_{206}/U_{238}	1se Pb_{206}/U_{238}	Pb_{207}/U_{235}	1se Pb_{207}/U_{235}	Pb_{208}/Th_{232}	1se Pb_{208}/Th_{232}	AGE Pb_{206}/U_{238} (Ma)	1se (Ma)	AGE Pb_{207}/U_{235} (Ma)	1se (Ma)
91500	0.07432	0.00181	0.17927	0.00238	1.8357	0.04529	0.0547	0.00115	1063	13.01	1058.3	16.22
91500(Copy1)	0.07288	0.00178	0.1791	0.00238	1.79829	0.04443	0.05401	0.00111	1062.1	13	1044.8	16.12
91500(Copy2)	0.07743	0.0018	0.18005	0.00238	1.92078	0.04539	0.05271	0.00106	1067.3	12.99	1088.3	15.78
91500(Copy3)	0.07668	0.00177	0.17628	0.00233	1.86223	0.04385	0.05319	0.00107	1046.6	12.76	1067.8	15.56
Plesovice	0.0528	0.00119	0.05303	0.00069	0.38559	0.00889	0.01646	0.00048	333.1	4.22	331.1	6.52
MVN3_z1.1_rim	0.05236	0.00131	0.04431	0.00058	0.31961	0.00813	0.01302	0.00024	279.5	3.6	281.6	6.25
MVN3_z1.1_core	0.05183	0.00127	0.04431	0.00058	0.31627	0.00792	0.01252	0.00024	279.5	3.6	279	6.11
MVN3_z1.2_rim	0.05264	0.002	0.044	0.00068	0.31834	0.01203	0.01137	0.0003	277.6	4.18	280.6	9.27
MVN3_z1.2_core	0.05203	0.00159	0.0448	0.00064	0.32085	0.00991	0.01196	0.00026	282.5	3.97	282.6	7.62
MVN3_z2_rim	0.05259	0.00135	0.04738	0.00065	0.34296	0.00898	0.01326	0.00033	298.4	4	299.4	6.79
MVN3_z2_rim2	0.05613	0.00302	0.04604	0.00082	0.35485	0.01887	0.01154	0.00043	290.1	5.08	308.4	14.14
MVN3_z2_core	0.05225	0.00142	0.04649	0.00063	0.33453	0.00927	0.01327	0.00029	292.9	3.88	293	7.05
MVN3_z3.1_rim	0.0525	0.00132	0.04594	0.00062	0.33211	0.00855	0.0133	0.00028	289.5	3.84	291.2	6.52
MVN3_z3.1_rim2	0.05101	0.00158	0.04693	0.00068	0.32939	0.01034	0.01327	0.00032	295.6	4.21	289.1	7.89
MVN3_z3.2_rim	0.05261	0.00133	0.04535	0.00062	0.32851	0.00852	0.01304	0.0003	285.9	3.84	288.4	6.51
MVN3_z3.2_core	0.05313	0.00164	0.04582	0.00065	0.33524	0.01045	0.01349	0.00035	288.8	4.02	293.6	7.95
MVN3_z3.3_core	0.05176	0.00158	0.04468	0.00063	0.3185	0.00982	0.01252	0.0003	281.8	3.89	280.7	7.56
MVN3_z5_rim	0.05244	0.002	0.04672	0.00073	0.3373	0.01292	0.01314	0.00042	294.4	4.52	295.1	9.81
MVN3_z5_core	0.05531	0.00206	0.04479	0.00069	0.34118	0.01275	0.01248	0.00035	282.5	4.24	298.1	9.65
MVN3_z6_rim1	0.05663	0.00427	0.07782	0.00177	0.6078	0.04528	0.0218	0.00125	483.1	10.61	482.2	28.6
MVN3_z6_rim2	0.05866	0.00322	0.04345	0.00082	0.34868	0.01894	0.013	0.00064	274.2	5.09	303.7	14.26
MVN3_z7.1_rim	0.05236	0.0018	0.04544	0.00068	0.32772	0.01139	0.01418	0.00039	286.4	4.19	287.8	8.71
MVN3_z7.2_rim	0.05631	0.00203	0.04573	0.0007	0.35468	0.01292	0.01359	0.00037	288.3	4.31	308.2	9.68
MVN3_z8.1_core	0.05361	0.00259	0.04579	0.00078	0.33814	0.01628	0.01331	0.00047	288.6	4.83	295.8	12.35
MVN3_z8.1_rim	0.05159	0.00253	0.04471	0.00075	0.31775	0.01556	0.01422	0.0005	282	4.65	280.2	11.99
MVN3_z8.2_rim1	0.05989	0.00256	0.03226	0.00054	0.26596	0.01151	0.01016	0.00035	204.7	3.39	239.5	9.23
91500(Copy4)	0.07757	0.00296	0.17267	0.00273	1.84525	0.07093	0.05241	0.00168	1026.8	15	1061.7	25.31
91500(Copy5)	0.07661	0.00303	0.18035	0.00289	1.90355	0.07589	0.05267	0.00175	1068.9	15.79	1082.3	26.54
91500(Copy6)	0.07385	0.00302	0.18114	0.00295	1.84303	0.07595	0.05597	0.00191	1073.2	16.08	1060.9	27.13
91500(Copy7)	0.0744	0.00319	0.17706	0.00294	1.81509	0.0782	0.05313	0.0019	1050.9	16.09	1050.9	28.21
Plesovice(Copy2)	0.05518	0.00237	0.05295	0.00088	0.40255	0.01752	0.01809	0.00076	332.6	5.4	343.5	12.68
MVN3_z8.2_rim2	0.05369	0.00233	0.04208	0.0007	0.31132	0.01363	0.01214	0.00044	265.7	4.34	275.2	10.55
MVN3_z9_rim	0.05336	0.00224	0.04618	0.00076	0.33952	0.0144	0.01448	0.00051	291	4.68	296.8	10.92
MVN3_z9_core1	0.05186	0.0028	0.04704	0.00088	0.33612	0.01824	0.01279	0.00055	296.3	5.4	294.2	13.86
MVN3_z9_core2	0.05351	0.00284	0.04605	0.00084	0.33958	0.01812	0.01374	0.00057	290.2	5.17	296.9	13.74
MVN3_z10.1_rim	0.05286	0.00324	0.04497	0.00091	0.32752	0.02021	0.01199	0.00058	283.6	5.64	287.7	15.46
MVN3_z10.2_core	0.05338	0.00275	0.0474	0.00087	0.34876	0.01804	0.01356	0.00058	298.6	5.35	303.8	13.58
MVN3_z11.1_rim	0.05416	0.00344	0.04616	0.00096	0.34464	0.02199	0.01349	0.00068	290.9	5.92	300.7	16.6
MVN3_z11.2_rim	0.05386	0.00284	0.04608	0.00085	0.34199	0.01817	0.01361	0.00058	290.4	5.21	298.7	13.74
MVN3_z11.3_rim	0.05549	0.00334	0.0465	0.00092	0.3556	0.02141	0.01386	0.00066	293	5.64	308.9	16.04

SAMPLE	**MVN3**								**SAMPLE**	**MVN3**		
Spot analysis	Pb_{207}/Pb_{206}	1se Pb_{207}/Pb_{206}	Pb_{206}/U_{238}	1se Pb_{206}/U_{238}	Pb_{207}/U_{235}	1se Pb_{207}/U_{235}	Pb_{208}/Th_{232}	1se Pb_{208}/Th_{232}	AGE Pb_{206}/U_{238} (Ma)	1se (Ma)	AGE Pb_{207}/U_{235} (Ma)	1se (Ma)
MVN3_z12_core	0.05252	0.00352	0.04504	0.00096	0.32602	0.02189	0.01326	0.00069	284	5.94	286.5	16.76
MVN3_z13.1_rim	0.05447	0.00338	0.04742	0.00095	0.3559	0.02209	0.01542	0.00077	298.6	5.88	309.2	16.54
MVN3_z13.2_rim	0.05179	0.00315	0.04561	0.00092	0.32555	0.01987	0.01344	0.00068	287.5	5.68	286.2	15.22
MVN3_z13.3_rim	0.05405	0.00366	0.04597	0.00099	0.34241	0.02313	0.01392	0.00076	289.7	6.08	299	17.5
MVN3_z14_rim	0.05317	0.0041	0.04414	0.00106	0.32336	0.02492	0.01434	0.00088	278.4	6.51	284.5	19.12
MVN3_z15_rim	0.05331	0.00618	0.04694	0.00157	0.34474	0.03956	0.01402	0.0013	295.7	9.69	300.8	29.87
MVN3_z16.1_rim	0.05281	0.00502	0.04616	0.00134	0.33563	0.03179	0.01204	0.00095	290.9	8.27	293.9	24.17
MVN3_z16.2_rim	0.05296	0.00363	0.0459	0.001	0.33494	0.02295	0.01276	0.00072	289.3	6.16	293.3	17.46
MVN3_z17_rim	0.05488	0.00356	0.04468	0.00095	0.33783	0.02193	0.01308	0.00072	281.8	5.85	295.5	16.64
MVN3_z17_core	0.05762	0.00606	0.04648	0.00145	0.36901	0.03859	0.01321	0.00114	292.9	8.96	318.9	28.62
MVN3_z18.1_rim	0.05385	0.0045	0.04696	0.0012	0.34841	0.02901	0.01346	0.00094	295.8	7.36	303.5	21.85
MVN3_z18.2_rim	0.05391	0.00458	0.04693	0.00123	0.34866	0.02952	0.01286	0.0009	295.7	7.57	303.7	22.22
MVN3_z19_core	0.05256	0.00571	0.04751	0.00156	0.34378	0.037	0.01296	0.00119	299.2	9.57	300	27.96
MVN3_z19_rim	0.06341	0.0057	0.04672	0.00129	0.40813	0.03635	0.02182	0.00166	294.3	7.96	347.5	26.21
Plesovice(Copy1)	0.05329	0.00824	0.05315	0.0024	0.38998	0.05977	0.01707	0.00234	333.8	14.68	334.4	43.66
91500(Copy8)	0.07462	0.00598	0.17934	0.00445	1.84391	0.14673	0.05337	0.0037	1063.3	24.32	1061.3	52.39
91500(Copy9)	0.07742	0.00628	0.176	0.00442	1.87766	0.15104	0.05409	0.0038	1045.1	24.22	1073.2	53.29
91500(Copy10)	0.07619	0.00632	0.18052	0.00462	1.8951	0.15593	0.05679	0.00409	1069.8	25.24	1079.4	54.69
91500(Copy11)	0.0744	0.00643	0.17818	0.00469	1.82659	0.15634	0.05151	0.00387	1057	25.69	1055.1	56.16

7.2 U-Pb DATING ON RUTILES

SAMPLE	**VM8**						**SAMPLE**	**VM8**				
Spot analysis	Pb_{207}/Pb_{206}	1se Pb_{207}/Pb_{206}	Pb_{206}/U_{238}	1se Pb_{206}/U_{238}	Pb_{207}/U_{235}	1se Pb_{207}/U_{235}	AGE Pb_{207}/Pb_{206} (Ma)	1se (Ma)	AGE Pb_{206}/U_{238} (Ma)	1se (Ma)	AGE Pb_{207}/U_{235} (Ma)	1 se (Ma)
SUGLUK-4	0.10639	0.00256	0.30498	0.00365	0.10511	4.48052	1738.5	43.48	1715.9	18.05	1727.4	19.47
SUGLUK-4	0.10897	0.00261	0.31299	0.00375	0.10993	4.70954	1782.3	43.14	1755.4	18.43	1768.9	19.55
SUGLUK-4	0.10744	0.00156	0.30002	0.00311	0.06291	4.45046	1756.4	26.32	1691.4	15.43	1721.8	11.72
PCAS207	0.17473	0.00368	0.35233	0.00439	0.17257	8.50065	2603.5	34.63	1945.7	20.94	2286	18.44
PCAS207	0.12544	0.00397	0.34104	0.00495	0.1804	5.90766	2035	54.92	1891.7	23.77	1962.4	26.52
VM8_3.1	0.74574	0.01662	0.29856	0.00476	0.61062	30.73617	4821.5	31.51	1684.2	23.62	3510.6	19.54
VM8_3.2	0.68217	0.01709	0.27876	0.00516	0.58914	26.23499	4693.6	35.6	1585.1	26	3355.3	21.96
VM8_3.3	0.76383	0.02695	0.18254	0.00405	0.5945	19.24179	4855.7	49.49	1080.8	22.06	3054	29.82
VM8_3.4	0.78544	0.01176	0.39277	0.00482	0.59374	42.59087	4895.6	21.19	2135.7	22.3	3832.9	13.83
VM8_3.5	0.5438	0.0123	0.12313	0.00183	0.18336	9.23661	4364.6	32.72	748.6	10.53	2361.8	18.19
VM8_3.6	0.68824	0.01166	0.21081	0.0026	0.30863	20.00582	4706.4	24.15	1233.1	13.83	3091.6	14.92
VM8_3.7	0.72611	0.02107	0.24071	0.00496	0.60058	24.09621	4783.3	40.96	1390.4	25.77	3272.3	24.3
VM8_3.8	0.66837	0.01204	0.16088	0.00205	0.23785	14.83102	4664.2	25.72	961.6	11.41	2804.5	15.26
VM8_3.9	0.73164	0.0216	0.21357	0.00407	0.56267	21.56716	4794.1	41.64	1247.8	21.61	3164.4	25.32
VM8_3.10	0.79433	0.01811	0.66041	0.01092	1.54924	72.35024	4911.6	32.1	3268.8	42.4	4361.3	21.45
VM8_4.1	0.57709	0.01567	0.11747	0.00195	0.22577	9.33062	4451.4	39.01	716	11.27	2371	22.19
VM8_4.2	0.65861	0.0202	0.14482	0.0029	0.34528	13.14428	4643	43.54	871.9	16.33	2690.1	24.79
SUGLUK-4	0.10697	0.00161	0.31251	0.00321	0.06687	4.61247	1748.4	27.32	1753	15.79	1751.5	12.1
SUGLUK-4	0.10556	0.00186	0.31336	0.00336	0.07752	4.56408	1724.1	32.06	1757.2	16.48	1742.7	14.15
PCAS207	0.14123	0.00254	0.37688	0.00421	0.1269	7.34436	2242.3	30.75	2061.7	19.7	2154.2	15.44
PCAS207	0.11549	0.00253	0.34089	0.00397	0.11483	5.43145	1887.5	38.93	1890.9	19.06	1889.8	18.13
VM8_4.3	0.59851	0.01348	0.1156	0.00171	0.1873	9.53907	4504.4	32.35	705.2	9.87	2391.3	18.05
VM8_4.4	0.80862	0.01572	0.46118	0.00657	0.9115	51.40973	4937	27.39	2444.8	28.97	4020	17.66
VM8_4.5	0.66314	0.01888	0.20042	0.00387	0.45039	18.32462	4652.8	40.45	1177.6	20.8	3006.9	23.67
VM8_4.6	0.70192	0.0155	0.23866	0.0038	0.4463	23.10993	4734.7	31.35	1379.7	19.76	3231.6	18.8
VM8_4.7	0.71476	0.01371	0.23828	0.00331	0.40077	23.49206	4760.7	27.25	1377.7	17.23	3247.5	16.61
VM8_4.8	0.65789	0.0212	0.14868	0.00297	0.37652	13.48416	4641.4	45.73	893.6	16.66	2714.2	26.4
VM8_4.9	0.6475	0.01484	0.17156	0.00263	0.30729	15.3188	4618.4	32.71	1020.7	14.48	2835.3	19.12
VM8_4.10	0.62619	0.02865	0.1534	0.00448	0.51387	13.23571	4570	64.68	920	25.03	2696.6	36.65
VM8_5.1	0.67976	0.01332	0.23176	0.00309	0.38041	21.71598	4688.5	27.92	1343.7	16.15	3171.1	17
VM8_6.1	0.60021	0.01876	0.13995	0.00271	0.31396	11.57191	4508.5	44.66	844.4	15.34	2570.4	25.36
VM8_6.2	0.61067	0.01335	0.17449	0.00246	0.28433	14.68775	4533.6	31.35	1036.8	13.47	2795.2	18.4
VM8_6.3	0.51785	0.00966	0.02293	0.00028	0.0274	1.63785	4292.8	27.15	146.2	1.78	984.9	10.55
SUGLUK-4	0.10626	0.00262	0.29568	0.00351	0.10252	4.33278	1736.2	44.42	1669.9	17.49	1699.6	19.52
SUGLUK-4	0.10527	0.00261	0.2977	0.00355	0.10309	4.32156	1719	44.94	1679.9	17.63	1697.5	19.67
PCAS207	0.11882	0.00299	0.35589	0.00443	0.14125	5.83358	1938.5	44.27	1962.7	21.05	1951.4	20.99
PCAS207	0.11545	0.00322	0.35272	0.00465	0.1511	5.61568	1886.9	49.44	1947.6	22.14	1918.5	23.19
VM8_6.4	0.62823	0.01325	0.11545	0.00147	0.18769	9.99555	4574.7	30.2	704.3	8.52	2434.4	17.33
VM8_6.5	0.72732	0.01429	0.17282	0.00209	0.30594	17.32615	4785.7	27.87	1027.6	11.49	2953.1	16.95
VM8_6.6	0.57822	0.01182	0.16086	0.00204	0.23486	12.82028	4454.2	29.46	961.5	11.35	2666.5	17.26

SAMPLE	**VM8**						**SAMPLE**	**VM8**				
Spot analysis	Pb_{207}/Pb_{206}	1se Pb_{207}/Pb_{206}	Pb_{206}/U_{238}	1se Pb_{206}/U_{238}	Pb_{207}/U_{235}	1se Pb_{207}/U_{235}	AGE Pb_{207}/Pb_{206} (ma)	1se (Ma)	AGE Pb_{206}/U_{238} (Ma)	1se (ma)	AGE Pb_{207}/U_{235} (ma)	1 se (ma)
VM8_6.7	0.58144	0.01273	0.14268	0.0019	0.22254	11.43516	4462.3	31.51	859.8	10.73	2559.3	18.17
VM8_4.11	0.56813	0.01501	0.11716	0.00179	0.21444	9.16762	4428.5	38.01	714.2	10.34	2354.9	21.41
VM8_4.12	0.72873	0.01197	0.31051	0.00334	0.47792	31.20486	4788.4	23.34	1743.2	16.42	3525.5	15.07
VM8_4.13	0.68594	0.01403	0.21834	0.00272	0.39008	20.65142	4701.5	29.1	1273.1	14.37	3122.4	18.29
VM8_4.14	0.66627	0.02398	0.24082	0.00548	0.6964	22.09671	4659.6	50.91	1391	28.49	3188	30.62
VM8_4.15	0.48038	0.01281	0.09675	0.00146	0.15085	6.40606	4182.1	38.87	595.4	8.56	2033.1	20.68
VM8_4.16	0.67528	0.01407	0.21167	0.00265	0.36901	19.70591	4679	29.69	1237.7	14.12	3077	18.1
VM8_4.17	0.60828	0.01304	0.12437	0.00167	0.20213	10.43658	4527.9	30.77	755.7	9.56	2474.3	17.95
VM8_4.18	0.67014	0.01611	0.16684	0.00229	0.32882	15.40807	4668	34.21	994.7	12.64	2840.8	20.35
PCAS207	0.13568	0.00321	0.32841	0.00398	0.13804	6.14394	2172.8	40.7	1830.7	19.33	1996.5	19.62
PCAS207	0.1164	0.00337	0.34703	0.00449	0.1541	5.56877	1901.6	51.08	1920.4	21.5	1911.3	23.82
SUGLUK-4	0.10966	0.0029	0.29627	0.00362	0.11264	4.47851	1793.8	47.42	1672.8	18.03	1727	20.88
SUGLUK-4	0.10817	0.00283	0.30555	0.00372	0.11339	4.55576	1768.8	47.17	1718.7	18.38	1741.2	20.72
SUGLUK-4	0.10621	0.00284	0.31461	0.00385	0.11709	4.60581	1735.4	48.21	1763.3	18.9	1750.3	21.21

16. APPENDIX 8: CHEMICAL U-Pb DATING

Spot analysis	UO_2	ThO_2	PbO	Tot wt%	U [ppm]	Th [ppm]	Pb_{meas} [ppm]	Pb_{calc}	$\Delta(Pb_{calc}-Pb_{meas})$	Age (guess)	Age (Ma)
VV1A-A1-1a	71.96	0.0	0.18	72.14	634323.2	13.18	1673.8	1673.7	0.0	18881614.4	18.9
VV1A-A5-1	73.17	0	0.36	73.53	644989.3	0.00	3364.2	3364.2	0.0	37258394.6	37.3
VV1A-A1-2a	92.82	0	2.38	95.20	818202.9	0.00	22093.9	22093.9	0.0	190034138.9	190.0
VV1A-A1-2b	93.02	0	2.39	95.41	819965.9	0.00	22186.7	22186.7	0.0	190415161.6	190.4
VV1A-A1-2c	92.51	0	2.37	94.88	815470.3	0.00	22001.1	22001.1	0.0	189872842.6	189.9
VV1A-A1-2d	92.88	0	2.43	95.31	818731.8	0.00	22558.1	22558.1	0.0	193828570.4	193.8
VV1A-A1-2e	92.70	0	2.44	95.14	817145.1	0.00	22650.9	22650.9	0.0	194981940.6	195.0
VV1A-A1-3	92.56	0.0596	1.86	94.48	815911.0	523.77	17266.7	17266.7	0.0	149495920.4	149.5
VV1A-A1-4	93.72	0	2.03	95.75	826136.3	0.00	18844.8	18844.8	0.0	160990896.7	161.0
VV1A-A1-5	93.70	0	2.17	95.87	825960.0	0.00	20144.4	20144.4	0.0	171945231.6	171.9
VV1A-A1-6	93.00	0	1.99	94.99	819789.6	0.00	18473.5	18473.5	0.0	159070476.0	159.1
VV1A-A1-7	91.94	0	1.56	93.50	810445.7	0.00	14481.7	14481.7	0.0	126538726.5	126.5
VV1A-A1-8	91.51	0	1.88	93.39	806655.3	0.00	17452.3	17452.3	0.0	152818246.9	152.8
VV1A-A9-1	86.25	0.0296	1.48	87.76	760288.7	260.13	13739.1	13739.1	0.0	127938062.4	127.9
VV1A-A9-2	85.11	0	0.87	85.98	750239.7	0.00	8047.6	8047.6	0.0	76333487.0	76.3
VV1A-A10-1	87.27	0	0.73	88.00	769280.0	0.00	6810.1	6810.1	0.0	63078167.1	63.1
VV1A-A11-1	88.82	0.0034	0.78	89.61	782943.1	29.88	7260.4	7260.4	0.0	66055040.1	66.1
VV1A-A12-1	92.56	0	0.65	93.21	815911.0	0.00	6042.4	6042.4	0.0	52821018.2	52.8
VV1A-A12-2	91.28	0	0.77	92.05	804627.9	0.00	7169.4	7169.4	0.0	63486000.3	63.5
VV1A-A12-3	90.61	0	0.91	91.52	798721.9	0.00	8486.7	8486.7	0.0	75617431.4	75.6
VV1A-A12-4	92.77	0	0.88	93.65	817762.1	0.00	8149.7	8149.7	0.0	70956244.3	71.0
VV1A-A1-9	92.66	0	1.57	94.23	816792.5	0.00	14574.6	14574.5	0.0	126362477.2	126.4
VV1A-A1-10	92.24	0	1.70	93.94	813090.2	0.00	15781.4	15781.4	0.0	137301673.1	137.3
VV1A-A1-11	87.36	0	1.37	88.73	770073.3	0.00	12717.9	12717.9	0.0	117061283.5	117.1
VV1B-A4-1	45.32	0	1.26	46.58	399493.2	0.00	11696.8	11696.8	0.0	205732866.3	205.7
VV1B-A5-1	79.43	0	0.07	79.50	700170.8	0.00	654.5	654.5	0.0	6696566.5	6.7
VV1B-A6-1	90.25	0.0137	0.70	90.96	795548.5	120.40	6488.0	6488.0	0.0	58135273.5	58.1
VV1B-A6-2	87.23	0	2.01	89.24	768927.4	0.00	18659.1	18659.1	0.0	171094694.5	171.1
VV1B-A6-3	89.62	0.0204	1.99	91.63	789995.1	179.28	18473.5	18473.5	0.0	164962529.7	165.0
VV1B-A6-4	89.91	0	1.29	91.20	792551.4	0.00	11975.3	11975.3	0.0	107202430.5	107.2
VV1B-A6-5	86.77	0	1.39	88.16	764872.5	0.00	12903.6	12903.6	0.0	119548763.0	119.5
VV1B-A6-6	89.63	0	2.26	91.89	790083.2	0.00	20979.9	20979.9	0.0	186932221.6	186.9
VV1B-A6-7	91.37	0	1.38	92.75	805421.2	0.00	12810.8	12810.8	0.0	112787737.3	112.8